

# Magnetic Field and Electric Current in the Solar Atmosphere

A thesis submitted in partial fulfilment of  
the requirements for the degree of

**Doctor of Philosophy**

*by*

**Sushree Sangeeta Nayak**

(Roll No. 16330007)

Under the guidance of

**Dr. Ramitendranath Bhattacharyya**

Professor

Udaipur Solar Observatory Division

Physical Research Laboratory, Ahmedabad, India.



Discipline of Physics

Indian Institute of Technology Gandhinagar

2021



To  
*my family*  
&  
*teachers*



# Declaration

I declare that this written submission represents my ideas in my own words and where others' ideas or words have been included, I have adequately cited and referenced the original sources. I also declare that I have adhered to all principles of academic honesty and integrity and have not misrepresented or fabricated or falsified any idea/data/fact/source in my submission. I understand that any violation of the above can cause disciplinary action by the Institute and can also evoke penal action from the sources which have thus not been properly cited or from whom proper permission has not been taken when needed.

(Signature)

(Name: Sushree Sangeeta Nayak)

(Roll No: 16330007)

Date: 24.06.2021



# CERTIFICATE

This is to certify that this thesis titled “**Magnetic Field and Electric Current in the Solar Atmosphere**” submitted by **Miss Sushree Sangeeta Nayak (Roll No. 16330007)** to the Indian Institute of Technology Gandhinagar, is a record of bona fide research work carried out under my supervision and has not been submitted elsewhere for a degree. I have read this dissertation and in my opinion, it is fully adequate, in scope and quality, for the degree of Doctor of Philosophy.



Dr. Ramitendranath Bhattacharyya  
Professor  
Udaipur Solar Observatory Division,  
Physical Research Laboratory,  
Ahmedabad, India.  
(Thesis Supervisor)

Date: 24.06.2021



---

## Acknowledgments

*I express my gratitude to my thesis supervisor Dr. Ramitendranath Bhattacharyya for his relentless patience during the thesis work. I feel blessed to work with such a humble mentor, who trusts my potential and lets me enjoy research without any restrictions. Thanks are due to the members of my Doctoral Studies Committee (DSC), Dr. Bhuwan Joshi, Prof. Shibu K. Mathew and Prof. Jitesh R. Bhatt, for their support. Their valuable suggestions and comments have not only enlightened me but helped me in evolving as a researcher. I am indebted to my collaborators Prof. Piotr K. Smolarkiewicz, Prof. Qiang Hu, Dr. Sanjay Kumar, Dr. Avijeet Prasad, and Dr. Girjesh R Gupta for enriching my knowledge in the field of computational and Solar Physics. I am thankful to Prof. Nandita Srivastava and Prof. Varun Sheel for letting me work with them during the course work. It is my great pleasure to thank all the faculty members who taught me during course work. I am obliged to the Dept. of Space, Govt. of India for the research grant offered to me during my tenure at PRL. I extend my gratitude to Dr. Anil Bhardwaj, Director, PRL, Ahmedabad and Prof. Sudhir K. Jain, Director, IIT, Gandhinagar for providing me timely administrative help and necessary facilities to carry out my research work. I am also thankful to Dr. Bhushit Vaishnav, Head Academic Services for his support with academic matters. I wish to acknowledge the support of Vikram-100 cluster and thank all the staff members of PRL computer center for providing excellent computational facilities. A special thanks is due to Mr. Jigar Raval for his magical spell over any computational issues. I thank SDO team members for providing data sets, and Vapor team members for their help in any technical issue. I appreciate the cooperation by administration and library staff members at USO, Ahmedabad and IIT, Gandhinagar. I am grateful to the staff of dispensary, canteen, house-keeping, and security personnel for making a healthy and safe environment during my time at USO and Ahmedabad.*

*I will be forever grateful to Litu, Karuna Bhai, Suvadip, Harish, Surendra, Priyank, Soumya, Sunita, Abdur, Nisha, Dipika and Avik for standing by me during difficult period of my life. I must thank Dr.(s) Deepak, Dipti, Supriya, Ranadeep, Rahul Yadav, Rahul Kushwaha, Subir, Akanksha, Sangeetha, and Mr.(s) Ayan, Prabir and Miss Sana for being kind and extending their help whenever I have asked for. Credits are due to Mrs Bharti Saradava, Late Mukesh M. Saradava, and Miss Bireddy Ramya for their affection, help and delicious dishes which make me feel like I am living in a homely environment. I am thankful to fellow students and post-docs at PRL for being a part of this journey. A big*

*thanks is to Sudarshan Bhaiya, Sohan ji, Vijay Bhaiya and Pradeep Bhaiya for their help without any hesitation in this deadly pandemic time. It may look unusual, but for the past four and half years, I have been attached to a squirrel family whose daily activities near my window (their temporary shelter and they like it), have kept me lively for these years.*

*It would be incomplete without accrediting Archana and Sandeep. The thesis would be unimaginable without your infinite affection, support and encouragements at every step of this phase of life. Without their constant support and motivation of my family members, I could not have completed the thesis work. My deep respect goes to all my teachers who have planted a seed of passion to do science from my childhood till now. Lastly, it would not have been possible without the unconditional love and support from my parents. A deep gratitude will never be enough in front of your dedication.*

**Sushree Sangeeta Nayak**

---

# Abstract

Transients like solar flares, coronal mass ejections (CMEs), coronal jets, etc. are ubiquitous in the solar atmosphere. For several decades, investigations including theoretical studies, numerical modeling and observations have been carried out to reveal the intriguing physics behind them. The events vary in energy, spatial and temporal scales; providing outstanding opportunities for a comprehensive study of the solar atmosphere. A better understanding of these events is not only of fundamental importance but is of practical significance to realize potential space-weather influences. A near-consensus exists in contemporary research that magnetic reconnection—a fundamental process in the solar atmosphere involving rearrangement of magnetic field line connectivity, conversion of stored magnetic energy to kinetic energy, heat and acceleration of charged particles—is responsible for the onset and the evolution of these events. Also, important is the site of magnetic reconnection where these transients are believed to be triggered. Magnetic null points (where the magnetic field vanishes), separators (connecting layers between null points), and quasi-separatrix surfaces (regions with a sharp change in field line connectivity) are the preferential locations where the vanishing of the magnetic field or local enhancement of the current density can initiate reconnection. Identifying these locations and realizing their influences on local magnetic field lines are interesting and important to investigate the dynamics near the transients. Therefore, the thesis aims to study the role of magnetic field and electric current in the transients and, specifically focuses on the topology near the locations of reconnection—highlighting their generation and evolution along with the impact on the neighboring magnetic flux systems.

The coronal magnetic field, where most of the transients are traced, is also important. The coronal magnetic field is obtained by extrapolating the photospheric magnetic field. Subsequently, the extrapolated field is used as an input to a magnetohydrodynamics (MHD) model to capture the evolution. The works in the thesis have utilized both extrapolated and analytically derived magnetic fields as the initial inputs. For the extrapolations, the non-force-free-field (NFFF)

model is employed in conjunction with the photospheric vector magnetograms from Helioseismic and Magnetic Imager (HMI) onboard Solar Dynamics Observatory (SDO). For the numerical simulation, we have used the well-established magnetohydrodynamics model EULAG-MHD. We have studied a blowout jet and a near co-temporal C-class flare hosted by the active region NOAA 12615 on 2016 December 5 via extrapolation and simulation. Near the jet, we find a pair of three-dimensional (3D) null points and a flux-rope (or mini-filament) lying below the nulls. In the simulation, the reconnection near the nulls initiates the jet and the cool materials escape from the mini-filament through the channel made by the ambient field lines of the corresponding spine axis. The simulation results validate the standard scenario where a mini-filament interacts with the ambient open field lines causing the jet material to eject (Sterling et al., 2015). In case of the C-class flare, we find the presence of a single 3D null and quasi-separatrix layer (QSL) in the extrapolated field. In the simulation, the dynamics near these topologies explain the flare onset and match well with the observational signatures.

We have then simulated an X-class flare on 2014 March 29, to understand the initiation process. In the extrapolated field we find one 3D null, a pair of flux ropes, a set of sheared arcades, and a set of magnetic loops connected to a distant region which, is affected by the flare. The MHD evolution also matches well with the observations. We have estimated the stored energy released during the process and found it to be  $\approx 6.8 \times 10^{31}$  ergs, again which is in agreement with the corresponding observational value. Another promising result is the value of Pearson correlation coefficient of  $\approx 0.7$  between the observed and simulated transverse magnetic fields toward the end of the simulation.

In the next work, we have explored a circular flare ribbon and found a 3D null co-located with the flare location. The footpoint motions of the field lines lying on the fan surfaces and spines are following the circular brightening and a distant region away from the ribbon location. These data-constrained simulations of different solar transients showcase the role of complex topologies and corroborate remarkably with observations, and hence, prove the efficacy of both

the extrapolation and MHD model.

Albeit their impact on triggering the transients, the generation of such null points in the solar atmosphere is counterintuitive. We sought out this issue by employing a two-pronged approach: (1) with the relaxation of a deformed potential null, and (2) relaxation of a modified Arnold-Beltrami-Childress (ABC) field—chaotic in nature and devoid of any null. The simulations show a spontaneous generation of 3D nulls, indicating their omnipresence in the solar atmosphere. Further, we also explore magnetic reconnections in the vicinity of the QSLs. We have investigated the effect of multiple sites of reconnection in a computational domain. The simulation results examine the role of plasma flow in presence of various topologies favoring magnetic reconnection. Overall, the thesis explores the importance of magnetic reconnection in the different solar transients via numerical and observational studies. Future studies will accommodate high-resolution magnetic field data from upcoming space and ground-based observations. Toward simulating more accurate dynamics of the transients, a data-driven model is also envisaged as a future assignment.

**Keywords:** Magnetic Reconnection; Magnetohydrodynamics; Magnetic fields; Corona; Flares; Activities.



# Contents

<b>Acknowledgements</b>	<b>i</b>
<b>Abstract</b>	<b>iii</b>
<b>List of Figures</b>	<b>xi</b>
<b>List of Tables</b>	<b>xxvii</b>
<b>1 Introduction</b>	<b>1</b>
1.1 Solar Flares . . . . .	5
1.2 Jets . . . . .	8
1.3 Coronal Mass Ejections . . . . .	11
1.4 Objective and Outline of the Thesis . . . . .	17
<b>2 Magnetic Reconnection, Extrapolation Models and Data Acquisition</b>	<b>19</b>
2.1 Magnetic Reconnection . . . . .	19
2.2 Coronal field models and extrapolation techniques . . . . .	28
2.2.1 Potential field . . . . .	30
2.2.2 The Linear-Force-Free-Field (LFFF) . . . . .	30
2.2.3 Non-linear-force-free-field (NLFFF) model . . . . .	33
2.2.4 Non-force-free-field (NFFF) model . . . . .	34
2.3 Data Acquisition . . . . .	37
2.3.1 Helioseismic and Magnetic Imager (HMI) . . . . .	38
2.3.2 Atmospheric Imaging Assembly (AIA) . . . . .	40

<b>3</b>	<b>Numerical Model</b>	<b>43</b>
3.1	Advection solver MPDATA . . . . .	44
3.1.1	Derivation of MPDATA . . . . .	44
3.1.2	EULAG-MHD . . . . .	51
3.2	Implicit large eddy simulation . . . . .	57
<b>4</b>	<b>Data-constrained Simulations</b>	<b>59</b>
4.1	Case-I: Simulation of a Coronal Jet . . . . .	59
4.1.1	NFFF Extrapolation of the AR 12615 . . . . .	61
4.1.2	Simulation Results and Discussions . . . . .	68
4.2	Case-II: Simulation of an X-class Eruptive Flare . . . . .	76
4.2.1	NFFF Extrapolation of AR 12017 . . . . .	77
4.2.2	Simulation Results and Discussions . . . . .	80
4.3	Case-III: Simulation of a Confined X-class Flare Associated with a Circular Flare Ribbon . . . . .	84
4.3.1	NFFF Extrapolation for the AR 12192 . . . . .	88
4.3.2	Simulation Results and Discussions . . . . .	93
4.4	Inferences . . . . .	98
<b>5</b>	<b>Simulations with Analytical Initial Conditions</b>	<b>101</b>
5.1	Generation of 3D nulls . . . . .	104
5.1.1	Initial Value Problems . . . . .	104
5.1.2	Simulation Results and Discussions . . . . .	105
5.2	Magnetic reconnection in the Presence of 3D Null and QSL . . . . .	113
5.2.1	Initial Value Problems . . . . .	114
5.2.2	Simulation Results and Discussions . . . . .	121
5.3	Inferences . . . . .	131
<b>6</b>	<b>Summary and Future Scopes</b>	<b>135</b>
6.1	Summary of The Thesis Work . . . . .	135
6.2	Future scopes . . . . .	138

**A Appendix** **141**

    A.1 Ideal limit of MHD,  $R_M \gg 1$  . . . . . 141

    A.2 Diffusive limit of MHD,  $R_M \ll 1$  . . . . . 143

**Bibliography** **145**

**List of Publications** **163**



# List of Figures

- 1.1 Magnetic loops in the solar atmosphere. . . . . 4
  
- 1.2 A schematic showing different stages of a flare; adapted from Benz (2017). . . . . 6
  
- 1.3 The schematic shows a modified version of CHSKP model; adapted from Shibata et al. (1995). . . . . 7
  
- 1.4 Two different types of jets, (a) an anemone jet, and (b) a two-sided jet; picture credit: (Shen, 2021). The arrow marks highlight the bright points near the base of both jets. . . . . 9
  
- 1.5 The figure depicts two different types of jets observed on Hinode on September 22, 2008, and September 20, 2008, respectively, (a) a standard jet, and (b) blowout jet; picture credit: (Moore et al., 2010). . . . . 9
  
- 1.6 A schematic depicting the eruption mechanism of a jet; adapted from Sterling et al. (2015). (a) Initial configuration, (b) the filament material is setting out to erupt, and (c) noteworthy is the both reconnections supporting the eruption of the cool material. . . 10
  
- 1.7 A numerical simulation showing the mini-filament eruption scenario in case of a jet; picture taken from Wyper et al. (2017). . . 11

1.8	The panels show two different types of CMEs captured by the Large Angle Spectrometric Coronagraph (LASCO) onboard SOHO; (a) a difference image of a narrow CME on the left with a less angular width and without any distinct three-part structure, and (b) a normal CME on the right with its characteristic three-part structure; picture credit for narrow cme (Kahler et al., 2001) and normal cme (Riley et al., 2008). . . . .	12
1.9	Eruption scenario in the tether-cutting model depicting the rise of the rise of the core flux system after the reconnection of the sheared field lines lying below it, picture credit: (Moore et al., 2001). . . . .	14
1.10	Eruption scenario in the breakout model showing the evolution of magnetic field with reconnection occurring near the null point situated above the central flux system or flux rope at the core, picture credit: (Antiochos et al., 1999). . . . .	15
1.11	MHD simulation showing the evolution of the magnetic field in torus unstable scenario, image credit:(Fan & Gibson, 2007). . . . .	16
1.12	MHD simulation showing the evolution of the magnetic field in kink unstable scenario, image credit:(Fan & Gibson, 2007). . . . .	16
2.1	Schematic representation of reconnection near an X-type null point.	20
2.2	Magnetic field lines near an o-type null point. . . . .	21
2.3	A schematic of a 3D null point with spine axis and fan plane with the null point located at the center. . . . .	22
2.4	Plot of a 3D null skeleton with its characteristic spine and fan field lines with the null point (marked by red iso-surface). . . . .	23
2.5	Depiction of (a) an oblique null, and (b) a spiral null. The red iso-surfaces shows the location of the null point. . . . .	24

2.6	Schematic representation of torsional spine reconnection, where the black and gray lines are magnetic field lines, the shaded surfaces are current density iso-surfaces, gray arrows indicate the direction of the current flow, while black arrows indicate the driving plasma velocity. Adapted from Pontin (2012). . . . .	25
2.7	Schematic of torsional fan reconnection, where different color field lines, shaded surfaces and arrows represent the same as depicted in Fig.-2.6. Adapted from Pontin (2012). . . . .	26
2.8	Schematic of spine–fan reconnection at an isolated null. Again, different color field lines, shaded surfaces and arrows represent the same as depicted in Fig.-2.6. Adapted from Pontin (2012). . .	26
2.9	Magnetic field lines near a fan-fan separator line. Adapted from Pontin (2012). . . . .	27
2.10	Distribution of $Q$ on the photospheric magnetogram plotted in iso-contours in the background. Picture credit: (Titov et al., 2002).	29
2.11	Depiction of the hyperbolic flux tube with magnetic flux surface $Q = 100$ on the same magnetogram shown in Fig.-2.10. Picture credit: (Titov et al., 2002). . . . .	29
2.12	Global magnetic field topology obtained with PFSS extrapolation. Image taken from <a href="http://www.cessi.in/solareclipse2020/images/obs_pred_eclipsedec2020_1.png">http://www.cessi.in/solareclipse2020/images/obs_pred_eclipsedec2020_1.png</a> . . . . .	31
2.13	variation of plasma beta over the atmosphere. Picture credit: Gary (2001). . . . .	34
2.14	The flowchart showing the algorithm used in the NFFF extrapolation (Hu et al., 2010). . . . .	37
2.15	A schematic showing the Zeeman effect an an atomic system. The magnetic field is aligned along the $z$ - and $x$ - axes respectively, showing the longitudinal (top) and transverse (bottom) Zeeman effect. Taken from Lites (2000). . . . .	39

- 
- 4.1 Evolution of the jet where the bright point is marked by an arrow. The base and the spire become well developed at  $\approx 06:00$  UT. . . . . 60
- 4.2 History of flare ribbons in 304 and 94 Å. Images in 304 Å show the development of flare ribbons, whereas dynamics of the overlying coronal loops are captured in 94 Å. Notable is a general ascent of loops, as indicated by changing positions of the arrow . . . . . 61
- 4.3 Number of iterations vs.  $E_n$ . The plot saturates asymptotically to 0.202, which indicates the extrapolated transverse field in the photosphere is within 20.2% of the magnetogram value whilst the longitudinal component  $B_z$  agrees exactly with the magnetogram. 62
- 4.4 (a) CEA projected vector magnetogram of AR 12615 at 05:48 UT on 2016 December 5 obtained from HMI. The saturated value of  $B_z$  is represented with the grayscale color bar. The blue and red arrows illustrate the vector plots of the transverse field components. (b) The reconstructed synthetic magnetogram. . . . . 63
- 4.5 Scatter plot of transverse components of the reconstructed vs. actual magnetic field. With a Pearson's coefficient of 1 as an exact match, the plot finds a value of 0.966. . . . . 64
- 4.6 (a) Top view of the extrapolated field lines. (b) Magnetic loops in 171 Å from the AIA at 05:48 UT, which is also the time slice for the magnetic field extrapolation. The field of view of the two panels are same. The general agreement with the 171 Å loops is appealing. (c) Lateral view of the extrapolated MFLs. The regions of interest are MFLs spanning a pair of 3D nulls (red and blue), a single 3D null (cyan and peach), and a QSL marked by the purple MFLs. . . . . 65

- 4.7 (a) Direct volume rendering (DVR) of the Lorentz force exerted by the extrapolated field. (b) DVR of the volume current density of the extrapolated field. The slower decay of volume current density with height in comparison to the Lorentz force, which signifies an effectively force-free corona, is important. (c) An additional plot showing the variations of Lorentz force and current over the height. 66
- 4.8 Left column shows close ups of the magnetic nulls (in pink) with corresponding MFLs and the MFLs for the QSL (in descending order). The right column is the corresponding top-down view where the bottom boundary is superimposed with  $\ln Q$  contours having  $\ln Q \in \{3, 6\}$ . The viewing angle of the panels is according to the orientation of the axes. The footpoints tracing the  $Q$ -contours, which have large values, signify a sharp change in MFL connectivity. A region with QSL is characterized by its large  $Q$  value. The presence of highly twisted MFLs—in yellow at the left. . . . . 67
- 4.9 Temporal variations of positive and negative magnetic fluxes across the photosphere. . . . . 69
- 4.10 Snapshots of field line evolution during  $t \in \{05 : 48, 06 : 05\}$  UT, covering the jet. Notable are the conversions of anchored MFLs constituting the rope into the outer spine (panel (d)). Consequently, the entrapped cold plasma can get funneled out along the open MFLs of the outer spine and generate the spire. Instantaneous velocity vectors are illustrated in green. Noticeably, the flow vectors become more field-aligned with time. . . . . 70
- 4.11 Jet corresponding MFLs overlaid with the boxed part of (b) 304 Å and (c) 131 Å images. The similarity is recognizable. . . . . 71

- 4.12 Depiction of the flux-rope evolution only. Noticeable is the development of the X-type null marked by red circles in panels (c) and (d). The null is the location for internal MRs envisaged in the standard scenario of flux-rope eruption. Further dynamics of the null is depicted in panels (e) and (f). The whole evolution covers approximately the first 5 minutes of the jet. . . . . 72
- 4.13 Sequences of the single null during its evolution in the time span  $\approx t \in \{05 : 48, 06 : 13\}$  UT. The left column shows a general ascent of MFLs after an initial contraction. The right column focuses on the MFL dynamics near the  $Q$ -contours. Footpoints of the two MFLs in pink are seen to trace the  $Q$ -contours. The motion is due to slip MRs as the tangential component of the local plasma flow (white arrows) is in a direction different than the footpoint motion. . . . . 73
- 4.14 Superimposition of extrapolated MFLs on the flare ribbons at 304 Å (panels (b) and (d)), 131 Å (panels (c) and (e)); each at two different viewing angles. The box on the top figure represents the span of the above two images with respect to the full active region cutout. The locations of the ribbons reasonably match with footpoints of the MFLs executing slip MRs. . . . . 74
- 4.15 Left-side footpoints of MFLs locating the QSL (marked by  $Q$ -constant contours) sustain a motion—which is more distinguishable in the animation. The sequence covers the range  $t \in \{05 : 48, 06 : 13\}$  UT (approx). The motion is because of slip MRs, as the tangential component of the bulk flow is directed differently. 75

- 4.16 Panels (a)–(d) correspond to the pre-flare stage and panels (e)–(h) belong to the flaring evolution. The high intensity regions are highlighted by the green contours in the channel  $1600 \text{ \AA}$  (panels (a) and (e)). Two regions R1 and R2 denoted by white boxes represent the locations of flare kernel and the distant brightening, respectively. A pair of the filaments is identified in  $304 \text{ \AA}$ , indicated by white arrows in panel (b). The pre-flare loops are shown in  $171 \text{ \AA}$  (panel (c)). The loops marked by green arrows connect R1 and R2 (panel (f)). White arrow in panel (d) marks the sigmoid in  $94 \text{ \AA}$  before the onset of the flare. Post-flare hot loops in  $94 \text{ \AA}$  are marked by white and green arrows in panel (h). 78
- 4.17 The plot shows the correlation between the observed and reconstructed transverse fields of AR12017. . . . . 79
- 4.18 Logarithmic variation of current and Lorentz force over the height in the extrapolated domain. . . . . 79
- 4.19 Panel (a) shows the extrapolated MFLs overlaid with the  $z$  component of  $\mathbf{B}$  on the bottom boundary of range  $\{-600, 600\}$ G. Important features of the MFLs are (1) a 3D null represented by pink and skyblue MFLs, (2) two MFRs (chartreuse and red colors), (3) a set of sheared arcades (ultramarine color) and, (4) the loops connecting the R1 and R2 (golden color). Insets in panel (a) depicts the zoomed-in view of the MFRs overlaid with the twist  $T_w$  on the bottom boundary with the range  $T_w \in \{-1.6, 1.6\}$  and the null point. Panel (b) illustrates the Direct Volume Rendering of current density. High values of current are evident near the MFRs (inset). . . . . 81

- 4.20 Simulated dynamics spanning the flaring time,  $t \in \{17:30, 18:10\}$ UT. Panel (a) depicts the MFLs at the start of the simulation. Important are the MRs (marked by green arrow in panel (b)) at the null which change the connectivity of the spine and fan MFLs. The footpoints of the fan surface MFLs almost trace the brightenings observed in  $304 \text{ \AA}$  at  $\approx 17:49$  UT (panel (c)). The sheared MFLs (in ultramarine) and the yellow MFLs (marked by red arrow) also appear to engage in MRs near the null. The post-reconnection MFLs (marked by black arrows in panel (d)) are comparable with the observed post-flare loops (Fig.-4.16). . . . . 83
- 4.21 Evolution of the MFRs and the overlying sheared arcades during the early phase,  $t \in \{17:30, 17:31\}$ UT. Panel (a) is overlaid with initial Lorentz force (in purple). Panels (b)-(f) are overplotted with streamlines of the flow (in dark green). Notable are the nearby legs of the ropes which are rooted in opposite polarities (panel (a)). The twist of both the ropes reduces with time (see panels (b)-(f)). . . . . 83
- 4.22 Temporal profile of the normalized kinetic (blue) and magnetic (yellow) energies. . . . . 84
- 4.23 (a) GOES 15 X-ray flux for AR 12192 on 24th October, 2014 plotted with time during the X3.1 flare event. Notable is the peak around 21:15 UT indicating the flare. (b) The evolution of positive and negative magnetic flux at the photospheric boundary during the flare. The vertical dashed lines mark the interval between onset and peak of the flare. Importantly, there is no appreciable flux change within the interval. . . . . 85

- 4.24 The AR 12192 observed in AIA 1600 Å (panel (a)) during the flare at 24th October, 2014 at 21:21 UT and AIA 131 Å (panel (b)) at 20:58 UT. The abscissa and ordinate are in arcsecond with one unit corresponding to a physical length of 720 km. Important is the circular brightening located approximately between 150 and 200 arcsecond along the abscissa. . . . . 86
- 4.25 (a) Photospheric vector magnetogram from HMI of AR 12192 remapped on a CEA projection at 20:46 UT on 2014-10-24, highlighting the magnetic field line topology before the flare. The black and white contours represent the negative and positive polarities of  $B_z$  whereas the red and blue arrows are the vector plots of the transverse magnetic field. (b) AIA 171 Å EUV image of the AR, highlighting the magnetic field line topology before the flare. . . . 87
- 4.26 Contour plots of the transverse field of the observed (panel (a)) and extrapolated (panel (b)) magnetic field shown at the photospheric boundary. . . . . 88
- 4.27 Scatter plot showing the correlation between the observed and extrapolated magnetic field. The red line is the expected profile for perfect correlation. . . . . 89
- 4.28 Top (panel (a)) and side-view (panel (b)) of the overall NFFF extrapolated magnetic field line topology for the AR 12192 on 2014, October 24, 20:46 UT. The bottom boundary represents the strength (in kG) of the  $B_z$  component of the magnetic field and the extrapolated fields lines are depicted in red and a small set of field lines close to the location of the 3D null—identified in the Fig.-4.29—are depicted in white. . . . . 90

- 4.29 The top- (panel (a)) and side-view (panel (b)) of the magnetic field lines drawn near one of the polarity-inversion lines, where the flare was later observed. The field line topology indicates the presence of a 3D null, complete with a dome-shaped fan and elongated spine. The red surface inside the field lines represents an iso-surface having 2.5% of the maximal field strength of  $B$  and locates the null. The height of the null is roughly 3 Mm from the photosphere. The bottom boundary is same as that of Fig.-4.28. . . . . 91
- 4.30 The spatial distribution of volume current density (panel (a)) and Lorentz force (panel (b)) in arbitrary units. Notably, appreciable current is present throughout the volume while most of the force is present only near the bottom boundary which sharply falls to zero with increase in height. . . . . 92
- 4.31 Side view of evolution of four sets of magnetic field lines close to location of the 3D null, shown at  $t = 0, 200, 400, 600, 800$  and  $1000$  in panels (a)-(f) respectively. The bottom boundary in all the panels represents the strength  $B_z$  on the photospheric plane as in Fig.-4.28 but now in grayscale for clarity. . . . . 94
- 4.32 Panels (a)-(f) spanning  $t = 0, 80, 160, 240, 320$  and  $400$ , illustrate rotation of the dome structure of the field lines constituting the 3D null. The cuboidal rake in the figure shows the volume where the seed points are chosen. The field lines are color-coded with respect to their distance in the  $y$  direction. This helps us to visualize the rotation of the field lines. . . . . 95
- 4.33 Panels (a)-(f) spanning  $t = 0, 200, 400, 600, 800$  and  $1000$ , illustrate the evolution of magnetic field lines (yellow), velocity field (green) and  $|\mathbf{J}|/|\mathbf{B}|$ . . . . . 96

- 4.34 Panels (a)-(f) spanning  $t = 0, 200, 400, 600, 800$  and  $1000$ , illustrate the slipping reconnections in the MFLs (shown in yellow) spanning the dome of the 3D null. The streamlines of the flow are shown in green. The bottom boundary shows contours of high values of  $\log Q$ . (An animation of this figure is available.) . . . . . 97
- 4.35 The AIA  $1600 \text{ \AA}$  and  $131 \text{ \AA}$  channel images as depicted in Fig.-4.24 are overlaid with the relevant magnetic field lines. Important is the almost exact match of footpoints with the location of the brightening. . . . . 98
- 5.1 History of the normalized (a) magnetic and (c) kinetic energies, along with the grid-averaged (b) field-aligned current density and (d) volume current density during the deformation with the sinusoidal initial velocity. Notable are the approximate constancy of the field-aligned current and a non-zero value of the volume current density at the terminal state. . . . . 106
- 5.2 MFL evolution during the deformation seen from two different angles. The MR initiates as the spine and fan approaches each other, panels (c) and (d). Important are the pitchfork bifurcation of the 3D null and the flux ropes, marked by arrows, as shown in panel (e) and (f), respectively. With MFLs drawn in a favorable viewing angle, the panel (f) shows the post-reconnection fan plane to be sandwiched between the two flux ropes (in magenta and blue). Also the net topological degree (denoted by  $D$ ) is preserved ( $D = +1$ ) which is in congruence with the theory. The magnetic field for the MFLs in panels (e) and (f) serves as the initial field for the relaxation. Red, green, and blue arrows mark  $x$ ,  $y$ , and  $z$  axes, respectively. . . . . 107

- 5.3 Evolution of the (a) magnetic energy, (b) field-aligned current density, (c) kinetic energy and (d) volume current density for the relaxation initiated with the magnetic field obtained by the sinusoidal deformation. The magnetic energy decays almost monotonically signifying relaxation of the magnetofluid. Both the energies attain a quasi-steady state from  $t \approx 100s$  onward. The first peak in the kinetic energy develops as the increase in flow velocity gets arrested by viscosity. Also important are the non-zero current density at the terminal state along with an overall decrease in the field-aligned current and hence, the twist; which is consistent with the decay of magnetic energy. . . . . 108
- 5.4 MFL evolution during the relaxation where the initial field was obtained by the sin flow deformation. Important is the generation of the null point and its fine-tuning across the panels (c)–(f) which belongs to the quasi-steady phase of evolution. The terminal null at the panel (f) is non-potential because of the non-zero volume current density. The change in connectivity of the blue MFL suggests occurrence of MR. . . . . 109
- 5.5 Panel (a) shows a single MFL ergodically spanning a local magnetic flux surface. Shifting the initial point for the MFL integration such as to increase the surface radius is documented in panels (b) and (c). After the attainment of a threshold radius, the flux surface is lost and the MFL becomes volume-filling as depicted in panel (d). . . . . 110
- 5.6 Evolution of (a) magnetic energy, (b) field-aligned current density, (c) kinetic energy and (d) volume current density for the relaxation initiated with the modified ABC magnetic field. The generation of the quasi-steady state is evident whereas the volume current density at the terminal state is non-zero. . . . . 111

- 5.7 Overall evolution of MFLs as the fluid relaxes from the initial modified ABC field. The change in connectivity of the blue MFL, panels (b) and (c), showcases an instance of MR. Such MRs and the corresponding connectivity changes play a crucial role in the relaxation. The development of the 3D null spans from the panels (b) to (d). . . . . 112
- 5.8 Evolution of MFLs in the neighborhood of the nulls depicted in panel (d) of Fig.-5.7. The arrowheads point the magnetic field directions. Notably, the nulls have both +1 and -1 topological degrees which suggest a conservation of net topological degree. . . 113
- 5.9 Side (panel (a)) and top (panel (b)) views of MFLs of the  $\mathbf{B}$  for  $c_0 = 0.1$ . While panels (c) and (d) illustrate side and top views of the MFLs for  $c_0 = 0.5$ . The MFLs are in the form of twisted closed (marked by navy blue color) as well as open magnetic loops (shown in grey color). All the panels are overplotted with  $B_z$  values on the  $z = 0$  plane. Yellow line represents the contour corresponding  $B_z = 0$ . . . . . 117
- 5.10 Panel (a) shows the neutral points and the field lines of the transverse field overlaid with the function  $\psi$  at  $z = 0$  plane. Large values of  $\psi$  represent the locations of neutral points. Notable is the existence of the nine X-type (one inside the domain and eight at the boundaries) and four spiral-type neutral points. Panel (b) depicts the magnetic nulls (in pink) and MFLs of  $\mathbf{B}_1$  overlaid with the corresponding  $Q$ -map at  $z = 0$ . The nine X-type neutral points of the transverse field also retain in  $\mathbf{B}_1$ . Noticeable is the larger values of  $Q$  near the sites of the spiral neutral points (marked by black arrows)—suggesting that the spiral neutral points correspond to QSLs in  $\mathbf{B}_1$ . In the figure, the domain size is marked as 1 instead of  $2\pi$  in all the directions. . . . . 117

- 5.11 Magnetic (topological) skeleton of the initial field  $\mathbf{B}$  in terms of 3D nulls, separatrix surfaces and spines for  $c_0 = 0.1$  (side view in panel (a) and top view in panel (b)) and  $c_0 = 0.5$  (side view in panel (c) and top view in panel (d)). Notable are straight spine axes and the dome-shaped separatrix or fan surfaces (intersecting bottom boundary) of the nulls. For  $c_0 = 0.1$ , the separatrix domes touch at the base of the quasi-separator at  $(\pi, \pi, 0)$  (panel (b)). For  $c_0 = 0.5$ , the separatrix domes are separate (panel (d)). . . . . 118
- 5.12 The structural skeleton (i.e., the separatrix skeleton plus the QSL quasi-skeleton) of  $\mathbf{B}$  with the bottom boundary being superimposed with  $\ln Q$  for  $c_0 = 0.1$  (side and top views in panels (a) and (b)) and  $c_0 = 0.5$  (side and top views in panels (c) and (d)). The existence of large  $Q$  (such that  $\ln Q \in \{2, 8\}$ ) represents the location of separatrices or QSLs. For both  $c_0$  values, notable is the presence of both the separatrices of the coronal nulls and also the QSLs associated with the central quasi-separator at  $(\pi, \pi, z)$  and the extra quasi-separators on the boundary. Also interesting is the larger  $Q$  values for  $c_0 = 0.1$  than 0.5 at the central quasi-separator at  $(\pi, \pi, z)$ . . . . . 119
- 5.13 Evolution of field lines of the transverse field (in cyan color) at  $z = 0$  plane for  $c_0 = 0.5$ . The figure is further overplotted with the streamlines of the flow (in green color), Lorentz force (red arrows) and, the neutral points (in pink). . . . . 123
- 5.14 Evolution of the topological skeleton of  $\mathbf{B}$  for  $c_0 = 0.5$  (Figs.-5.10(c) and (d)). Panel (a) is overlaid with Lorentz force (red arrows) at the bottom boundary. The rotation of the separatrix surfaces is evident from the movement of the blue MFLs (further marked by black arrows). . . . . 124

- 5.15 Evolution of a 3D null along with the fan surface (represented by cyan MFLs) for  $c_0 = 0.5$ . The figure is further overplotted with two sets of MFLs (in yellow) situated below the dome and the  $J - 70$  surfaces (in pink). The movement of MFLs of the dome is marked by a blue MFL. Important are the appearances of the  $J - 70$  surfaces at the fan surface and change in the connectivities of the yellow MFLs. . . . . 125
- 5.16 Evolution of 3D nulls with bottom boundary being overplotted with  $\ln Q$  ( $c_0 = 0.5$ ). The regions of strong  $Q$  in the initial field are marked by QL in panel (a). We also plot the streamlines of plasma flow (green arrows) near the three QSLs marked by rectangular boxes in panel (a), some of which are separatrices. Currents having sufficiently high values are shown at a  $z$ -constant plane (in pink). The motion of the dome MFLs is depicted from the blue MFLs. The direction of the MFLs movement is largely different from the flow direction—manifesting the flipping MFLs in the separatrices and QSLs. . . . . 126
- 5.17 Time sequences of the transverse field (in cyan color) at the bottom boundary for  $c_0 = 0.1$ . The flow (green arrows), the Lorentz force (red arrows) and the neutral points (in pink) are also overplotted in the figure. . . . . 127
- 5.18 Time profile of the magnetic skeleton (3D nulls, separatrix dome surfaces and spines) of  $\mathbf{B}$  for  $c_0 = 0.1$  (see Figs.-5.10(a) and (b)). Red arrows in panel (a) show the direction of Lorentz force at the lower boundary. Evident is rotational motion of the separatrix domes, as illustrated by the blue MFLs and black arrows. . . . . 128

- 5.19 Time evolution of a 3D null with the fan surface and spine (denoted by cyan MFLs) for  $c_0 = 0.1$ . The figure is further overlaid with two sets of magnetic loops located at different heights (in colors green and yellow) under the fan surface at  $t = 0s$  and, the  $J - 70$  surfaces (in pink). The motion of dome MFLs can be tracked by a blue MFL. Notable are the appearances of the  $J - 70$  surfaces inside the fan surface which later extend toward the fan (marked by black arrows in panel (c)). With time, the yellow MFLs change their connectivities. . . . . 129
- 5.20 Time evolution of MFLs in the vicinity of a  $J - 70$  surface for  $c_0 = 0.1$ . Initially, the MFLs are in form of closed parallel loops situated at two different heights (panel (a)). As time progresses, the loops become increasingly non-parallel, resulting in the formation of CS. 130
- 5.21 Time profile of 3D nulls with  $lnQ$  being superimposed at the lower boundary for  $c_0 = 0.1$ . Two sets of MFLs (in colors purple and green) are plotted near the QSL located in the central region around  $(\pi, \pi, z)$ . The figure also shows the streamlines of plasma flow (grey arrows) and initial Lorentz force (red arrows) near the QSL. Notable is the change in the topology of the purple and green MFLs. . . . . 130
- 5.22 Histories of kinetic (top panel) and magnetic (bottom panel) energies for  $c_0 = 0.1$  and  $c_0 = 0.5$ . The solid line is for  $c_0 = 0.1$ , while the dashed line corresponds to  $c_0 = 0.5$ . The energies are normalized to the initial total energies. Notable is the higher height of the peaks in the kinetic energy and the larger decay of the magnetic energy for  $c_0 = 0.1$  than  $c_0 = 0.5$ . . . . . 132

# List of Tables

- 2.1 Primary ions observed by AIA; Adapted from Lemen et al. (2012). 41



# Chapter 1

## Introduction

To quote E. N. Parker, “if it were not for its variable magnetic field, the Sun would have been a rather uninteresting star” (Low, 1996). The solar dynamo continuously converts this magnetic field into toroidal and poloidal components, back and forth, as the magnetic field lines (MFLs) break into the photosphere by the magnetic buoyancy (Parker, 1994), creating magnetically Active Regions (ARs). The corresponding magnetic field lines thread through the solar atmosphere—located above the photosphere, constituting the chromosphere ( $\approx 2$  Mm), transition region ( $\approx 10^4$  km) and the solar corona (from 2 Mm onward). The solar atmosphere being at a temperature  $> 4000\text{K}$ , it is at a plasma state—the fourth state of matter comprising almost 97% of the visible universe (<https://farside.ph.utexas.edu/teaching/plasma/Plasma/Plasmahtml.html>). In conjugation with the plasma, the magnetic field provides a cradle for a myriad of fundamental processes which manifest themselves as spectacular transient events. The events heat the plasma, release energies in the range  $10^{26-32}$  ergs while accelerating charged particles, particularly when the Sun is magnetically active and the plasma is most structured. Understanding these events is essential because of their fundamental nature as well as their possible influence on the space assets. Importantly, magnetic reconnection (MR): the process in which magnetic energy gets converted into heat and accelerates charged particles along with a general rearrangement of magnetic field lines, are believed to be responsible for the transients. The MRs are ubiquitous in both astrophysical and laboratory plasmas.

Examples are the tail of magnetosphere, the accretion disks, the tokamak, the reverse field pinch etc. and can explain the million degree Kelvin temperature of the solar corona (Parker, 1994).

Traditionally, most of the solar coronal plasma is approximated to have a large electrical conductivity and governed by the equations of single fluid magnetohydrodynamics, hereafter referred as magnetohydrodynamics (MHD) (Alfvén, 1942). The MHD description treats the plasma as a continuum, coupling Maxwell's equations with Navier-Stokes equations and is valid if the system size and time scale are much larger than the ion skin depth and the ion gyroperiod. To satisfy the quasineutrality condition, the volume current density is expressed by the Ampere's law and the displacement current is neglected. The MHD equations along with their physical significance are listed below.

- Equation of motion (conservation of momentum)

$$\rho \frac{D\mathbf{v}}{Dt} = -\nabla p + \frac{1}{4\pi}(\nabla \times \mathbf{B}) \times \mathbf{B} + \rho \mathbf{g}, \quad (1.1)$$

where,  $\frac{D}{Dt} \equiv$  total derivative,  $p$  is the kinetic or gas pressure,  $\rho \equiv$  plasma density,  $\mathbf{B} \equiv$  magnetic field,  $\mathbf{v} \equiv$  plasma velocity,  $g \equiv$  gravitational acceleration.

- Continuity equation (conservation of mass)

$$\frac{\partial \rho}{\partial t} + \nabla \cdot (\rho \mathbf{v}) = 0, \quad (1.2)$$

- Solenoidality condition

$$\nabla \cdot \mathbf{B} = 0, \quad (1.3)$$

- Ampere's law in pre-Maxwellian form

$$\nabla \times \mathbf{B} = \frac{4\pi}{c} \mathbf{J}, \quad (1.4)$$

- Induction equation

$$\nabla \times \mathbf{E} = -\frac{1}{c} \frac{\partial \mathbf{B}}{\partial t}, \quad (1.5)$$

- Ohm's law

$$\mathbf{E} + \frac{\mathbf{v} \times \mathbf{B}}{c} = \eta \mathbf{J}, \quad (1.6)$$

- Energy equation

$$\frac{d}{dt} \left( \frac{p}{\rho^\gamma} \right) = 0, \quad (1.7)$$

where,  $\mathbf{J}$  is the current density,  $\eta$  is the electrical resistivity and  $\gamma$  is the ratio of specific heats. As evident, the MHD equations are a combination of hydrodynamic equations and Maxwell's equations satisfying the quasineutrality that is fundamental to plasma.

Eq.s-1.4, 1.5 and 1.6 can be combined to generate the induction equation,

$$\frac{\partial \mathbf{B}}{\partial t} - \nabla \times (\mathbf{v} \times \mathbf{B}) = \lambda \nabla^2 \mathbf{B}. \quad (1.8)$$

$\lambda \equiv \frac{\eta c^2}{4\pi}$  is the magnetic diffusivity. The ratio between the advective term ( $\nabla \times (\mathbf{v} \times \mathbf{B})$ ) and the diffusive term ( $\lambda \nabla^2 \mathbf{B}$ ) defines the Magnetic Reynolds number

$$R_M = vL/\lambda, \quad (1.9)$$

where  $L \equiv$  the length scale over which the magnetic field varies. The  $R_M$  determines the effect of advection over the diffusion in a fluid, specifying two important limits of MHD. If  $R_M \gg 1$ , then the induction equation reduces to

$$\partial \mathbf{B} / \partial t - \nabla \times (\mathbf{v} \times \mathbf{B}) = \mathbf{0}, \quad (1.10)$$

which ensures magnetic field lines to be tied with the plasma parcels (see Appendix A)—the flux-freezing condition. For example, magnetic field lines traces the plasma loops observed in the corona, shown in Fig.-1.1. Along with the Ampere's law, a general picture then emerges. An unbalanced force accelerates plasma parcels through the Eq.-1.1. Consequently, the frozen-in field lines will deform and generate a current in accordance with the Ampere's law. The flow-

field interaction can sharpen the magnetic field gradient by a local decrease in  $L$ , in effect, decreasing  $R_M$  and the induction equation reduces to the other limit,

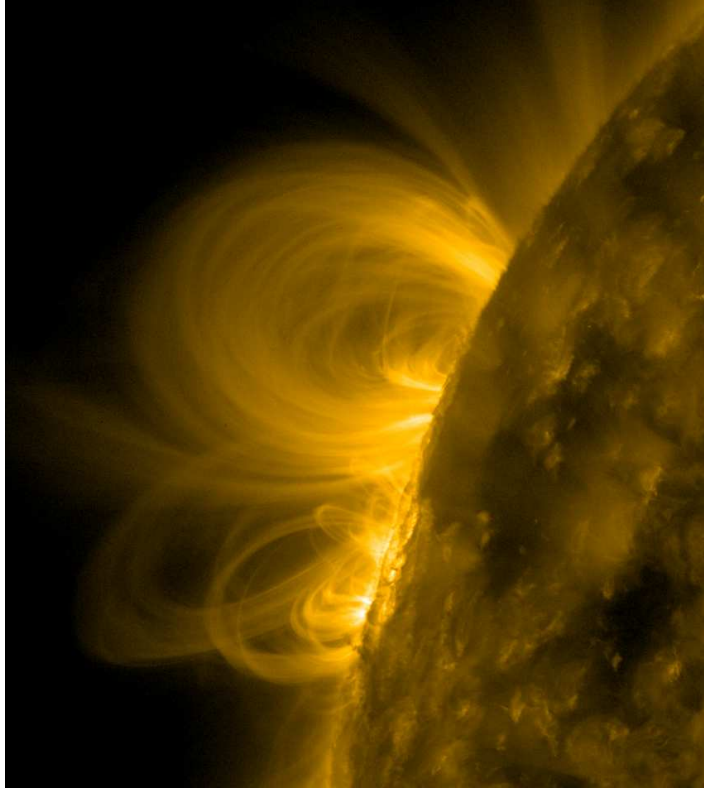


Figure 1.1: Magnetic loops in the solar atmosphere.

$$\partial \mathbf{B} / \partial t = \lambda \nabla^2 \mathbf{B}. \quad (1.11)$$

The above equation represents the diffusive limit of the induction equation which describes MFLs to diffuse out from the plasma parcels over a time scale  $\tau_d = L^2/\lambda$ , known as the diffusion time scale (see Appendix A). If the orientations of these diffused field lines from different plasma parcels are favorable, the MFLs can reconnect and generate the solar transients. In the following we present a brief overview of these transients, the list is not exhaustive but focuses on those relevant to the thesis. Importantly, in the frozen-in limit, the magnetic field lines trace the plasma structure whereas the diffusion limit is achieved by an increase in the current density. In consequence, both the magnetic field and the current are important to understand the solar transients.

## 1.1 Solar Flares

Flares are the most intense radiative emissions from the solar atmosphere. They are of interest from their discovery on September 1, 1859 by R.C. Carrington and R. Hodgson (Carrington, 1859; Hodgson, 1859). Many studies have revealed their occurrences, sources of emission, associated magnetic configuration and their impact; utilizing both ground and space based observatories. The flares are not only observed over the whole range of electromagnetic spectrum but also have different temporal scales. The various stages of a flare includes

- pre-flare phase or precursor phase: where the building up of energy occurs with heating of the plasma, soft X-ray (SXR) emission is also detected at this stage.
- impulsive phase: where the stressed energy is released and particles accelerate, the signature is the X-ray footpoint sources appearing at the chromospheric height.
- intermittent phase or flash phase: where intensity in  $H\alpha$  increases rapidly.
- decay phase: where the coronal plasma relaxes (Benz, 2017). The stages of a flare in multi-wavelengths are depicted in the Fig.-1.2.

There is a near-consensus that the flares occur as the magnetic free energy stored in twisted magnetic field lines are released by magnetic reconnection. For the typical length scale and magnetic field on a sunspot, this stored magnetic energy can be

$$E \approx \left(\frac{B^2}{8\pi}\right)L^3 \approx 10^{33}\left(\frac{B}{10^3G}\right)\left(\frac{L}{10^9cm}\right) \text{ ergs}, \quad (1.12)$$

which is sufficient enough to produce a large flare (Shibata & Magara, 2011). Giovanelli (1947, 1948); Hoyle (1950) in their work, first suggested the role of hyperbolic X-type neutral points (where magnetic field vanishes) for the excitation of particles during flares and auroras. Later, (Dungey, 1953) in his work, first proved that the X-type neutral point to be a likely site to release charged particles in astrophysical plasmas. Further indirect evidences support similar

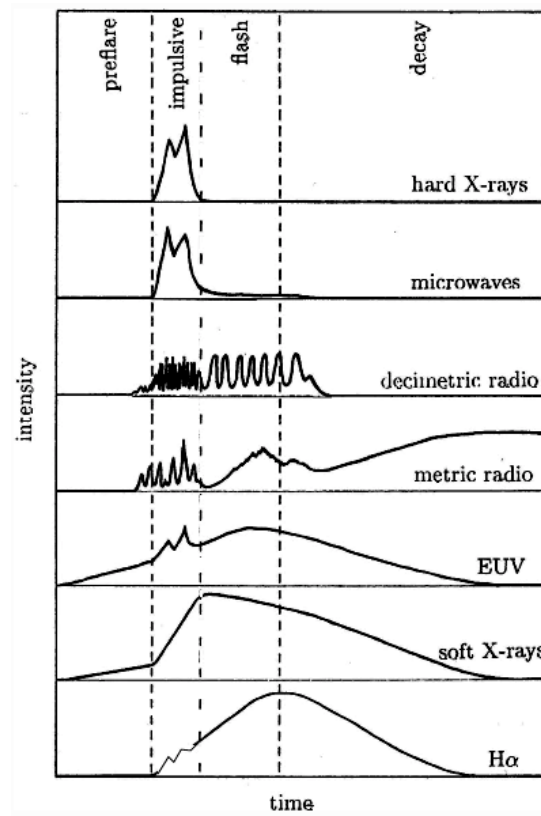


Figure 1.2: A schematic showing different stages of a flare; adapted from Benz (2017).

reconnection assisted events in other astrophysical plasmas also (Verbunt, 1982; Mullan, 1986; Romanova & Lovelace, 1992; Drenkhahn & Spruit, 2002; Gianios, 2010). The standard flare model by Carmichael (1964); Sturrock (1966); Hirayama (1974); Kopp & Pneuman (1976); Svestka & Cliver (1992) (CHSKP model) is based on magnetic reconnection and is explained in the schematic 1.3. Essential to the standard flare model is the existence of a magnetic flux rope, which is a set of twisted magnetic field lines anchored on the photosphere and confines the cooler plasma material. The rope is quantified by the winding number or twist ( $T_w$ ) parameter which measures the number of turns the field lines make about the axis while going from positive to negative polarity, across the polarity inversion line (PIL). Studies from Yan et al. (2001); Roussev et al. (2003) showed the optimal winding number is  $> 2$  whereas, Amari & Luciani (1999); Aulanier & Demoulin (1998); Régnier & Amari (2004); van Ballegoijen (2004); Su (2007); Savcheva & van Ballegoijen (2009) suggest the number is

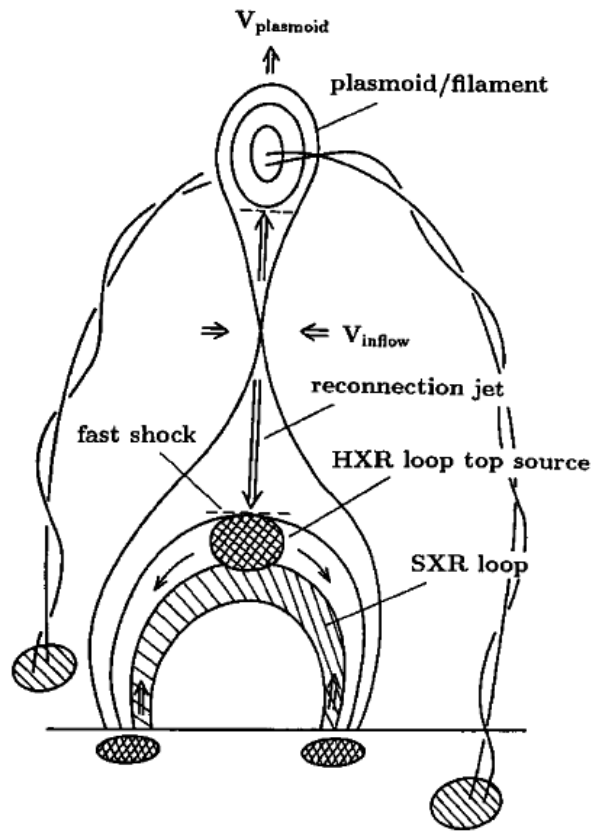


Figure 1.3: The schematic shows a modified version of CHSKP model; adapted from Shibata et al. (1995).

$< 2$ . Antiochos et al. (1994) suggested the number to be even less than 0.5. Importantly, if the rope activates and begins to rise, it stretches the overlying field lines and generates a magnetic vacuum below it. The local drop in magnetic pressure brings oppositely directed field lines toward each other, developing an extended current sheet (CS) that onsets magnetic reconnection, which manifests itself as the flare. The reconnection also accelerates charged particles which move along the post-reconnection magnetic field lines and ultimately impact the lower atmosphere. Consequently, the ambient plasma is heated and the corresponding pressure imbalance causes a plasma upflow. This upflow gradually fills up the magnetic loops with plasma. The process is known as chromospheric evaporation and the field lines being visible in the soft X-ray, are called the soft X-ray loops. The details are in (Benz, 2017; Shibata & Magara, 2011).

## 1.2 Jets

Jets are the collimated eruptions from the solar atmosphere. These are energetically  $10^4$ - $10^5$  orders less than the flares (Pucci et al., 2013; Raouafi et al., 2016) and can be of many varieties—like chromospheric jets, surges, spicules, microspicules, and large coronal jets. The nomenclature is based on their observational traits. They differ in length scales and also the formation heights in the solar atmosphere. The jets are reckoned as smaller versions of the large filament eruptions like in CMEs. They are ubiquitous and are visible in the active regions, coronal holes, quiet sun, and preferably in boundaries with open coronal field lines. Jets are seen in different wavelengths like in  $H\alpha$ , extreme UV and X-rays and can have different temperatures. Several instruments such as Solar and Heliospheric Observatory (SOHO; (Domingo et al., 1995)), the Transition Region and Coronal Explorer (TRACE; (Handy et al., 1999)), the Reuven Ramaty High Energy Solar Spectroscopic Imager (RHESSI; (Lin et al., 2002)), the Hinode (Kosugi et al., 2007), the Solar Terrestrial Relations Observatory (STEREO; (Kaiser et al., 2008)), the Solar Dynamics Observatory (SDO; (Pesnell et al., 2012)), and the Interface Region Imaging Spectrograph (IRIS; (De Pontieu et al., 2014)) have recorded jets in the past and still are doing so. Some ground based observatories have also contributed in the study of the jets. Shibata et al. (1994) arranged the jets into two types. One is the straight anemone jet and the other is the two-sided jet. In case of an anemone jet, a collimated plasma erupts (the spire part) with a bright point (at the base part) behind it or in the inverted Y-shape (also referred as lambda or Eiffel tower shape) whereas the two sided jet has bipolar plasma columns spreading out from the central bright point. Panel-(a) in Fig.-1.4 shows an anemone jet and the panel-(b) shows a two-sided jet. The anemone jets are again classified into two sub-types (1) standard jets and (2) blowout jets based on their appearances (Moore et al., 2010). A standard jet has a narrower spire part in comparison to that of a blowout jet. The Fig.-1.5 shows one standard jet in panel-(a) and one blowout jet in panel-(b), respectively. The coronal jets are mostly reconnection driven phenomena. Shimojo et al. (1998) provided a

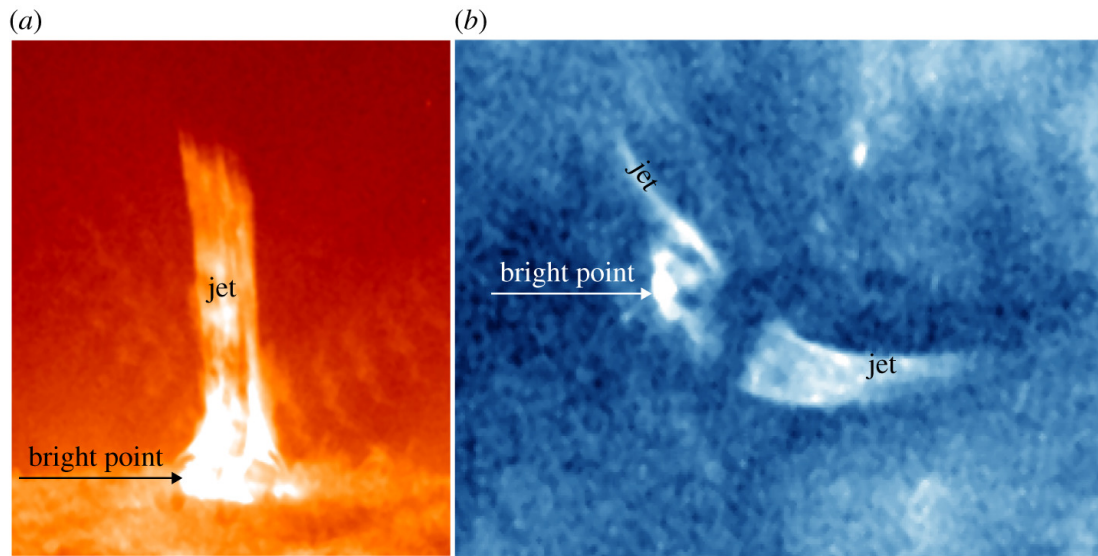


Figure 1.4: Two different types of jets, (a) an anemone jet, and (b) a two-sided jet; picture credit: (Shen, 2021). The arrow marks highlight the bright points near the base of both jets.

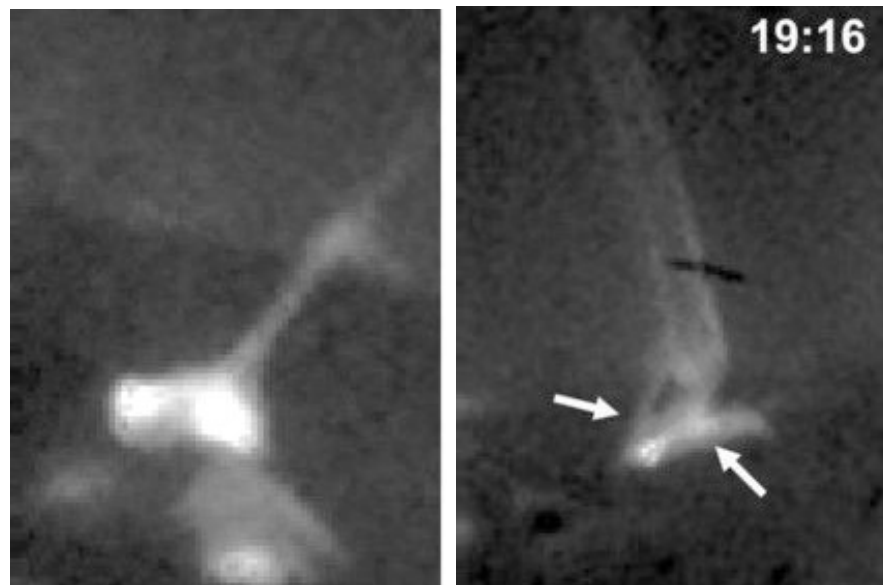


Figure 1.5: The figure depicts two different types of jets observed on Hinode on September 22, 2008, and September 20, 2008, respectively, (a) a standard jet, and (b) blowout jet; picture credit: (Moore et al., 2010).

standard jet model via magnetic reconnection. Also, studies by (Yokoyama & Shibata, 1995; Shimojo et al., 1996; Canfield et al., 1996; Shimojo & Shibata, 2000) have highlighted the role of reconnection in standard jets. In their work, Shibata et al. (1992) attributed the origin of jets observed by the Soft X-ray Telescope on Yokoh (Tsuneta et al., 1991) to magnetic reconnection and the

consequent release of twist. Sterling et al. (2015) have further revised the scenario by investigating 20 random X-ray jets. According to them, the process of X-ray jet formation is similar to large-scale eruptions, but in smaller scales. The scenario of jet formation involves erosion of cool plasma from a mini-filament structure involving a two-step reconnection process with the ambient field lines. First, the field lines underlying the filament material reconnect with formation of hot loops close to the solar surface. Hence the reconnection is called as the internal reconnection. Afterwards, when the filament ascends through the channel of the ambient and enveloping field lines, reconnection occurs above the filament between oppositely oriented field lines. This second reconnection is named as the external reconnection. As a result, the plasma material escapes through the open field lines with a wide spire and forms the blowout jet. On the other hand, if the external reconnection ceases before the arrival of the filament, then a standard jet results, trapping the cool material underneath the enveloping field. The discussed scenario is illustrated in Fig.-1.6. Recently, Wyper et al. (2017) have

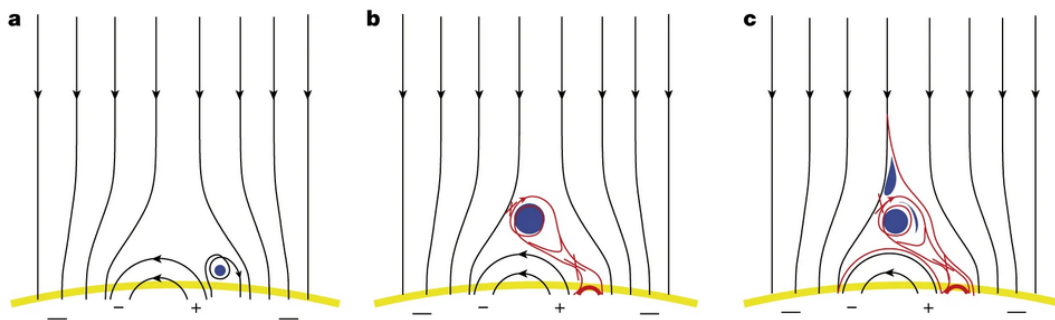


Figure 1.6: A schematic depicting the eruption mechanism of a jet; adapted from Sterling et al. (2015). (a) Initial configuration, (b) the filament material is setting out to erupt, and (c) noteworthy is the both reconnections supporting the eruption of the cool material.

given an universal model for eruption of CME and jet, shown in Fig.-1.7, where they claim the eruptions to follow the breakout model. The jets can be due to flux cancellation also, as reported by Panesar et al. (2016, 2017, 2018) and flux emergence (Mulay et al., 2016). The details of different eruption mechanisms and origins can be found in the comprehensive reviews by Raouafi et al. (2016); Shen (2021).

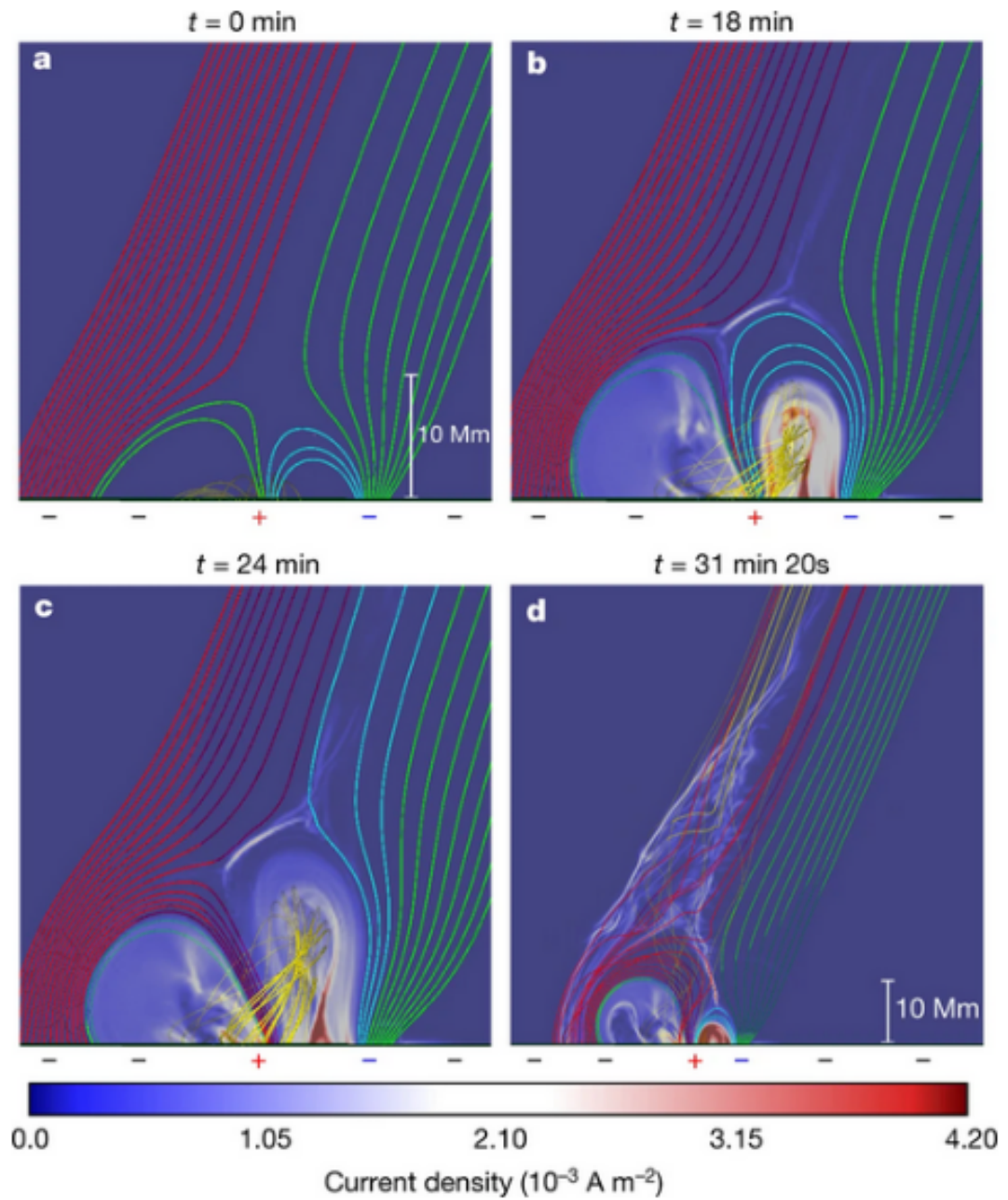


Figure 1.7: A numerical simulation showing the mini-filament eruption scenario in case of a jet; picture taken from Wyper et al. (2017).

### 1.3 Coronal Mass Ejections

CMEs are the gigantic eruptions from the solar atmosphere into the interplanetary medium. A typical CME has a three-part structure: (1) the bright frontal loop, (2) the dark cavity, and behind it (3) the bright core. The mass contained in a CME ranges from  $1 \times 10^{11} - 4 \times 10^{13} \text{ kg}$  with average value of  $3 \times 10^{12}$

(Jackson, 1985; Gopalswamy & Kundu, 1992; Hudson et al., 1996). The projected velocity of a CME ranges from 20 – 2000 km/s, reaching upto 3500 km/s (Chen, 2011). Based on their angular width, they are known as narrow CMEs with smaller angular width blue( $\approx 10^\circ$ ) and normal CMEs with larger angular width. They are depicted in Fig.-1.8. The normal CMEs oriented toward Earth are known as the halo CMEs.

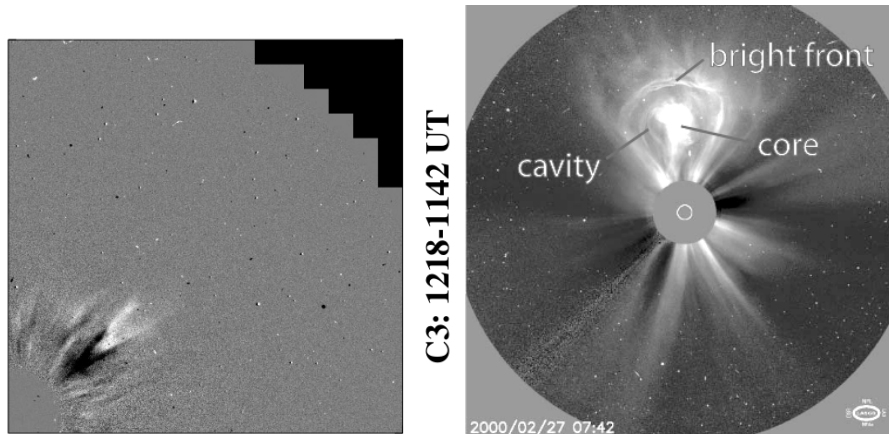


Figure 1.8: The panels show two different types of CMEs captured by the Large Angle Spectrometric Coronagraph (LASCO) onboard SOHO; (a) a difference image of a narrow CME on the left with a less angular width and without any distinct three-part structure, and (b) a normal CME on the right with its characteristic three-part structure; picture credit for narrow cme (Kahler et al., 2001) and normal cme (Riley et al., 2008).

Possible reasons for triggering of these two types of CMEs are different. Narrow CMEs, shown in the Fig.-1.8, are mainly due to EUV jets and these jets may be associated with flares occurring down below the atmosphere. The normal CMEs are also linked with flares though not always. They mainly possess a filament—an elongated structure carrying cold and dense plasma hanging on the solar atmosphere, also called prominence when viewed at the solar limb during their initiation phase. The eruption process is generally explained by the standard flare model or the CHSKP model (previously discussed). Nevertheless, reconnection may not be always responsible for triggering CMEs. Presence of a flux rope has been successfully explained the three part structures of normal CMEs since they can carry material, own current (because of winding of the field lines owing to photospheric motions) and hence store the magnetic energy.

When, the flux rope becomes unstable, it starts to rise forming a current layer near the footpoints of the rope which leads to reconnection. As a result the plasma above the reconnection region gets ejected. However, it is not necessary to have a pre-existing flux rope since the rope may develop in-situ by reconnection of sheared field lines.

As a precursor to the eruption, sigmoidal structures, observed in SXR are contemplated as a proxy to filament lying below it (Canfield et al., 1999). Different triggering mechanisms are proposed with the help of observations and numerical modeling. In their tether-cutting model, Moore et al. (2001) have provided a plausible triggering mechanism, which is shown in the Fig.- 1.9. In the panel-(a) of the schematic, there are a set of strongly sheared arcades, and visibly less sheared overarching arcades hanging over the atmosphere. Owing to the action of shearing motion, the strongly sheared arcades reconnect and a long field line above and a short field line below the point of reconnection are formed. The plasma begins to move in both directions. The resulting plasma flow further pushes the newly formed filament to rise. Simultaneous removal of arching field lines occur forming a current sheet above the neutral line and also produces two flare ribbons on the surface. Studies by van Ballegoijen & Martens (1989) along with a numerical simulation by Amari et al. (2003) also supports a similar mechanism, but with an inclusion of flux cancellation on generating helical field lines and subsequent eruption as CME due to reconnection. Studies considering shearing motions are also found to be engendering eruptions (Deng et al., 2001; Aly, 1990; Mikic & Linker, 1994; Kusano et al., 2004). Antiochos et al. (1999) have argued about another mechanism known as magnetic breakout model, which relies on the reconnection between sheared arcades and the surrounding flux systems in a multi polar eruptive flare system. The schematic is shown in Fig.-1.10.

In their work, Lynch et al. (2004) have compared the observational features with their MHD simulation result and found the support of breakout model in explaining the CME. Archontis & Török (2008); MacTaggart & Hood (2009) have also explored a similar scheme in their models. Later studies provided the

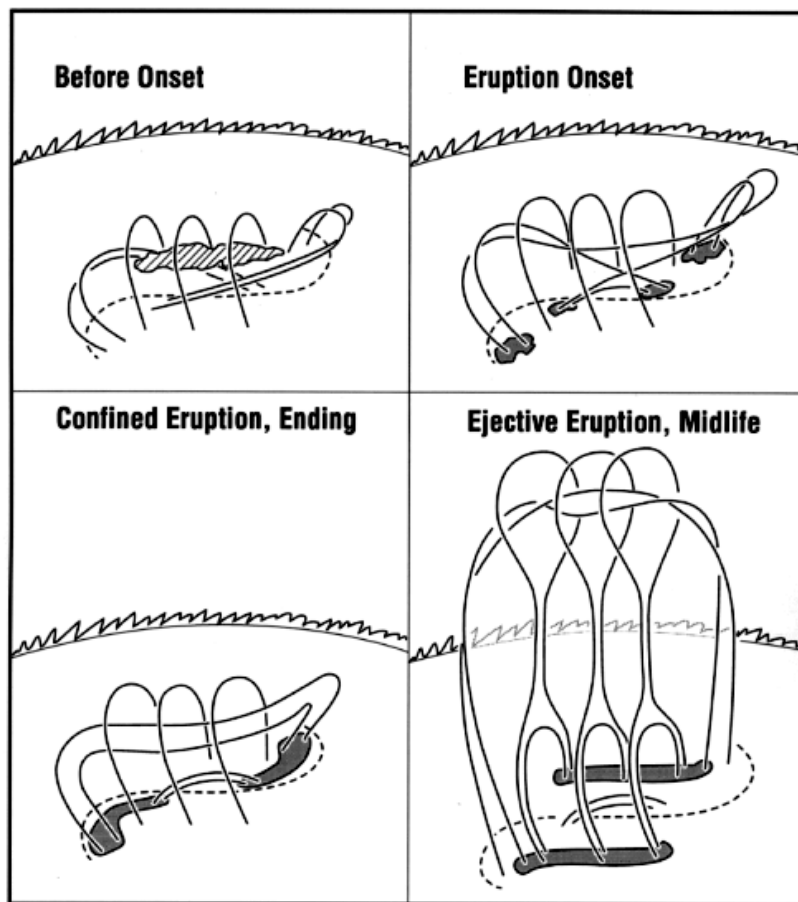


Figure 1.9: Eruption scenario in the tether-cutting model depicting the rise of the core flux system after the reconnection of the sheared field lines lying below it, picture credit: (Moore et al., 2001).

evidences for CMEs to be triggered by the breakout model (Tang, 1987; Aulanier et al., 2000; Li & Luhmann, 2006; Ugarte-Urra et al., 2007). Emergence of flux before eruption and their reconnection between the pre-existing field lines are also found to reinforce CME eruption (Feynman & Martin, 1995), which is later validated by Chen & Shibata (2000); Chen (2008). According to the model, emerging fluxes reconnect with pre-existing flux systems in the filament and hence decreases the local magnetic pressure. The lateral loops then rush toward the low pressure region and a current sheet forms. If the emerging fluxes appear outside of the filament, they reconnect with the pre-existing loops and consequently the overlying loops expand, creating a current sheet below the filament (Fig.-(1) in (Chen, 2008)). The eruption mechanisms may also rely on ideal MHD instabilities of the flux rope/filament, namely torus instability

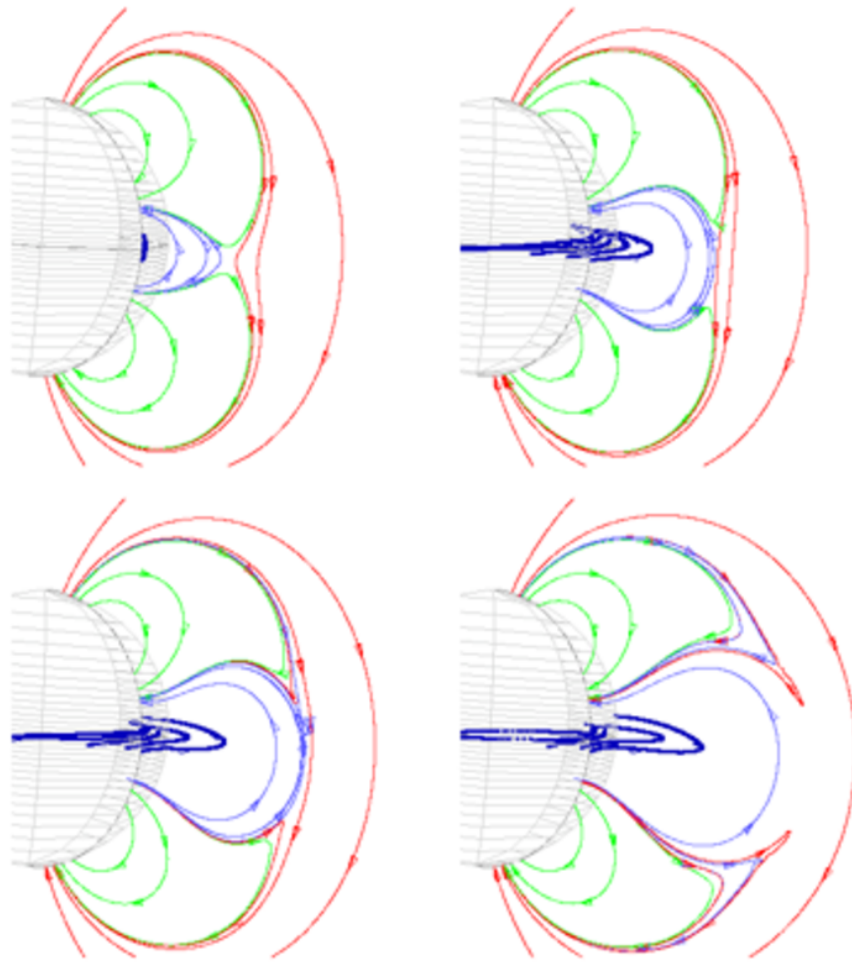


Figure 1.10: Eruption scenario in the breakout model showing the evolution of magnetic field with reconnection occurring near the null point situated above the central flux system or flux rope at the core, picture credit: (Antiochos et al., 1999).

(Fan & Gibson, 2007; Kliem & Török, 2006; Chen, 1989) and kink instability (Sakurai, 1976; Hood & Priest, 1979; Mikic et al., 1990; Török & Kliem, 2005; Inoue & Kusano, 2006). The formalism based on the torus instability or the lateral kink instability relies on the stability model of toroidal current ring discussed in Shafranov (1966); Bateman (1978). In brief, the eruption onsets if the external/overlying field falls rapidly along the major axis of the torus (the flux rope is envisaged as a half-cut torus). This fall is quantified by the critical decay index  $n = -\frac{\partial(\log |\mathbf{B}|)}{\partial(\log z)}$ , where  $\mathbf{B}$  is the strength of the external magnetic field and  $z$  is the height above the photosphere. Whereas, in the helical kink instability, the magnetic flux rope confining the filament material about the axis

gets twisted and develops a writhe. When the winding number of the MFLs around the axis exceeds the threshold value of 1.25 turns, the flux rope erupts. The scenario for both the instabilities are depicted in the Fig.-1.11 and Fig.-1.12.

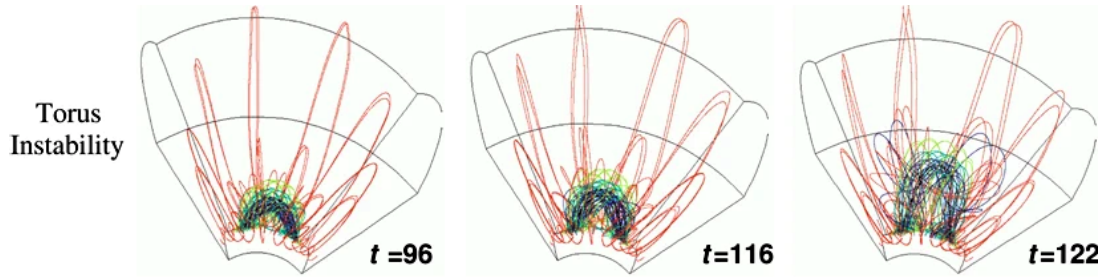


Figure 1.11: MHD simulation showing the evolution of the magnetic field in torus unstable scenario, image credit:(Fan & Gibson, 2007).

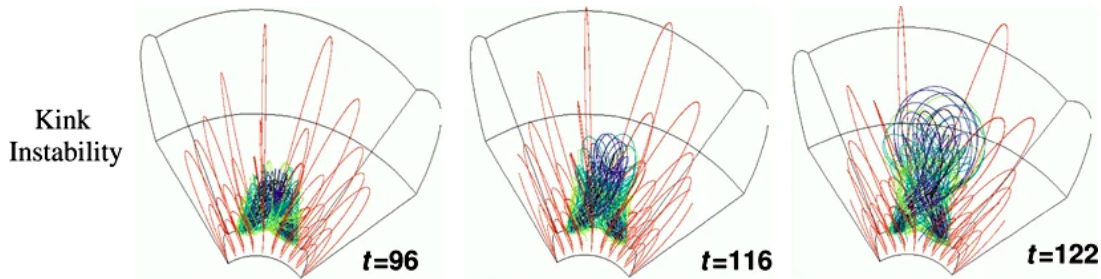


Figure 1.12: MHD simulation showing the evolution of the magnetic field in kink unstable scenario, image credit:(Fan & Gibson, 2007).

As a whole, magnetic reconnection is proposed as the underlying cause of the solar transients like the flares, jets and CMEs. It is established that both the magnetic field and current density are important to understand the reconnection driven events, the frozen-in condition enabling the magnetic field to determine the global evolution of a magnetic structure whereas the reconnection itself is due to a reduction in the length over which the magnetic field varies and hence, an enhancement of magnetic Reynolds number. The importance will be highlighted later in the thesis, as and when necessary. Few other properties are of worth mentioning. Most of these transients initiate predominantly at lower solar atmosphere and depends on the local morphology of MFLs. It is then imperative to explore the MFL dynamics near reconnection sites and their effect on the global evolution of a magnetic structure to understand the transients—the objective of the thesis. For the purpose we have carried out three dimensional numerical

simulations using both analytical initial magnetic field along with magnetic field extrapolated from solar magnetograms. For ready reference, a more detailed objective of the thesis along with its structure is listed in the next section.

## 1.4 Objective and Outline of the Thesis

As described upfront, the objective of the the thesis is to numerically explore dynamics of magnetic reconnection and its influence on the evolution of MFLs (magnetic field lines) near and away from the reconnection sites. The requirement is to understand the relevant magnetic topology and the current density along with their evolution. The reconnection sites are identified by studying the MFL topology obtained from coronal magnetic field extrapolations using photospheric magnetograms as well as by analytical constructions. Both approaches are necessary. The MHD simulations initiated with extrapolated MFLs, the so-called data-constrained simulations, are realistic and the simulated dynamics can readily be compared with the observations. Contrarily, simulations with analytical initial field give more control and focuses on exploring a particular aspect of the reconnection along with basics of the involved magnetic topology. Importantly, active region MFLs are twisted and hence, mostly three-dimensional (3D). Consequently, 3D reconnections initiated with 3D magnetic nulls and Quasi-Separatrix-Layers (QSLs) are of utmost importance. The thesis specifically focuses on 3D reconnections using state-of-the-art simulations and data analysis tools. For convenience, we catalog the chapter titles below along with brief notes.

Chapter 2 is on *Magnetic Reconnection, Extrapolation Models and Data Acquisition* and lays down the basic ideas of magnetic reconnection with special focus on its 3D variant. Also various coronal field extrapolation models are discussed while emphasizing the non-force-free-field (NFFF) model by Hu et al. (2008); Hu & Dasgupta (2008); Hu et al. (2010).

Chapter 3 titled *Numerical Model* introduces the EULAG-MHD model, used extensively for the simulations.

Chapter 4 describes *Data-constrained Simulations* where extrapolated mag-

netic fields are used as initial conditions. To understand the reconnection process, the simulated transients are selected to be of topologically and energetically different to mitigate any conceptual bias.

Chapter 5 *Simulations with Analytical Initial Conditions* presents the simulations initiated with the analytical initial conditions.

Chapter 6 *Summary and Future Scopes* summarizes the thesis and discusses future scopes.

# Chapter 2

## Magnetic Reconnection, Extrapolation Models and Data Acquisition

The objective of the thesis being to numerically explore MR (magnetic reconnection) driven coronal transients with a particular focus on the magnetic topology and associated current density, in the following we present the salient features of MR. We also briefly discuss different extrapolation models and their relevance in the coronal physics.

### 2.1 Magnetic Reconnection

In the early days, the MR was also termed as magnetic merging (Vasyliunas, 1975) and their investigation first started using two-dimensional (2D) analyses. In 2D, hyperbolic X-type neutral points (Pontin et al., 2004) can host MRs. The schematic in Fig.-2.1 shows the configuration of an X-point topology where the orange and blue color field lines have different connectivities. The black straight lines distinguish different topological domains and are known as the separatrices. The neutral point having  $|\mathbf{B}| = \mathbf{0}$  is located at their intersection.

The configuration can be obtained by writing the magnetic field as

$$\mathbf{B} = y\hat{\mathbf{i}} + x\hat{\mathbf{j}}, \quad (2.1)$$

where  $\hat{\mathbf{i}}$  and  $\hat{\mathbf{j}}$  are unit vectors along  $x$  and  $y$  directions of a Cartesian coordinate system. In response to an unbalanced force, a pair of oppositely directed field lines (say, AB and DC) comes to close proximity near the neutral point where they diffuse out because of a loss in the condition of flux-freezing. At the neutral point the two field lines reconnect, change their connectivities to AC and DB, subsequently leaving the reconnection region with the outflow indicated by the double horizontal arrow. In another scenario, a combination of two Y type nulls can develop which, can be envisaged by an asymmetric compression of the X-type null. Such Y-type nulls are characterized by strong current densities, or current sheets, localized on a plane across which the magnetic field flips sign.

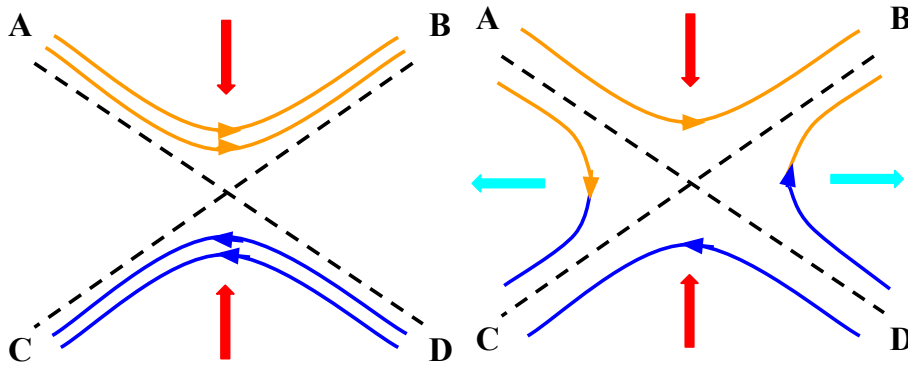


Figure 2.1: Schematic representation of reconnection near an X-type null point.

For completeness, the MFLs are tangential to the local magnetic field vector  $\mathbf{B}$  and are the solutions of

$$\frac{dx_i}{ds} = \frac{B_{x_i}}{|\mathbf{B}|}, \quad i = 1, 2, 3, \quad (2.2)$$

are the three indices of a Cartesian coordinate system. Another type is the O-type null, located at the point of collapse of a closed field line. The field lines are shown in the Fig.-2.2.

In order to explain the energy release in flares, Sweet and Parker (Parker,

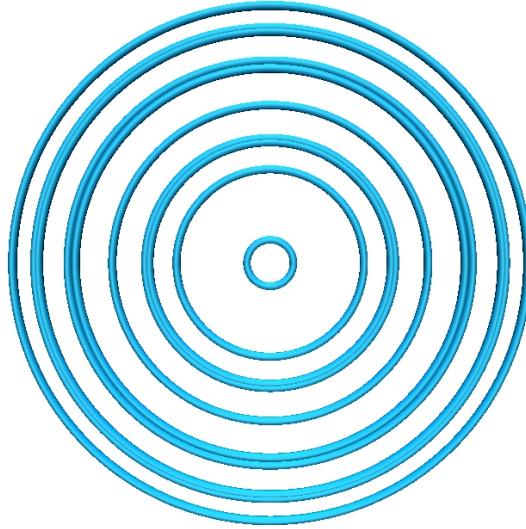


Figure 2.2: Magnetic field lines near an o-type null point.

1957; Sweet, 1958) modeled the magnetized plasma to be in steady-state and 2D. They further proposed anti-parallel magnetic field lines to get pushed toward each other forming a current sheet of length  $2L$  and width  $2l$ . Subsequently, the anti-parallel field lines reconnect and in the process generate kinetic energy and heat (via Ohmic dissipation). However, the obtained reconnection rate was slower in comparison to what is theorized in flares and hence, it is known as the slow-reconnection model. Compared to the Sweet-Parker model, the Petschek model (Petschek, 1964) yields a faster reconnection rate. Further improvement in 2D reconnection models were made by including two-fluid and kinetic effects (Zweibel & Yamada, 2009). Though the scenario in 2D aids us in understanding the reconnection process, in reality we find complex 3D magnetic structures in the solar atmosphere and in other astrophysical systems. In 3D, the reconnection is more complex and may not necessarily involve anti-parallel field lines. Instead, there exist many plausible sites for MRs in the likes of null points, separators and non-null locations such as quasi-separatrix layers (QSLs). We will discuss each regime as a primer to understand the works carried out in the thesis.

The Fig.-2.3 illustrates the topology of a linear 3D null, where the MFLs increase linearly from the origin (Priest & Forbes, 2000) when expanded in a Taylor's series. Magnetic field for such linear null in the Cartesian coordinates

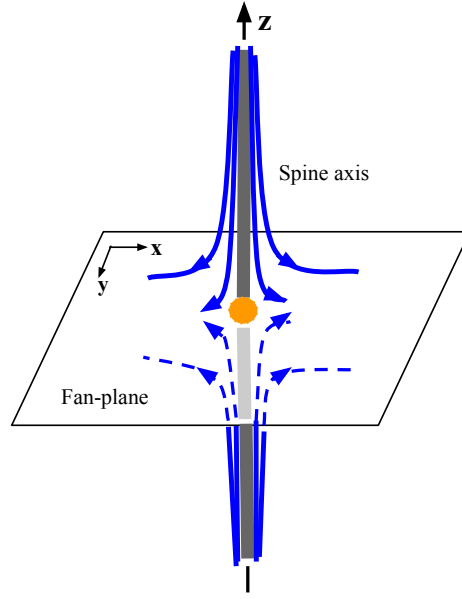


Figure 2.3: A schematic of a 3D null point with spine axis and fan plane with the null point located at the center.

can be written as

$$\mathbf{B}(x, y, z) = x\hat{i} + ay\hat{j} - (a + 1)z\hat{k}, \quad (2.3)$$

so that  $\nabla \cdot \mathbf{B} = 0$ . The solution to the field line equation for  $a = 1$  is

$$y = Cx \quad \& \quad z = K/x^2, \quad (2.4)$$

and the location of the null point is at  $x = y = z = 0$ . The Fig.-2.4 plots MFLs for the 3D null pertaining to  $C = 1$ . In the Fig.-2.4, the sets of MFLs asymptotically approaching the null point constitute the spine or  $\gamma$ -line whereas the surface to which the receding MFLs are tangential, is called the fan plane or  $\Sigma$ -plane (Priest & Titov, 1996; Lau & Finn, 1990). The fan plane separates the different topological domains of magnetic flux and hence also is known as separatrix surface. In general,  $\mathbf{B}$  for generating linear null points in 3D can be written as

$$\begin{pmatrix} B_x \\ B_y \\ B_z \end{pmatrix} = \begin{pmatrix} 1 & \frac{1}{2}(b - j_{\parallel}) & 0 \\ \frac{1}{2}(b + j_{\parallel}) & a & 0 \\ 0 & j_{\perp} & -a - 1 \end{pmatrix} \begin{pmatrix} x \\ y \\ z \end{pmatrix}$$

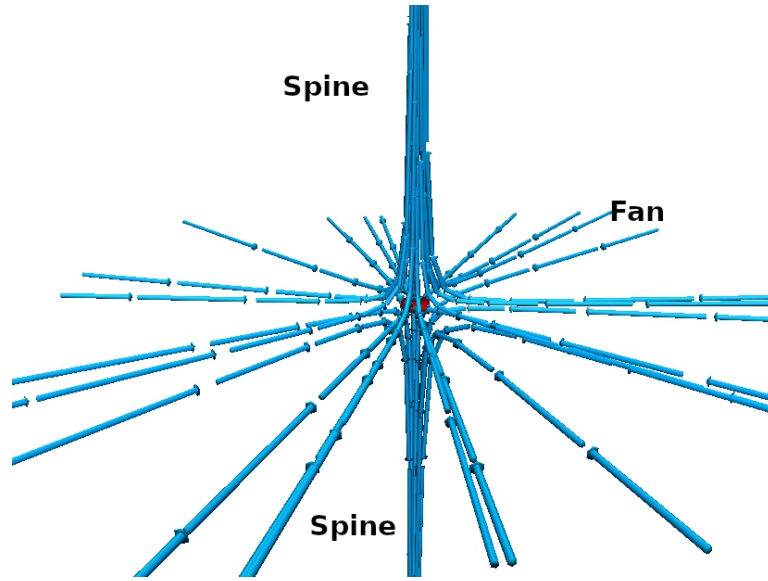


Figure 2.4: Plot of a 3D null skeleton with its characteristic spine and fan field lines with the null point (marked by red iso-surface).

Where  $j_{\perp}$  and  $j_{\parallel}$  are the current densities perpendicular and parallel to the spine. If  $j_{\perp}$  is non-zero, the fan surface is inclined to the spine at a certain angle and the corresponding null is known as the oblique null. When the  $j_{\parallel}$  along the spine exceeds a critical value, the eigen values of the matrix in Eq.-2.1 are not real anymore and the null is called a spiral null. The oblique and spiral nulls are plotted in Fig.-2.5.

When the spine field lines approach (or recede) toward (or away from) the null and those on fan recede (or approach) away from (or toward) the null, the null points are termed as positive (or negative) (Priest & Forbes, 2000). The null presented in the Fig.-2.4 is called a proper radial null, since the fan field lines are straight lines directed radially outward. If  $a \neq 1$  in the Eq.-2.3, the field lines are not straight lines anymore and such nulls are termed as improper radial nulls (Priest & Forbes, 2000).

Reconnection involving null points are classified into different regimes. In kinematic models, Pontin et al. (2004); Pontin et al. (2005) found that the alignment of electric current dictates the reconnection process. According to Pontin et al. (2004); Wyper & Jain (2010), when current becomes parallel to the spine of the null, there will be counter-rotational flows having center on the spine.

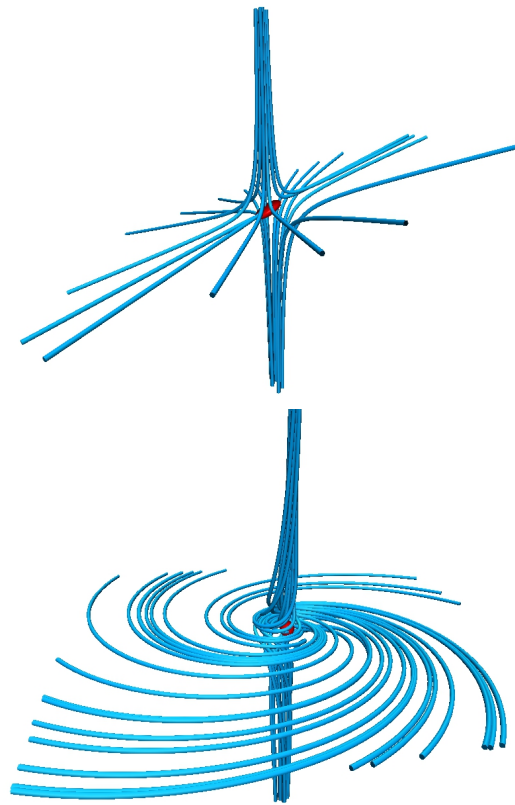


Figure 2.5: Depiction of (a) an oblique null, and (b) a spiral null. The red iso-surfaces shows the location of the null point.

This leads to rotational slippage of the field lines due to reconnection. Notably, there is no transport of magnetic flux across either the spine or the fan (Pontin, 2012). Whereas, flux transport occurs if the current is parallel to the fan surface. In order to find current density near the null, Rickard & Titov (1996) along with Pontin & Galsgaard (2007) found the accumulation of current along the spine axis for an isolated 3D null when disturbed by rotational and shearing motion. From these investigations, two types of reconnection stem out. Upon rotational disturbances on fan, a current tube forms by the winding of field lines around the spine in parallel to it. So, there will be a rotational slippage of field lines. This is known as torsional spine reconnection and is shown in the Fig.-2.6. In torsional fan reconnection, a planar current layer develops (Galsgaard et al., 2003) near the fan when the spine is rotated, shown in Fig.-2.7. In another scenario called the spine-fan reconnection model, either the spine or the fan field lines are perturbed by the disturbances in the form of a shear, the null collapses

to form a localized current layer in a Y-type manner (depicted in the Fig.-2.8) reconnection. The current is transported via both spine and fan while remaining parallel to the fan surface. Here also, transfer of magnetic flux occur through both spine and fan. Then, in the separator reconnection, the joining line or the separator line, between two nulls oriented perpendicular to each other (shown in Fig.-2.9), result in formation of current layer near it (Longcope & Cowley, 1996; Longcope, 1996). Parnell et al. (2010b,a) has observed the formation of current away from the null points.

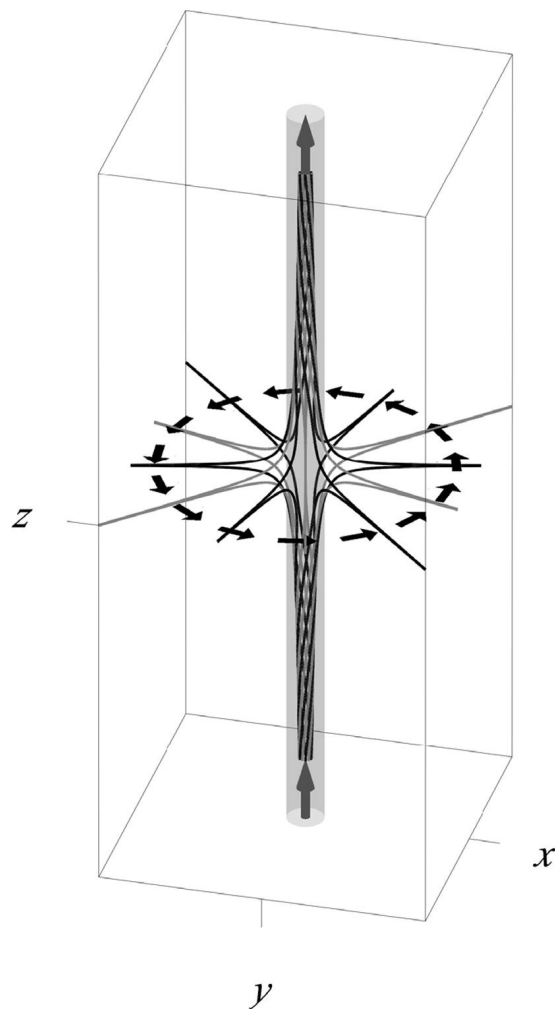


Figure 2.6: Schematic representation of torsional spine reconnection, where the black and gray lines are magnetic field lines, the shaded surfaces are current density iso-surfaces, gray arrows indicate the direction of the current flow, while black arrows indicate the driving plasma velocity. Adapted from Pontin (2012).

Non-null reconnection refers to magnetic reconnection in the absence of any null points and in presence of a sharp change in the magnetic field line con-

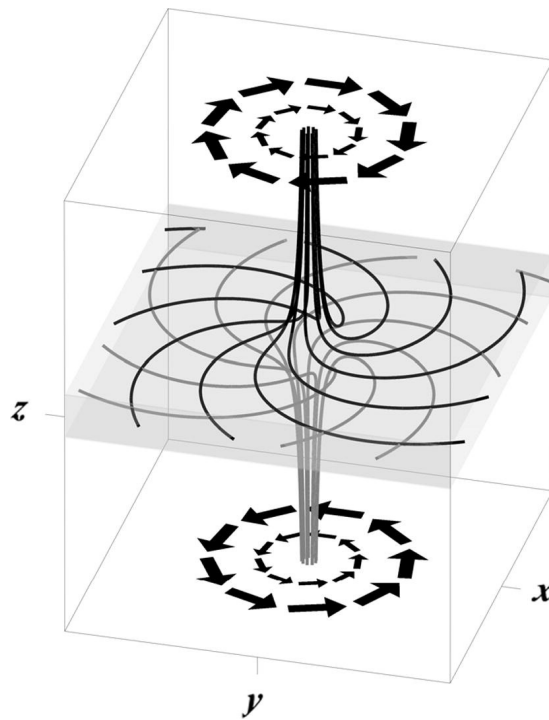


Figure 2.7: Schematic of torsional fan reconnection, where different color field lines, shaded surfaces and arrows represent the same as depicted in Fig.-2.6. Adapted from Pontin (2012).

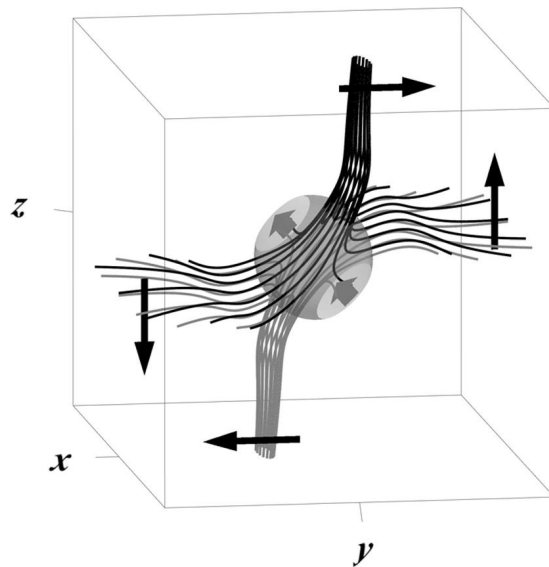


Figure 2.8: Schematic of spine–fan reconnection at an isolated null. Again, different color field lines, shaded surfaces and arrows represent the same as depicted in Fig.-2.6. Adapted from Pontin (2012).

nectivity. This is also known as magnetic flipping (Priest & Forbes, 1992) or slip-running reconnection when the motion of field lines exceed the Alfvén speed (Aulanier et al., 2006). This concept was already proposed by Schindler et al.

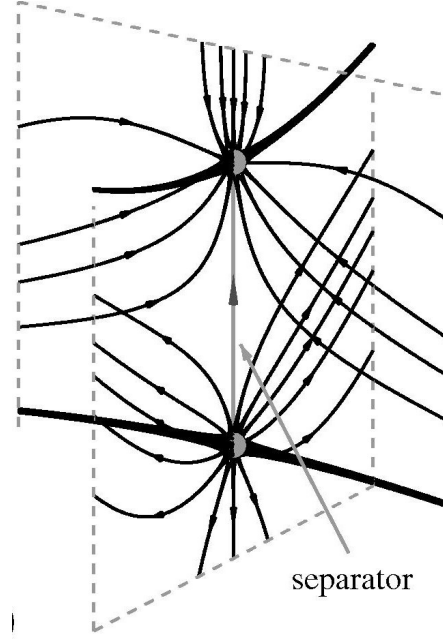


Figure 2.9: Magnetic field lines near a fan-fan separator line. Adapted from Pontin (2012).

(1988) where the non-null reconnection was called as finite- $\mathbf{B}$  reconnection. Considering Ohm's law as stated in Schindler et al. (1988),

$$\mathbf{E} + \mathbf{v} \times \mathbf{B} = \mathbf{R}, \quad (2.5)$$

where  $\mathbf{R}$  is a finite vector and represents the non-idealness in the plasma in form of collisions, fluctuations and particle inertia. The presence of this non-idealness can be important in a localized region with sharp gradient, with length scale smaller than the ion Larmour radius. These locations can become potential sites for current enhancement (Schindler et al., 1988). A convenient form of  $\mathbf{R}$  in presence of Ohmic dissipation can be  $\eta\mathbf{J}$ , where  $\eta$  is the electrical resistivity. Necessary and sufficient condition for reconnection is that the magnetic field be nonzero in the diffusion region and  $\mathbf{B} \times (\nabla \times \mathbf{R}) \neq 0$  at a given point—located at the diffusion region. An important parameter here is the electric field ( $E_{\parallel}$ ) parallel to the magnetic field. If  $\int E_{\parallel} ds$  along a measurable set of field lines in diffusion region is nonzero, then the effect of reconnection is felt outside the region and we get global reconnection; otherwise, the reconnection is local. For example, the process of plasmoid formation is by global finite- $\mathbf{B}$  reconnection. QSLs are

such preferential locations for formation of current sheets and reconnections to occur without any presence of null points. QSLs are the type of location where there occurs a drastic change in the magnetic field line connectivity (Demoulin et al., 1996, 1997; Titov, 2007). This change is quantified by the value of the squashing factor  $Q$ . To elucidate, we consider two footpoints  $P_1(x_1, y_1)$  and  $P_2(x_2, y_2)$ . When mapped from  $P_1$  to  $P_2$ , the Jacobian associated with it is given by

$$D_{1,2} = \begin{pmatrix} \frac{\partial x_2}{\partial x_1} & \frac{\partial x_2}{\partial y_1} \\ \frac{\partial y_2}{\partial x_1} & \frac{\partial y_2}{\partial y_1} \end{pmatrix} = \begin{pmatrix} a & b \\ c & d \end{pmatrix} \quad (2.6)$$

yielding to,

$$Q = \frac{a^2 + b^2 + c^2 + d^2}{|\mathbf{B}_{n,1}(x_1, y_1)/\mathbf{B}_{n,2}(x_2, y_2)|}, \quad (2.7)$$

where  $\mathbf{B}_{n,1}(x_1, y_1)$  and  $\mathbf{B}_{n,2}(x_2, y_2)$  are the components normal to the target planes.  $Q > 2$  determines the degree of squashing and the location of QSL (Liu et al., 2016). Intersection of QSLs make a Hyperbolic Flux Tube, which is also a potential site of reconnection (Titov et al., 2002; Titov, 2007). The plot of  $Q$  for a submerged poles model of Sweet's configuration and a Hyperbolic Flux Tube are shown in the Fig.-2.10 and Fig.-2.11, adapted from Titov et al. (2002).

## 2.2 Coronal field models and extrapolation techniques

The last section highlights the importance of magnetic topology in magnetic reconnection. Consequently, crucial is to determine the magnetic topology of the coronal field to understand MR there. In absence of a reliable direct measurement of the coronal magnetic field, the viable alternative is to employ various models of the solar coronal magnetic field. In the following, we briefly introduce these models.

The standard is the force-free approximation of the corona (Lüst & Schlüter, 1954; Chandrasekhar, 1956) which treats it as a low  $\beta$  plasma ( $\beta \equiv 8\pi p/B^2$ )

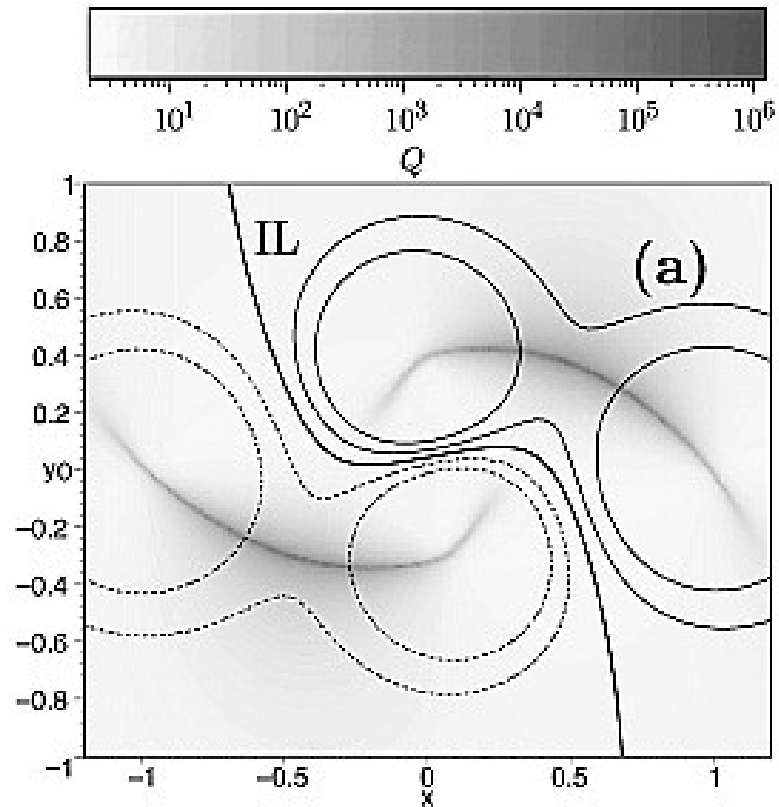


Figure 2.10: Distribution of  $Q$  on the photospheric magnetogram plotted in isocontours in the background. Picture credit: (Titov et al., 2002).

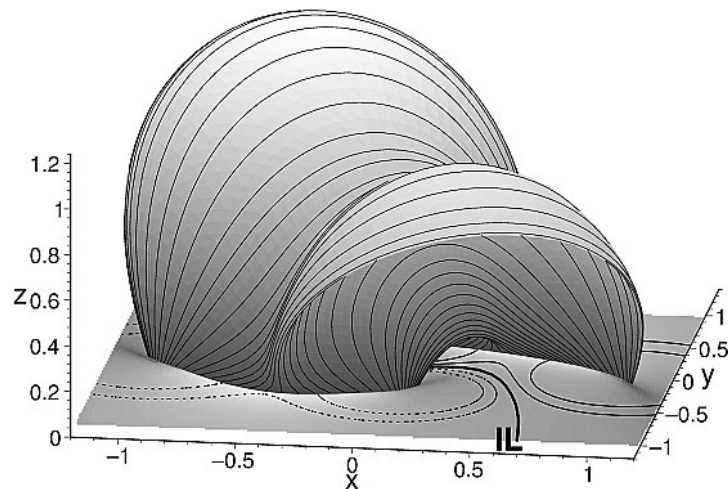


Figure 2.11: Depiction of the hyperbolic flux tube with magnetic flux surface  $Q = 100$  on the same magnetogram shown in Fig.-2.10. Picture credit: (Titov et al., 2002).

where the magnetic pressure  $B^2$  dominates over the plasma pressure  $p$ . With all other forces neglected and assuming the global corona to be under equilibrium,

the Lorentz force

$$\mathbf{J} \times \mathbf{B} = 0, \quad (2.8)$$

from Eq.-1.1.

### 2.2.1 Potential field

The simplest non-trivial solution of Eq.-2.8 is  $\mathbf{J} = 0$ , or the magnetic field to be potential or current-free. The magnetic field can be found by solving the Laplace's equation satisfied by the magnetic scalar potential with appropriate boundary conditions. The coronal extrapolation of such field requires only the line-of-sight field of a magnetogram. The idea is to solve the Laplace boundary value problem with photosphere as the lower boundary and any desired height in the corona as the upper boundary. The Laplace's equation is given by

$$\nabla^2 \Phi = 0, \quad (2.9)$$

$\Phi$  being the scalar potential. The model is popularized as the potential source surface model (PFSS) where the source surface lies at around 2.5 solar radii and the magnetic field lines from there are assumed to be radial. The Fig.-2.12 shows the field lines obtained using the PFSS model. Although the PFSS model is proved to be useful in explaining many interesting observations, however, the active region MFLs responsible for transients have to be twisted to store excess magnetic energy and hence are non-potential.

### 2.2.2 The Linear-Force-Free-Field (LFFF)

The LFFF model satisfies Eq.-2.8 by assuming  $\mathbf{J} \parallel \mathbf{B}$ , or,

$$\nabla \times \mathbf{B} = \alpha_0 \mathbf{B}, \quad (2.10)$$

where  $\alpha_0$  is a constant. It represents the magnetic circulation per unit flux and is related to the twist of a field line. With the MFL twist constant everywhere,

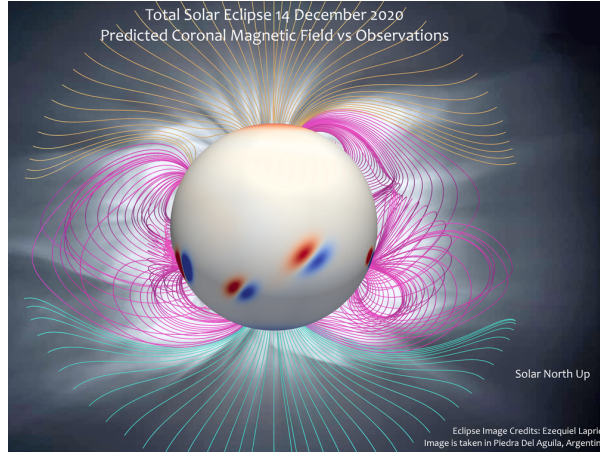


Figure 2.12: Global magnetic field topology obtained with PFSS extrapolation. Image taken from [http://www.cessi.in/solareclipse2020/images/obs\\_pred\\_eclipsedec2020\\_1.png](http://www.cessi.in/solareclipse2020/images/obs_pred_eclipsedec2020_1.png).

the LFFF model is applicable to only a small region as observations directly suggest MFLs to be non-uniformly twisted. The  $\alpha$  can be computed from vector magnetograms in the following way,

$$\alpha(x, y) = \mu_0 J_{z0} / B_{z0} \quad (2.11)$$

and

$$J_{z0} = \frac{\partial B_{y0}}{\partial x} - \frac{\partial B_{x0}}{\partial y}, \quad (2.12)$$

where  $B_x$ ,  $B_y$ , and  $B_z$  are the three magnetic field components and  $J_{z0}$  is the vertical current density measured on the photosphere. Taking curl of Eq.-2.10,

$$(\nabla^2 + \alpha^2)\mathbf{B} = \mathbf{0}, \quad (2.13)$$

which is the vector Helmholtz equation for magnetic field and solution to this equation is given by Chandrasekhar & Kendall (1957). According to them, a force-free-field with constant  $\alpha$  can be written explicitly with two components, one poloidal and one toroidal, owing to the selection of a gauge for the vector potential and solenoidal constraint. Hence,  $\mathbf{B}$  in a Cartesian coordinate system

can be written as,

$$\mathbf{B} = \frac{1}{\alpha_0} \nabla \times \nabla \times (\psi \hat{e}_z) + \nabla \times (\psi \hat{e}_z), \quad (2.14)$$

and applying it to 2.13, we get

$$B_x = \sum_{m,n=1}^{\infty} \frac{C_{mn}}{\lambda_{mn}} \exp(-r_{mn}z) \cdot \left\{ \alpha \frac{\pi n}{L_y} \sin(\pi m x / L_x) \cos(\pi n y / L_y) - r_{mn} \frac{\pi m}{L_x} \cos(\pi m x / L_x) \sin(\pi n y / L_y) \right\}, \quad (2.15)$$

$$B_y = \sum_{m,n=1}^{\infty} \frac{C_{mn}}{\lambda_{mn}} \exp(-r_{mn}z) \cdot \left\{ \alpha \frac{\pi m}{L_x} \cos(\pi m x / L_x) \sin(\pi n y / L_y) + r_{mn} \frac{\pi n}{L_y} \sin(\pi m x / L_x) \cos(\pi n y / L_y) \right\}, \quad (2.16)$$

$$B_z = \sum_{m,n=1}^{\infty} C_{mn} \exp(-r_{mn}z) \cdot \sin(\pi m x / L_x) \sin(\pi n y / L_y), \quad (2.17)$$

where  $\lambda_{mn} = \pi^2(m^2/L_x^2 + n^2/L_y^2)$  and  $r_{mn} = \sqrt{\lambda_{mn} - \alpha^2}$  (Nakagawa & Raadu, 1972; Seehafer, 1978; Wiegelmann & Sakurai, 2012). For the solution of LFFF equation, several techniques are exploited, like Green's functions, Fourier transforms in different coordinate systems (Levine & Altschuler, 1974; Nakagawa & Raadu, 1972; Levine & Altschuler, 1974; Chiu & Hilton, 1977; Nakagawa et al., 1978; Alissandrakis, 1981; Wu & Wang, 1984, 1985; Semel, 1988; Durrant, 1989; Gary, 1989; Yan, 1995; Kusano & Nishikawa, 1996; Abramenko & Yurchishin, 1996; Amari et al., 1998; Clegg et al., 1999, 2000). For photospheric magnetograms,  $B_z$  for  $z = 0$  is considered and comparing with Eq.-2.17, the coefficients  $C_{mn}$  can be found out. The construction of LFFF for magnetogram is done by adapting the procedures documented in Seehafer (1978). There the original magnetogram of dimension  $0 \rightarrow L_x$  in  $x$  and  $0 \rightarrow L_y$  in  $y$  is stretched to dimension  $-L_x \rightarrow L_x$  in  $x$  and  $-L_y \rightarrow L_y$  in  $y$  to maintain the flux balance. Subsequently, the coefficient  $C_{mn}$  is computed using fast fourier transform (FFT) from this new modified magnetogram. For a consistent solution for Eq.-2.17,  $r_{mn}$  should

be real, positive and  $\alpha^2$  should be less than the maximum value

$$\alpha^2 = \pi^2 \left( \frac{1}{L_x^2} + \frac{1}{L_y^2} \right) \quad (2.18)$$

If  $L_x = L_y$ , then,  $\alpha \in (-\sqrt{2}\pi, \sqrt{2}\pi)$  (Wiegelmann & Sakurai, 2012). The difficulty with the LFFF model is that an univalued  $\alpha$  is not sufficient for the coronal magnetic loops (Leka & Skumanich, 1999; Leka, 1999).

### 2.2.3 Non-linear-force-free-field (NLFFF) model

The equation for NLFFF is

$$\nabla \times \mathbf{B} = \alpha(r)\mathbf{B}, \quad (2.19)$$

$$\nabla \alpha \cdot \mathbf{B} = 0. \quad (2.20)$$

The  $\alpha$  here is a function of position implying different twist in different locations whereas the second condition comes from the solenoidality of  $\mathbf{B}$ , making the twist constant along a given field line. Implementation of NLFFF for real magnetogram is challenging. However, there are numerous procedures aimed to solve the problem from different approaches viz. vertical integration (Wu & Wang, 1985; Cuperman et al., 1989, 1990b,a; Wu et al., 1990; Demoulin et al., 1992; Song et al., 2006, 2007), Grad-Rubin methods (Sakurai, 1981; Amari et al., 1997, 1999; Wiegelmann, 2004; Amari et al., 2006; Inhester & Wiegelmann, 2006; Wheatland, 2006; Wheatland & Régnier, 2009; Malanushenko et al., 2009), boundary integrals (Yan & Sakurai, 1997, 2000; He & Wang, 2008), optimization (Wheatland et al., 2000; Wiegelmann, 2004), MHD evolutionary techniques (Yang et al., 1986) and force-free electrodynamics (Contopoulos, 2013). A comparative analysis between these algorithms is discussed in (Schrijver et al., 2006, 2008; Metcalf et al., 2008; De Rosa et al., 2009).

### 2.2.4 Non-force-free-field (NLFFF) model

The NLFFF has to preprocess data to make the photosphere force-free for mathematical continuity. In the process, precision is lost since the photospheric plasma is of high  $\beta$  and is not force-free. Interestingly, it is suggested by Gary (2001) that the plasma- $\beta$  is negligible only at the mid-corona, see Fig.-2.13. More-

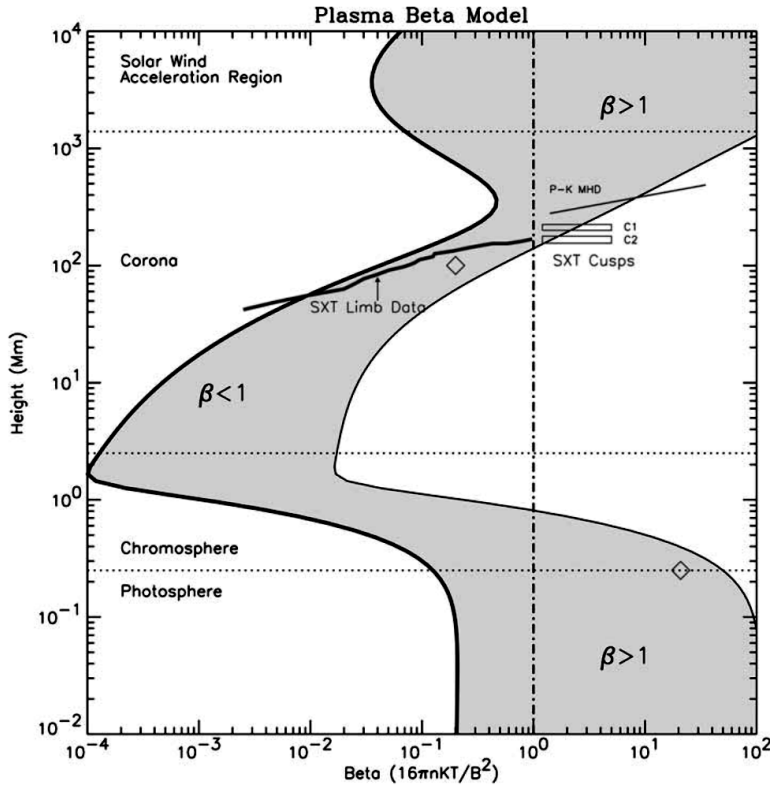


Figure 2.13: variation of plasma beta over the atmosphere. Picture credit: Gary (2001).

over, for both LFFF and the NLFFF, the solution does not match the boundary conditions i.e. the  $\alpha$ -value computed from the data may generally not be the same at both ends of a field line in the extrapolated field. Consequently, in the thesis we use a model that allows for non-force-free magnetic field on the photosphere while the Lorentz force decays with height. Several other non-force-free models are put forwarded to obtain the coronal magnetic field. Wiegmann & Neukirch (2006); Wiegmann et al. (2007) have adapted the optimization scheme to solve the magnetohydrostatic equation. In their non-force-free model, Gary & Alexander (1999) have tried to construct the coronal magnetic field by com-

binning photospheric magnetograms and the structures of coronal loops. For a detailed discussion on the algorithms, efficacy of all the models, see (Wiegelmann & Sakurai, 2012; Régnier, 2013).

In the thesis, we follow the method developed by Hu & Dasgupta (2006, 2008); Hu et al. (2008, 2010). The extrapolation method is based on the principle of minimum dissipation rate (MDR) (Bhattacharyya & Janaki, 2004) which is applicable to open dissipative systems like the solar corona (Bhattacharyya et al., 2007). According to the principle, the terminal state of a relaxing magnetofluid is determined by minimizing the total (Ohmic+viscous) dissipation rate while keeping the generalized helicity dissipation rates invariant.

The model essentially solves an inhomogeneous double-curl Beltrami equation for the magnetic field  $\mathbf{B}$  given by Bhattacharyya & Janaki (2004); Bhattacharyya et al. (2007)

$$\nabla \times \nabla \times \mathbf{B} + a_1 \nabla \times \mathbf{B} + b_1 \mathbf{B} = \nabla \psi. \quad (2.21)$$

where  $a_1$  and  $b_1$  are the constants which depends on the parameters of the system. The equation can be cast in an auxiliary form,

$$\nabla \times \nabla \times \mathbf{B}^* + a_1 \nabla \times \mathbf{B}^* + b_1 \mathbf{B}^* = 0, \quad (2.22)$$

where,  $\mathbf{B}$  is replaced by  $\mathbf{B} = \mathbf{B}^* + \nabla \psi / b_1$ . Then the solution to the auxiliary equation will be

$$\mathbf{B}^* = \lambda_1 \mathbf{Y}_1 + \lambda_2 \mathbf{Y}_2 \quad (2.23)$$

where,  $\mathbf{Y}_1$  and  $\mathbf{Y}_2$  are the Chandrasekhar-Kendall functions, forming a complete orthonormal basis and satisfying the Linear-Force-Free equation  $\nabla \times \mathbf{Y}_i = \zeta_i \mathbf{Y}_i$ . If we write the solution in terms of original field variable  $\mathbf{B}$ , then it turns out that,

$$\mathbf{B} = \lambda_1 \mathbf{Y}_1 + \lambda_2 \mathbf{Y}_2 + \nabla \psi \quad (2.24)$$

where the solution is a superposition of three force-free fields, two of them being LFFFs and one being potential field. When applied to the real magnetogram data, the algorithm of the NFFF model works in the following way. The magnetic

field is constructed as (Hu et al., 2010)

$$\mathbf{B} = \sum_{i=1,2,3} \mathbf{B}_i; \quad \nabla \times \mathbf{B}_i = \alpha_i \mathbf{B}_i, \quad (2.25)$$

where  $\alpha_i$  being constant for a given  $\mathbf{B}_i$ . Each subfield  $\mathbf{B}_i$  is a LFFF and  $\alpha_1 \neq \alpha_2 \neq \alpha_3$ . Hereafter we follow the notations used in Hu et al. (2008, 2010) to maintain homogeneity. Without any loss of generality, we further take  $\alpha_1 \neq \alpha_3$ , and  $\alpha_2 = 0$  which makes  $B_2$  a potential field. Thereafter, an optimal pair  $\alpha = \{\alpha_1, \alpha_3\}$  is attained using an iterative trial-and-error method which finds a pair  $\{\alpha_1, \alpha_3\}$  that minimizes the average deviation between the observed ( $\mathbf{B}_t$ ) and the computed ( $\mathbf{b}_t$ ) transverse field on the photospheric boundary, expressed by the metric

$$E_n = \left( \sum_{i=1}^M |\mathbf{B}_{t,i} - \mathbf{b}_{t,i}| \times |\mathbf{B}_{t,i}| \right) / \left( \sum_{i=1}^M |\mathbf{B}_{t,i}|^2 \right) \quad (2.26)$$

where  $M = N^2$ , represents the total number of grid points on the transverse plane. The grid points are weighted with respect to the strength of the observed transverse field to minimize the contribution from weaker fields, see (Hu et al., 2008, 2010), for further details. The extrapolated  $\mathbf{B}$  is essentially a solution of the equation

$$\nabla \times \nabla \times \nabla \times \mathbf{B} + a_1 \nabla \times \nabla \times \mathbf{B} + b_1 \nabla \times \mathbf{B} = 0 \quad (2.27)$$

where  $a_1$  and  $b_1$  are constants. Since Eq.-2.27 involves the evaluation of the second-order derivative,  $\nabla \times \nabla \times \mathbf{B}_z = -\nabla^2 B_z$  at  $z = 0$ , evaluation of  $\mathbf{B}$  requires magnetograms at two different values of  $z$ . In order to work with the generally available single-layer vector magnetograms an algorithm was introduced by Hu et al. (2010). The flowchart is presented in Fig.-2.14. This algorithm involves additional iterations to successively correct the potential sub-field  $\mathbf{B}_2$ . The system is reduced to second order by taking initial guess  $\mathbf{B}_2 = 0$  which makes it easier to determine the boundary condition for  $\mathbf{B}_1$  and  $\mathbf{B}_3$  using the method

described earlier. If the calculated value of minimum  $E_n$  is not satisfactory, then a potential field corrector to  $\mathbf{B}_2$  is calculated from the difference in observed and computed transverse fields, i.e.  $\mathbf{B}_t - \mathbf{b}_t$ . The difference value is added to the previous  $\mathbf{B}_2$ , in expectation of an improved match between the transverse fields measured by  $E_n$ . Further details will be presented later in the thesis during the extrapolation of active region magnetic fields.

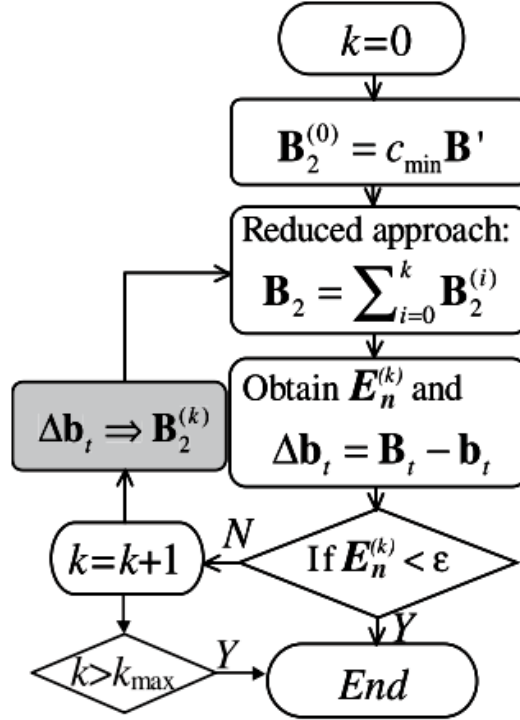


Figure 2.14: The flowchart showing the algorithm used in the NFFF extrapolation (Hu et al., 2010).

## 2.3 Data Acquisition

In the thesis, we complement the extrapolations and numerical simulation with multi-wavelength observations. Also for extrapolations, data from photospheric magnetograms are required. For the purpose, we employ data from the space-based instrument Solar Dynamics Observatory (SDO) because of its high-resolution data products. SDO is a mission under NASA Living With a Star (LWS) program. It was launched on 2010 February 11 from Kennedy Space Center in Florida. It is positioned in a geosynchronous orbit. The SDO provides

variety of data sets like magnetic field, imaging of different layers, Doppler velocity for full disk and active region patches extracted with advanced algorithms unprecedentedly for 24 hours. There are three payloads in SDO: (1) Atmospheric Imaging Assembly (AIA), (2) Helioseismic and Magnetic Imager (HMI), and (3) Extreme ultraviolet Variability Explorer (EVE). The thesis will use two of the three instruments, AIA and HMI.

### 2.3.1 Helioseismic and Magnetic Imager (HMI)

HMI (Schou et al., 2012) aims to study oscillations and the magnetic field at the solar surface. HMI observes the full solar disk at 6173 Å with a resolution of 1 arcsecond. The data types are: dopplergrams (maps of solar surface velocity), continuum filtergrams (broad-wavelength photographs of the solar photosphere), and both line-of-sight and vector magnetograms (maps of the photospheric magnetic field). See <http://hmi.stanford.edu/> for more details. HMI consists of a refracting telescope, a polarization selector, an image stabilization system, a narrow band tunable filter and two 4096 pixel CCD cameras with mechanical shutters and control electronics. Images are made in a sequence of tuning and polarizations at a 4-second cadence for each camera. One camera is dedicated to a 45s Doppler and line-of-sight field sequence while the other to a 90s vector field sequence. The magnetic field on the Sun's photosphere is measured by using Zeeman's effect which explains the splitting of spectral lines in the presence of magnetic field. For a weak field, the splitting depends on the magnetic field strength ( $\delta\lambda \propto B$ ). With respect to an observer, along the line-of-sight, the lines split into shifted circular polarized  $\sigma$  components and an unshifted  $\pi$  component (see Fig.-2.15). If the radiation is along the magnetic field, then the observer will be able to see the circularly polarized components and the effect is known as longitudinal Zeeman effect, depicted in Fig.-2.15. Whereas, if the direction of the radiation is perpendicular to the magnetic field, then the observer see the linearly polarized components and the effect is transverse Zeeman effect, depicted in Fig.-2.15. The polarization is described by the Stokes parameter ( $I$ ,  $Q$ ,  $U$ , and  $V$ ), where  $I$  represents the total intensity of the radiation,  $Q$  represents the

intensity difference between vertical and horizontal linear polarization,  $U$  is the intensity difference between linear polarization at  $+45^\circ$  and  $-45^\circ$  and  $V$  is the intensity difference between right and left hand circular polarization. The Stokes

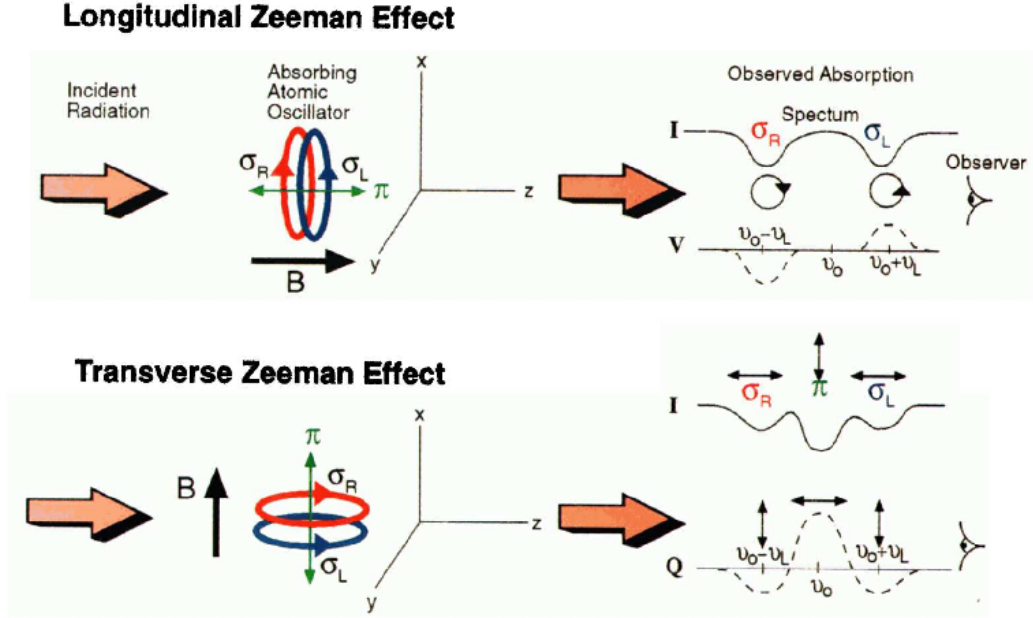


Figure 2.15: A schematic showing the Zeeman effect an an atomic system. The magnetic field is aligned along the  $z$ - and  $x$ - axes respectively, showing the longitudinal (top) and transverse (bottom) Zeeman effect. Taken from Lites (2000).

parameter can be written as (Venkatakrisshnan & Gosain, 2008):

$$I = \langle E_x E_x^* \rangle + \langle E_y E_y^* \rangle \quad (2.28)$$

$$Q = \langle E_x E_x^* \rangle - \langle E_y E_y^* \rangle, \quad (2.29)$$

$$U = 2\text{Re} \langle E_x E_y^* \rangle, \quad (2.30)$$

$$V = 2\text{Im} \langle E_x E_y^* \rangle, \quad (2.31)$$

where,  $E_x$  and  $E_y$  are components of Electric field and  $\langle \rangle$  represents the expectation value. For a strong magnetic field, the magnetic field is estimated by spectropolarimeter which provides the Stokes profile with proper atmospheric model like inclusion of line formation mechanism and radiative transfer equations.

HMI provides the full disk vector magnetic measurement with the measured Stokes vector at six wavelengths across the Fe I absorption line at  $6173 \text{ \AA}$ . It

employs the Very Fast Inversion of Stokes Vector (VFISV) (Borrero et al., 2011) algorithm to obtain the field components from the observed Stokes parameters. Then to resolve the  $180^\circ$  ambiguity in the transverse fields, which arises due to the azimuthal angle associated with the polarization, the minimum energy method by Metcalf (1994); Leka et al. (2009) is used after inversion. Two types of data sets are available at HMI pipeline: (1) full disk of temporal cadence 720s and 135s and (2) a cylindrical equal-area active region patch with temporal cadence of 720s, for details <http://jsoc.stanford.edu/jsocwiki/HARPDDataSeries>. The components of the field are the azimuthal  $B_p$ , the zenith  $B_t$  and radial  $B_r$  and  $B_x$ ,  $-B_y$  and  $B_z$  in heliographic co-ordinates respectively. For details of the data products, see [http://jsoc.stanford.edu/HMI/Vector\\_products.html](http://jsoc.stanford.edu/HMI/Vector_products.html).

### 2.3.2 Atmospheric Imaging Assembly (AIA)

The Atmospheric Imaging Assembly (AIA) (Lemen et al., 2012) provides an unprecedented observation of the solar corona with a field of view of at least 1.3 solar diameters in multiple wavelengths simultaneously, at a resolution of about 1 arcsec ( $4096 \times 4096$ -pixel images) in 10 wavelengths of ultraviolet (UV) and extreme ultraviolet (EUV) windows every 10 seconds <https://aia.lmsal.com/>. With combination of data from other SDO instruments and from other observatories, it aims to develop a better understanding of the physics behind the activity seen in the Sun's atmosphere. The AIA gathers data of both the quiescent and activity phases which are essential to study the evolution of the magnetic field in the the atmosphere and its impact on the space-weather. The AIA is an array of 4 telescopes that together provide full-disk images of the solar corona at 1 arcsec resolution. The AIA instrument consists of four generalized Cassegrain telescopes that are optimized to observe in narrow band-passes in UV and EUV in order to observe solar emissions from the transition region and corona. Table 2.1 details the observation channels of AIA along with the corresponding regions of solar atmosphere at a characteristic temperature (Lemen et al., 2012).

Table 2.1: Primary ions observed by AIA; Adapted from Lemen et al. (2012).

Channel	Primary ion(s)	Region of atmosphere	Char. log(T)
4500	continuum	photosphere	3.7
1700	continuum	temperature minimum, photosphere	3.7
304	He II	chromosphere, transition region	4.7
1600	C IV + cont.	transition region, upper photosphere	5.
171	Fe IX	quiet corona, upper transition region	5.8
193	Fe XII, XXIV	Corona and hot flare plasma	6.2, 7.3
211	Fe XIV	active-region corona	6.3
335	Fe XVI	active-region corona	6.4
94	Fe XVIII	flaring corona	6.8
131	Fe VIII, XXI	transition region, flaring corona	5.6, 7.0



# Chapter 3

## Numerical Model

A successful numerical simulation of active region dynamics requires a stringent satisfaction of the condition of flux-freezing away from the reconnection sites, while at the sites the requirement is to break the flux-freezing and allow for diffusion of magnetic field lines. In other words, the necessity is an intermittent diffusivity that appears only when and where the MRs occur. For our computations, we utilize the well established numerical model EULAG-MHD (Smolarkiewicz & Charbonneau, 2013) which is an extension of the hydrodynamic model EULAG predominantly used in atmospheric and climate research (Prusa et al., 2008). The EULAG-MHD is based on the spatio-temporally (at least) second-order accurate non-oscillatory forward-in-time (NFT) advection scheme multidimensional positive definite advection transport algorithm, MPDATA, (Smolarkiewicz & Margolin, 1998; Smolarkiewicz, 2006). The accuracy of MPDATA ensures the satisfaction of the flux-freezing with a high fidelity away from the reconnection region. Additionally, a feature unique to MPDATA and important in our calculations is its proven effectiveness in generating an intermittent and adaptive residual dissipation, whenever the concerned advective field is under-resolved (Margolin et al., 2006). The magnetic nulls and QSLs in the absence of magnetic diffusion provides an unbound sharpening of the corresponding field gradient and inevitably generates under-resolved scales. The MPDATA then produces the residual dissipation to regularize these scales through onset of simulated magnetic reconnections. In the following we present salient features of

the EULAG-MHD relevant to our simulations.

### 3.1 Advection solver MPDATA

MPDATA is a finite-difference algorithm invented by P. K. Smolarkiewicz in the early 1980's (Smolarkiewicz, 1983, 1984; Smolarkiewicz & Clark, 1986). The algorithm is at least second-order accurate, positive definite, conservative, and computationally efficient. The second-order accuracy in MPDATA is achieved by utilizing the first-order accurate donor cell (also known as upstream or upwind) scheme in an iterative manner. The first iteration is a simple donor cell differencing. With a donor cell solution obtained from first iteration, MPDATA increases the accuracy of the calculation by estimating and compensating (second-order) truncation error in the second iteration. Similarly, additional iterations can be performed to approximately compensate the residual error produced from previous iteration which further enhance the accuracy.

Since its invention, MPDATA is extended to curvilinear coordinates, full monotonicity preservation, third-order accuracy and variable sign fields; details can be found in (Smolarkiewicz & Margolin, 1998; Smolarkiewicz, 2006). Here we discuss basic concepts underlying the design of the MPDATA scheme in Cartesian coordinates.

#### 3.1.1 Derivation of MPDATA

To fix ideas, we consider a simple one-dimensional advection equation,

$$\frac{\partial \varphi}{\partial t} + \frac{\partial(k\varphi)}{\partial x} = 0, \quad (3.1)$$

for a scalar variable  $\varphi$ . The velocity  $k$  may also be a function of space and time.

The donor cell discretization of the advection equation is given by,

$$\varphi_i^{n+1} = \varphi_i^n - \frac{\delta t}{\delta x} (k_{i+\frac{1}{2}} \varphi_r^n - k_{i-\frac{1}{2}} \varphi_l^n), \quad (3.2)$$

where  $\varphi_r^n$  and  $\varphi_l^n$  are chosen depending on the sign of  $k_{i+\frac{1}{2}}$  and  $k_{i-\frac{1}{2}}$ :

$$\varphi_r^n = \begin{cases} \varphi_i^n, & k_{i+\frac{1}{2}} > 0, \\ \varphi_{i+1}^n, & k_{i+\frac{1}{2}} < 0, \end{cases} \quad (3.3)$$

and

$$\varphi_l^n = \begin{cases} \varphi_{i-1}^n, & k_{i-\frac{1}{2}} > 0, \\ \varphi_i^n, & k_{i-\frac{1}{2}} < 0, \end{cases} \quad (3.4)$$

with the integer and half-integer indices corresponding to cell centers and cell walls. In Eq.-(3.2),  $\varphi_i^{n+1}$  on the LHS is the solution sought at the grid point  $(t^{n+1}, x_i)$  with  $\delta t = t^{n+1} - t^n$  and  $\delta x = x_{i+1} - x_i$  representing temporal and spatial increments respectively. The above case distinctions can be avoided by writing the Eq.-(3.2) in the following form,

$$\begin{aligned} \varphi_i^{n+1} = \varphi_i^n - \frac{\delta t}{2\delta x} [k_{i+\frac{1}{2}}(\varphi_i^n + \varphi_{i+1}^n) - k_{i-\frac{1}{2}}(\varphi_{i-1}^n + \varphi_i^n) \\ + |k_{i+\frac{1}{2}}| |(\varphi_i^n - \varphi_{i+1}^n)| - |k_{i-\frac{1}{2}}| |(\varphi_{i-1}^n - \varphi_i^n)|]. \end{aligned} \quad (3.5)$$

Notably, if the sign of  $k$  determines the flow direction, this scheme always chooses the values of  $\varphi$  (for a given time) which lies in the upstream direction (Griebel et al., 1998). The donor cell approximation in flux form is expressed as,

$$\varphi_i^{n+1} = \varphi_i^n - [F(\varphi_i^n, \varphi_{i+1}^n, U_{i+\frac{1}{2}}) - F(\varphi_{i-1}^n, \varphi_i^n, U_{i-\frac{1}{2}})], \quad (3.6)$$

where the flux function  $F$  is

$$F(\varphi_L, \varphi_R, U) \equiv [U]^+ \varphi_L + [U]^- \varphi_R, \quad (3.7)$$

with  $U \equiv \frac{a\delta t}{\delta x}$  represents the dimensionless local Courant number while,  $[U]^+ \equiv 0.5(U + |U|)$  and  $[U]^- \equiv 0.5(U - |U|)$  denoting the nonnegative and non-positive parts of the Courant number (Smolarkiewicz & Margolin, 1998; Smo-

larkiewicz, 2006).

The donor cell scheme is conditionally stable and the corresponding stability condition, for every time step, has a form

$$\max \left( \frac{|k_{i+\frac{1}{2}}| \delta t}{\delta x} \right) \leq 1 \quad \forall i. \quad (3.8)$$

Moreover, under the condition (3.8), the scheme is also positive definite, implying: if  $\varphi_i^0 \geq 0 \quad \forall i$  then  $\varphi_i^n \geq 0 \quad \forall i$  and  $n$ . These two properties as well as low computational cost and low phase error make the scheme (3.6) attractive for the numerical evaluation of the advection equation. However, the scheme being first-order accurate (both in space and time) produces large implicit numerical diffusion.

Toward quantifying the diffusion in (3.6), for simplicity we assume  $k$  to be constant and  $\varphi$  to be nonnegative. A straightforward truncation analysis, expanding all dependent variables in a second-order Taylor series about the time level  $n$  and spatial point  $i$ , reveals that the scheme more accurately approximates the advection-diffusion equation

$$\frac{\partial \varphi}{\partial t} + \frac{\partial(k\varphi)}{\partial x} = \frac{\partial}{\partial x} \left( K \frac{\partial \varphi}{\partial x} \right), \quad (3.9)$$

where the diffusion coefficient

$$K = \frac{\delta x^2}{2\delta t} (|U| - U^2). \quad (3.10)$$

In other words, the scheme estimates the solution of the advection equation with a second-order truncation error. To enhance the accuracy, it is necessary to construct a numerical estimate of the error and subtract it from (3.6). The basic strategy, fundamental to all MPDATA schemes, is then to once again utilize a donor cell approximation to calculate the error term in order to preserve the properties of donor cell scheme. To do so, the error term, the RHS term of (3.9), is rewritten as

$$e^1 \equiv \frac{\partial}{\partial x} \left( K \frac{\partial \varphi}{\partial x} \right) = \frac{\partial(k^1 \varphi)}{\partial x}, \quad (3.11)$$

where  $e^1$  symbolizes error term and  $k^1 \equiv \frac{K}{\varphi} \frac{\partial \varphi}{\partial x}$  is termed as pseudo velocity. The superscript (1) is used to mark the first iteration for subtracting the error. To compensate the error, we again use the donor cell scheme but this time with the pseudo velocity  $k^1$  and the  $\varphi^{n+1}$  already available from (3.6) in lieu of the physical velocity  $k$  and the  $\varphi^n$ . A first-order accurate estimate of the pseudo velocity is

$$k_{i+\frac{1}{2}}^1 \equiv \frac{2K}{\delta x} \frac{\varphi_{i+1}^{(1)} - \varphi_i^{(1)}}{\varphi_{i+1}^{(1)} + \varphi_i^{(1)}} \quad (3.12)$$

where  $\varphi^{(1)}$  represents the first-order accurate  $\varphi^{n+1}$  estimated from (3.6). The modified Courant number is  $V_{i+\frac{1}{2}}^1 \equiv \frac{k_{i+\frac{1}{2}}^1 \delta t}{\delta x}$ . In the second iteration, we subtract a donor cell estimate of the error to improve the accuracy. The equation of the second iteration is

$$\varphi_i^2 = \varphi_i^1 - [F(\varphi_i^1, \varphi_{i+1}^1, V_{i+\frac{1}{2}}^1) - F(\varphi_{i-1}^1, \varphi_i^1, V_{i-\frac{1}{2}}^1)], \quad (3.13)$$

which estimates  $\varphi^{n+1}$  which is the second-order accurate while preserving the sign of  $\varphi$ . It is an easy matter to show that, like the donor cell scheme, MPDATA is consistent and conditionally stable (Smolarkiewicz, 1983; Smolarkiewicz & Margolin, 1998; Smolarkiewicz, 2006). But, in contrast to the donor scheme, MPDATA does not contain strong numerical implicit diffusion because of the improved accuracy.

The extension of MPDATA to multiple dimension is straightforward. To demonstrate, we consider a simple two-dimensional advection equation,

$$\frac{\partial \varphi}{\partial t} + \frac{\partial(k\varphi)}{\partial x} + \frac{\partial(l\varphi)}{\partial y} = 0, \quad (3.14)$$

where  $k$  and  $l$  are velocities in  $x$  and  $y$  directions. The corresponding donor cell approximation is then

$$\begin{aligned} \varphi_{i,j}^{n+1} = & \varphi_{i,j}^n - [F(\varphi_{i,j}^n, \varphi_{i+1,j}^n, U_{i+\frac{1}{2},j}) - F(\varphi_{i-1,j}^n, \varphi_{i,j}^n, U_{i-\frac{1}{2},j})] \\ & - [F(\varphi_{i,j}^n, \varphi_{i,j+1}^n, V_{i,j+\frac{1}{2}}) - F(\varphi_{i,j-1}^n, \varphi_{i,j}^n, V_{i,j-\frac{1}{2}})], \end{aligned} \quad (3.15)$$

where the flux function is similar to (3.7) and,  $U \equiv \frac{k\delta t}{\delta x}$  and  $V \equiv \frac{l\delta t}{\delta y}$  are Courant numbers. Further, the Taylor's series expansion of (3.15) about the cell point  $(i, j)$  and the time level  $n$  with constant velocities yields the following advection-diffusion equation,

$$\frac{\partial \varphi}{\partial t} + \frac{\partial(k\varphi)}{\partial x} + \frac{\partial(l\varphi)}{\partial y} = K \frac{\partial^2 \varphi}{\partial x^2} + L \frac{\partial^2 \varphi}{\partial y^2} - \frac{UV\delta x\delta y}{\delta t} \frac{\partial^2 \varphi}{\partial x\partial y}, \quad (3.16)$$

with  $K \equiv \frac{\delta x^2}{2\delta t}(|U| - U^2)$  and  $L \equiv \frac{\delta y^2}{2\delta t}(|V| - V^2)$ . To estimate the truncation error using the donor cell scheme, we rewrite the error terms, the RHS terms of (3.16), in the following form

$$K \frac{\partial^2 \varphi}{\partial x^2} + L \frac{\partial^2 \varphi}{\partial y^2} - \frac{UV\delta x\delta y}{\delta t} \frac{\partial^2 \varphi}{\partial x\partial y} = \frac{\partial}{\partial x}(k^1\varphi) + \frac{\partial}{\partial x}(l^1\varphi) \quad (3.17)$$

where

$$k^1 \equiv \frac{K}{\varphi} \frac{\partial \varphi}{\partial x} - \frac{UV\delta x\delta y}{2\delta t} \frac{1}{\varphi} \frac{\partial \varphi}{\partial y} \quad \text{and} \quad l^1 \equiv \frac{L}{\varphi} \frac{\partial \varphi}{\partial y} - \frac{UV\delta x\delta y}{2\delta t} \frac{1}{\varphi} \frac{\partial \varphi}{\partial x} \quad (3.18)$$

are pseudo velocities in  $x$  and  $y$  directions. Utilizing these velocities and updated value of  $\varphi^{n+1}$  from (3.15), the donor cell scheme is used to estimate the error. In the second iteration, the error is subtracted to enhance the accuracy.

### 3.1.1.1 Extension to generalized transport equation

The general transport equation is

$$\frac{\partial \varphi}{\partial t} + \nabla \cdot (\mathbf{k}\varphi) = R, \quad (3.19)$$

where  $R$  combines all forcing and source terms. In general, both  $R$  and velocity  $\mathbf{k}$  depend on variable  $\varphi$ . The forward-in-time discretization of (3.19) is assumed as,

$$\frac{\varphi^{n+1} - \varphi^n}{\delta t} + \nabla \cdot (\mathbf{k}^{n+\frac{1}{2}} \varphi^n) = R^{n+\frac{1}{2}}. \quad (3.20)$$

Expansion of (3.20) into the second-order Taylor series about the time level  $n$  shows that the scheme (3.20) approximates to the equation

$$\frac{\partial \varphi}{\partial t} + \nabla \cdot (\mathbf{k} \varphi) = R - \nabla \cdot \left[ 0.5 \delta t \mathbf{k} (\mathbf{k} \cdot \nabla \varphi) + 0.5 \delta t \mathbf{k} \varphi (\nabla \cdot \mathbf{k}) \right] + \nabla \cdot (0.5 \delta t \mathbf{k} R) + \mathcal{O}(\delta t^2). \quad (3.21)$$

In RHS of (3.21), all  $\mathcal{O}(\delta t)$  truncation errors originated by uncentered time differencing in (3.20) are already expressed by spatial derivatives. Specification of the time levels of both the advective velocity and the forcing term as  $n+1/2$  in (3.20) eliminates  $\mathcal{O}(\delta t)$  truncation errors which are proportional to their temporal derivatives (Smolarkiewicz & Clark, 1986). From (3.21), it is clear that the formulation of second-order accurate forward-in-time scheme for (3.19) requires the compensation of  $\mathcal{O}(\delta t)$  truncation errors to at least the second-order accuracy.

For such a formulation, we note  $\mathcal{O}(\delta t)$  error terms in (3.21) have two distinct components. The first component is merely due to advection and does not involve the forcing  $R$ . In contrast, the second component depends on the forcing  $R$ . Toward compensating the first component, notable is the reduction of (3.19) to homogeneous transport equation for  $R = 0$ . Then, MPDATA scheme retains the form of the basic scheme (subsection 5.2.1) where the first donor cell iteration utilizes the advective velocity  $\mathbf{k}^{n+\frac{1}{2}}$  and  $\varphi^n$ , and subsequent iterations use pseudo velocities and  $\varphi$  calculated from the preceding iteration; for details cf. (Smolarkiewicz, 1991; Smolarkiewicz & Margolin, 1993, 1998; Smolarkiewicz, 2006). Compensation of the second component requires subtracting of a first-order accurate approximation of the error from the RHS of (3.20). A simple, efficient, and second-order accurate MPDATA for (3.19) can then be symbolically written as,

$$\varphi_i^{n+1} = \mathcal{A}_i(\varphi^n + 0.5\delta t R^n, \mathbf{k}^{n+\frac{1}{2}}) + 0.5\delta t R_i^{n+1}, \quad (3.22)$$

where  $\mathcal{A}$  denotes the basic MPDATA advection scheme (Smolarkiewicz, 1991; Smolarkiewicz & Margolin, 1993). In this equation, we assume  $R^{n+\frac{1}{2}} = 0.5(R^n + R^{n+1})$  with  $R^{n+1}$  representing  $\mathcal{O}(\delta t^2)$  accurate approximation of  $R$  at time level  $(n+1)$ . Noticeably, first donor cell iteration in the MPDATA scheme uses the auxiliary variable  $\varphi^n + 0.5\delta t R^n$  in lieu of the physical variable  $\varphi^n$  with a physical advective velocity  $\mathbf{k}^{n+\frac{1}{2}}$ . The advection of the auxiliary field is important for preserving the global accuracy and stability of the forward in time approximations (Smolarkiewicz, 1991; Smolarkiewicz & Margolin, 1993, 1997).

The advective velocity at intermediate  $n + \frac{1}{2}$  time level may be approximated by linear interpolation or extrapolation

$$\mathbf{k}^{n+\frac{1}{2}} = \frac{1}{2}(\mathbf{k}^{n+1} + \mathbf{k}^n), \quad (3.23)$$

$$\mathbf{k}^{n+\frac{1}{2}} = \frac{1}{2}(3\mathbf{k}^n - \mathbf{k}^{n-1}), \quad (3.24)$$

either of which is sufficient to maintain second-order accuracy in (3.22). For the subtleties involved in a particular choice of  $\mathbf{k}^{n+\frac{1}{2}}$ , readers are referred to (Smolarkiewicz & Clark, 1986).

### 3.1.1.2 Nonoscillatory MPDATA

The basic MPDATA scheme discussed above preserves sign<sup>1</sup> but not monotonicity of the advected variables (Smolarkiewicz, 1983, 1984; Smolarkiewicz & Clark, 1986) and, in general, the solutions are not free of spurious oscillations particularly in presence of steep gradients (Smolarkiewicz & Grabowski, 1990; Smolarkiewicz, 1991). However, MPDATA is made fully monotone (Smolarkiewicz, 1991) by adapting the flux-corrected-transport (FCT) methodology (Boris & Book, 1973; Book et al., 1975; Boris & Book, 1976). Actually, MPDATA is well

<sup>1</sup>For historical reasons, we refer to this property as positive-definiteness in the previous subsections.

suitable for this kind of approach for a number of reasons. First, the initial MPDATA iteration is the donor cell scheme—a low-order monotone scheme which is commonly used as the reference in the FCT design. Second, assuring monotonicity of subsequent iterations provides a higher-order accurate reference solution for the next iteration with the effect of improving the overall accuracy of the resulting FCT scheme. Third, since all MPDATA iterations have similar low phase errors characteristic of the donor cell scheme (Smolarkiewicz & Clark, 1986), the FCT procedure mixes solutions with consistent phase errors. This benefits significantly the overall accuracy of the resulting FCT scheme (Smolarkiewicz & Grabowski, 1990).

### 3.1.2 EULAG-MHD

The numerical model EULAG is an established model for simulating fluid flows across a wide range of scales and physical scenarios (Prusa et al., 2008). The name EULAG alludes to the capability to solve the fluid equations in either an Eulerian (Smolarkiewicz & Margolin, 1993) or a Lagrangian (Smolarkiewicz & Pudykiewicz, 1992) mode. The numerics of EULAG are unique, owing to a combination of MPDATA advection schemes, robust elliptic solver, and generalized coordinate formulation enabling grid adaptivity. The EULAG-MHD is a spin-off of the numerical model EULAG (Smolarkiewicz & Charbonneau, 2013). Here, we describe the numerical apparatus of EULAG-MHD utilized for our calculations.

#### 3.1.2.1 Governing equations of EULAG-MHD

MHD equations for an incompressible magnetofluid with infinite electrical conductivity are cast in the following form

$$\frac{d\mathbf{v}}{dt} = -\nabla\pi + \frac{1}{4\pi\rho_0}\mathbf{B} \cdot \nabla\mathbf{B} + F_\nu, \quad (3.25)$$

$$\frac{d\mathbf{B}}{dt} = \mathbf{B} \cdot \nabla\mathbf{v} - \mathbf{B}\nabla \cdot \mathbf{v}, \quad (3.26)$$

$$\nabla \cdot \mathbf{v} = 0, \quad (3.27)$$

$$\nabla \cdot \mathbf{B} = 0, \quad (3.28)$$

in non-rotating Cartesian coordinates. The Lagrangian derivative is related the Eulerian derivative in the usual manner

$$\frac{d}{dt} \equiv \frac{\partial}{\partial t} + (\mathbf{v} \cdot \nabla). \quad (3.29)$$

Importantly, by incompressibility we mean  $\frac{d\rho}{dt} = 0$  and  $\rho \neq \text{constant}$ . Although incompressibility approximation is a restrictive approximation for the coronal plasma, but was used in earlier works also (Dahlburg et al., 1991; Aulanier et al., 2005). Moreover, the compressibility of the fluid is important for the thermodynamics of the coronal loops (Ruderman & Roberts, 2002) whereas the magnetic topology is not affected by viscosity. On the RHS of the momentum transport equation (3.25),  $\pi$  is a density normalized pressure in which thermodynamic pressure is subsumed to magnetic pressure.  $F_\nu$  symbolizes the viscous drag force. All other symbols have their usual meaning.

On a general note, EULAG's governing equations are formulated and solved in transformed time-dependent generalized curvilinear coordinates

$$(\bar{t}, \bar{\mathbf{x}}) \equiv (t, F(t, \mathbf{x})). \quad (3.30)$$

The physical domain  $(t, x)$ , where the physical problem is posed, is assumed to be any stationary orthogonal coordinate system (i.e., Cartesian, spherical and cylindrical). Moreover, the transformed horizontal coordinates  $(\bar{x}, \bar{y})$  are assumed to be independent of the vertical coordinate  $z$  (Prusa & Smolarkiewicz, 2003). The calculations carried out in this thesis implement the physical domain to be Cartesian and, therefore both the computational domain and the physical domain are identical, i.e.,  $(\bar{t}, \bar{x}) \equiv (t, x)$ . Here, we present the details of the EULAG-MHD for Cartesian domain. The generalized coordinate formulation of EULAG-MHD utilizes the rigorous tensorial exposition of MHD equations; cf. (Smolarkiewicz & Charbonneau, 2013).

### 3.1.2.2 Numerics

Utilizing equations (3.27) and (3.28), the momentum transport equation (3.25) and the induction equation (3.26) can be rewritten as,

$$\frac{\partial \Psi}{\partial t} + \nabla \cdot (\mathbf{v} \Psi) = \mathbf{R} \quad (3.31)$$

where

$$\Psi = \{\mathbf{v}, \mathbf{B}\}^T \quad (3.32)$$

represents the vector of dependent variables and

$$\mathbf{R} = \{\mathbf{R}_v, \mathbf{R}_B\}^T \quad (3.33)$$

denotes the RHS forcing terms in (3.25) and (3.26). Notably, in (3.31), the Lorentz force term of the momentum transport equation and the convective term of the induction equation are cast in the conservative forms via relations,

$$\mathbf{B} \cdot \nabla \mathbf{B} = \nabla \cdot \mathbf{B} \mathbf{B}, \quad \mathbf{B} \cdot \nabla \mathbf{v} = \nabla \cdot \mathbf{B} \mathbf{v}. \quad (3.34)$$

In addition, an ad hoc term  $-\nabla \pi^*$  is added to RHS of the induction equation, in the spirit of the pressure  $\pi$  in the momentum transport equation, to ensure  $\nabla \cdot \mathbf{B} = 0$  in numerical integrations.

The equation (3.31) is integrated using nonoscillatory forward-in-time algorithm MPDATA. Following section (3.1.1.1), an EULAG template algorithm for integration of the (3.31) can be compactly written as,

$$\Psi_i^{n+1} = \mathcal{A}_i(\Psi^n + 0.5\delta t \mathbf{R}^n, \mathbf{v}^{n+\frac{1}{2}}) + 0.5\delta t \mathbf{R}_i^{n+1} \equiv \hat{\Psi}_i + 0.5\delta t \mathbf{R}_i^{n+1}, \quad (3.35)$$

where  $\Psi_i^{n+1}$  is the solution sought at the grid point  $(t^{n+1}, x_i)$ .

For an inviscid dynamics ( $F_\nu=0$ ), the model template algorithm (3.35) is implicit for all dependent variables in (3.25) and (3.26) because all forcing terms are assumed to be unknown at time level  $n+1$ . To retain the proven structure

of (3.35) for the MHD system, EULAG-MHD template can be viewed as

$$\Psi_i^{n+1,q} = \hat{\Psi}_i + \frac{\delta t}{2} \mathbf{L}\Psi \Big|_i^{n+1,q} + \frac{\delta t}{2} \mathbf{N}(\Psi) \Big|_i^{n+1,q-1} - \frac{\delta t}{2} \nabla\Theta \Big|_i^{n+1,q}, \quad (3.36)$$

where the RHS forcing  $\mathbf{R}$  is decomposed into linear term  $\mathbf{L}\Psi$  with  $\mathbf{L}$  denoting a linear operator, non linear-term  $\mathbf{N}(\Psi)$ , and potential term  $-\nabla\Theta$  with  $\Theta \equiv (\pi, \pi, \pi, \pi^*, \pi^*, \pi^*)$ . In (3.36),  $q = 1, \dots, m$  numbers fixed point iterations. The algorithm (3.36) is still implicit with respect to the forcing terms  $\mathbf{L}\Psi$  and  $-\nabla\Theta$ . Using straight-forward algebraic manipulations, the representation (3.36) can be cast into a closed form

$$\Psi_i^{n+1,q} = [\mathbf{I} - 0.5\delta t\mathbf{L}]^{-1} \left( \hat{\Psi} - 0.5\delta t\nabla\Theta^{n+1,q} \right)_i, \quad (3.37)$$

where the explicit element is modified to

$$\hat{\Psi} \equiv \hat{\Psi} + 0.5\delta t\mathbf{N}(\Psi) \Big|^{n+1,q-1}. \quad (3.38)$$

The viscous forcing within this algorithm frame work is incorporated by integrating explicitly to the first-order accuracy in time and then adding to the the auxiliary argument of MPDATA operator  $\mathcal{A}$ . Now the argument modifies as  $\tilde{\Psi} \equiv \Psi^n + 0.5\delta t(\mathbf{R}^n + 2\tilde{\mathbf{R}})$  where  $\tilde{\mathbf{R}}$  symbolizing the first-order time accurate viscous forcing. All the dependent variables being spatially co-located in (3.37), the time updated  $\Psi$  is obtained by solving two the discrete elliptic equations for  $\pi$  and  $\pi^*$  generated by the solenoidality constraints (3.27) and (3.28) discretized consistently with the divergence operator implied by  $\mathcal{A}$ ; see (Prusa et al., 2008). Under appropriate boundary conditions, these elliptic equations are solved iteratively using a preconditioned generalized conjugate residual (GCR) algorithm (Eisenstat, 1983; Eisenstat et al., 1983; Smolarkiewicz et al., 1997). Because the GCR is an iterative scheme, to distinguish the iterations appearing in (3.36) and in the GCR solver, the iteration in (3.36) is refereed as “outer”, while the iteration corresponds to GCR is termed as “inner”. The convergence of the outer iteration is generally controlled by the time step of the model and monitored

by the convergence of the inner iteration in the GCR solvers (Smolarkiewicz & Szmelter, 2009, 2011). With the completion of the outer iteration loop, the solution updates and, the total implicit forcing  $\mathbf{RI} = \mathbf{L}\Psi - \nabla\Theta$  in (3.36) is returned as  $\mathbf{RI}_i^n = \frac{2}{\delta t}(\Psi_i^n - \hat{\Psi}_i)$ . While, the total explicit forcing  $\mathbf{RE} = \mathbf{N}(\Psi) + \tilde{\mathbf{R}}$  is calculated according to its definition using the updated solution, so  $\mathbf{RE}_i^n = \mathbf{RE}_i(\Psi^n)$ . The total forcing  $\mathbf{R} = \mathbf{RI} + \mathbf{RE}$  is then stored for the use in the subsequent time step in the auxiliary argument of MPDATA operator in (3.35).

In the following, we briefly discuss the actual implementation of iterative formulation of (3.35). The iterations progress stepwise such that the most current update of a dependent variable is used in the ongoing step, wherever possible. Each outer iteration has two distinct blocks. The first block involves the integration of the momentum transport equation where the magnetic field enters the Lorentz force and is taken as supplementary. Being at the half of a single outer iteration, it is denoted by the index  $q-1/2$ . This block ends with the final update of the velocity via the solution of the elliptic equation for  $\pi$ . Hence, this block actually mirrors standard EULAG solution of hydrodynamic equations (Prusa et al., 2008), leading to the nomenclature “hydrodynamic block”. The second block, referred as “magnetic block”, uses the current updates of the velocities to integrate the induction equation. It ends with the final update of the magnetic field via the solution of the elliptic equation for  $\pi^*$  to clean the divergence of magnetic field. In the following we summarize sequence of steps fulfilled at each outer iteration for integrating the MHD Eq.s-(3.25)-(3.28). For brevity, the superscripts  $n$  are dropped everywhere as by now there should be no ambiguity. Moreover, at  $q = 1$  the initial guess for  $\mathbf{v}$  and  $\mathbf{B}$  is assumed as  $\mathbf{v}^0 = 2\mathbf{v}^{n+1} - \mathbf{v}^n$  and  $\mathbf{B}^0 = 2\mathbf{B}^{n+1} - \mathbf{B}^n$ , respectively.

The first step of the hydrodynamic block starts with the estimation of the magnetic field  $\mathbf{B}^{q-1/2}$  at time  $t^{n+1}$  by inverting the induction equation,

$$\mathbf{B}_i^{q-1/2} = \hat{\mathbf{B}}_i + 0.5\delta t \left[ \mathbf{B}^{q-1/2} \cdot \nabla \mathbf{v}^{q-1} - \mathbf{B}^{q-1/2} \text{tr}\{\nabla \mathbf{v}^{q-1}\} \right]_i. \quad (3.39)$$

The subsequent step uses this latest magnetic field to obtain velocity following

the standard EULAG procedure,

$$\mathbf{v}_i^q = \hat{\mathbf{v}}_i + \frac{0.5\delta t}{\rho_0\mu_0}(\nabla \cdot \mathbf{B}\mathbf{B})_i^{q-1/2} - 0.5\delta t(\nabla\pi)_i^q. \quad (3.40)$$

Plugging this velocity in the discrete form of the Eq.-(3.27) produces the elliptic equation for the pressure  $\pi$ , the solution of which provides the updated solenoidal velocity  $\mathbf{v}$ .

The first step of the magnetic block begins with estimation of magnetic field  $\mathbf{B}^{q-1/4}$  at  $t^{n+1}$  using the update velocity, and the latest magnetic field is evaluated implicitly in analogy to (3.39):

$$\mathbf{B}_i^{q-1/4} = \hat{\mathbf{B}}_i + 0.5\delta t \left[ \mathbf{B}^{q-1/4} \cdot \nabla \mathbf{v}^q - \mathbf{B}^{q-1/4} \text{tr}\{\nabla \mathbf{v}^q\} \right]_i. \quad (3.41)$$

where the superscript  $q - 1/4$  symbolized as such for being a quarter of iteration away from the accomplishment. The subsequent step follows in the spirit of the momentum transport equation, using the conservative form of the forcing terms in the induction equation:

$$\mathbf{B}_i^q = \hat{\mathbf{B}}_i + 0.5\delta t(\nabla \cdot \mathbf{B}^{q-1/4}\mathbf{v}^q)_i - 0.5\delta t(\nabla\pi^*)_i^q. \quad (3.42)$$

Implementing the magnetic field in the discrete form of the solenoidality condition (3.28) produces the elliptic equation for auxiliary pressure term  $\pi^*$ , the solution of which provides the updated solenoidal magnetic field  $\mathbf{B}$ .

EULAG-MHD is parallelized with MPI (Message Passing Interface) supporting NetCDF for writing output data and NCAR graphics for visualization. The model is presently running on the High Performance Computing Cluster: Vikram-100, operational at Physical Research Laboratory, which is a hundred teraflops machines with 97 computing nodes and offers 2,328 CPU cores, 1,15,200 GPU Cores, 25 terabytes (TB) of RAM and 300 TB of high performance parallel filesystem (<https://www.prl.res.in/hpc>). For visualization, we also complement the NCAR Graphics with the VAPOR (Visualization and Analysis for Ocean, Atmosphere, and Solar Researchers) which can easily handle data up-to terabytes

(Clyne & Rast, 2005). We have adopted its field line advection technique to plot the magnetic field lines under the influence of flow vector (Clyne & Rast, 2005).

## 3.2 Implicit large eddy simulation

As discussed above, EULAG-MHD is based on MPDATA advection scheme. Notably, the higher-order truncation terms of MPDATA provide an implicit turbulence model (Domaradzki et al., 2003; Margolin et al., 2006) and hence, allow to conduct large eddy simulations (LESs) without using an explicit subgrid model (Smolarkiewicz & Prusa, 2002; Domaradzki et al., 2003; Domaradzki & Radhakrishnan, 2005; Rider, 2006; Prusa et al., 2008). In contrast to the standard LESs which filter out the under-resolved scales by applying explicit subgrid-scale models, MPDATA filter-outs the under-resolved scales by utilizing the residual dissipation—intermittent and adaptive to generation of under-resolved scales—produced via numerics which mimics the action of explicit subgrid scale turbulence models. In literature, such calculations relying on the properties of nonoscillatory numerics are referred as implicit large eddy simulations (ILESs). A comprehensive review of ILES with numerous examples are provided in the volume edited by Grinstein et al. (Grinstein et al., 2007), including applications to local and global solar/stellar convection.

In a simulation having fixed grid resolution, under-resolved scales appear at the reconnection regions. MPDATA then removes these under-resolved scales by producing locally effective residual dissipation, sufficient to sustain monotonic nature of the solution. Being intermittent and adaptive, the residual dissipation, as mentioned above, facilitate the model to perform ILESs. Such ILESs performed with the model have already been successfully utilized to simulate regular solar cycles (Ghizaru et al., 2010), with the rotational torsional oscillations subsequently characterized and analyzed in (Beaudoin et al., 2013). The simulations conducted with EULAG-MHD continue relying on the effectiveness of ILES in regularizing the onset of magnetic reconnections, concurrent and collocated with the reconnection sites (Kumar et al., 2013, 2015a; Kumar & Bhattacharyya,

2016).

In summary, the chapter describes the numerical models EULAG-MHD used to explore the MHD relaxation. The numerical models are based on (at least) second-order accurate (both in space and time) non-oscillatory forward in-time advection scheme MPDATA. MPDATA basically utilizes the donor-cell scheme in iterative manner to improve the accuracy of the solution while preserving the properties of the donor cell scheme. We discuss the derivation of MPDATA along with its features which are relevant to our calculations. Then, we review the numerics of the numerical model EULAG-MHD. The model employs the established frame-work of EULAG with an additional magnetic block to solve the induction equation. Notably, the proven property of MPDATA to produce locally adaptive residual dissipations in response to generation of under-resolved scales, facilitates the numerical model to carry out computations in the spirit of implicit large eddy simulations.

# Chapter 4

## Data-constrained Simulations

The chapter explores various types of solar transients characterized by different physical properties using data-constraint MHD simulations. The focus is on the coronal jets and solar flares, providing unprecedented information about reconnection processes, the responsible magnetic topologies and the dynamics of the MFLs as they evolve. Additionally, the simulations being initiated with photospheric magnetic field, are of direct relevance to observations. Hence, each simulation is augmented with multi-wavelength images of the associated regions for verification as well as to enrich the present understanding.

### 4.1 Case-I: Simulation of a Coronal Jet

The observational signature of coronal jets have been extensively studied in the literature. Specially, the blowout jets stand out because of their contribution to the CMEs. The jet that we simulate occurred on 2016 December 5 hosted by a bipolar active region NOAA 12615, located near the disk center (*S07W32*; <https://www.solarmonitor.org/?date=20161205>). It was found to be concurrent with a C1.2 flare occurring on the same active region, providing us an excellent opportunity to cover both the transients in a single simulation. A rigorous analysis of various observational aspects of the event had already been done by Joshi et al. (2017b)—which further helped us to interpret simulation results. The lifespan of the jet is shown in the Fig.-4.1 in 304 Å channel of the

AIA on board the SDO. The cutouts are processed by remapping through the

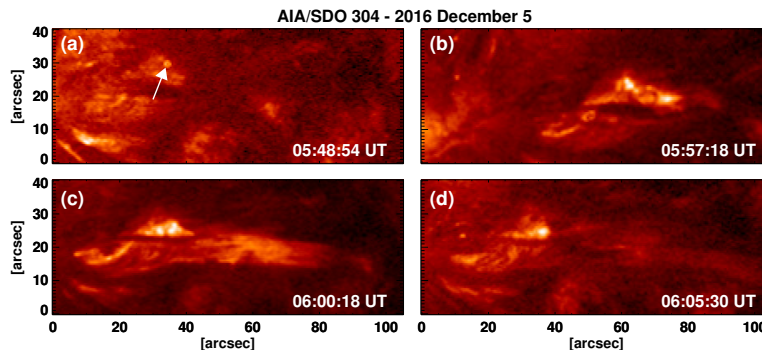


Figure 4.1: Evolution of the jet where the bright point is marked by an arrow. The base and the spire become well developed at  $\approx 06:00$  UT.

Lambert cylindrical equal-area (CEA) projection and then transformed into the heliographic coordinates (Gary & Hagyard, 1990). The panel (a) shows the appearance of a bright point (indicated by the arrow) at 05:48:54 UT which marks the location where MRs probably originate. Afterwards, the immediate neighborhood of the point gets brightened, but asymmetrically (panels (b) and (c)). For instance at 05:57:18 UT (panel (b)) the region at the bottom of the bright point is brighter than the top, signifying a possibility that after reconnection MFLs are more closely packed at the bottom. At 06:00:18 UT (panel (c)) the base and spire of the jet are well recognizable. Later, the jet starts decaying as depicted in panel (d).

In Fig.-4.2, we plot histories of the footpoint brightening in the channel 304 Å (chromosphere) and dynamics of magnetic loops in 94 Å (flaring corona) near the flaring region. The flare ribbons start to develop at  $\approx 06:00$  UT, later become prominent, seen in panels (c) and (d), and finally diffuse and the surrounding region brightens up. The panels (a) to (e) at 94 Å shows the evolution of the coronal loops covering the active region and highlights their expansion (indicated by arrows) during the flare. Within the purview of the standard flare model (Shibata, 1999), a development of flare ribbons suggests presence of magnetic flux-rope. Interestingly, no matching filament was observed in any of the AIA channels immediately before, during or after the flare.

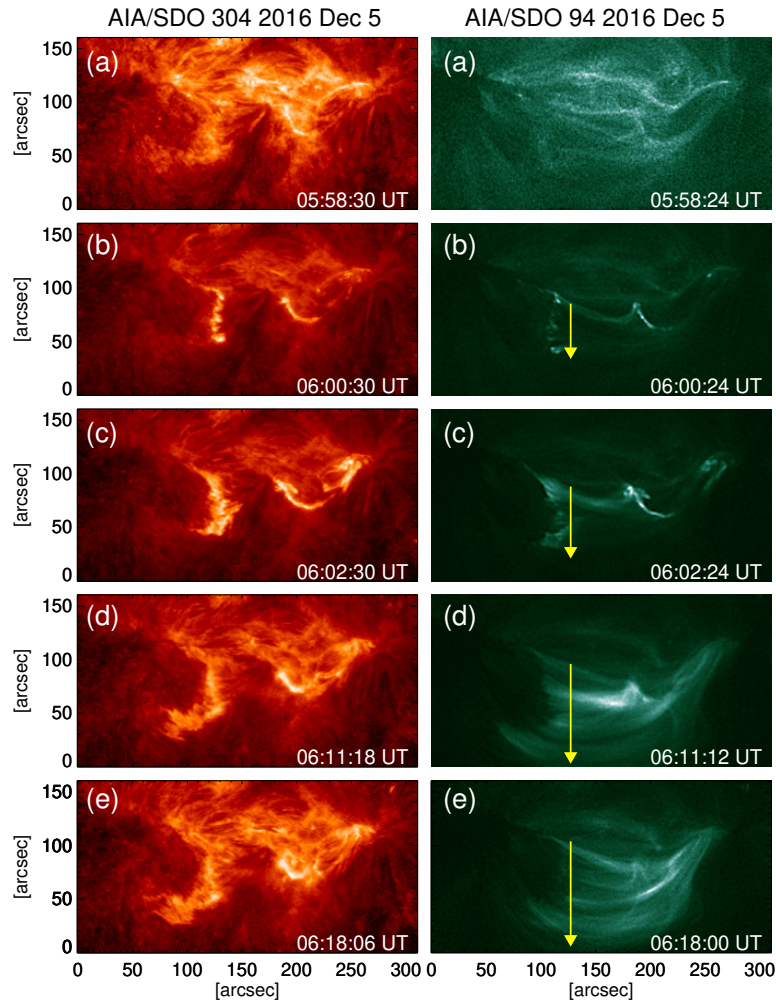


Figure 4.2: History of flare ribbons in 304 and 94 Å. Images in 304 Å show the development of flare ribbons, whereas dynamics of the overlying coronal loops are captured in 94 Å. Notable is a general ascent of loops, as indicated by changing positions of the arrow

#### 4.1.1 NFFF Extrapolation of the AR 12615

In order to extrapolate the magnetic field of AR12615, we consider the magnetogram of “hmi.sharp\_cea\_720s” data series on December 5 2016 at 05:48 UT from the HMI/SDO. The original downloaded magnetogram cutout was of dimensions  $611 \times 246$  pixels along  $x$  and  $y$  axes of a Cartesian coordinate system. To minimize the computational cost, we have extrapolated with a re-binned domain of  $384 \times 156 \times 156$  grids in the  $x$ ,  $y$  and  $z$  directions respectively. The corresponding physical domain is  $\approx 220$  Mm in the  $x$  direction and  $\approx 89$  Mm in the  $y$  and  $z$  direction.

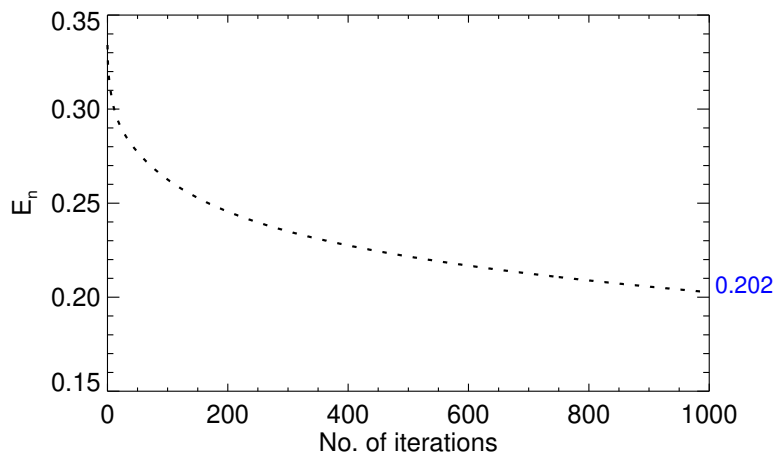


Figure 4.3: Number of iterations vs.  $E_n$ . The plot saturates asymptotically to 0.202, which indicates the extrapolated transverse field in the photosphere is within 20.2% of the magnetogram value whilst the longitudinal component  $B_z$  agrees exactly with the magnetogram.

The extrapolation has an acceptable error of  $E_n = 0.202$  or 20.2% in the transverse fields, plotted in Fig.-4.3. In Fig.-4.4a and Fig.-4.4b, we have shown the vector plots of transverse components ( $B_x$  and  $B_y$ ) on the longitudinal component  $B_z$  on the photosphere for original and reconstructed magnetograms respectively.

The calculated Pearson correlation coefficient between the pair of transverse components is found to be strong with a value of  $\approx 0.966$  and the scatter plot is depicted in Fig.-4.3. The average magnetic field at the bottom boundary is  $\approx 700$  G, that makes  $\beta \approx 2.83$  with an estimated gas pressure of  $\approx 5.5$  kPa, using  $p = nk_B T$ , where the number density  $n$  and temperature  $T$  have their typical photospheric values for sunspots while  $|\rho d\mathbf{v}/dt| \approx |\mathbf{J} \times \mathbf{B}|$ —rationalizing use of the NFFF extrapolation.

Altogether, the qualitative and quantitative correspondences between the original and the reconstructed magnetograms are remarkable.

The extrapolated MFLs over the whole computational domain are presented in Fig.-4.6a while the coronal loops at the same time in  $171 \text{ \AA}$  are plotted in Fig.-4.6b. Noteworthy is their visual agreement. A side view of the MFLs are shown in Fig.-4.6c. The distribution of Lorentz force and current density over the extrapolated volume are depicted in Fig.-4.7a,4.7b with a Direct Volume

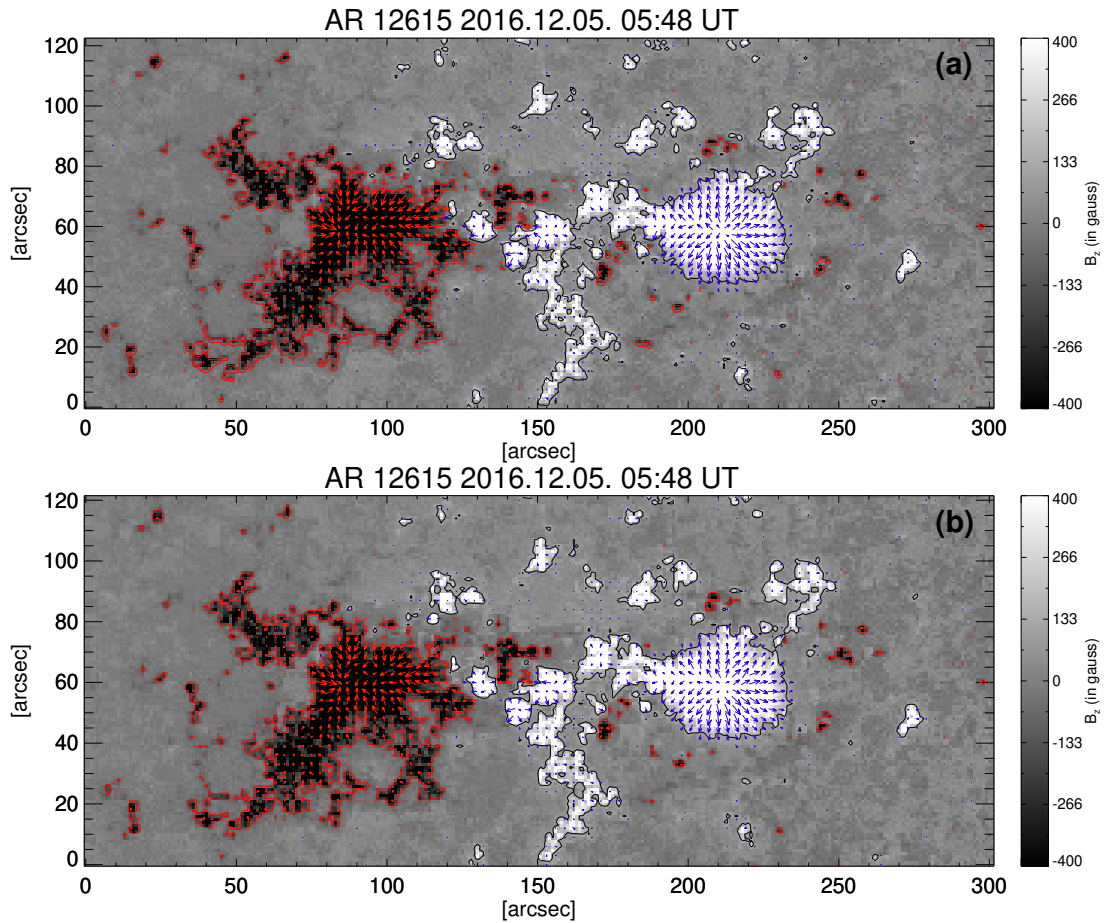


Figure 4.4: (a) CEA projected vector magnetogram of AR 12615 at 05:48 UT on 2016 December 5 obtained from HMI. The saturated value of  $B_z$  is represented with the grayscale color bar. The blue and red arrows illustrate the vector plots of the transverse field components. (b) The reconstructed synthetic magnetogram.

Rendering (DVR). In Fig.-4.7c, we have provided an additional plot showing the variations of Lorentz force and current averaged over  $x$  and  $y$  as a function of  $z$ .

Important is the faster decay of the Lorentz force than the current density, effectively making the corona approximately force-free while retaining the current. Auxiliary analysis shows that the Lorentz force decreases by 99% at a height of  $\approx 83$  Mm, while the current density decreases only by 9% of its initial value. This indicates that the corona to be reasonable force-free while retaining a finite current density.

Fig.-4.8 has featured three magnetic structures pertinent to the onset of MRs and co-located with the jet and the flare. They are described in detail in the following:

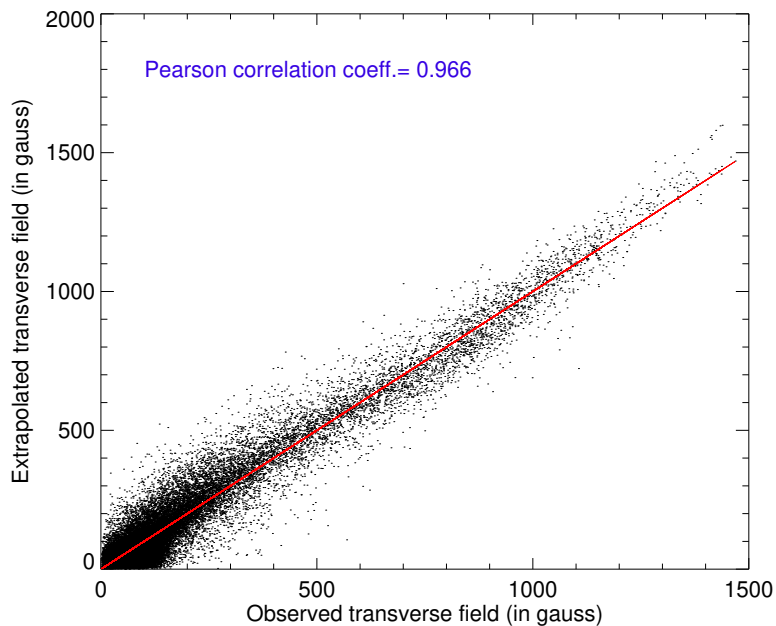


Figure 4.5: Scatter plot of transverse components of the reconstructed vs. actual magnetic field. With a Pearson’s coefficient of 1 as an exact match, the plot finds a value of 0.966.

1. A pair of 3D nulls are found adjacent to the jet and marked by the orange arrow in Fig.-4.6a. The corresponding spines and fans in the 3D null skeleton are depicted in red and blue colors. In the 3D nulls, the open MFLs constitute the outer spines leaving outward the region whereas the inner spines are anchored below, shown in Fig.-4.8a. The nulls are highlighted in pink colors and their locations are found by using the procedure employed in Kumar et al. (2013). The procedure adapts a Gaussian function

$$\psi = \exp \left[ - \sum_{i=x,y,z} \frac{(B_i - B_0)^2}{d_0^2} \right], \quad (4.1)$$

where  $B_0$  and  $d_0$  are constants that defines an iso-value of  $B_i$  and the spread of the Gaussian respectively. For  $B_0 \approx 0$  and a small  $d_0$ , the function  $\psi$  takes significant values only if  $B_i \approx 0$  for each  $i$ . A 3D null is then the location where the three iso-surfaces having iso-values  $B_i = B_0$  intersect. The procedure is realization of Dirac-Delta function in a discretized grid. However, there are other null detection techniques as described in Parnell et al. (1996, 2010b); Olshevsky et al. (2020). Additionally, we overlay the

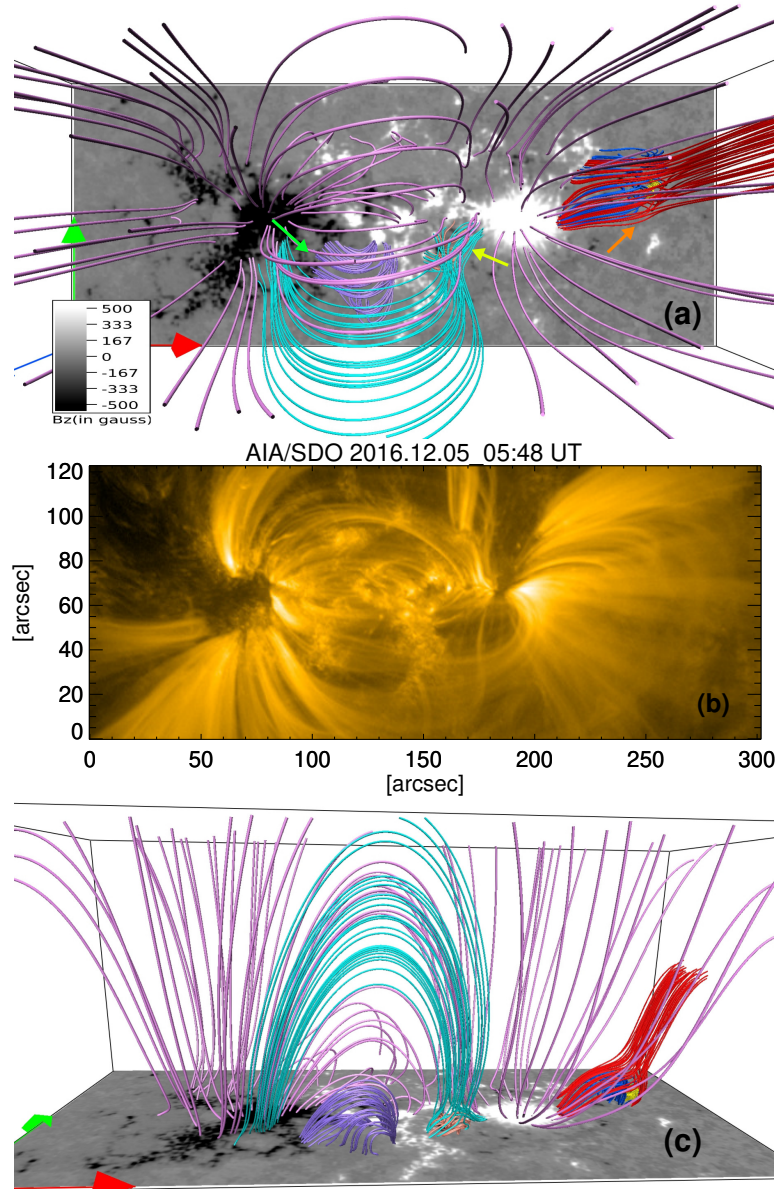


Figure 4.6: (a) Top view of the extrapolated field lines. (b) Magnetic loops in  $171 \text{ \AA}$  from the AIA at 05:48 UT, which is also the time slice for the magnetic field extrapolation. The field of view of the two panels are the same. The general agreement with the  $171 \text{ \AA}$  loops is appealing. (c) Lateral view of the extrapolated MFLs. The regions of interest are MFLs spanning a pair of 3D nulls (red and blue), a single 3D null (cyan and peach), and a QSL marked by the purple MFLs.

bottom boundary with the  $Q$ -map estimated by using the code of Liu et al. (2016) (mentioned in chapter 2). The map presented in panel (b), Fig.-4.8, highlights the interesting matching between the footpoints of inner (blue color) and outer (red color) spines with the contours of large  $Q$  values as  $\ln Q \in \{3, 6\}$ . It is well known that the region having a large  $Q$  is favorable

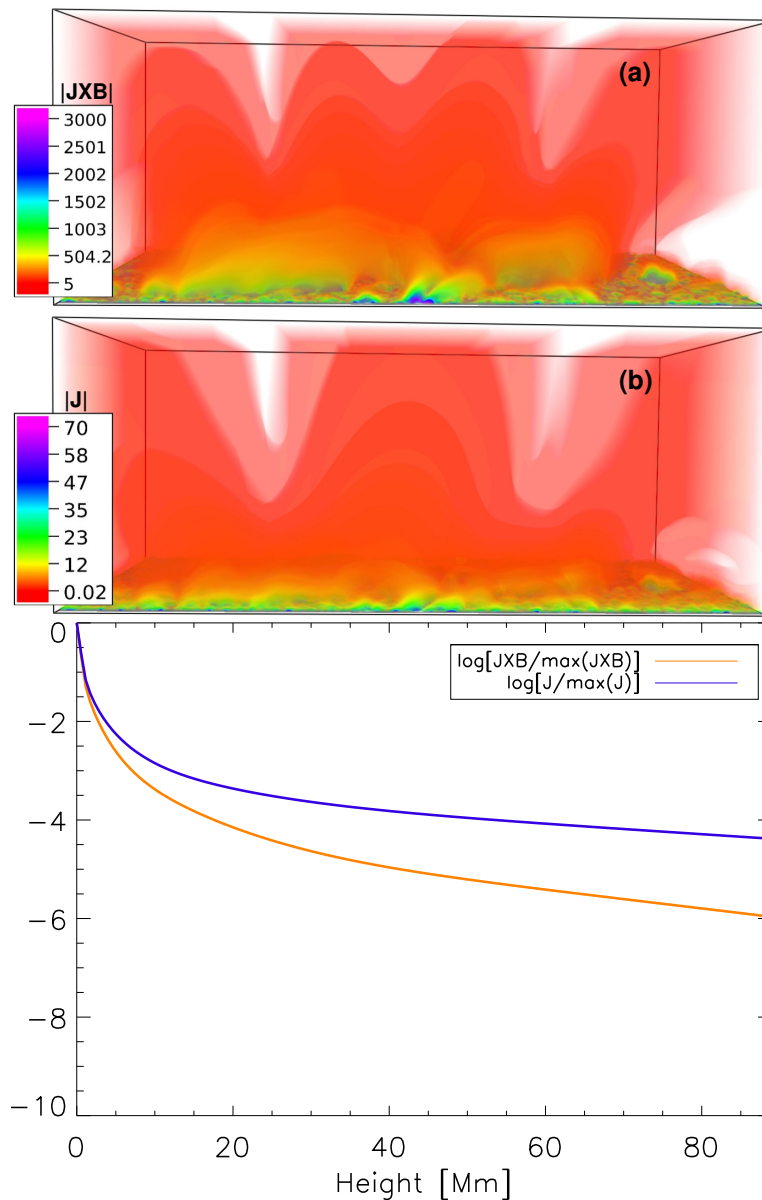


Figure 4.7: (a) Direct volume rendering (DVR) of the Lorentz force exerted by the extrapolated field. (b) DVR of the volume current density of the extrapolated field. The slower decay of volume current density with height in comparison to the Lorentz force, which signifies an effectively force-free corona, is important. (c) An additional plot showing the variations of Lorentz force and current over the height.

for initiating slipping MRs (Démoulin, 2006). There is also a set of twisted MFLs in yellow color constituting a flux rope and is located below the inner fan of the nulls.

2. A single 3D null with the characteristic spine (cyan color MFLs) and fan (peach color MFLs) is located in the flaring region. It is pointed by the

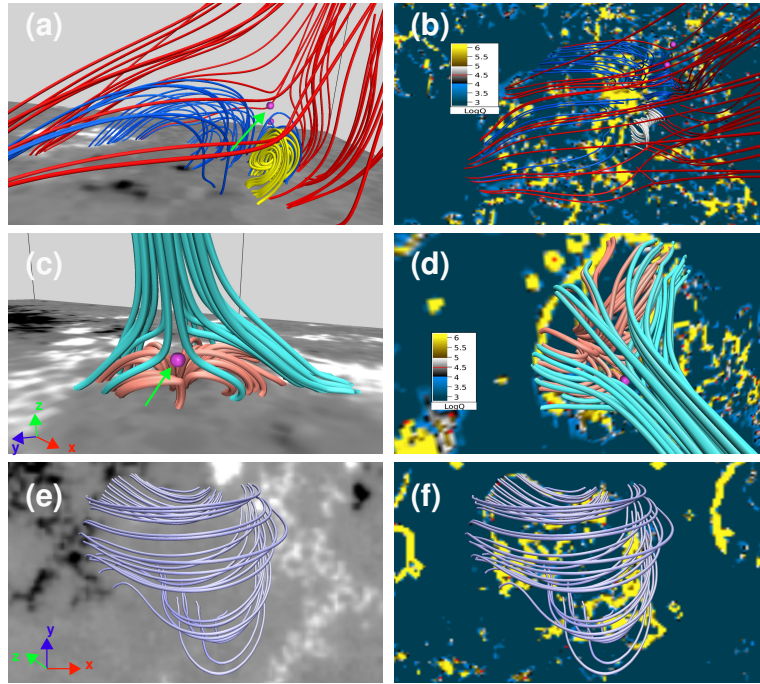


Figure 4.8: Left column shows close ups of the magnetic nulls (in pink) with corresponding MFLs and the MFLs for the QSL (in descending order). The right column is the corresponding top-down view where the bottom boundary is superimposed with  $\ln Q$  contours having  $\ln Q \in \{3, 6\}$ . The viewing angle of the panels is according to the orientation of the axes. The footpoints tracing the  $Q$ -contours, which have large values, signify a sharp change in MFL connectivity. A region with QSL is characterized by its large  $Q$  value. The presence of highly twisted MFLs—in yellow at the left.

yellow arrow (in Fig. 6a). In Fig.-4.8c, we have provided a zoomed in view of the null, highlighted with the null location. The pink colored iso-surface denotes the location of null, detected by the procedure mentioned above. The height of the null is found to be at  $\approx 3.3$  Mm or in the low corona. Unlike the pair of nulls near the jet, the outer and inner spines of the null are rooted within the extrapolation domain. Again here, in the  $Q$ -map plotted in the panel (d), the footpoints trace large  $Q$  contours ( $\ln Q \in \{3, 6\}$ ), marking it a suitable site for slipping reconnections.

3. A QSL (green arrow in Fig.-4.6a) with MFLs depicted in purple color, co-located with the eastward flare ribbon is situated at the left of the above null and in between the major negative polarity region and the single null. Panels -(e) and (f) illustrate the zoomed in view of QSL and the contours

of high  $Q$ -value where  $\ln Q \in \{3.5, 5\}$  respectively. The large  $Q$ -value indicates the sharp change in field line connectivity which can facilitate the reconnection.

### 4.1.2 Simulation Results and Discussions

The following MHD equations govern the dynamics of an ideal, incompressible, thermally homogeneous and having perfect electrical conductivity plasma:

$$\frac{\partial \mathbf{v}}{\partial t} + (\mathbf{v} \cdot \nabla) \mathbf{v} = -\nabla p + (\nabla \times \mathbf{B}) \times \mathbf{B} + \frac{\tau_a}{\tau_\nu} \nabla^2 \mathbf{v}, \quad (4.2a)$$

$$\nabla \cdot \mathbf{v} = 0, \quad (4.2b)$$

$$\frac{\partial \mathbf{B}}{\partial t} = \nabla \times (\mathbf{v} \times \mathbf{B}), \quad (4.2c)$$

$$\nabla \cdot \mathbf{B} = 0, \quad (4.2d)$$

using standard notations in dimensionless form. The normalizations for various terms in Equation (4.2) are,

$$\mathbf{B} \longrightarrow \frac{\mathbf{B}}{B_0}, \quad \mathbf{v} \longrightarrow \frac{\mathbf{v}}{v_a}, \quad L \longrightarrow \frac{L}{L_0}, \quad t \longrightarrow \frac{t}{\tau_a}, \quad p \longrightarrow \frac{p}{\rho v_a^2}. \quad (4.3)$$

The constants  $B_0$  and  $L_0$  are selected as the average magnetic field strength and length-scale of the vector magnetogram. Further,  $v_a \equiv B_0/\sqrt{4\pi\rho_0}$  is the Alfvén speed and  $\rho_0$  is the mass density. The  $\tau_a$  and  $\tau_\nu$  are respectively Alfvén transit time ( $\tau_a = L_0/v_a$ ) and viscous diffusion time scale ( $\tau_\nu = L_0^2/\nu$ ),  $\nu \equiv$  kinematic viscosity. The ratio  $\tau_a/\tau_\nu$  is an effective viscosity of the system which, along with other forces, influences the magnetofluid evolution. These equations are used to obtain the evolution of other transients in this chapter.

The MHD simulation is initiated with the above extrapolated field from a motionless state where the magnetofluid is assumed to be incompressible and having a perfect electrical conductivity. The fluid is relaxed to quasi-steady terminal state achieved by appropriate force balance. The initial Lorentz force drives the plasma and generates plasma flow. All components of volume  $\mathbf{B}$  and

flow velocity except for  $B_z$ , are continued to the boundaries for a given time step (Kumar et al., 2015a), ensuring the net magnetic flux to be zero in the computational domain. The bottom boundary is approximated to follow the line-tied boundary condition by keeping  $B_z$  fixed. The approximation is validated from the minimal flux change i.e. only 4% of its initial value, shown in Fig.-4.9.

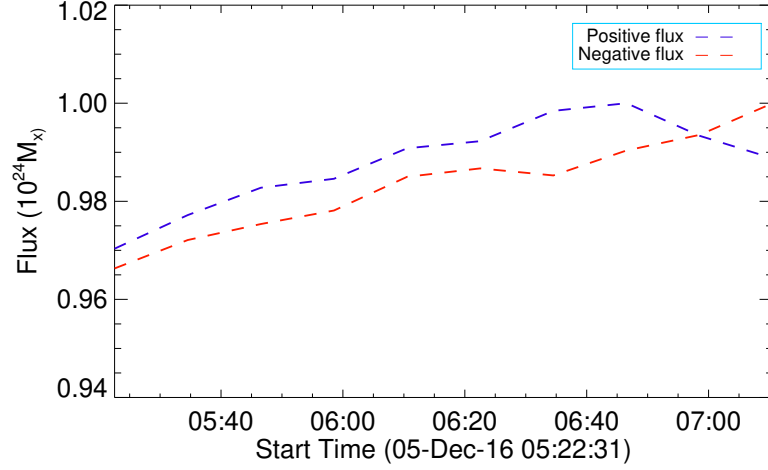


Figure 4.9: Temporal variations of positive and negative magnetic fluxes across the photosphere.

The dimensionless constant  $\tau_a/\tau_\nu$  in the Eq.-4.2 is set at  $\approx 2 \times 10^{-3}$ , which is roughly three orders of magnitude larger than its coronal value. The higher value of  $\tau_a/\tau_\nu$  accelerates the viscous relaxation without altering magnetic topologies and minimizes the computation cost. The density  $\rho_0$  is set to 1 while the kinematic viscosity is  $\nu$  to 0.005, in scaled units. The dimensionless spatial step size is  $\Delta x = 0.0026$ . The temporal step size is considered as  $\Delta t = 2 \times 10^{-3}$  to satisfy the Courant-Friedrichs-Lewy (CFL) stability condition (Courant et al., 1967). The computation run time is  $1000 \Delta t$ , roughly amounting to an observation time of  $\approx 33$  minutes. The magnetic Reynold's number  $R_M$  throughout the simulation is infinity except during MRs facilitated by the MPDATA assisted reconnection.

#### 4.1.2.1 Evolution of the jet:

The evolution of MFLs surrounding the jet is illustrated in the Fig.-4.10. Here, we retain the same MFLs as depicted in panels (a), (b) of Fig.-4.8 where the MFLs in blue and red constitute the 3D nulls and the yellow MFLs, the flux-

rope. The generated flow velocity are depicted in green colored arrows, implying their absence at  $t = 0$ . The reconnection commences at the null points depleting magnetic pressure there. Consequently, the flux-rope rises toward the nulls, but asymmetrically. After the rise, the MFLs of flux-rope take part in the reconnection near the null and become a part of the outer or the inner spine. Because of this, a channel is created for the ejection of cooler plasma contained in the rope. The post-reconnection loops also form below the nulls. To track the interim

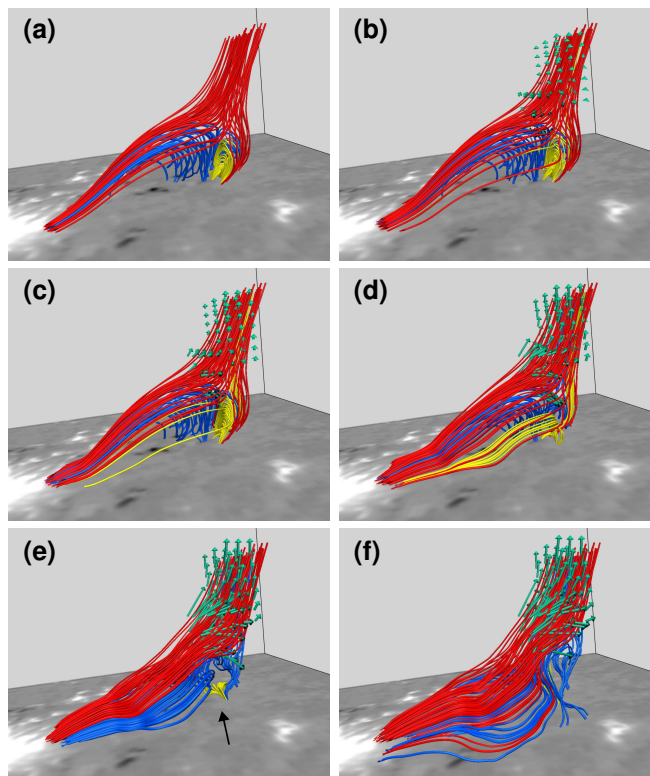


Figure 4.10: Snapshots of field line evolution during  $t \in \{05 : 48, 06 : 05\}$  UT, covering the jet. Notable are the conversions of anchored MFLs constituting the rope into the outer spine (panel (d)). Consequently, the entrapped cold plasma can get funneled out along the open MFLs of the outer spine and generate the spire. Instantaneous velocity vectors are illustrated in green. Noticeably, the flow vectors become more field-aligned with time.

evolution the simulated field lines are overlaid with the images with  $304 \text{ \AA}$  and  $131 \text{ \AA}$  at  $\approx 05:59$  UT with the simulated field lines (see Fig.-4.11) and find an astounding overlap of bright structures with MFLs.

The detailed dynamics of the rope is shown in Fig.-4.12. The cyan-colored MFLs in panel (a) are less twisted, present in the neighborhood of the rope (yel-

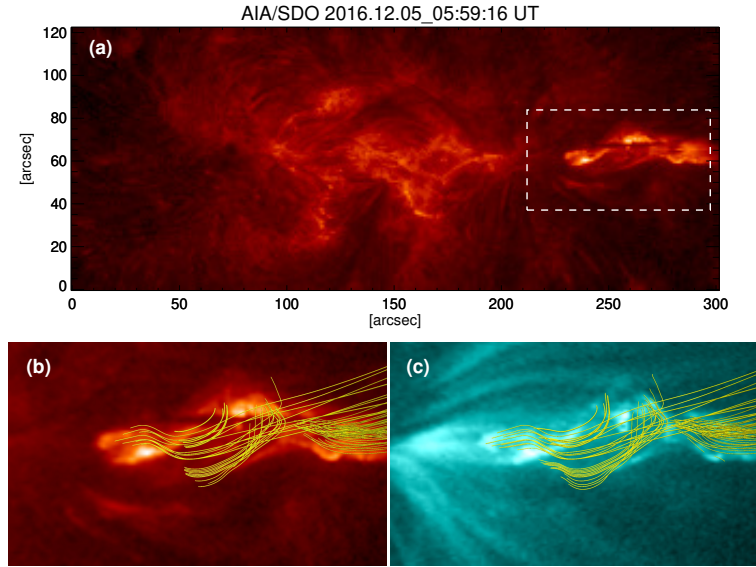


Figure 4.11: Jet corresponding MFLs overlaid with the boxed part of (b) 304 Å and (c) 131 Å images. The similarity is recognizable.

low MFLs). Notable is the transition from panel (b) to (c) as the MFLs change their connectivity and join with the rope. Such changes in connectivity are signatures of reconnection and indeed an X-type null clearly appears at panel (c), marked by the red circles. Additionally, the conversion of less twisted MFLs to rope is a telltale sign of internal MRs during flux-rope activation (Kumar et al., 2016). Moreover, velocity vectors (in green) throughout the evolution are—en gros—in line with the outer spine indicating a mass flow along it. The maximum flow speed is found to be  $\approx 300$  km/s whereas in Joshi et al. (2017b), the projected speed of the jet is found to be 200 km/s at coronal temperature. Generally, the scenario is compatible with a mini-filament eruption and the findings are congruent with the model proposed by Moore et al. (2013); Sterling et al. (2015). The salient features of the simulated evolutions

#### 4.1.2.2 Evolution of the single null and the QSL:

In Fig.-4.13, the evolution of the single 3D null near the flare is shown. Panels (a), (c), (e), and (g) depict the dynamics of the complete loops whereas evolution at the near- neighborhood of the null is demonstrated in panels (b), (d), (f), and (h). The bottom boundary is overlaid with the  $Q$ -map. Evident is the

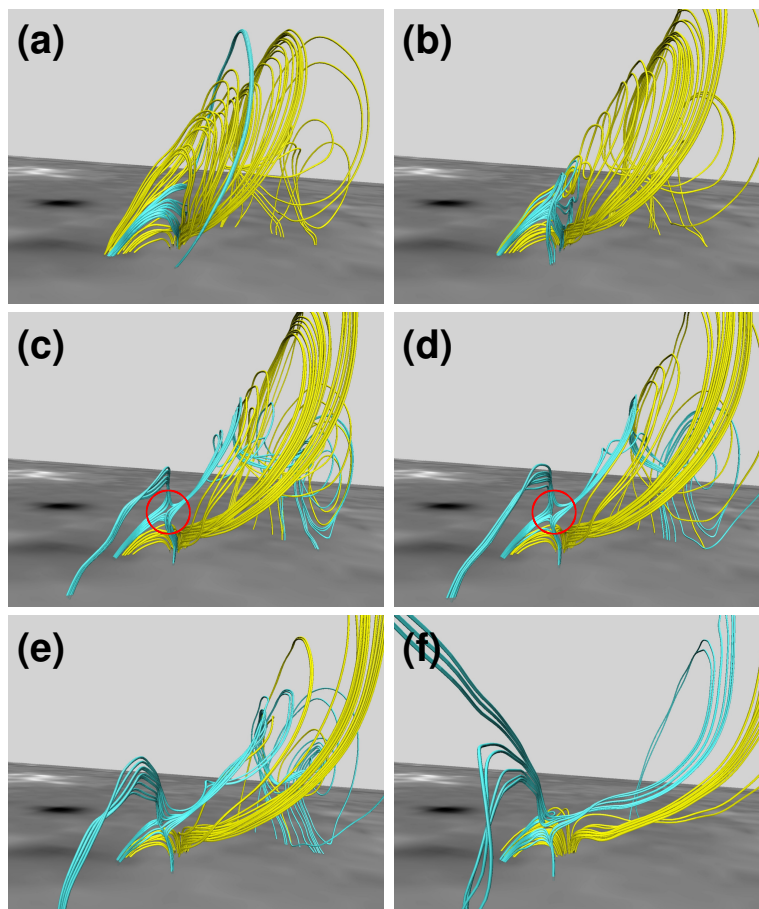


Figure 4.12: Depiction of the flux-rope evolution only. Noticeable is the development of the X-type null marked by red circles in panels (c) and (d). The null is the location for internal MRs envisaged in the standard scenario of flux-rope eruption. Further dynamics of the null is depicted in panels (e) and (f). The whole evolution covers approximately the first 5 minutes of the jet.

movement of MFLs such that their footpoints are always on the instantaneous  $Q$ -constant contours (depicted in color). The white arrows represent the direction of the plasma flow tangential to the  $z = 0$  plane and visibly different from the apparent rotation of the MFLs; assigning their motion to slipping MRs instead of a bodily displacement of the plasma. Moreover, at its peak intensity ( $\approx 06:03$  UT), the westward ribbon traces the corresponding  $Q$ -contours (Fig.-4.14) which further corroborates the inference. Additionally, the closer inspection of the inner spine dynamics shows composing MFLs (in peach color) to reconnect and get transferred to the outer spine. The reconnected MFLs are seen to ascend and contract toward the end of the evolution. Such ascend is expected in flares and also the terminal contraction is in agreement with the confined nature of

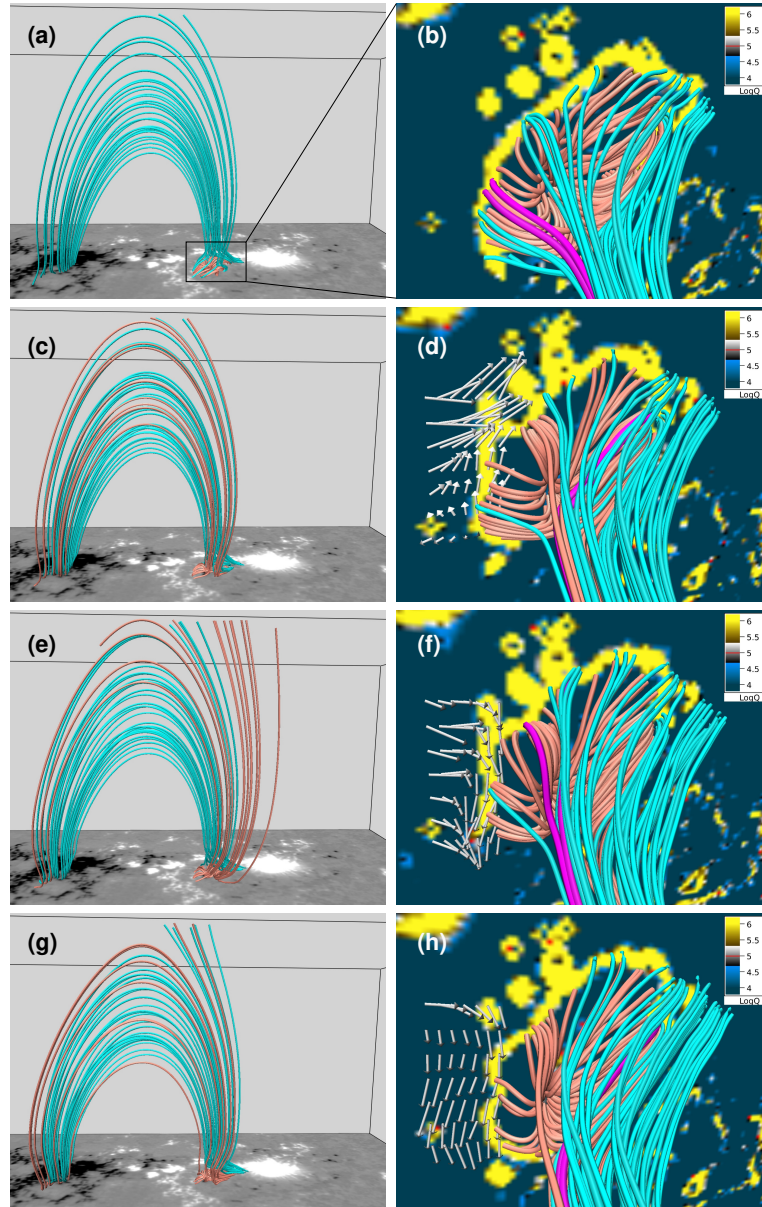


Figure 4.13: Sequences of the single null during its evolution in the time span  $\approx t \in \{05 : 48, 06 : 13\}$  UT. The left column shows a general ascent of MFLs after an initial contraction. The right column focuses on the MFL dynamics near the  $Q$ -contours. Footpoints of the two MFLs in pink are seen to trace the  $Q$ -contours. The motion is due to slip MRs as the tangential component of the local plasma flow (white arrows) is in a direction different than the footpoint motion.

the flare. Importantly, Fig.-4.2 has already conferred the likelihood of such an ascend from observations.

In Fig.-4.15, the purple colored MFLs of the QSL terminate at footpoints located on the eastern (left) side of the  $Q$ -constant contours having  $\ln Q \in \{3.5, 5\}$ .

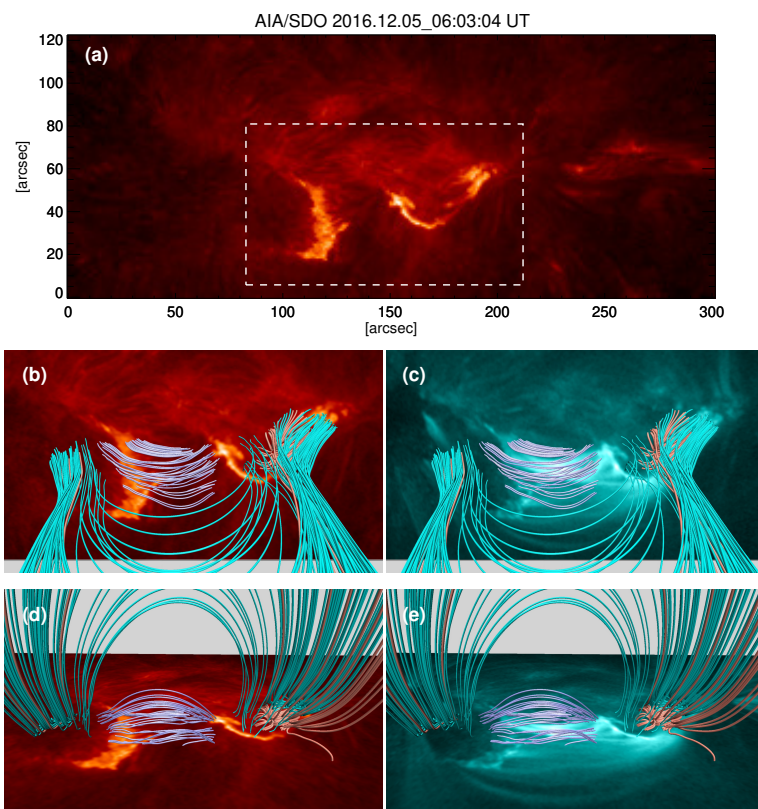


Figure 4.14: Superimposition of extrapolated MFLs on the flare ribbons at  $304 \text{ \AA}$  (panels (b) and (d)),  $131 \text{ \AA}$  (panels (c) and (e)); each at two different viewing angles. The box on the top figure represents the span of the above two images with respect to the full active region cutout. The locations of the ribbons reasonably match with footpoints of the MFLs executing slip MRs.

Identity of these MFLs during evolution are maintained by using identical initial coordinates for the field line integration at each time step. The green arrows represent projections of flow vectors on the  $z = 0$  plane, near the eastern side of the  $Q$ -constant contours. Evident from the figure is the apparent motion of MFLs as their footpoints lying on the  $Q$ -constant contours trace those contours. With the velocity vectors being pointed along a direction different than the foot-point motion, the MFLs actually slip and change magnetic connectivity because of MRs. The coincidence of the  $Q$ -constant contours with the Eastward flare ribbon, Fig.-4.2, indicates the credibility of the simulation.

To conclude from the above dynamics, the involvement of 3D nulls in two energetically different events—a flare and a jet, is indicative of an inherent scale-invariance of MR. To contemplate, additional to its demonstration of flux-rope

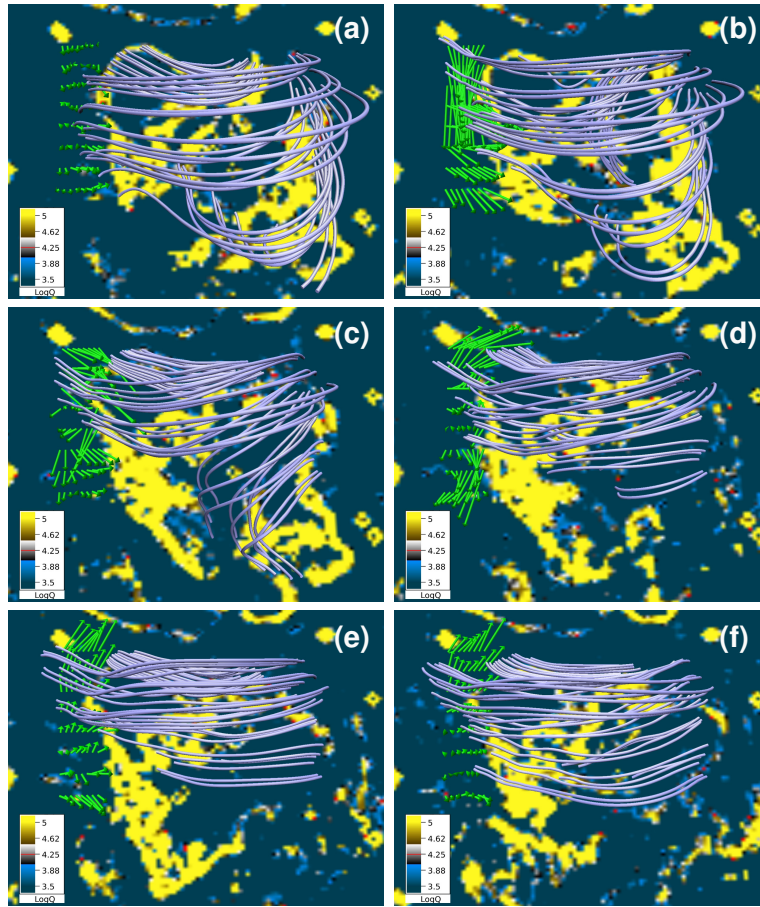


Figure 4.15: Left-side footpoints of MFLs locating the QSL (marked by  $Q$ -constant contours) sustain a motion—which is more distinguishable in the animation. The sequence covers the range  $t \in \{05 : 48, 06 : 13\}$  UT (approx). The motion is because of slip MRs, as the tangential component of the bulk flow is directed differently.

eruptions at 3D null being responsible for blowout jets—the simulation also highlights the importance of MFL complexity in developing flares. A possibility opens up where multiple nulls and QSLs can be present in a complex AR, leading to flares. The aforesaid flares can lack a well extended flux-rope and the resulting absence of plasma confinement will prohibit subsequent CMEs. Definitely, being outside the scope of the standard flare model, such flares warrant further attentions. Toward this, an interesting data-constrained simulation of an eruptive flare is presented as the next case study.

## 4.2 Case-II: Simulation of an X-class Eruptive Flare

Toward understanding the MHD of an observed flare, we carry out data-constrained numerical study of a flaring active region initialized with the NFFF extrapolation. We choose the AR 12017 for its magnetic complexity while possessing a  $\beta\delta$  type structure, located at N10W32 (<https://www.solarmonitor.org>). Particularly, we concentrate on the onset of the well documented X1.0 flare at 17:48 UT on 2014 March 29, which produces a halo CME.

The X1.0 flare is captured by AIA/SDO, IRIS, EUV Imaging Spectrometer (EIS; (Culhane et al., 2007))/Hinode, RHESSI, Interferometric Bidimensional Spectropolarimeter at the Dunn Solar Telescope (DST/IBIS), Flare Monitoring Telescope (FMT), Halpha Solar Telescope for Argentina (HASTA), and Facility Infrared Spectrometer (FIRS) at the Dunn Solar Telescope. Due to its availability of unprecedented observational data resources, different aspects were studied. Judge et al. (2015) reports on the sunquake by spectral and polarimetric studies from line profiles of Si I and He I where as Young et al. (2015) has studied the foot point emissions near the flare ribbons and the post-flare loop arcade. Their study shows an agreement with the standard flare model. Further, Kleint et al. (2015) reports on the fast acceleration of the filament during the eruption while Woods et al. (2017) reports on the drivers of the eruption and they propose the role of tether-cutting reconnection on eruption of the filament. Again, Woods et al. (2018) report on the eruption with findings of two filaments in the flaring region. They suggest that one of the filaments first gets triggered by the tether-cutting reconnection and later becomes torus unstable, ultimately leading to the eruption. Kleint et al. (2018) also present their study on the photospheric and chromospheric magnetic changes during the flare. Though these studies focus on the eruption mechanism from an observational basis, corresponding 3D MHD simulations are scarce. This motivates us to bridge the gap between the observational and numerical aspects.

The flare starts at around 17:35 UT, while it peaks at 17:48 UT and ends

at 17:54 UT. In Fig.-4.16, we have plotted the episode of the flare in the UV (1600 Å) and EUV (304 Å, 171 Å, 94 Å) channels of AIA/SDO. The images here, are processed with the routine AIA\_PREP.PRO available in the Solarsoft packages and spans over the life time of the flare. Fig.-4.16(a)–(d) represent the pre-flare stage in the upper-photosphere/chromosphere (1600 Å, 304 Å) and the corona (171 Å, 94 Å), while Fig.-4.16(e)–(h) illustrate the ongoing flare evolution. The green contours in panels (a) and (e) are plotted to locate the regions with high intense brightenings. Initially, the contours with high intensity are densely populated near the flare kernel and then spread to the neighborhood or toward the east of the kernel, as the flare proceeds. For clearer identification, we have marked the kernel of the flare by “R1” and the distant region by “R2” in white boxes (panel (a)). The channel 304 Å in panel (b) depicts a pair of filament structures (marked by white arrows). The pre-flare loop structures can be seen in the 171 Å channel (panel (c)). The large-scale loops marked by the green arrows appear to connect the region R1 and R2 (panel (c)), which disappeared during the flare (panel (g)). From the 94 Å channel, the signature of hot sigmoid (loops with S-shaped morphology) is observed (marked by white arrow in panel (d)) which is co-spatial with R1. The post-flare hot loops are shown in panel (h) (highlighted by white and green arrows).

### 4.2.1 NFFF Extrapolation of AR 12017

We obtain the non-force-free coronal magnetic field of AR12017 using the photospheric vector magnetogram of HMI/SDO at 17:30 UT ( $\approx 5$  minutes prior to the flare start time). We use the “hmi.b\_135s” series of the magnetogram and transform it to a cylindrical equal area projected map where the bottom boundary is approximately flux balanced. The cutout is made using the “mapproj” option given in <http://jsoc.stanford.edu/>. The cutout of the magnetogram is extended to  $600 \times 648$  grids along  $x$  and  $y$  axes in a Cartesian coordinate system. Then it is carefully rescaled to  $300 \times 324$  grids in the  $x$  and  $y$  directions respectively to reduce the computational time, while preserving the inherent magnetic structures. The height of the computational box is 300 grids. The physical di-

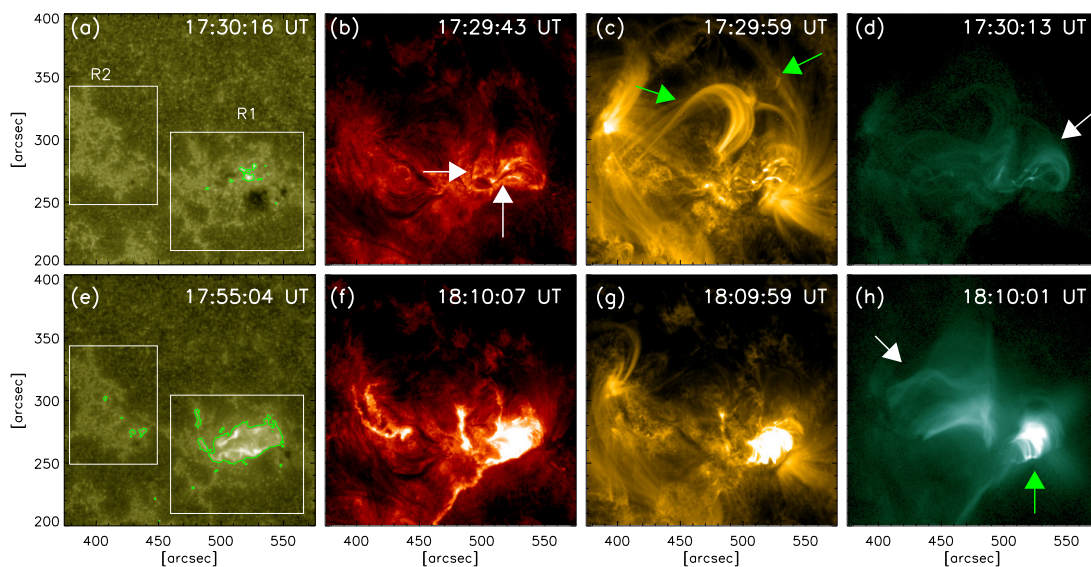


Figure 4.16: Panels (a)–(d) correspond to the pre-flare stage and panels (e)–(h) belong to the flaring evolution. The high intensity regions are highlighted by the green contours in the channel  $1600 \text{ \AA}$  (panels (a) and (e)). Two regions R1 and R2 denoted by white boxes represent the locations of flare kernel and the distant brightening, respectively. A pair of the filaments is identified in  $304 \text{ \AA}$ , indicated by white arrows in panel (b). The pre-flare loops are shown in  $171 \text{ \AA}$  (panel (c)). The loops marked by green arrows connect R1 and R2 (panel (f)). White arrow in panel (d) marks the sigmoid in  $94 \text{ \AA}$  before the onset of the flare. Post-flare hot loops in  $94 \text{ \AA}$  are marked by white and green arrows in panel (h).

mensions are  $\approx 216 \text{ Mm}$  in the  $x$ ,  $\approx 233 \text{ Mm}$  in the  $y$  and  $\approx 216 \text{ Mm}$  in the  $z$  directions. The  $E_n$  is found to be saturated to  $\approx 0.31$ , a reasonably small value, after  $1.8 \times 10^4$  number of iteration with  $\alpha_{1,2} \in \{0.0179, -0.0179\}$ . Next we estimate the deviation between the observed and reconstructed transverse magnetic fields. The Pearson correlation coefficient calculated between the observed and reconstructed transverse magnetic fields is found to be  $\approx 0.91$  and is shown in the Fig.-4.17. Notably, the corresponding Lorentz force is found to decrease faster than the current with height (shown in Fig.-4.18), which effectively makes the corona almost force-free, adhering to the usual description of the solar atmosphere.

The extrapolated MFLs are depicted in Fig.-4.19(a), overlaid with  $|B_z|$  map (in gray scale) on the bottom boundary. Within the extrapolated volume, one 3D null, a pair of magnetic flux ropes (MFRs), a set of sheared arcades and field line connectivity between the regions R1 and R2 (Fig.-4.16(a)) exist in the

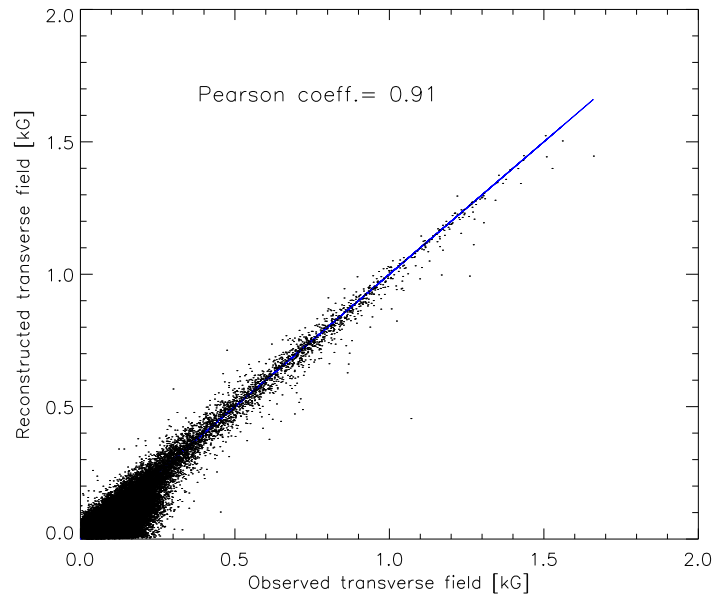


Figure 4.17: The plot shows the correlation between the observed and reconstructed transverse fields of AR12017.

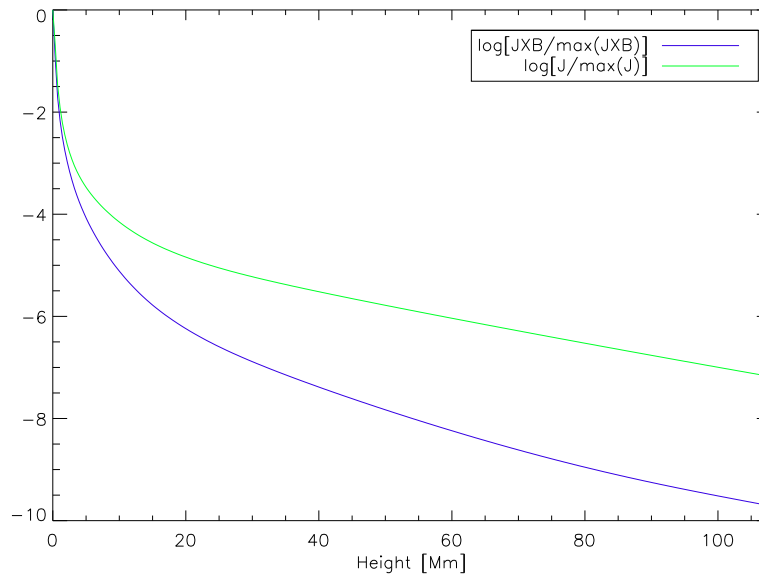


Figure 4.18: Logarithmic variation of current and Lorentz force over the height in the extrapolated domain.

vicinity of the flare. The spine located above the null and the corresponding dome-shaped fan surface are constituted by the skyblue MFLs whereas the spine located below the null and associated dome surface are comprised of the pink MFLs. Noticeable is the linking of the upper spine to the region R2 while the field lines along the fan surface surround the region R1. The location of the

null is detected using the same technique described in the Eq.-4.1 and height of the null point is  $\approx 25$  Mm from the photosphere. The figure further highlights the pair of MFRs, colored in chartreuse (hereafter MFR1) and red (hereafter MFR2); along with the twist parameter  $T_w$  (Liu et al., 2016). The large  $T_w$  indicates helical nature of the field lines constituting the MFRs. Importantly, in 304 Å (Fig.-4.16(b)), the two filaments observed are nearly co-spatial with the two MFRs. However, previous studies by Kleint et al. (2018); Yang et al. (2016) based on the NLFFF extrapolation, found the presence of a single MFR along with quasi-separatrix layers and no 3D null. Additionally, a set of sheared arcades colored in ultramarine overlie the MFRs and are located below the dome of the 3D null (Fig.-4.19(a)). The magnetic connectivity between the R1 and R2 regions can be seen from the golden colored magnetic loops. The distributions of current density in the volume are shown in Fig.-4.19(b). Notably, the current is larger at lower heights, in particular near the MFRs (inset in Fig.-4.19(b)).

## 4.2.2 Simulation Results and Discussions

The MHD simulation is performed by using Eq.-4.2. Similar to the Case I, it starts with a motionless state and the associated Lorentz force pushes the magnetofluid to initiate the dynamics. We have approximated the boundary to be line-tied where the  $z$  component of the magnetic field  $\mathbf{B}$  is kept constant at the bottom boundary, which is reasonable since the maximal variation of magnetic flux through the photosphere is only 7% of its initial value during the flare. All other components are continued to the boundaries for a given time step, Nayak et al. (2019). The mass density  $\rho_0$  and kinematic viscosity  $\nu$  are set to 1 and 0.0001 respectively. The plasma- $\beta$  at the coronal height remains  $\leq 0.05$  throughout the simulation. The total simulation time is  $\approx 40$  minutes of the flaring period, covering the time range shown in the AIA channels (Fig.-4.16).

Fig.-4.20 shows the dynamics of the MFLs during the flare. Panel (a) illustrates the topologies at the initial state. First, the reconnections initiate at the 3D null which rearrange the corresponding spine and fan MFLs. The location of reconnection is marked by the green arrow in the panel (b). Due to lowering

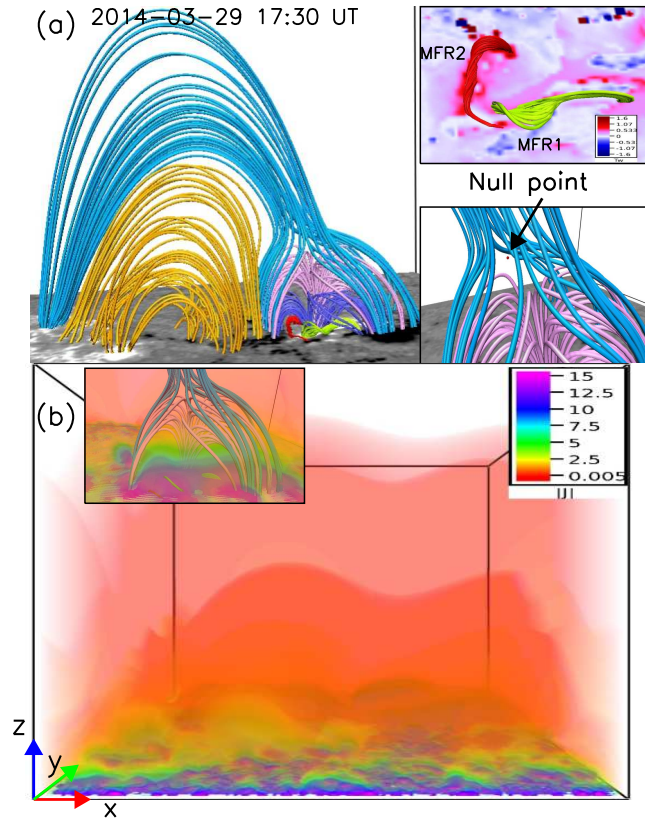


Figure 4.19: Panel (a) shows the extrapolated MFLs overlaid with the  $z$  component of  $\mathbf{B}$  on the bottom boundary of range  $\{-600, 600\}$ G. Important features of the MFLs are (1) a 3D null represented by pink and skyblue MFLs, (2) two MFRs (chartreuse and red colors), (3) a set of sheared arcades (ultramarine color) and, (4) the loops connecting the R1 and R2 (golden color). Insets in panel (a) depicts the zoomed-in view of the MFRs overlaid with the twist  $T_w$  on the bottom boundary with the range  $T_w \in \{-1.6, 1.6\}$  and the null point. Panel (b) illustrates the Direct Volume Rendering of current density. High values of current are evident near the MFRs (inset).

of the magnetic pressure near the null point, the surrounding field lines sucked toward it (marked by red arrow in panel (b)) and further participate in the reconnection process. Noteworthy is the connectivity change in the field lines from the lower spine and fan (in pink) to the upper spine and fan (in skyblue). In panel (c), we overplot the intensity image in  $304 \text{ \AA}$  at  $\approx 17:49 \text{ UT}$ , with the co-temporal field line structures of the 3D null. The footpoints of MFLs lying on the fan surface match well with the observed chromospheric brightenings. These brightenings result from the dissipation of energy in the denser chromosphere by the transferred accelerated charged particles after reconnections near the 3D null (Masson et al., 2009; Jiang et al., 2013).

The ultramarine colored sheared MFLs located over the MFR1 appear to rise upward (Fig.-4.20(b) and (d)). Arguably, the rise is because of the removal of overlying pink MFLs of fan through MRs at the null. The rising sheared MFLs ultimately approach the vicinity of the null and take part in MRs (Fig.-4.20(d)). To examine the evolution of the MFRs, in Fig.-4.21, we show the enlarged views of the corresponding evolution overlaid with the sheared MFLs, streamlines of the flow, and initial Lorentz force (panel (a)). Notable is the continuous decrease in the twist of the MFRs in the early phase of the evolution. For an explanation, we note that the nearby legs of the MFR1 and MFR2 are anchored at opposite polarity regions (Fig.-4.21(a)) and hence, are oppositely directed. Because of the favorable initial Lorentz force (Fig.-4.21(a)), they seem to move toward each other and reconnect—a possible cause for the decrease in the twist. In addition to that, the flow generated near the ropes untwist them (Fig.-4.21(b)) and gradually aligns along vertical direction—uplifting the sheared MFLs. With time, the MFLs of the ropes (as well as the sheared MFLs) become almost perpendicular to the bottom PILs, akin to potential field loops (Prasad et al., 2020). These visibly less twisted loops (in chartreuse and ultramarine colors) located above the main PIL almost agree with the observed post-flare arcades marked by the green arrow in Fig.-4.16(f). The rise and the simultaneous removal of the overlying loop systems, shown in panels (b) and (d) of Fig.-4.20, are mostly in agreement with the observed loop dynamics depicted in the 171 Å images in Fig.-4.16. Importantly, the golden MFLs, being connected to the regions R1 and R2, may transport the charged particles to the region R2 by participating in the null-point reconnections and lead to the brightenings in the R2 as depicted in Fig.-4.16(d). Interestingly, the post-reconnection golden MFLs are nearly similar to the loops marked by the white arrow in Fig.-4.16(f).

We have compared the horizontal magnetic field components at the end of the simulation with their observed values by calculating the Pearson correlation coefficient. We obtain the value of the coefficient to be 0.703, which shows a reasonable correlation between the two. We have also estimated the free energy released during the entire simulation period. Fig.-4.22 shows the evolution of

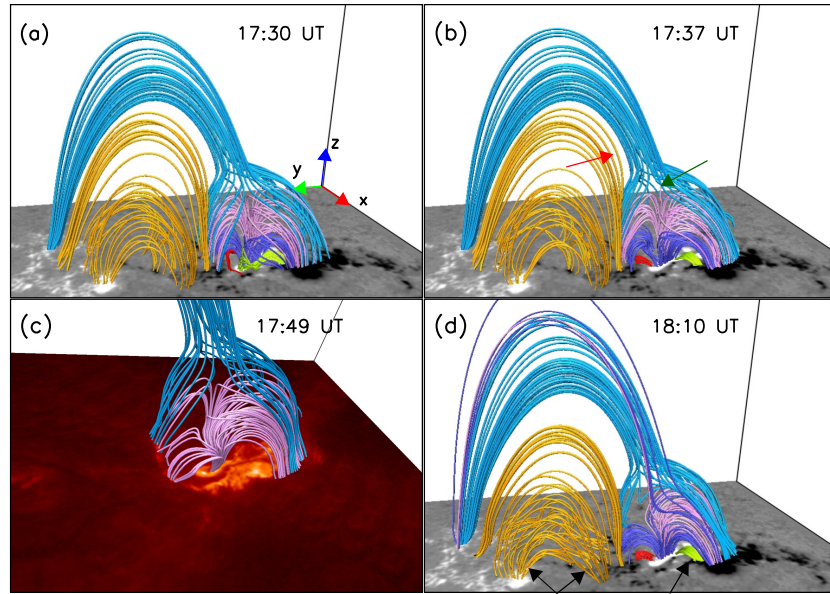


Figure 4.20: Simulated dynamics spanning the flaring time,  $t \in \{17:30, 18:10\}$ UT. Panel (a) depicts the MFLs at the start of the simulation. Important are the MRs (marked by green arrow in panel (b)) at the null which change the connectivity of the spine and fan MFLs. The footpoints of the fan surface MFLs almost trace the brightenings observed in  $304 \text{ \AA}$  at  $\approx 17:49$  UT (panel (c)). The sheared MFLs (in ultramarine) and the yellow MFLs (marked by red arrow) also appear to engage in MRs near the null. The post-reconnection MFLs (marked by black arrows in panel (d)) are comparable with the observed post-flare loops (Fig.-4.16).

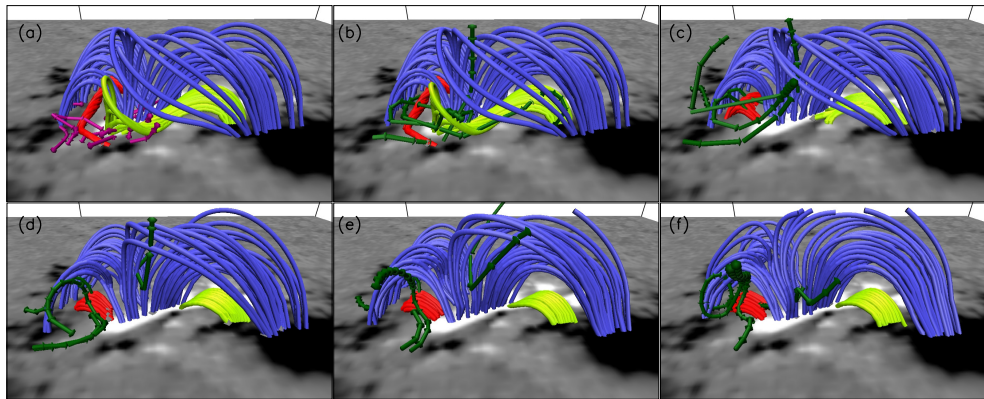


Figure 4.21: Evolution of the MFRs and the overlying sheared arcades during the early phase,  $t \in \{17:30, 17:31\}$ UT. Panel (a) is overlaid with initial Lorentz force (in purple). Panels (b)-(f) are overplotted with streamlines of the flow (in dark green). Notable are the nearby legs of the ropes which are rooted in opposite polarities (panel (a)). The twist of both the ropes reduces with time (see panels (b)-(f)).

kinetic and magnetic energies (normalized to the initial total energy). The magnetic energy is decreased by  $\approx 10\%$  of its initial value, which corresponds to a

release of free energy  $\approx 6.8 \times 10^{31}$  ergs. Interestingly, this release is comparable to the same from the observations (Aschwanden et al., 2014). We have observed the topological inference of this expelled energy in the panel (d) of Fig.-4.20 at the end of the evolution, where the MFLs appear to be losing their twists.

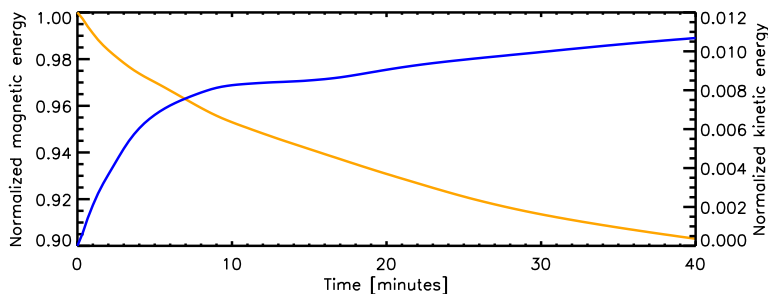
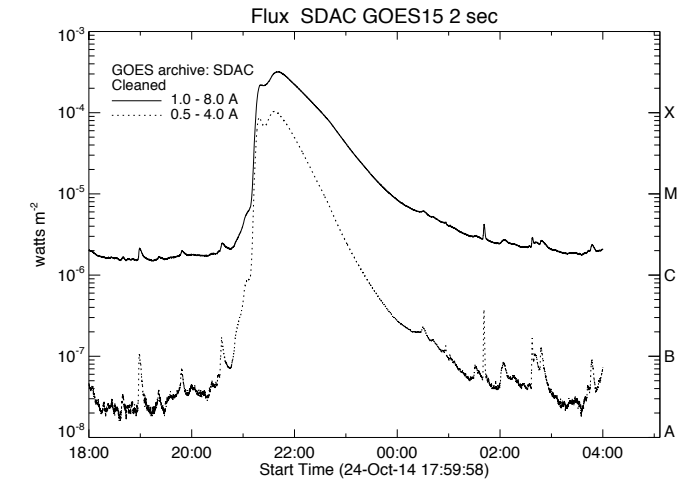


Figure 4.22: Temporal profile of the normalized kinetic (blue) and magnetic (yellow) energies.

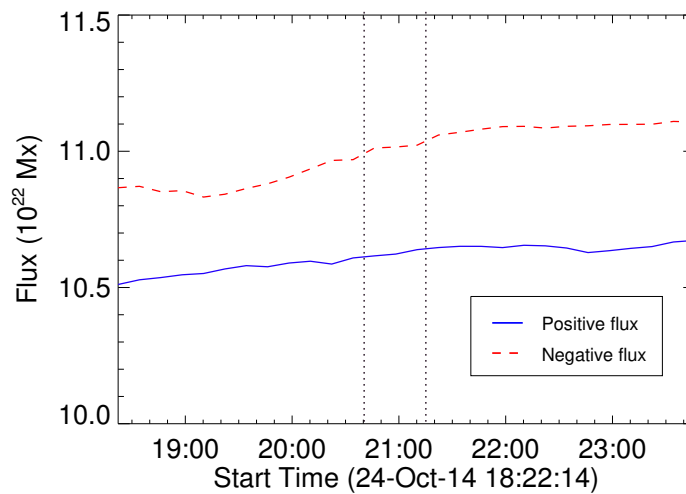
### 4.3 Case-III: Simulation of a Confined X-class Flare Associated with a Circular Flare Ribbon

The AR12192 was the largest active region in the solar cycle 24 and has produced many X-class flares (Chen et al., 2015). On October 24, 2014 around 21:15 UT, it has produced the strongest X3.1 flare which was found to be not associated with CME (Sun et al., 2015; Sarkar & Srivastava, 2018). Jiang et al. (2016) found no presence of flux rope to explain the confined nature whereas the onset of the flare was attributed to tether-cutting reconnections (Moore et al., 2001) between sheared arcades. Further studies of successive strong X-class flares triggered by tether-cutting MRs, in the same AR, were also reported in Chen et al. (2015). Contrarily, using NLFFF extrapolation, Inoue et al. (2016) found a multiple flux tube system located near a PIL to be favorable for the tether-cutting reconnections. They attributed the stability of the flux tube system to the overlying strong tethering MFLs. Similar results were also reported in Chen et al. (2015), where the mean decay index of the horizontal background field

was found to be less than the typical threshold required for the torus instability (Kliem & Török, 2006) to take place. An alternative explanation was provided by Zhang et al. (2017) who attributed the confined nature to the complexity of the involved magnetic field structures.



(a)



(b)

Figure 4.23: (a) GOES 15 X-ray flux for AR 12192 on 24th October, 2014 plotted with time during the X3.1 flare event. Notable is the peak around 21:15 UT indicating the flare. (b) The evolution of positive and negative magnetic flux at the photospheric boundary during the flare. The vertical dashed lines mark the interval between onset and peak of the flare. Importantly, there is no appreciable flux change within the interval.

The confined X3.1 flare was of long duration, lasting for 6 to 7 hours as shown in Fig.-4.23(a). The figure shows the GOES 15 X-ray flux observed during this

event in the 1-8 Å and 0.5-4 Å channels. Notably the vertical magnetic field flux at the photosphere was approximately conserved during the flare. This is shown in Fig.-4.23(b) which depicts the evolution of negative (dashed line in red) and positive magnetic fluxes (continuous line in blue), calculated by using the photospheric vector magnetograms from the HMI/SDO.

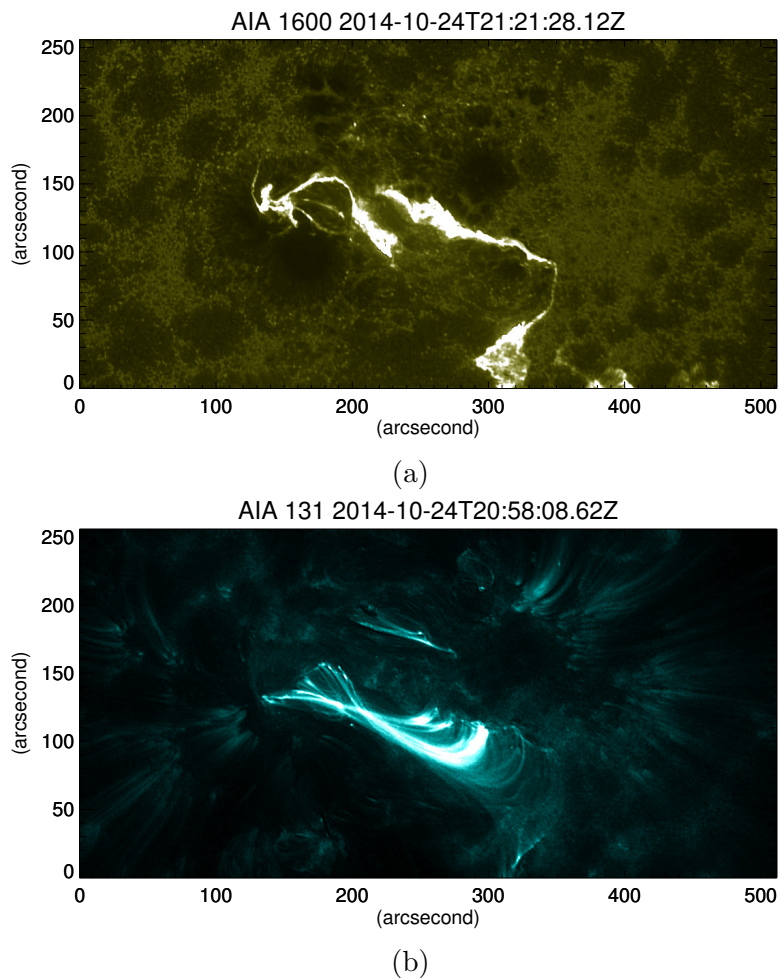


Figure 4.24: The AR 12192 observed in AIA 1600 Å (panel (a)) during the flare at 24th October, 2014 at 21:21 UT and AIA 131 Å (panel (b)) at 20:58 UT. The abscissa and ordinate are in arcsecond with one unit corresponding to a physical length of 720 km. Important is the circular brightening located approximately between 150 and 200 arcsecond along the abscissa.

Importantly, a circular brightening was observed in the chromospheric flare ribbons at the ultra-violet (UV) 1600 Å channel preceded by a brightening of the flaring loops in the EUV channel 131 Å of the AIA/SDO. The brightenings occur in the interval 21:20 to 21:35 UT in the 1600 Å channel (Fig.-4.24 (a))

and is co-located with the brightening in the  $131 \text{ \AA}$  channel as seen around 20:58 UT, which is just before the X-class flare. The circular flare ribbons are known to map MFLs constituting the fan plane of a 3D null on the photosphere (Masson et al., 2009). To our knowledge, the generation of the circular ribbon was not reported in the earlier works which is the main focus here.

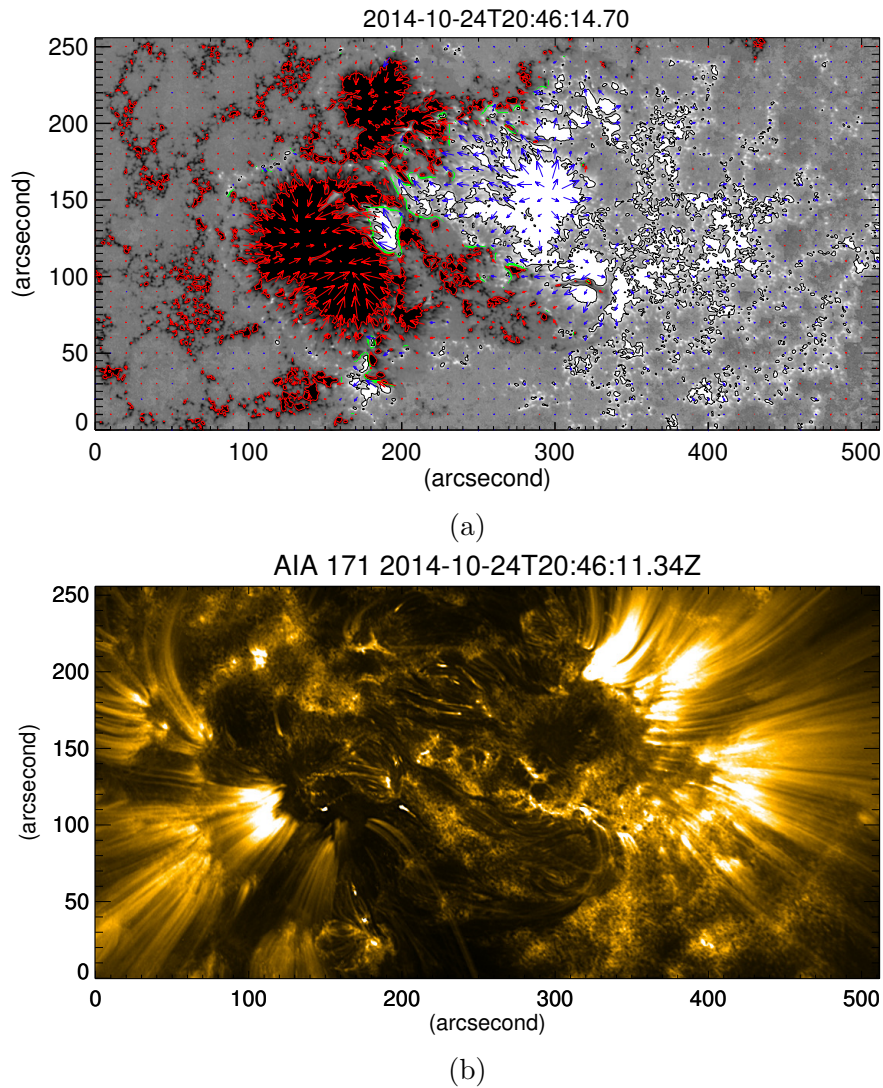


Figure 4.25: (a) Photospheric vector magnetogram from HMI of AR 12192 remapped on a CEA projection at 20:46 UT on 2014-10-24, highlighting the magnetic field line topology before the flare. The black and white contours represent the negative and positive polarities of  $B_z$  whereas the red and blue arrows are the vector plots of the transverse magnetic field. (b) AIA  $171 \text{ \AA}$  EUV image of the AR, highlighting the magnetic field line topology before the flare.

### 4.3.1 NFFF Extrapolation for the AR 12192

The magnetograms are taken from the ‘hmi.sharp\_cea\_720s data series’ that provides full-disk vector magnetograms of the Sun with a temporal cadence of 12 minutes and a spatial resolution of  $0''.5$ . The dotted vertical lines mark the beginning and peak phase of the flare. Hence, to a good approximation, the vertical magnetic field  $B_z$  at the bottom boundary remains constant during the interval. Due to this, here also we have used the line-tied boundary like previous cases.

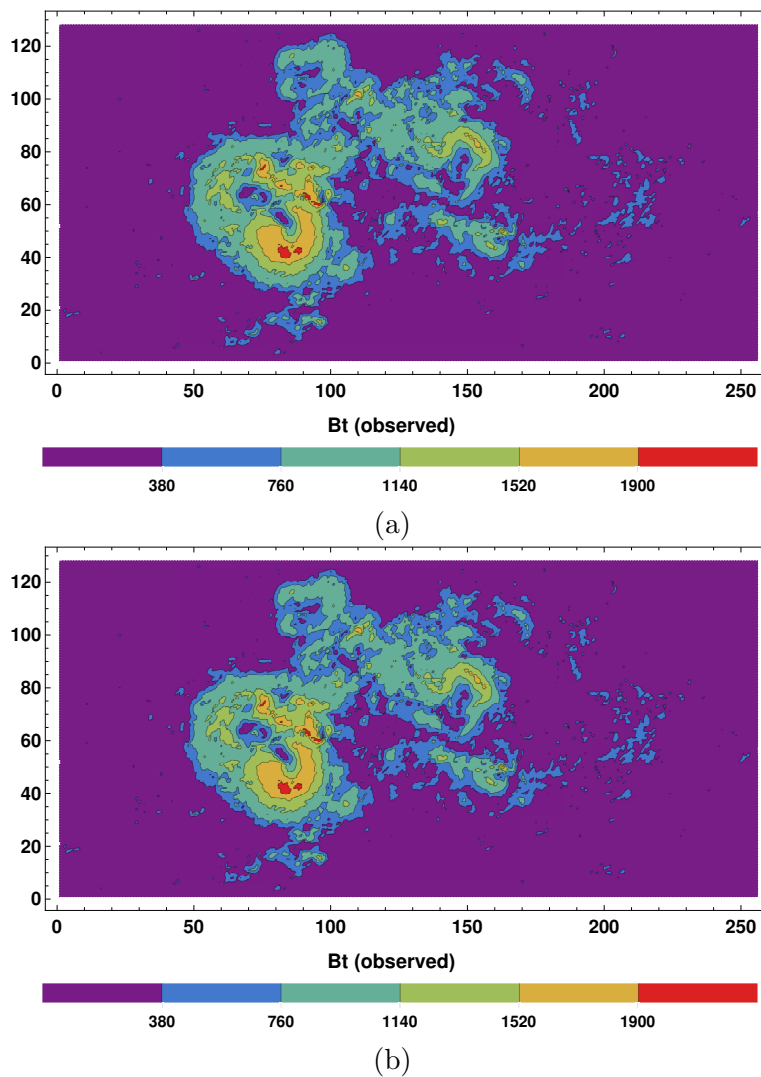


Figure 4.26: Contour plots of the transverse field of the observed (panel (a)) and extrapolated (panel (b)) magnetic field shown at the photospheric boundary.

We consider the magnetogram on October 24, 20:46 UT obtained from the SDO/HMI. The vector field shown in Fig.-4.25(a) corresponds to an original

cutout of dimension  $1024 \times 512$  pixels. The field is rescaled and extrapolated over a computational domain having  $256 \times 128 \times 128$  grids in the  $x$ ,  $y$  and  $z$  directions to reduce the expensive computational cost. The corresponding physical domain covers 360 Mm in the  $x$  direction and 180 Mm in the  $y$  and  $z$  direction, respectively. The best-fit values obtained for the  $\alpha$  parameters in this case are  $\alpha = \{0.1145, -0.0016\}$  which corresponds to an  $E_n = 0.31$ .

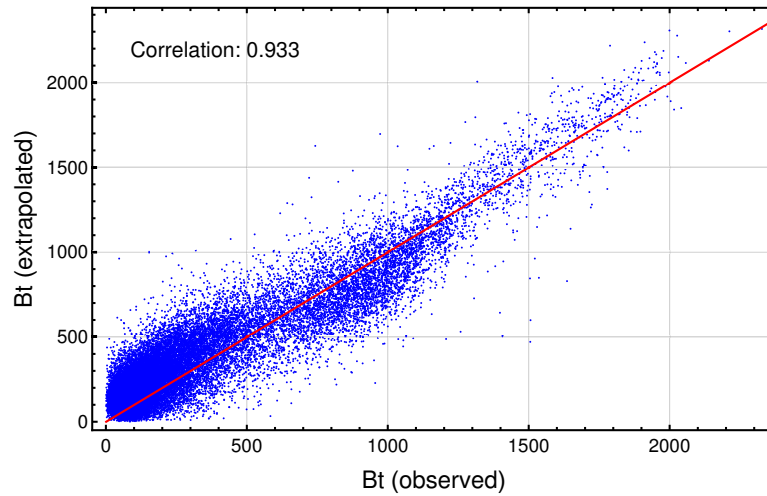
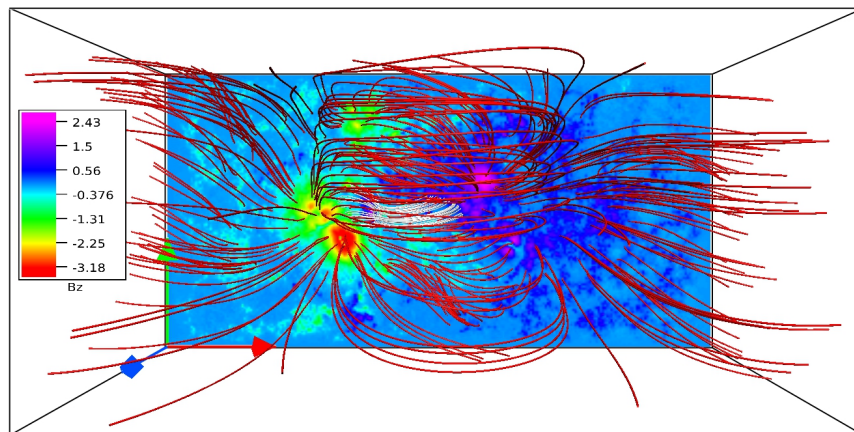


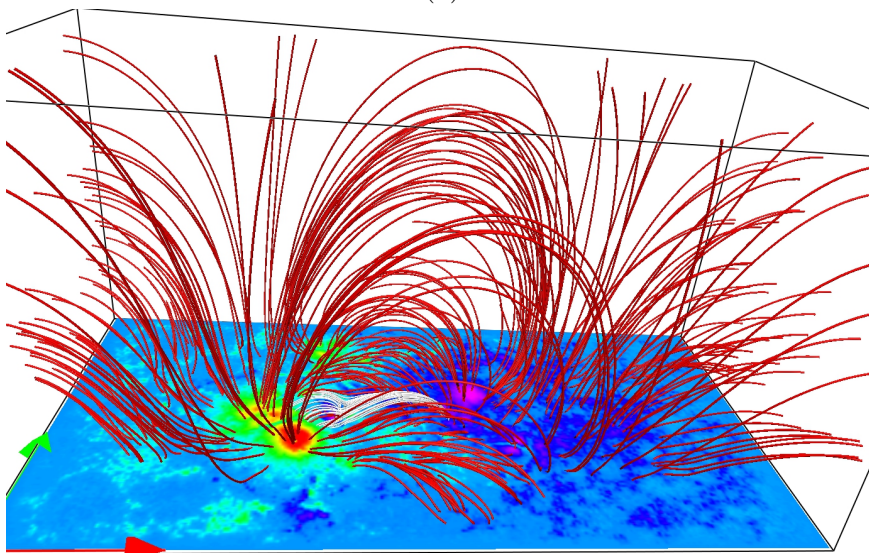
Figure 4.27: Scatter plot showing the correlation between the observed and extrapolated magnetic field. The red line is the expected profile for perfect correlation.

The contour plots for the transverse components of the observed and extrapolated fields at the photospheric boundary are shown in Fig.-4.26. The figure indicates most of the large scale magnetic features to be well-captured by the extrapolated field. The scatter plot of the observed and the extrapolated fields is shown in Fig.-4.27. The plot documents the agreement to be better for the higher field side. The Pearson-r correlation between the two fields is 0.933, which is acceptable.

The top and side views of MFLs over the full vector magnetogram are shown in Fig.-4.28 with the field lines being depicted in red. A smaller set of MFLs in the vicinity of the flaring region (around 21:15 UT) are shown in white. The white MFLs resemble the topology of a 3D magnetic null (Lau & Finn, 1990) and are shown in greater detail in Fig.-4.29. The similarity of MFL morphology of the extrapolated field (panel (b) of Fig.-4.28) with the observed EUV structure



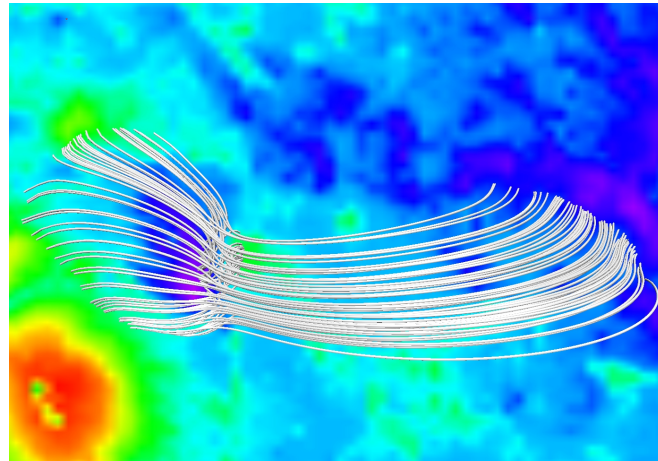
(a)



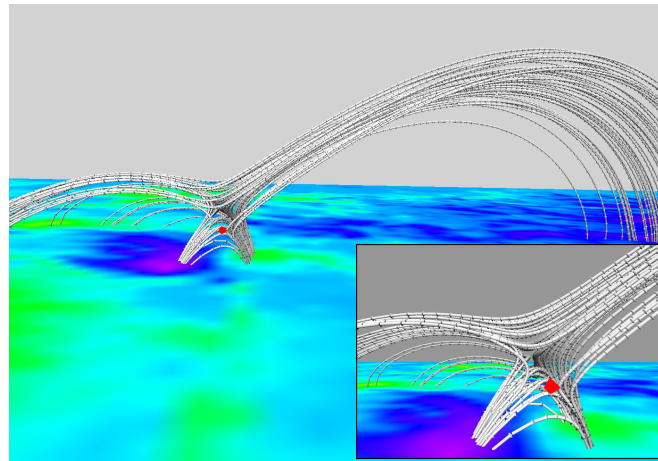
(b)

Figure 4.28: Top (panel (a)) and side-view (panel (b)) of the overall NFFF extrapolated magnetic field line topology for the AR 12192 on 2014, October 24, 20:46 UT. The bottom boundary represents the strength (in kG) of the  $B_z$  component of the magnetic field and the extrapolated fields lines are depicted in red and a small set of field lines close to the location of the 3D null—identified in the Fig.-4.29—are depicted in white.

(panel (b) of Fig.-4.25) advocates effectiveness of the extrapolation. The MFL geometry is characterized by the presence of high and low-lying loops. Notably the low-lying MFLs, depicted in white, connecting the weak positive polarity with the surrounding negative polarity regions generate the 3D null. Fig.-4.29(a) corroborates the 3D null to be complete with a dome shaped fan and an elongated spine. The panel (b) of Fig.-4.29 depicts MFLs on a stack of planes which are approximately tangential to the spine. The MFLs are overlaid with an iso-surface



(a)



(b)

Figure 4.29: The top- (panel (a)) and side-view (panel (b)) of the magnetic field lines drawn near one of the polarity-inversion lines, where the flare was later observed. The field line topology indicates the presence of a 3D null, complete with a dome-shaped fan and elongated spine. The red surface inside the field lines represents an iso-surface having 2.5% of the maximal field strength of  $B$  and locates the null. The height of the null is roughly 3 Mm from the photosphere. The bottom boundary is same as that of Fig.-4.28.

(in red) of  $|\mathbf{B}|$  having an iso-value which is 2.5% of its maximum (magnified in the inset). The iso-surface locates the 3D null. The height of the null point is roughly 3 Mm from the photospheric plane. Notably, the MFLs constituting the dome intersect the bottom boundary to generate footpoints that are distributed in a circular pattern. The MFLs below the null point form an elongated arcade, as seen in the inset of Fig.-4.29.

The direct volume renderings of volume current density  $|\mathbf{J}|$  and Lorentz force

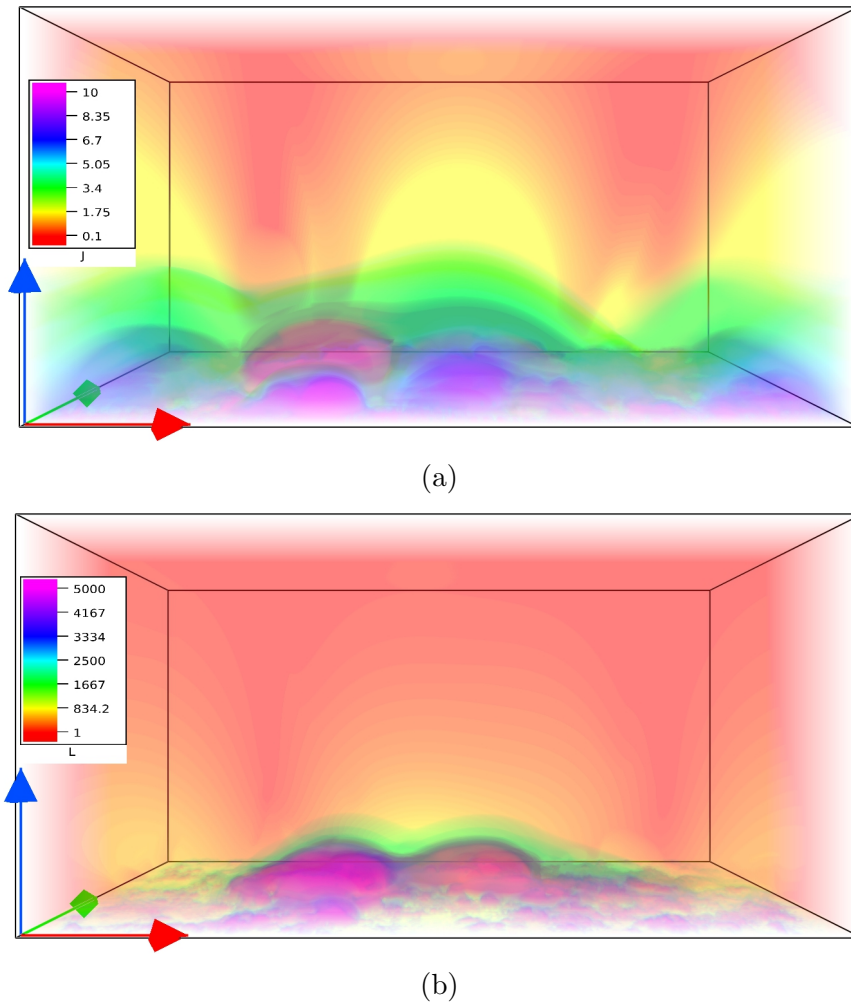


Figure 4.30: The spatial distribution of volume current density (panel (a)) and Lorentz force (panel (b)) in arbitrary units. Notably, appreciable current is present throughout the volume while most of the force is present only near the bottom boundary which sharply falls to zero with increase in height.

are depicted in Fig.-4.30. Noticeably, the regions of large Lorentz force and high current overlap with those of high values of  $|B_z|$ , which can be realized by a direct comparison with Fig.-4.28(b). The values for  $|\mathbf{J}|$  and Lorentz force are mentioned in arbitrary units as we are mostly interested in their variations with height. The figure reveals a sharp decay of the Lorentz force with height (by a factor of 1/5000) while the current shows a decay by only a factor of 1/100.

### 4.3.2 Simulation Results and Discussions

The simulations are initialized from a motionless state with the initial magnetic field given by the NFFF extrapolation and the magnetofluid idealized to be thermally homogeneous and having perfect electrical conductivity. The flow is generated as the initial Lorentz force pushes the plasma. To ensure the net magnetic flux to be zero in the computational domain, all components of volume  $\mathbf{B}$  except for  $B_z$ , are continued to the boundaries for a given time step (Kumar et al., 2015a). At the bottom boundary,  $B_z$  is kept constant (line-tied boundary) since the change of magnetic flux at the boundary is minimal (see Fig.-4.23(b)). For the simulation, we set the dimensionless constant  $\tau_a/\tau_\nu \approx 7 \times 10^{-3}$ , which is roughly two orders of magnitude larger than its coronal value. The higher value of  $\tau_a/\tau_\nu$  speeds up the relaxation because of a more efficient viscous dissipation without affecting magnetic topologies. The density is set to  $\rho_0 = 1$  and kinematic viscosity to  $\nu = 0.002$ , in scaled units. The spatial unit step  $\Delta x = 0.0078$ , while the time step is taken as  $\Delta t = 5 \times 10^{-3}$ . The results presented here pertain to a run for 1000  $\Delta t$  which roughly corresponds to an observation time of one and half hour. Notably, the  $R_M$  throughout the simulation is infinity expect during MRs facilitated by the MPDATA driven dissipation.

Fig.-4.31 depict MFL evolution in the neighborhood of the 3D null. The  $B_z$  contours are plotted on the bottom boundary. Four sets of MFLs are highlighted. The fan and the spine of the null are made by the yellow MFLs whereas the red MFLs are overlying the null. The blue MFLs are located inside the dome whereas the arcade below the null is formed by the green MFLs. With evolution, the null and the constituent yellow MFLs do not sustain an appreciable ascent whereas the red MFLs expand significantly to a threshold height ( $\approx 78$  Mm), after which they contract. To explore the underlying physics, we note the arcade MFLs (in green) and the dome (yellow) constitute an X-type geometry cf. panel (b) of Fig.-4.29. As reconnection occurs at the X-type null, blue MFLs come out of the dome and overlays it. The consequent increase in local magnetic pressure pushes the red MFLs upward, resulting in their overall rise. Furthermore, the red MFLs get stretched as they rise and at a threshold generate enough magnetic tension

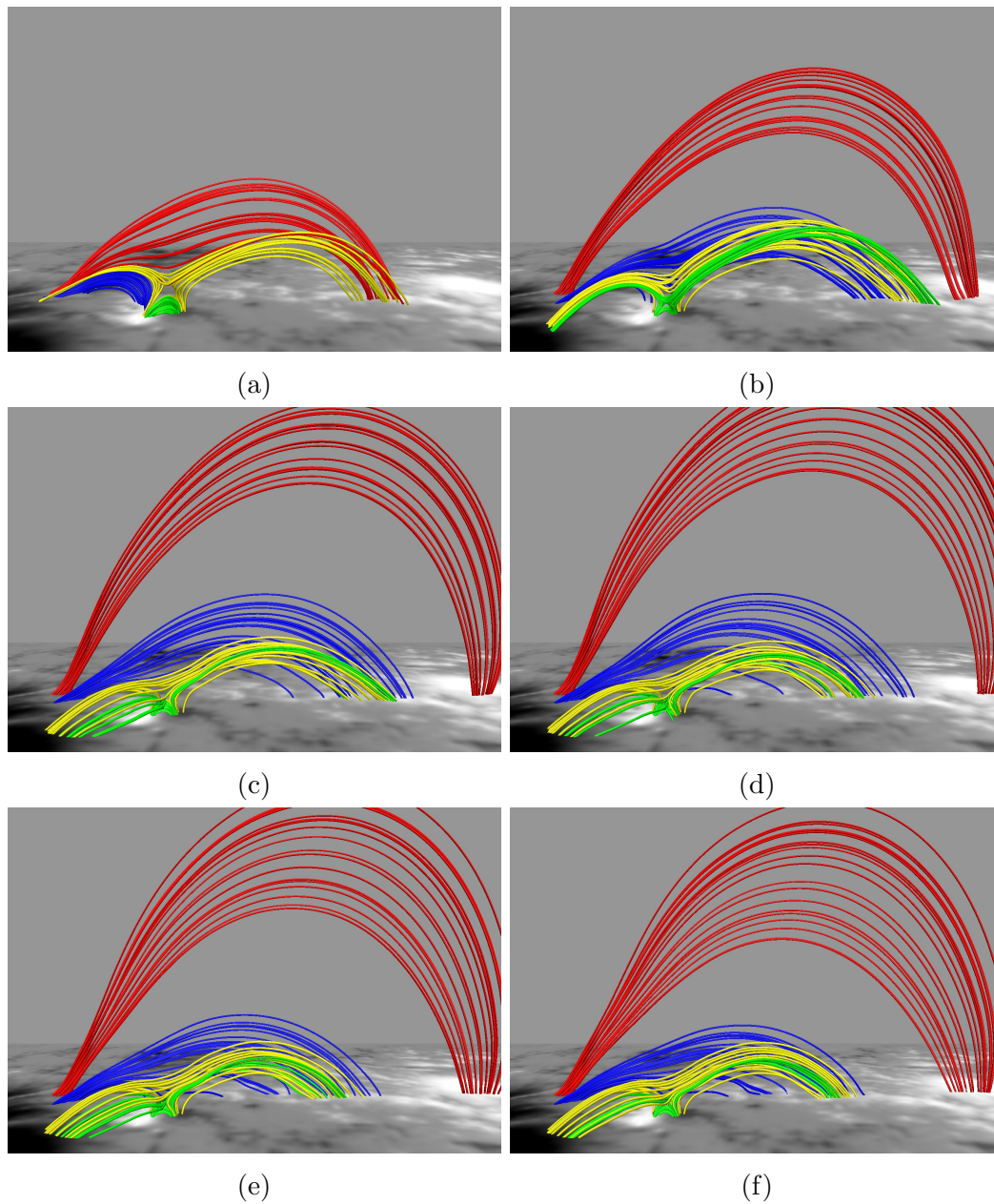


Figure 4.31: Side view of evolution of four sets of magnetic field lines close to location of the 3D null, shown at  $t = 0, 200, 400, 600, 800$  and  $1000$  in panels (a)-(f) respectively. The bottom boundary in all the panels represents the strength  $B_z$  on the photospheric plane as in Fig.-4.28 but now in grayscale for clarity.

to stop additional upward motion. Interestingly, we also fail to identify a flux rope like (Jiang et al., 2016), which further agrees with the confined nature of the flare.

The simulated 3D null appears to rotate with evolution (Fig.-4.32). For aiding visualization, the MFLs have been color-coded based on their distance along the

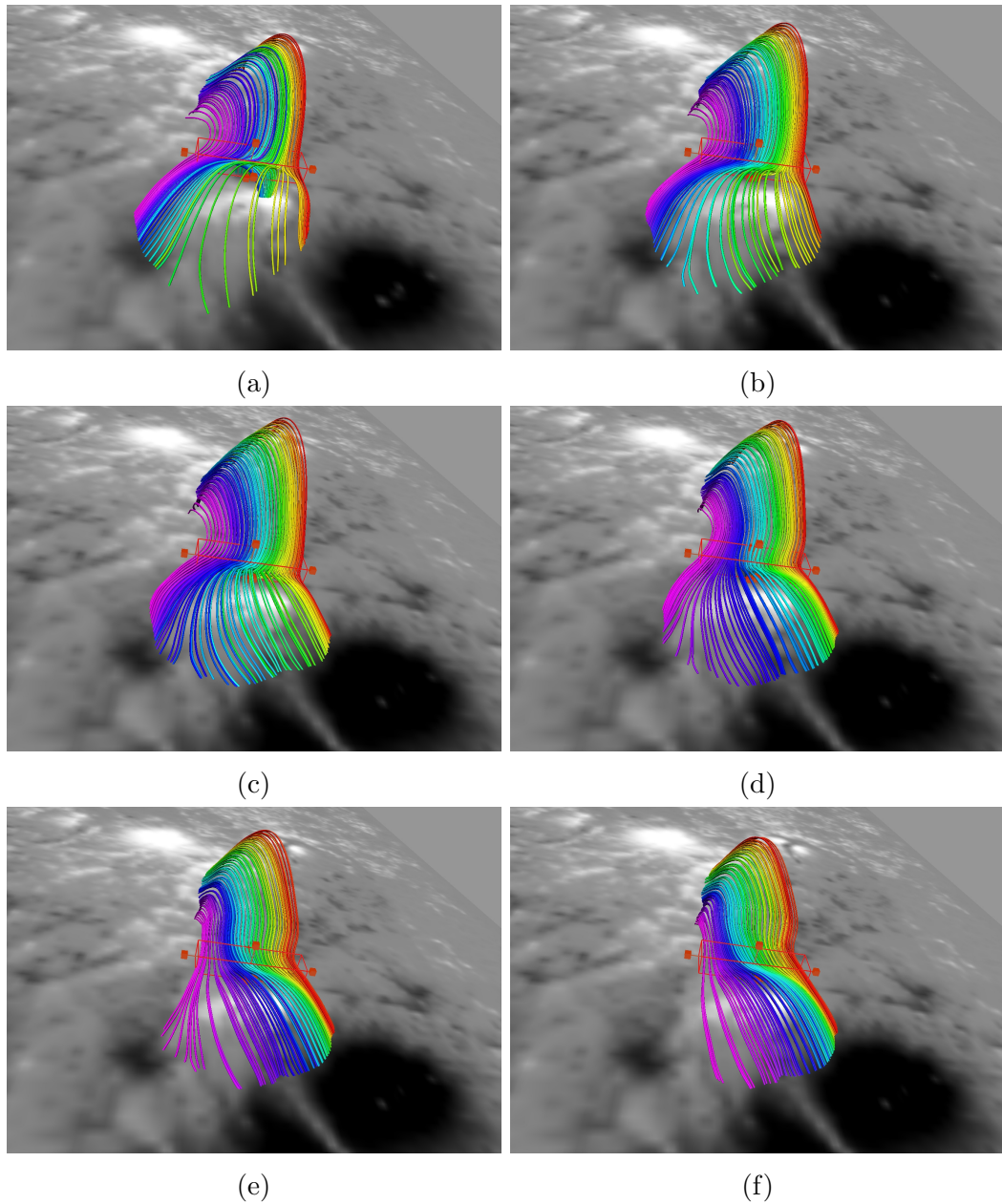


Figure 4.32: Panels (a)-(f) spanning  $t = 0, 80, 160, 240, 320$  and  $400$ , illustrate rotation of the dome structure of the field lines constituting the 3D null. The cuboidal rake in the figure shows the volume where the seed points are chosen. The field lines are color-coded with respect to their distance in the  $y$  direction. This helps us to visualize the rotation of the field lines.

$y$  axis. We have also shown the volume wherein the seed points of MFLs are located. When viewed from the top, an anti-clockwise rotation of the MFLs is quite prominent which matches well with the dynamics seen in the AIA 131 Å channel. This similarity with observations makes the simulation credible.

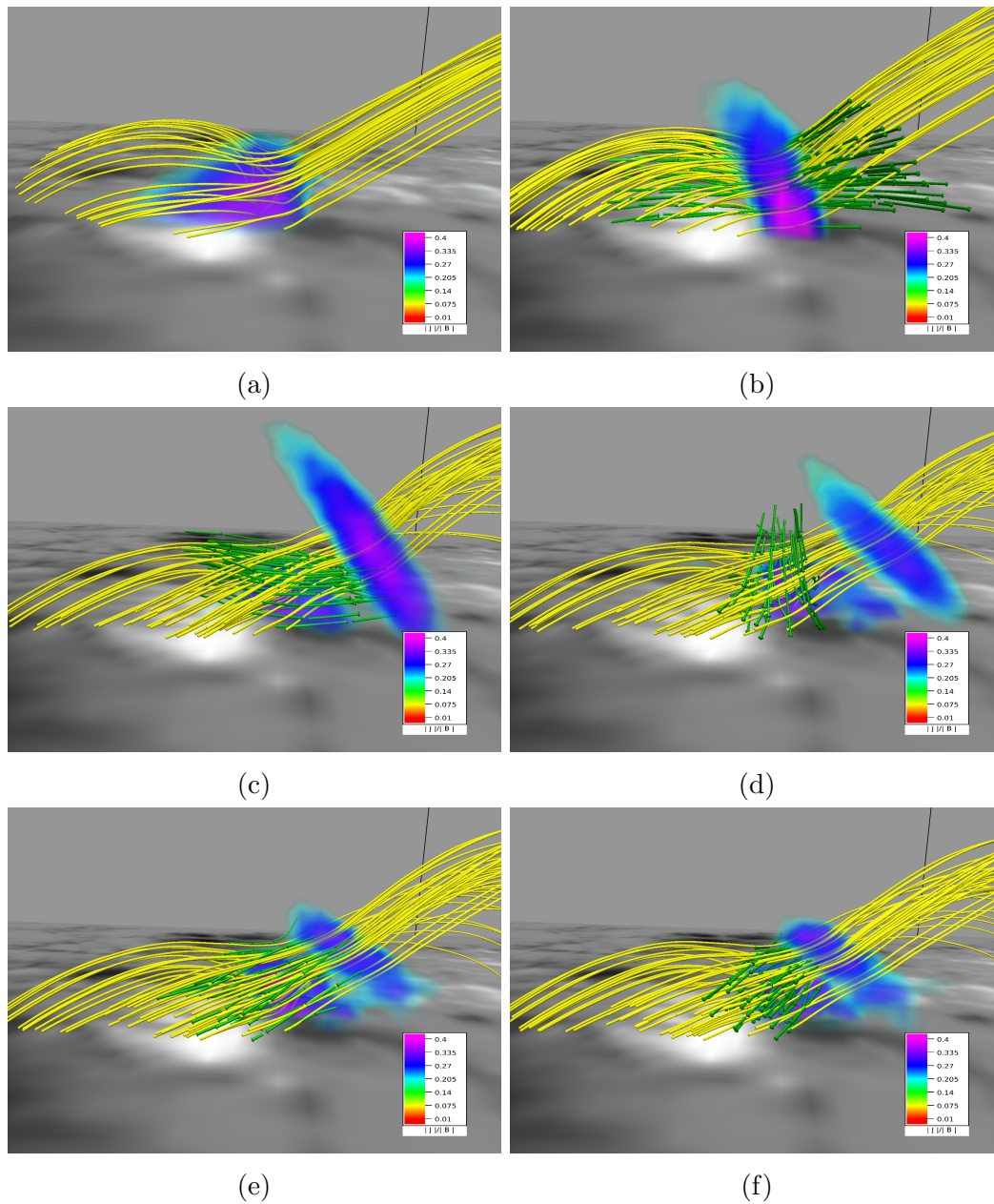


Figure 4.33: Panels (a)-(f) spanning  $t = 0, 200, 400, 600, 800$  and  $1000$ , illustrate the evolution of magnetic field lines (yellow), velocity field (green) and  $|\mathbf{J}|/|\mathbf{B}|$ .

The Fig.-4.33 is also overlaid with streamlines (green) and  $|\mathbf{J}|/|\mathbf{B}|$ . Noticeable is the initial high value of  $|\mathbf{J}|/|\mathbf{B}|$  near the null. The value increases with time, becoming maximum at  $t = 400$ , decaying subsequently. The peaking of  $|\mathbf{J}|/|\mathbf{B}|$  is indicative of magnetic reconnections occurring near the null. The resultant outflow is shown by the red streamlines.

For further investigation, Fig.-4.34 plots the  $Q$ -map where the squashing

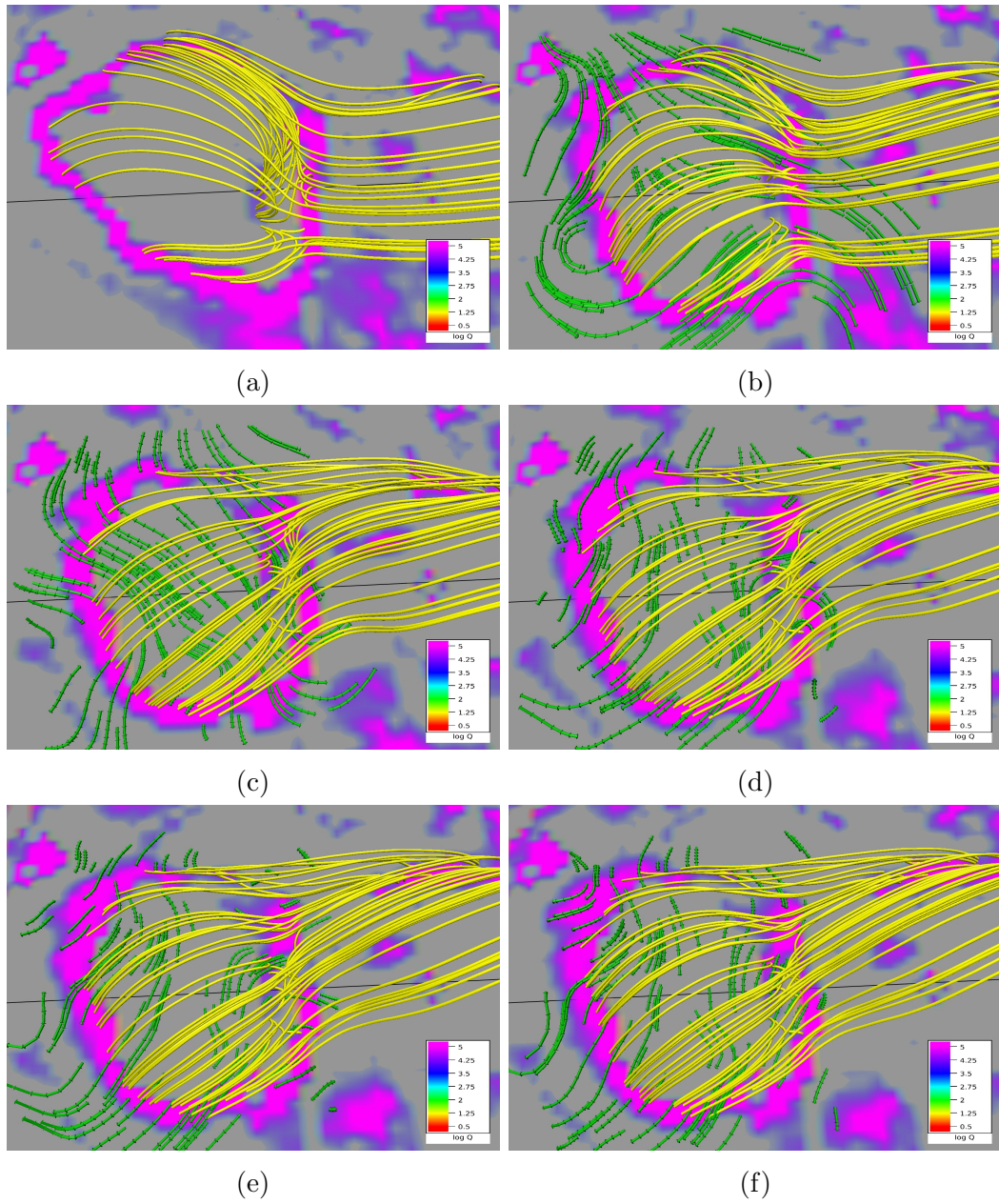


Figure 4.34: Panels (a)-(f) spanning  $t = 0, 200, 400, 600, 800$  and  $1000$ , illustrate the slipping reconnections in the MFLs (shown in yellow) spanning the dome of the 3D null. The streamlines of the flow are shown in green. The bottom boundary shows contours of high values of  $\log Q$ . (An animation of this figure is available.)

factor  $Q$  is calculated by following Demoulin et al. (1996); Liu et al. (2016) and ascertains the dome to have high gradient of magnetic connectivity which results in slipping reconnections (Aulanier et al., 2007). The subsequent change in magnetic connectivity manifests as the seeming MFL rotation. For validation,

we note the co-located flow (in green) is not along the rotation and hence, cannot cause it.

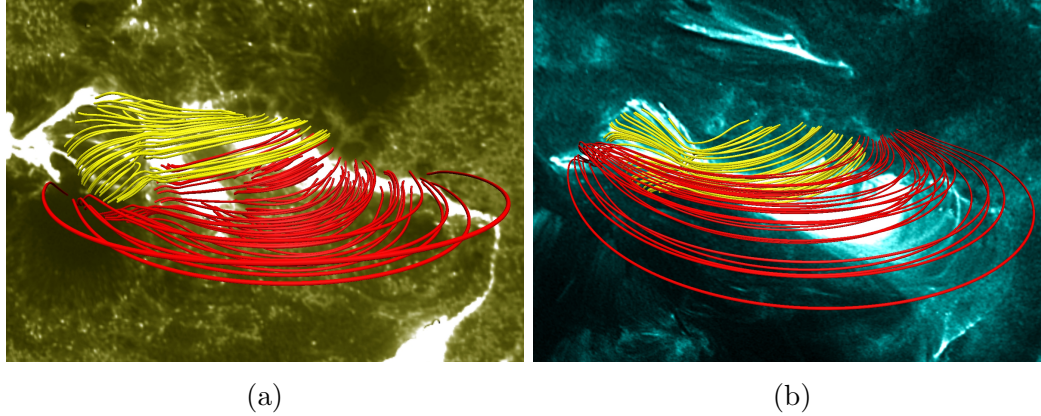


Figure 4.35: The AIA 1600 Å and 131 Å channel images as depicted in Fig.-4.24 are overlaid with the relevant magnetic field lines. Important is the almost exact match of footpoints with the location of the brightening.

In panels (a) and (b) of Fig.-4.35, we overlay intensity structures in wavelengths 1600 Å at 21:25 UT and 131 Å at 20:50 UT with corresponding MFLs. Importantly, the almost exact match of the footpoints for both wavelengths with brightenings not only establishes the importance of the 3D null in the circular flare ribbon but also being in agreement with the contemporary understanding, validates the effectiveness of the NFFF extrapolation in constructing an appropriate coronal field model.

## 4.4 Inferences

The chapter focuses on the data-constrained numerical simulation of active region transients where the photospheric magnetic field is directly used to generate the coronal magnetic field. The transients considered here are a blowout jet and two flares of C- and X- class. Interestingly, the blowout jet is also accompanied with a C-class class flare, giving an unique opportunity to explore two near-simultaneous events in a single simulation. Additionally, the computations are in the spirit of the ILES. The MRs are mimicked when the field variables are under resolved whereas, away from the reconnection sites the condition of the

---

flux-freezing is ensured by the second order accurate MPDATA. The simulations paint a scenario that is different from the standard flare model and highlights the role of 3D nulls and QSLs in initiating the transients. Particularly, 3D nulls are found to be ubiquitous in all the three simulations and warrant further attention. In the next chapter, we develop relevant initial value problems using analytical means to explore the 3D reconnections in a more tractable way.



# Chapter 5

## Simulations with Analytical Initial Conditions

Magnetic null points are ubiquitous in the solar atmosphere which we have witnessed in all of the transients explored in the chapter 4. Other extrapolated fields have shown their abundances in the lower atmosphere during the activity minimum (Régnier et al., 2008; Longcope & Parnell, 2009). Three-dimensional nulls were also found to be responsible for the Bastille Day Flare (Aulanier et al., 2000) and causing coronal mass ejections via magnetic breakout (Lynch et al., 2008). A concise list of natural systems where 3D nulls are important can be found in Wyper et al. (2012); Wyper & Pontin (2014a,b). Recent simulations have emphasized the role of repeated MRs in driving various eruptive events occurring in the solar atmosphere and heating the corona to its  $10^6\text{K}$  temperature (Parker, 1994; Shibata & Magara, 2011; Kumar et al., 2013; Prasad et al., 2017; Joshi et al., 2017a). The coronal MFLs anchored to an active region are inherently 3D because of their twist. The consequent possibility of triggering solar flares by 3D null facilitating MRs is interesting and merits attention. The numerical simulations reported in Kumar et al. (2013) explore the possibility by attributing the onset of current sheets to deformation of magnetic separator at the neighborhood of 3D nulls. Importantly, the presence of magnetic nulls constrains the dynamics of magnetofluids. Utilizing the induction equation of the ideal MHD, Hornig & Schindler (1996) have emphasized the null to preserve

its identity during evolution—due to vanishing of the Lagrangian time derivative  $D\mathbf{B}/Dt$  where  $\mathbf{B} = 0$ —in the strict absence of any magnetic energy dissipation. They further extended the notion of the magnetic topology and the preservation of the null to non-ideal plasmas by assuming a velocity  $\mathbf{w}$ , satisfying

$$\mathbf{w} \times \mathbf{B} = \mathbf{v} \times \mathbf{B} - \eta \mathbf{J}, \quad (5.1)$$

in usual notations. The  $\mathbf{w}$  has contributions from the bulk plasma velocity  $\mathbf{v}$  and the MFL diffusion. A first order Taylor expansion of  $\mathbf{B}$  in the neighborhood of the  $\iota^{\text{th}}$  3D null, located at  $\mathbf{x}_\iota(t) = \mathbf{x}(\mathbf{x}_\iota, t_0)$ , gives for sufficiently smooth field (Greene, 1992; Murphy et al., 2015)

$$\mathbf{B} = \nabla \mathbf{B}|_{\mathbf{x}_\iota} \cdot (\mathbf{x} - \mathbf{x}_\iota), \quad (5.2)$$

which exposes the importance of the Jacobian matrix  $\nabla \mathbf{B}|_{\mathbf{x}_\iota}$  for field topology. In particular, the quantity

$$D \equiv \sum_{\iota} \text{sign}(\det(\nabla \mathbf{B}|_{\mathbf{x}_\iota})), \quad (5.3)$$

is conserved (Hornig & Schindler, 1996) and is known as the overall topological degree (Greene, 1992; Longcope, 2005). In effect, the conservation suggests the nulls to appear (or disappear) in pairs of opposite topological degrees unless they move across the boundaries of a domain.

Although 3D nulls are studied extensively, the present understanding falls short in explaining their ubiquity which is not self-explanatory. To elucidate further, we note, a way to construct a 3D null is to follow the technique of the magnetic charge model where distinct sources or magnetic “charges” are used to construct the photospheric magnetic field (Barnes et al., 2005). Let the resultant magnetic field of  $N - 1$  such charges to be  $\mathbf{B}_1$  at a location  $\mathbf{r}_1$ . In principle,  $\mathbf{B}_1$  can be balanced by placing another magnetic charge having a field  $-\mathbf{B}_1$  at  $\mathbf{r}_1$ . For the configuration, the net field at the point  $\mathbf{r}_1$  is zero—rendering it a 3D null. This special magnetic configuration lacks generality and only represents

---

a charge distribution for a specific outcome. With the MHD equations being inherently non-linear, a maintenance of this particular alignment of charges in a complexly evolving magnetofluid is presumably non-trivial and merits further attention. Hence, it is essential to take a deeper look at the physics behind the onset of 3D nulls in naturally existing plasmas. Indeed, Albright (1999) conjectured magnetic nulls to be an autonomous outcome of a turbulent plasma evolution and emphasized the importance of 3D MHD simulations for realizing the same. The role of 3D nulls in constraining the dynamics of an evolving plasma is also explored with MHD simulations. For instance, Kumar & Bhattacharyya (2016) argued in favor of the possibility that MRs at autonomously developed current sheets near 3D nulls are crucial for an onset of circular flare ribbons. Recent simulations by Thurgood et al. (2017) have demonstrated spontaneously generated oscillations associated with MRs, initiated by localized collapse of a 3D null under the influence of external MHD waves. The null detection technique also got refined over the years and presently the one developed by Haynes & Parnell (2007) effectively uses the tri-linear method to locate 3D nulls with subgrid-scale accuracy.

Additional to the generation of 3D nulls, the interplay of different reconnection scenarios existing in a system is also intriguing. Other coronal locations like separators and quasi-separators, as discussed in chapter 2, are responsible for reconnection. Additional to the pre-existing preferential locations such as nulls, separators and QSLs, MHD simulations with idealized scenario of infinite electrical conductivity show that the potential sites for reconnection can naturally be generated because of the inherent dynamics (Kumar et al., 2014, 2015b).

The magnetofluid evolution being congruent with the Parker's magnetostatic theorem (Parker, 1972, 1994, 2012), attributes the generation of such sites to a development of favorable magnetic stresses which naturally bring non-parallel magnetic field lines to close proximity. As a result, layers of intense volume current density ( $\mathbf{J}$ ) or the current sheets originate. In the presence of slight but non-zero magnetic diffusivity, as the case for the coronal plasma, the CSs get dissipated by magnetic reconnections.

In the above backdrop, the presented MHD simulations aim to numerically explore the formation of null points, the magnetic reconnections in the presence of 3D nulls and QSLs; and to examine the role of such MRs in shaping-up the dynamics. In order to achieve the above goals we have constructed justifiable initial magnetic topologies with analytical models but similar to the topologies found in the solar corona. To understand the genesis of 3D nulls, we have proceeded with two suitable initial magnetic fields. Next, to understand interplay between different potential sites of reconnection, we have considered two cases and report the dynamics found during the evolution. The detailed discussions pertaining to the two cases are presented below.

## 5.1 Generation of 3D nulls

### 5.1.1 Initial Value Problems

The first set of initial magnetic field is obtained by deforming MFLs associated with an isolated 3D null at  $(x, y, z) = (0, 0, 0)$  (Parnell et al., 1996), having components

$$B_x = \mathcal{C} x , \quad B_y = \mathcal{C} y , \quad B_z = -2\mathcal{C} z , \quad (5.4)$$

defined on a Cartesian domain  $[-\pi, \pi] \times [-\pi, \pi] \times [-\pi, \pi]$ , discretized on the  $64 \times 64 \times 64$  regular grid with open boundaries.  $\mathcal{C} = 1$  [Gs · cm<sup>-1</sup>]. In all relevant illustrations, the 3D null is constructed by the procedure introduced in chapter 4 and documented in Kumar et al. (2013).

To explore the dynamics of null formation, we conduct simulations characterized by two sets of initial condition. In the first, a given magnetic null is deformed by a prescribed flow and subsequently relaxed to a terminal state. In the second set, the initial magnetic field is casted in the form,

$$B_x = c_0(0.5 A \sin(z) + 1.5 C \cos(y)), \quad (5.5)$$

$$B_y = c_0(0.5 B \sin(x) + 1.5 A \cos(z)), \quad (5.6)$$

$$B_z = c_0(0.5 C \sin(y) + 1.5 B \cos(x)). \quad (5.7)$$

and is constructed by a linear superposition of two Arnold-Beltrami-Childress (ABC) fields, each of which is a solution of the linear-force-free equation (Dombre et al., 1986; Ram et al., 2014; Kumar et al., 2017) and is chaotic. The modified field (5.5)-(5.7) is topologically similar to the ABC field (Kumar et al., 2017) which is well known to be chaotic in three dimensions and regular in two dimensions. Likewise, the superposed field is also two-dimensional with the MFLs tangential to global flux surfaces when any one of the constants  $A$ ,  $B$  or  $C$  is set to zero. Avoidance of having 3D magnetic nulls within the computational volume requires  $A = B = 1$  and  $C \notin \{0.3142, 3.01\}$  (Kumar et al., 2017).

## 5.1.2 Simulation Results and Discussions

### 5.1.2.1 Case-I, Deformation and Relaxation of a potential 3D null point

The governing equations (in CGS units) used to deform the 3D null are:

$$\rho_0 \left[ \frac{\partial \mathbf{v}}{\partial t} + (\mathbf{v} \cdot \nabla) \mathbf{v} \right] = -\nabla p + \frac{1}{4\pi} (\nabla \times \mathbf{B}) \times \mathbf{B} + \nu \nabla^2 \mathbf{v} , \quad (5.8)$$

$$\nabla \cdot \mathbf{v} = 0 , \quad (5.9)$$

$$\frac{\partial \mathbf{B}}{\partial t} = \nabla \times (\mathbf{v} \times \mathbf{B}) , \quad (5.10)$$

$$\nabla \cdot \mathbf{B} = 0 , \quad (5.11)$$

in usual notations, where  $\nu$  is the kinematic viscosity. The pressure perturbation  $p$ , about a thermodynamically uniform ambient state, satisfies the elliptic boundary value problem, generated by imposing the incompressibility constraint (5.9) on the momentum equation (5.8); see Bhattacharyya et al. (2010) and the references therein.

The deformation of MFLs is achieved by numerically integrating (4.2a)-(4.2d) with the initial solenoidal flow  $\mathbf{v} = (v_x, v_y, v_z)$  specified as

$$v_x = 0 , \quad v_y = 0.5 \sin(z) , \quad v_z = 0, \quad (5.12)$$

whose stagnation plane includes the null at  $z = 0$ , and the selected amplitude

ensures a smooth traceable evolution of the flow. The kinematic viscosity is  $\nu = 0.01$  and  $\rho_0 = 1$ , and the spatial and temporal grid increments are  $\Delta x = \Delta y = \Delta z = 0.09817$  and  $\Delta t = 0.016$ , respectively, all in the cgs units.

The overall system dynamics are depicted in Fig.-5.1, whose panels (a) and (c) show the histories of the total magnetic and kinetic energy normalized by the initial magnetic energy. The evolution proceeds without any large-scale recon-

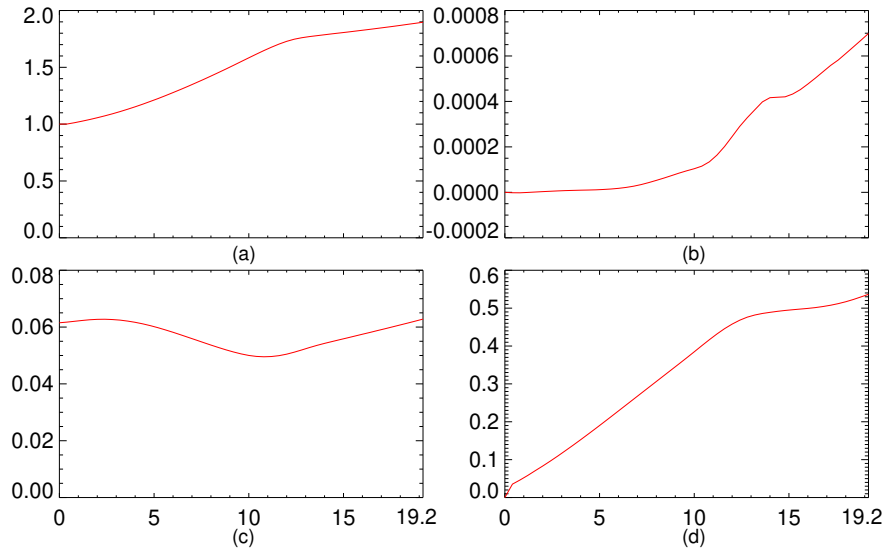


Figure 5.1: History of the normalized (a) magnetic and (c) kinetic energies, along with the grid-averaged (b) field-aligned current density and (d) volume current density during the deformation with the sinusoidal initial velocity. Notable are the approximate constancy of the field-aligned current and a non-zero value of the volume current density at the terminal state.

nection, evidenced by the small change in the domain-averaged  $\mathbf{J} \cdot \mathbf{B}$  plotted in panel (b). The corresponding evolution of MFLs is shown in Fig.-5.2. The two spine axes are pushed toward the fan plane by the initial Lorentz force, resulting in a spine-fan reconnection. Consequently, the initial 3D null (topological degree: +1) bifurcates into two 3D nulls (inset in panel (e) of Fig.-5.2) of degrees +1 (left) and +1 (right) along with two disjoint flux ropes depicted at the panel (f), generating a null with topological degree -1. The overall topological degree is then still +1 and as theorized, preserved during the evolution. Wyper & Pontin (2014a,b) have also reported similar results where the spine-fan reconnection was occurred due to an initial tanh velocity profile. The agreement between the two simulations not only corroborates the theory but simultaneously justifies

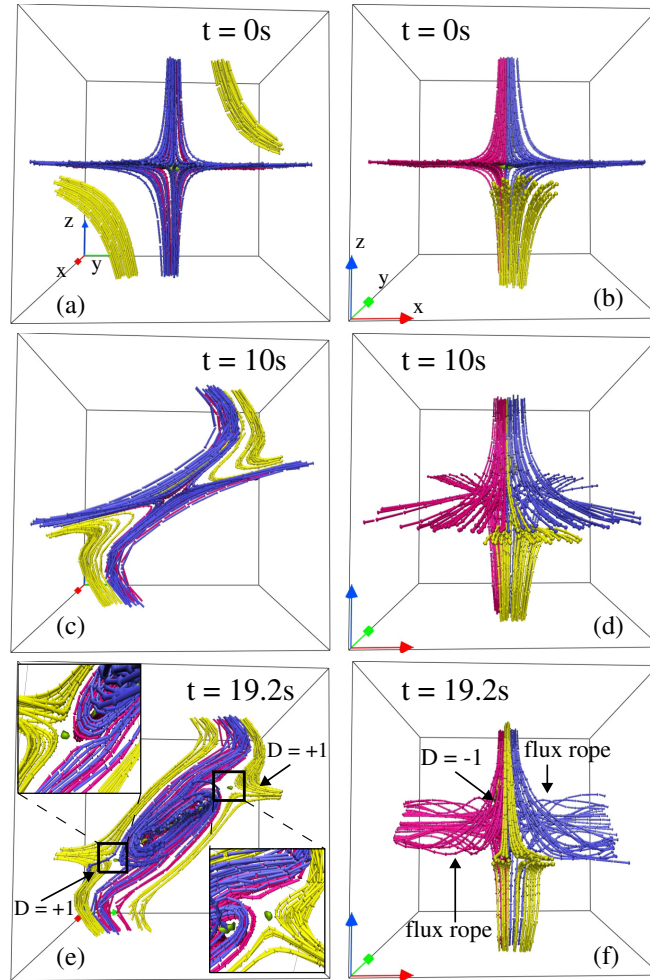


Figure 5.2: MFL evolution during the deformation seen from two different angles. The MR initiates as the spine and fan approaches each other, panels (c) and (d). Important are the pitchfork bifurcation of the 3D null and the flux ropes, marked by arrows, as shown in panel (e) and (f), respectively. With MFLs drawn in a favorable viewing angle, the panel (f) shows the post-reconnection fan plane to be sandwiched between the two flux ropes (in magenta and blue). Also the net topological degree (denoted by  $D$ ) is preserved ( $D = +1$ ) which is in congruence with the theory. The magnetic field for the MFLs in panels (e) and (f) serves as the initial field for the relaxation. Red, green, and blue arrows mark  $x$ ,  $y$ , and  $z$  axes, respectively.

the null-detection technique used here. As expected, the average  $|\mathbf{J}|$  increases as the MFLs get deformed more and more. The deformation is terminated at  $t \approx 19.2s$ .

Subsequently, the plasma is relaxed from the above terminal state while setting the velocity and pressure perturbation to zero. The density is set to unity, and the simulation is executed on the identical  $(64 \times 64 \times 64)$  grid. The overall

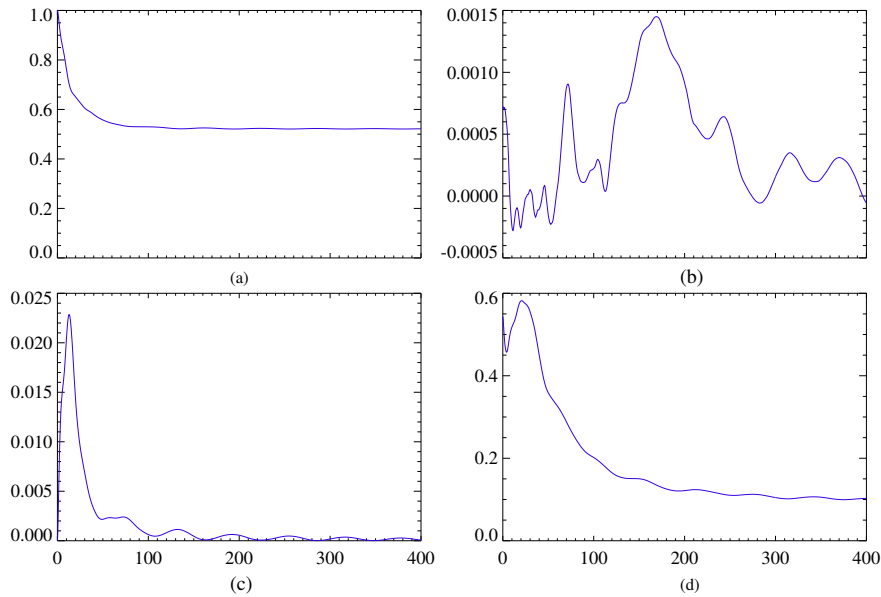


Figure 5.3: Evolution of the (a) magnetic energy, (b) field-aligned current density, (c) kinetic energy and (d) volume current density for the relaxation initiated with the magnetic field obtained by the sinusoidal deformation. The magnetic energy decays almost monotonically signifying relaxation of the magnetofluid. Both the energies attain a quasi-steady state from  $t \approx 100s$  onward. The first peak in the kinetic energy develops as the increase in flow velocity gets arrested by viscosity. Also important are the non-zero current density at the terminal state along with an overall decrease in the field-aligned current and hence, the twist; which is consistent with the decay of magnetic energy.

dynamics can be assessed from the history of the magnetic and kinetic energies plotted in Figs.-5.3(a) and 5.3(c). Important in both the plots is the attainment of a quasi-steady state from  $t \approx 100s$  onward. The average MFL twist (quantified by the field-aligned current) oscillates, Fig.-5.3(b). The evolution of MFLs depicted in Fig.-5.4 suggests that the formation of the 3D null (panel (f)) is due to a simultaneous coalesce of the three nulls in a (reverse) pitchfork bifurcation. The reconnections seen here can be inferred from the connectivity change of blue MFL from the panel (c) to (d). The MFL is identified by keeping the initial point for the field line integration fixed at every instant. The average current at the quasi-steady state is non-zero, Fig.-5.3(d), making this newly formed null different from the preceding current-free case. Incidentally, Parnell et al. (1997) considered an ideal fluid at the equilibrium, and by employing a linear perturbation analysis they have inferred that the Lorentz force cannot be balanced by a

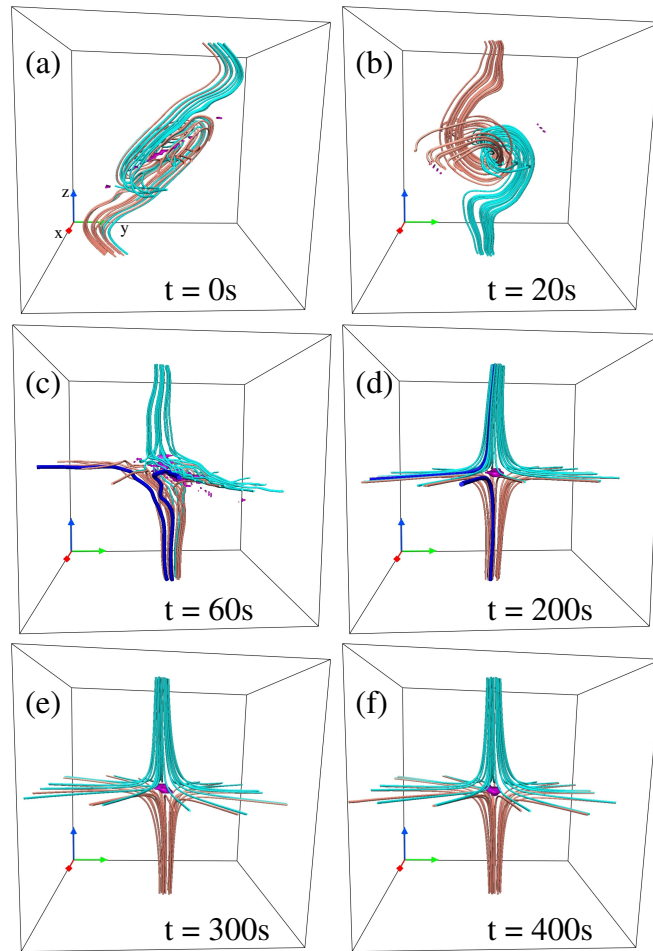


Figure 5.4: MFL evolution during the relaxation where the initial field was obtained by the sin flow deformation. Important is the generation of the null point and its fine-tuning across the panels (c)–(f) which belongs to the quasi-steady phase of evolution. The terminal null at the panel (f) is non-potential because of the non-zero volume current density. The change in connectivity of the blue MFL suggests occurrence of MR.

pressure gradient for a 3D null. Our findings do not necessarily contradict their result, because our simulation includes non-linear effects, and the fluid is not at equilibrium due to the viscous dissipation of kinetic energy along with the MR driven irrecoverable loss of magnetic energy. Nevertheless, the simulation also shows a decrease in current density with the progress of the quasi-steady state, thus offering the possibility of a complete decay of the current density with time.

### 5.1.2.2 Case-II, Relaxation of a chaotic magnetic field

The simulation is executed with  $64 \times 64 \times 64$  grid resolution with other model parameters and the boundary condition are being kept identical to the previous simulation. The coarse resolution is preferred to enhance MRs. The constant  $C$  is set to 0.2. To focus on ideas, three field lines, each starting from a different spatial location, are shown to generate three concentric local flux surfaces; panels (a)-(c) of Fig.-5.5. The MFLs tangential to each flux surfaces are regular. As shown in

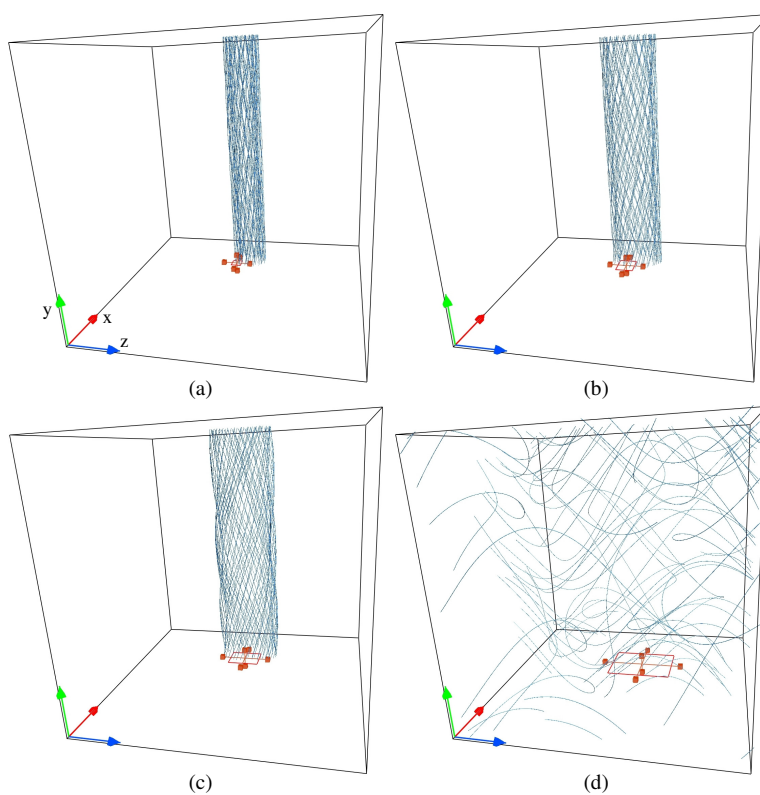


Figure 5.5: Panel (a) shows a single MFL ergodically spanning a local magnetic flux surface. Shifting the initial point for the MFL integration such as to increase the surface radius is documented in panels (b) and (c). After the attainment of a threshold radius, the flux surface is lost and the MFL becomes volume-filling as depicted in panel (d).

Kumar et al. (2017), with a shift in its initial location the MFL becomes chaotic and volume-filling; panel (d). The volume encompassed by the outermost closed flux surface then quantifies the regularity or periodicity of the MFLs. An increase in  $C \in \{0.1, 0.3\}$  decreases the above threshold volume and hence, increases the chaoticity of the MFLs (Kumar et al., 2017).

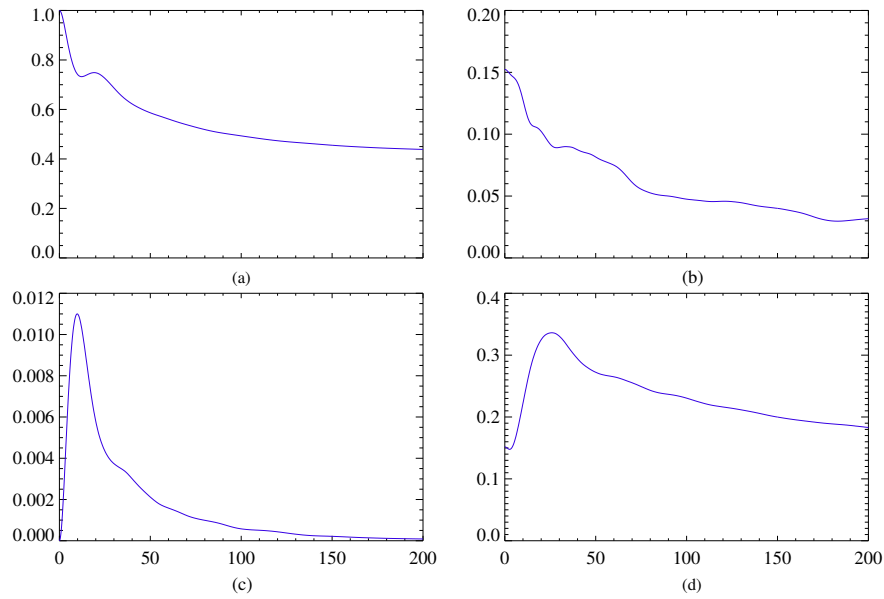


Figure 5.6: Evolution of (a) magnetic energy, (b) field-aligned current density, (c) kinetic energy and (d) volume current density for the relaxation initiated with the modified ABC magnetic field. The generation of the quasi-steady state is evident whereas the volume current density at the terminal state is non-zero.

The histories of the magnetic and kinetic energies are plotted in panels (a) and (c) of Fig.-5.6 showing attainment of the quasi-steady state from  $t \approx 150s$  onward. A decrease in the field-aligned current density (panel (b)) indicates a decrease in the MFL twist during the relaxation quantifying a substantial change in the global magnetic topology and frequent occurrence of MRs. The plot of the current density depicted in Fig.-5.6(d) suggests the magnetic field remains non-potential throughout its evolution. The overall MFL dynamics is illustrated in Fig.-5.7. In evolution, MRs manifest as changes in the field line connectivity. One such plausible change is demonstrated by the blue MFL in its passage from the panel (b) to (c) where the MFL is again identified by maintaining the initial point for the field line integration same at different instants. The nulls are drawn with the constants  $B_0 = 0.00001$  and  $d_0 = 0.0004$ , respectively. To gain further insight, in Fig.-5.8, we track the evolution of MFLs in the neighborhood of the nulls depicted in panel (d) of Fig.-5.7. The direction of the magnetic field is indicated by arrows while the oppositely directed spine pairs are colored cyan and peach for easy identification. The nulls found are of mixed topological degrees (+1 and -1) which approximately concurs with the invariance of the

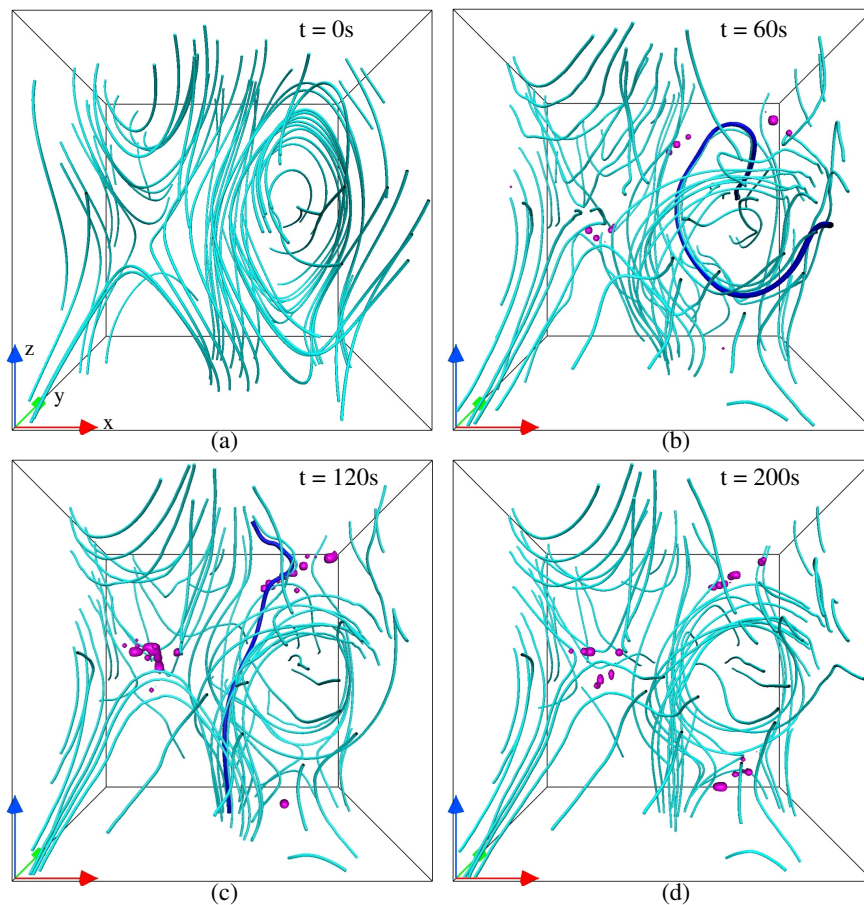


Figure 5.7: Overall evolution of MFLs as the fluid relaxes from the initial modified ABC field. The change in connectivity of the blue MFL, panels (b) and (c), showcases an instance of MR. Such MRs and the corresponding connectivity changes play a crucial role in the relaxation. The development of the 3D null spans from the panels (b) to (d).

overall topological degree. Such pair-generations occur at other instances too. Because the amplitude of  $C$  is proportional to the chaoticity of the MFLs, a series of low-resolution simulations is performed to assess the effect of  $C$  on the 3D null generation. The calculations are carried out on  $32 \times 32 \times 32$  grid with  $C = 0.1, 0.2$  and  $0.3$ . The values are restricted to  $0.3$  since auxiliary analyses found that a choice of  $C \gg A \approx B$  actually reduces the chaoticity. Current carrying nulls having mixed topological degrees appear in each of these simulations (not shown), confirming the null generation to be independent of the grid resolution and chaoticity.

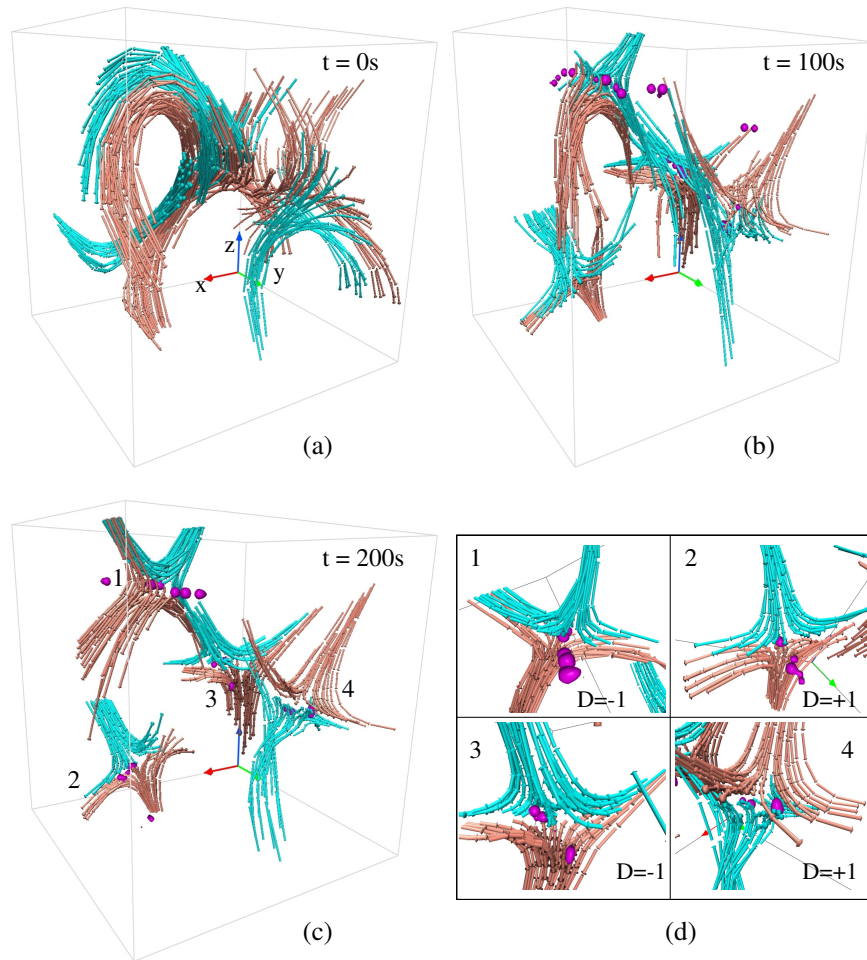


Figure 5.8: Evolution of MFLs in the neighborhood of the nulls depicted in panel (d) of Fig.-5.7. The arrowheads point the magnetic field directions. Notably, the nulls have both  $+1$  and  $-1$  topological degrees which suggest a conservation of net topological degree.

## 5.2 Magnetic reconnection in the Presence of 3D Null and QSL

To understand the interplay between different reconnection mechanisms, in the following we execute a simulation by analytically constructing a new initial magnetic field. The initial field is characterized by having two 3D magnetic nulls—morphologically similar to the ones observed in the solar corona, and QSLs. Additionally, the magnetic fields are envisaged to support the Lorentz force to naturally initiate dynamics without any prescribed boundary flow.

### 5.2.1 Initial Value Problems

To achieve a complex magnetic topology with 3D nulls and QSLs, the initial magnetic field is established by modifying the field in Kumar & Bhattacharyya (2017) based on the superposition of a constant vertical field over a LFFF, defined in a Cartesian domain. Particularly, to achieve a configuration consistent with solar coronal loops, the magnetic field is set to decay exponentially along the  $z$ -direction in the positive half-space  $\Gamma$  defined by ( $z \geq 0$ ). Consequently, the  $z = 0$  plane is treated as the photosphere. Moreover, the constant vertical magnetic field with straight MFLs is not likely to alter the topology of the LFFF appreciably and, hence, the superposed field  $\mathbf{B}$  is expected to be topologically similar to the unperturbed LFFF. Relevantly, the solar corona is thought to be in the state of force-free equilibrium under the approximation of a thermodynamic pressure that is negligibly small compared to the magnetic pressure (Priest, 2014).

As proposed, the initial magnetic field is derived by superposing a 3D LFFF  $\mathbf{B}_1$  and a uniform vertical field  $\mathbf{B}_2$ , where the components of  $\mathbf{B}_1$  are,

$$B_{1x} = \sin(x - y) \exp(-z), \quad (5.13)$$

$$B_{1y} = -\sin(x + y) \exp(-z), \quad (5.14)$$

$$B_{1z} = 2 \sin(x) \sin(y) \exp(-z). \quad (5.15)$$

The magnetic circulation per unit flux of  $\mathbf{B}_1$  has a value of unity and measures the twist of the corresponding MFLs (Parker, 1994; Kumar et al., 2014). The superposed field  $\mathbf{B}$  is

$$\mathbf{B} = \mathbf{B}_1 + c_0 \mathbf{B}_2, \quad (5.16)$$

where the superposition coefficient  $c_0$  relates the amplitudes of the two superposing fields and determines the deviation of  $\mathbf{B}$  from the force-free equilibrium (Kumar & Bhattacharyya, 2017). Explicitly,

$$B_x = \sin(x - y) \exp(-z), \quad (5.17)$$

$$B_y = -\sin(x + y) \exp(-z), \quad (5.18)$$

$$B_z = 2 \sin(x) \sin(y) \exp(-z) + c_0, \quad (5.19)$$

in the domain  $\Gamma$  which, physically extends from 0 to  $2\pi$  while having periodic and open boundaries in the lateral ( $x$  and  $y$ ) and the vertical directions, respectively. As the LFFF  $\mathbf{B}_1$  being exponentially decaying along  $z$ , all the three components of  $\mathbf{B}$  are also exponentially decaying functions along the vertical.

The Lorentz force is

$$\mathbf{J} \times \mathbf{B} = c_0(\mathbf{B}_1 \times \mathbf{B}_2) \quad (5.20)$$

which is non-zero for  $c_0 \neq 0$  and has the functional form

$$(\mathbf{J} \times \mathbf{B})_x = -c_0 \sin(x + y) \exp(-z), \quad (5.21)$$

$$(\mathbf{J} \times \mathbf{B})_y = -c_0 \sin(x - y) \exp(-z), \quad (5.22)$$

$$(\mathbf{J} \times \mathbf{B})_z = 0. \quad (5.23)$$

Clearly, the initial Lorentz force acts laterally. For the simulations, we select  $c_0 = 0.1$  and  $c_0 = 0.5$  to obtain two sets of initial magnetic fields with different magnitudes of Lorentz force—allowing us to assess the role of different dynamical evolution of the MFLs on the MRs.

To explore the geometrical similarity of the initial MFLs with the coronal MFLs, in Fig.-5.9 we depict the MFLs of  $\mathbf{B}$  for the cases  $c_0 = 0.1$  (panels (a) and (b)) and  $c_0 = 0.5$  (panels (c) and (d)). The figure shows a physical resemblance of the MFLs to the open and the closed coronal loops.

To carefully examine the magnetic topology of the initial field  $\mathbf{B}$ , first we plot neutral points in its transverse field (obtained by setting  $B_z = 0$  in  $\mathbf{B}$ ). Notably, in all relevant illustrations, the neutral point is depicted by using the numerical

technique documented in chapter 4 and Nayak et al. (2020). Fig.-5.10(a) shows the neutral points in the transverse field overlaid with corresponding field lines at  $z = 0$  plane. Notably, the field line geometry near these neutral points suggests that there are four spiral-type nulls (Lau & Finn, 1990) at  $(x, y) = (\pi/2, \pi/2)$ ,  $(\pi/2, 3\pi/2)$ ,  $(3\pi/2, \pi/2)$ ,  $(3\pi/2, 3\pi/2)$ , and one X-type null (Kumar et al., 2015b) at  $(x, y) = (\pi, \pi)$  inside the computational box. To further verify, we have checked that the eigenvalues for the X-type null are real  $(\sqrt{2}, -\sqrt{2})$  and, for the spiral nulls are complex numbers (for example the eigenvalues of a spiral null at  $(\pi/2, \pi/2)$  are  $(1 + i, 1 - i)$ ). In addition to these five nulls, there are eight X-type nulls at the boundaries of the domain. Relevantly, MRs can occur on separators with spiral-type as well as X-type neutral points in the perpendicular plane (Parnell et al., 2011). Next we note that the superposition of  $B_{1z}$  (Eq.-5.15) on the transverse field generates  $\mathbf{B}_1$ . In Fig.-5.10(b), we illustrate the magnetic nulls in  $\mathbf{B}_1$  overplotted with its MFLs. Nine X-type neutral lines are evident in  $\mathbf{B}_1$  which are co-located with the X-type nulls of the transverse field at  $z = 0$  plane. However, the four spiral nulls get destroyed in  $\mathbf{B}_1$ . To relate the location of the spiral nulls to the possible QSLs, we also plot the  $Q$ -map at the bottom boundary in Fig.-5.10(b) by using the code of Liu et al. (2016). Notably, the regions with large  $Q$ -values include both separatrices and QSLs (Titov et al., 2002). Important are the large  $Q$ -values at the locations of the spiral nulls (marked by black arrows in Fig.-5.10(b)), suggesting that some of the spiral nulls (of the transverse field) convert into the QSLs for  $\mathbf{B}_1$ .

To describe the topological structure of  $\mathbf{B}$ , in Fig.-5.11, we examine its magnetic skeleton by plotting magnetic nulls, separatrix surfaces and spines. The skeleton of  $\mathbf{B}$  is shown for the chosen  $c_0 = 0.1$  (panels (a) and (b)) and  $c_0 = 0.5$  (panels (c) and (d)). For  $c_0 = 0.1$ , the panels (a) and (b) of the figure confirm the presence of two 3D nulls located at the height  $z \approx 0.955\pi$  over the sites of the two spiral nulls (i.e., at  $(\pi/2, 3\pi/2)$  and  $(3\pi/2, \pi/2)$ ) of the transverse field. The 3D nulls have well-defined spine axes and dome-shaped separatrix or fan surfaces whose feet coincide with many of the regions of strong  $Q$  in Fig.-5.12. Similarly, for  $c_0 = 0.5$ , panels (c) and (d) of Fig.-5.11 show the existence of a pair of 3D nulls

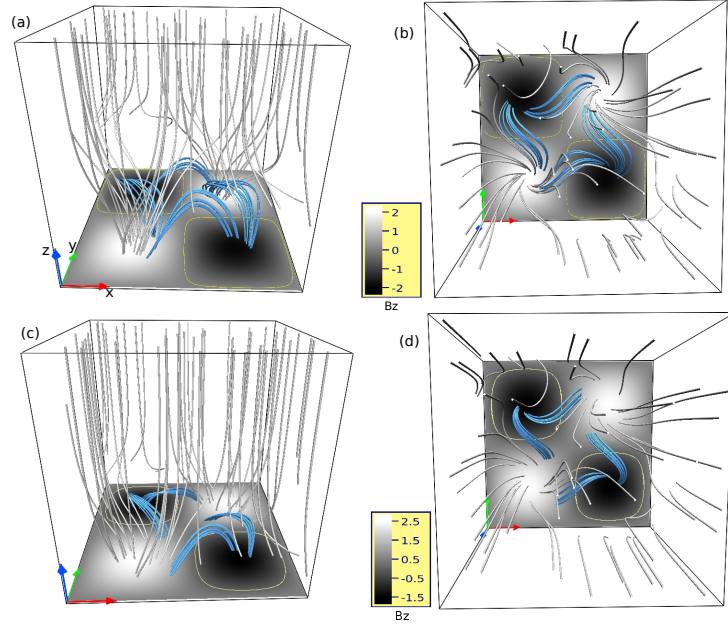


Figure 5.9: Side (panel (a)) and top (panel (b)) views of MFLs of the  $\mathbf{B}$  for  $c_0 = 0.1$ . While panels (c) and (d) illustrate side and top views of the MFLs for  $c_0 = 0.5$ . The MFLs are in the form of twisted closed (marked by navy blue color) as well as open magnetic loops (shown in grey color). All the panels are overplotted with  $B_z$  values on the  $z = 0$  plane. Yellow line represents the contour corresponding  $B_z = 0$ .

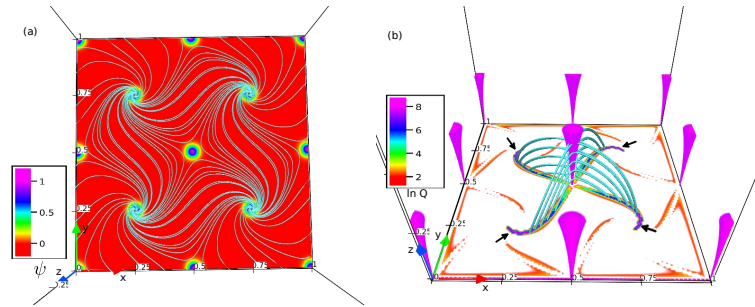


Figure 5.10: Panel (a) shows the neutral points and the field lines of the transverse field overlaid with the function  $\psi$  at  $z = 0$  plane. Large values of  $\psi$  represent the locations of neutral points. Notable is the existence of the nine X-type (one inside the domain and eight at the boundaries) and four spiral-type neutral points. Panel (b) depicts the magnetic nulls (in pink) and MFLs of  $\mathbf{B}_1$  overlaid with the corresponding  $Q$ -map at  $z = 0$ . The nine X-type neutral points of the transverse field also retain in  $\mathbf{B}_1$ . Noticeable is the larger values of  $Q$  near the sites of the spiral neutral points (marked by black arrows)—suggesting that the spiral neutral points correspond to QSLs in  $\mathbf{B}_1$ . In the figure, the domain size is marked as 1 instead of  $2\pi$  in all the directions.

over the two spiral nulls of the transverse field. The coordinates of the nulls are  $(x, y, z) \approx (\pi/2, 3\pi/2, 0.44\pi)$  and  $(3\pi/2, \pi/2, 0.44\pi)$ . We have also analytically

verified the locations of the nulls in  $\mathbf{B}$  which are  $(x, y, z) = (\pi/2, 3\pi/2, \ln(2/c_0))$  and  $(3\pi/2, \pi/2, \ln(2/c_0))$  for  $c_0 = 0.1$  and  $0.5$ —matching well with the locations obtained from the employed numerical technique. Importantly, for both cases, the overall morphology of the nulls is similar to the 3D nulls obtained with the extrapolated coronal fields (Longcope & Parnell, 2009; Platten et al., 2014; Prasad et al., 2018; Nayak et al., 2019; Prasad et al., 2020). The MFLs constituting the dome-shaped separatrix surfaces predominately intersect the bottom boundary and the intersection points, or the footpoints, trace nearly-closed circular curves—further advocating the similarity.

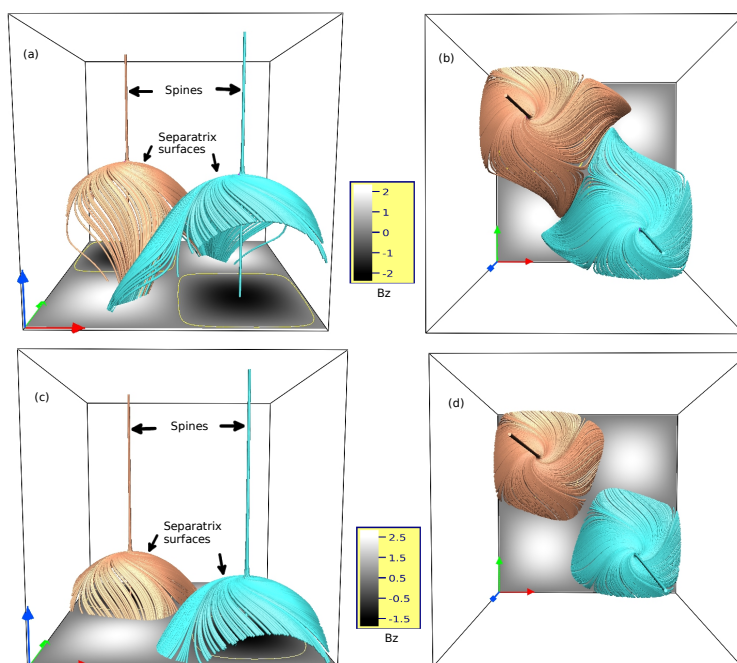


Figure 5.11: Magnetic (topological) skeleton of the initial field  $\mathbf{B}$  in terms of 3D nulls, separatrix surfaces and spines for  $c_0 = 0.1$  (side view in panel (a) and top view in panel (b)) and  $c_0 = 0.5$  (side view in panel (c) and top view in panel (d)). Notable are straight spine axes and the dome-shaped separatrix or fan surfaces (intersecting bottom boundary) of the nulls. For  $c_0 = 0.1$ , the separatrix domes touch at the base of the quasi-separator at  $(\pi, \pi, 0)$  (panel (b)). For  $c_0 = 0.5$ , the separatrix domes are separate (panel (d)).

Additionally, as shown in Fig.-5.11, the 3D nulls are located at higher heights and, therefore, their separatrix domes are larger for  $c_0 = 0.1$  than  $0.5$ . Fig.-5.11(b) demonstrates that, from a top view, the separatrix surfaces of the 3D nulls for  $c_0 = 0.1$  seem to touch in the vicinity of the points  $(x, y) = (\pi, \pi)$  along

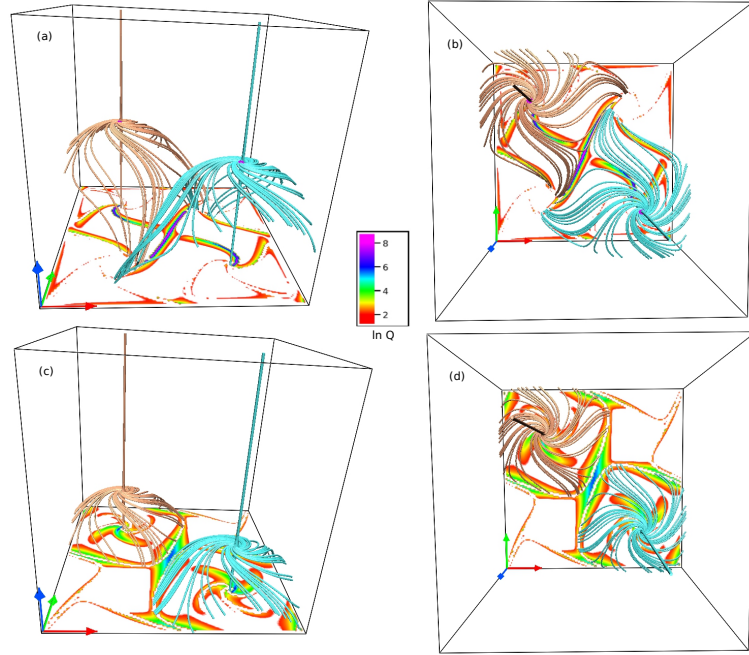


Figure 5.12: The structural skeleton (i.e., the separatrix skeleton plus the QSL quasi-skeleton) of  $\mathbf{B}$  with the bottom boundary being superimposed with  $\ln Q$  for  $c_0 = 0.1$  (side and top views in panels (a) and (b)) and  $c_0 = 0.5$  (side and top views in panels (c) and (d)). The existence of large  $Q$  (such that  $\ln Q \in \{2, 8\}$ ) represents the location of separatrices or QSLs. For both  $c_0$  values, notable is the presence of both the separatrices of the coronal nulls and also the QSLs associated with the central quasi-separator at  $(\pi, \pi, z)$  and the extra quasi-separators on the boundary. Also interesting is the larger  $Q$  values for  $c_0 = 0.1$  than  $0.5$  at the central quasi-separator at  $(\pi, \pi, z)$ .

$z$  and, as a result, the geometry of the MFLs in the vicinity is resembling to a quasi-separator (or Hyperbolic Flux Tube). The neutral X-line  $(\pi, \pi, z)$  of  $\mathbf{B}_1$  (see Fig.-5.10(b)) turns into the quasi-separator when the vertical field  $\mathbf{B}_2$  is added. To further confirm, we expand components of  $\mathbf{B}$  in a Taylor series in the immediate vicinity of  $x = \pi, y = \pi, z = 0$  to get

$$B_x = x - y, \quad (5.24)$$

$$B_y = -(x + y) + 2\pi, \quad (5.25)$$

$$B_z = c_0, \quad (5.26)$$

which attest the absence of the X-type null at  $(x, y, z) = (\pi, \pi, 0)$ . However, for

both  $c_0 = 0.5$  and  $0.1$  the nearby geometry is that of a Hyperbolic Flux Tube. Interesting is the orientation of the MFLs of the hyperbolic flux tube for  $c_0 = 0.1$ , which is expected to be favorable for initiating MRs. In comparison to  $c_0 = 0.1$  case, the magnitude of  $\mathbf{B}_2$  is larger for  $c_0 = 0.5$  case and, consequently, the corresponding separatrix dome surfaces are separate—leading to the elimination of the favorable orientation in this case (see Fig.-5.11(d)).

For further investigation, in Fig.-5.12 we illustrate the topological skeleton of  $\mathbf{B}$  overlaid with the  $Q$ -map at the bottom boundary for both  $c_0 = 0.1$  (panels (a) and (b)) and  $c_0 = 0.5$  (panels (c) and (d)). Note that for both the cases, large  $Q$  exists at the central region near the point  $(\pi, \pi, 0)$ . The presence of the large  $Q$  suggests that a X-line (i.e., a line of X-points in  $z$ -constant planes) located along  $(\pi, \pi, z)$  (see Fig.-5.10) converts into a quasi-separator (or hyperbolic flux tube) by the addition of the constant vertical field  $c_0\mathbf{B}_2$  to  $\mathbf{B}_1$ . Noticeably, because of a smaller  $c_0$ , the  $Q$  values in the central region are higher for  $c_0 = 0.1$  in comparison to  $c_0 = 0.5$ —indicating a more favorable location for reconnection provided the flows are appropriate. Moreover, the large  $Q$  values near the boundaries for  $\mathbf{B}$  (Fig.-5.12) are almost co-spatial with the rest of the X-type neutral lines of  $\mathbf{B}_1$  (and the X-type neutral points of the transverse field) located at boundaries (Fig.-5.10)—indicating toward the transformation of all the neutral lines into QSLs. In addition, in the initial field  $\mathbf{B}$ , unlike  $\mathbf{B}_1$ , QSLs seem to be absent over the two spiral nulls of the transverse field located at  $(\pi/2, \pi/2, z)$  and  $(3\pi/2, 3\pi/2, z)$ . The absence can be attributed to the addition of the constant field  $\mathbf{B}_2$  to  $\mathbf{B}_1$ . From Figs.-5.12(a) and (b), we also note the existence of large  $Q$  values near the footpoints of the MFLs of the separatrix dome surfaces for  $c_0 = 0.1$ . Similarly, Figs.-5.12(c) and (d) show the presence of the contours of large  $Q$  approximately co-located with inner and outer vicinity of the foot-points of the dome separatrices for the case  $c_0 = 0.5$ . Relevantly, Titov (2007) suggested that the QSLs determine the quasi-skeleton of a magnetic field and one can define the structural skeleton which is the sum of the topological skeleton and the quasi-skeleton. Hence, Fig.-5.12 plots the structural skeleton of the initial field  $\mathbf{B}$ .

Based on the above analysis, overall, the selected initial magnetic fields can be divided into two broad categories. The first one (belonging to  $c_0 = 0.5$ ) supports a relatively simpler topology with a pair of coronal 3D nulls located at low heights and a central quasi-separator. The corresponding separatrix surfaces do not touch to each-other and, hence, are independent. While the second one (corresponding to  $c_0 = 0.1$ ) also contains a pair of 3D nulls and a central quasi-separator. But, for this case, the coronal nulls are situated at greater heights and the separatrix surfaces appear to interact with the larger  $Q$  values in the central region of the computational domain—making the case more suitable for QSL reconnection in addition to the null point reconnection at the coronal nulls. This further justifies the selection of the two particular  $c_0$  values.

### 5.2.2 Simulation Results and Discussions

The presented simulations are governed by the Eqs.-4.2a-4.2d. The size of the computational box is spanned  $128 \times 128 \times 128$  grids in  $x$ ,  $y$  and  $z$ -directions, resolving the domain  $\Gamma$ . The initial states are characterized by the magnetic field  $\mathbf{B}$  given by equations (5.17)-(5.19) and the velocity field  $\mathbf{v} = 0$ . Simulations are performed with  $c_0 = 0.1$  and  $0.5$ . The lateral boundaries ( $x$  and  $y$ ) are chosen to be periodic, while magnetic fluxes at the vertical boundaries are kept fixed to zero (Kumar et al., 2015a). At the bottom boundary, the  $z$ -components of  $\mathbf{B}$  and  $\mathbf{v}$  are kept fixed to their initial values (line-tied boundary condition). In the conducted simulations, the dimensionless coefficient  $\tau_a/\tau_\nu \approx 10^{-4}$ , which is roughly one orders of magnitude larger than its coronal value (Prasad et al., 2018). The larger  $\tau_a/\tau_\nu$ , however, is expected to only speed-up the evolution without an effect on the corresponding change in the topology of MFLs. The initial Lorentz force pushes the plasma from the initial static state and imparts dynamics. To examine the onset of MRs, in the following, we analyze the evolution of the two sets  $c_0 = 0.1$  and  $0.5$  separately. For  $c_0 = 0.5$ , the 3D nulls are located at lower heights and the corresponding separatrix domes are fairly independent (see Fig.-5.11). Therefore, we first consider this case.

### 5.2.2.1 Set I, $c_0 = 0.5$

Here, the initial magnetic field which consists a pair of 3D nulls and a central quasi-separator. For a careful inspection of the simulated dynamics, in Fig.-5.13, we first present the evolution of the transverse field overlaid with the plasma flow (projected at  $z = 0$  plane) and the Lorentz force at the bottom boundary. Notable are the reversal of the direction of initial Lorentz force (marked by red color) with generation of rotational flow (in green color) around the spiral nulls in the early phase of evolution.

Fig.-5.14 shows the time sequences of the magnetic skeleton of the initial field  $\mathbf{B}$  (Fig.-5.11). From Fig.-5.14, notable is the rotation of the separatrix domes of the 3D nulls. In the figure, black arrows and motion of the blue MFLs clearly mark the direction of the rotation. The rotation appears to be initiated by the Lorentz force after  $t = 3.2s$  (see Figs.-5.13 and 5.14(a)). Initially, the rotation is in clockwise direction (Fig.-5.14(b)). This increases the twist and hence, the tension in the MFLs of the separatrix domes (panel (c)). Eventually, the magnetic tension changes the direction of rotation and the MFLs rotate in counter-clockwise direction (panel (d)). The twist of the MFLs then decreases with time. Such twisting and untwisting rotational motion of the MFLs is expected to repeat in time and, ultimately, get damped by the viscous drag force.

To investigate the MRs at the 3D nulls, the time evolution of the spine and the separatrix fan surface of a 3D null located at  $(3\pi/2, \pi/2, 0.44\pi)$  is shown in Fig.-5.15. In the figure, we also plot two sets of MFLs (in yellow) which are situated under the dome-shaped fan surface at  $t = 0s$ . Moreover, to demonstrate the current sheet formation, we overlay the figure with iso-surfaces of current density  $|\mathbf{J}|$  having an iso-value which is 70% of the maximal value of  $|\mathbf{J}|$ . The selection of the iso-value is based on an optimization of constructing a smooth and identifiable iso-surface with a large iso-value. We call these iso-surfaces  $J - 70$  and identify them as the CSs because they are 2D manifolds and not the boundaries of 3D volumes. Notably, the yellow MFLs do not appear to co-rotate with the MFLs of the fan surface (as evident from the motion of the blue MFL). This seems to generate favorable contortion in the MFLs—making the yellow

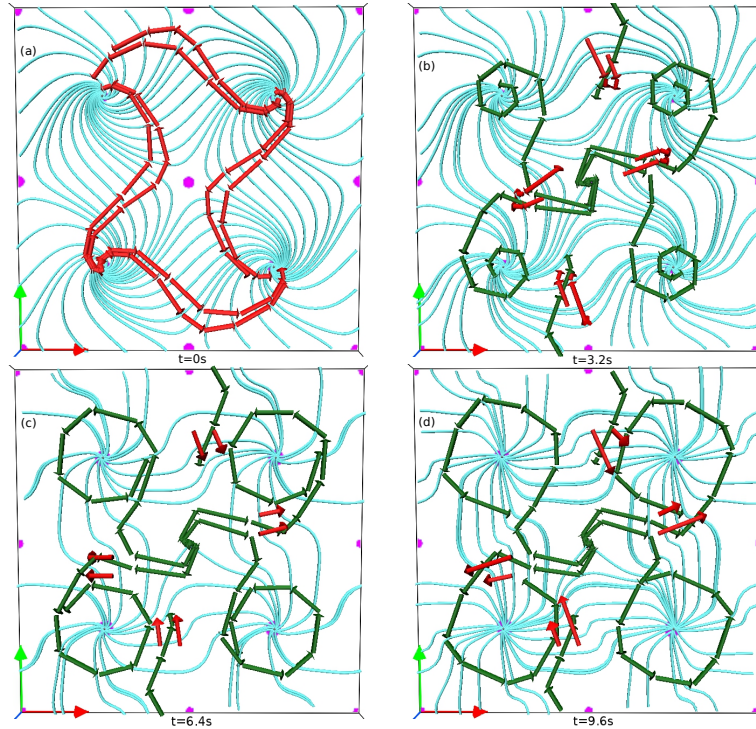


Figure 5.13: Evolution of field lines of the transverse field (in cyan color) at  $z = 0$  plane for  $c_0 = 0.5$ . The figure is further overplotted with the streamlines of the flow (in green color), Lorentz force (red arrows) and, the neutral points (in pink).

MFLs and the MFLs of the fan, non-parallel. Consequently, the CSs develop in the vicinity of the fan surface (panel (b)). In addition, the yellow MFLs rise toward the 3D null and, eventually come out of the dome. This is a clear indication of the change in connectivities of the yellow MFLs, suggesting the occurrence of torsional fan reconnections at the 3D null (Priest & Pontin, 2009; Pontin et al., 2013). With reconnections, the CSs dissipate and the contortion in the MFLs decrease with time (panel (d)). Similar evolution is found for the other 3D null.

Fig.-5.16 depicts the time profile of the  $Q$ -map at the bottom boundary overlaid with the 3D nulls. To locate the QSLs, we plot the skeleton of the separatrix surfaces and, then the extra features in the  $Q$ -map (marked by QL in Fig.-5.16(a)) are identified as the QSLs (also shown in Fig.-5.12). Relevantly, as mentioned in Section 2, these QSLs correspond to the X-type nulls of the transverse field (see Figs.-5.10 and 5.13). To explore the possibility of reconnections near the

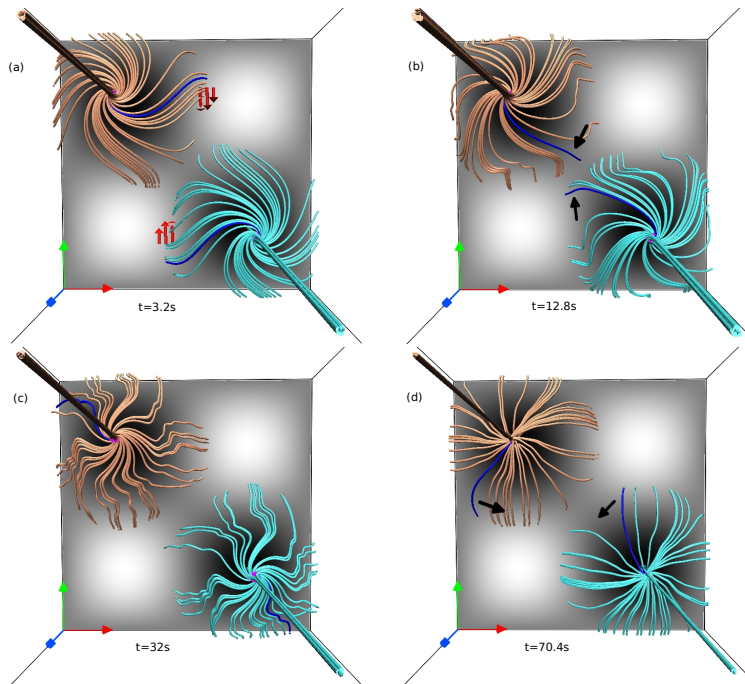


Figure 5.14: Evolution of the topological skeleton of  $\mathbf{B}$  for  $c_0 = 0.5$  (Figs.-5.10(c) and (d)). Panel (a) is overlaid with Lorentz force (red arrows) at the bottom boundary. The rotation of the separatrix surfaces is evident from the movement of the blue MFLs (further marked by black arrows).

QSLs, Fig.-5.16 is overlaid with plasma flow (green arrows) near the regions of three QSLs marked by rectangular boxes in Fig.-5.16(a), as representative cases. Additionally, the current density  $|\mathbf{J}|$  having values around 35% of its maximal value are plotted on a  $z$ -constant plane (in pink) situated near the bottom boundary. Notably, the direction of plasma flow (green arrows) is visibly different from the direction of the motion of MFLs (showcased by the blue MFLs) in the vicinity of the separatrices—a telltale sign of the flipping or slipping of field lines (Priest & Forbes, 1992; Aulanier et al., 2006; Janvier, 2017). Moreover, with time, the currents start to appear near the fan separatrix regions (although remains negligible at  $(\pi, \pi, 0)$ )—further supporting the CS development and the onset of the reconnections in the vicinity of the separatrices. Under the simulated viscous relaxation, such appearances of the CSs can be attributed to the autonomous development of the favorable forcing (Kumar et al., 2015b). However, the strength of the currents near QSLs is almost half of the strength at the fan surfaces of the 3D nulls (Fig.-5.15)—indicating the reconnections near QSLs

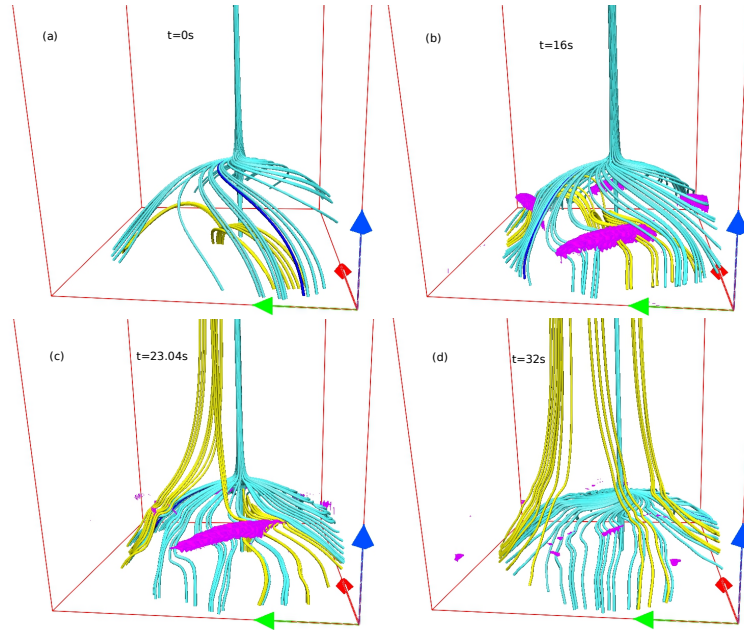


Figure 5.15: Evolution of a 3D null along with the fan surface (represented by cyan MFLs) for  $c_0 = 0.5$ . The figure is further overplotted with two sets of MFLs (in yellow) situated below the dome and the  $J - 70$  surfaces (in pink). The movement of MFLs of the dome is marked by a blue MFL. Important are the appearances of the  $J - 70$  surfaces at the fan surface and change in the connectivities of the yellow MFLs.

to be less energetically efficient than the 3D nulls. This supports the proposal of Priest & Forbes (1989, 1992) that the more efficient reconnections require the favorable geometry of MLFs (such as separatrix, QSL, null or separator) as well as the favorable flows. It appears that both are present at the 3D nulls, while the favorable flow is missing in the case of the QSL around the point  $(\pi, \pi, 0)$ .

### 5.2.2.2 Set II, $c_0 = 0.1$

As found in the initial field, the 3D nulls for this case are located at greater heights in comparison to  $c_0 = 0.5$  and the separatrix surfaces touch in the central region that is located around the line  $(\pi, \pi, z)$ —leading to an MFL geometry favorable to MRs. Fig.-5.17 depicts the time sequences of the field lines of the transverse field during their evolution. The figure also plots plasma flow (denoted by green arrows) projected on the lower boundary and the Lorentz force (marked by red arrows). Noticeably, in response to the initial Lorentz force, a rotational flow is produced near the spiral nulls of the transverse field.

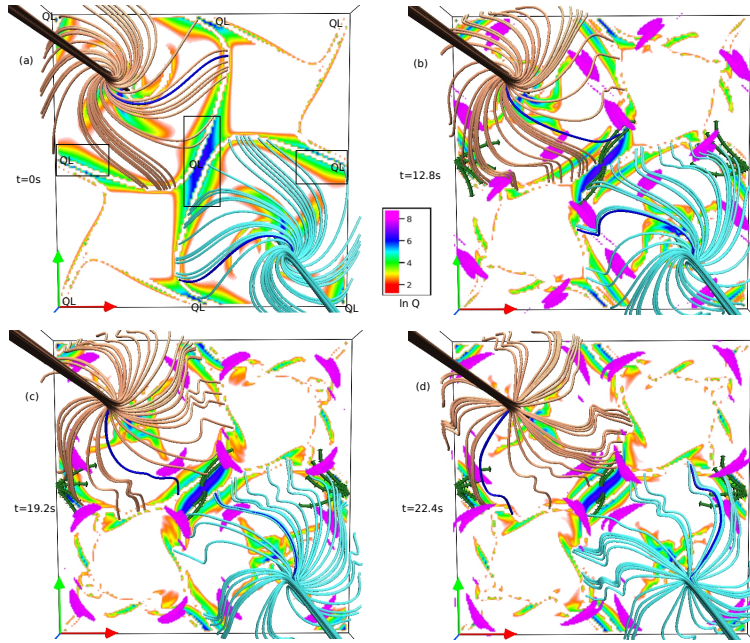


Figure 5.16: Evolution of 3D nulls with bottom boundary being overplotted with  $\ln Q$  ( $c_0 = 0.5$ ). The regions of strong  $Q$  in the initial field are marked by QL in panel (a). We also plot the streamlines of plasma flow (green arrows) near the three QSLs marked by rectangular boxes in panel (a), some of which are separatrices. Currents having sufficiently high values are shown at a  $z$ -constant plane (in pink). The motion of the dome MFLs is depicted from the blue MFLs. The direction of the MFLs movement is largely different from the flow direction—manifesting the flipping MFLs in the separatrices and QSLs.

To have an overall understanding of the dynamics, in Fig.-5.18, we show the time sequences of the topological skeleton in the forms of the 3D nulls and the corresponding spines and separatrix surfaces. The initial Lorentz force (marked by red arrows in panel (a)) appears to push the footpoints of the separatrix domes and initiate the rotational motion of the domes (also evident from Fig.-5.17). When viewed from the top, the rotation is in counter-clockwise direction—illustrated by the blue MFLs and black arrows. Similar to the case of  $c_0 = 0.5$ , it enhances the twist and, consequently, magnetic tension in the MFLs (see Fig.-5.18(c)) which, finally, reverses the direction of rotation in clockwise direction (cf. Fig.-5.18(d)). The rotational motion is found to oscillate in time and eventually gets damped by the viscosity.

To explore the initiation of MRs at the 3D nulls, in Fig.-5.19, we display the evolution of a 3D null situated at  $(3\pi/2, \pi/2, 0.955\pi)$  along with the correspond-

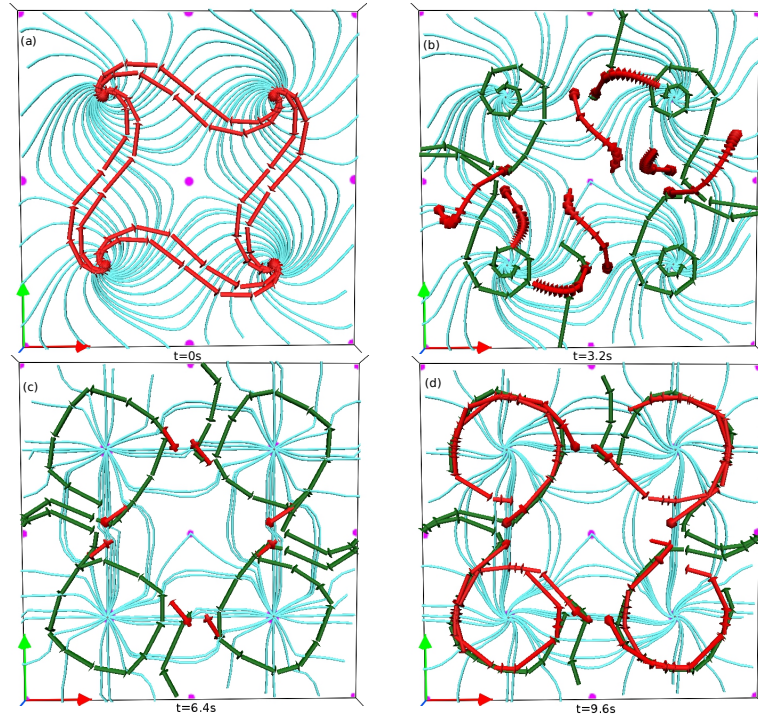


Figure 5.17: Time sequences of the transverse field (in cyan color) at the bottom boundary for  $c_0 = 0.1$ . The flow (green arrows), the Lorentz force (red arrows) and the neutral points (in pink) are also overlotted in the figure.

ing separatrix surface. The figure is further overlaid with the  $J - 70$  surfaces and two sets of magnetic loops of different heights, initially located under the separatrix dome. Importantly, in this case, the CSs appear to form below the dome surface and, then extend toward the dome (marked by black arrows in Fig.-5.19(c)). The figure indicates that the initially parallel yellow and green loops become increasingly non-parallel and lead to the CS formation. To confirm this, in Fig.-5.20, we analyze the evolution of MFLs in the vicinity of a  $J - 70$  surface. At  $t = 0s$ , the MFLs are in the form of two different loop systems situated at two different heights (Fig.-5.20(a)). The corresponding MFLs at lower and higher heights are marked by colors green and yellow respectively. The arrowheads represent the directions of the MFLs. These initially parallel MFLs start to become non-parallel from  $t \approx 10s$  onward, ultimately leading to the appearance of the  $J - 70$  surface and its subsequent spatial extension. Such spontaneous development of CSs is in accordance with the Parker's magnetostatic theorem. Further, from Fig.-5.19, as the CSs approach the separatrix surface, the yellow

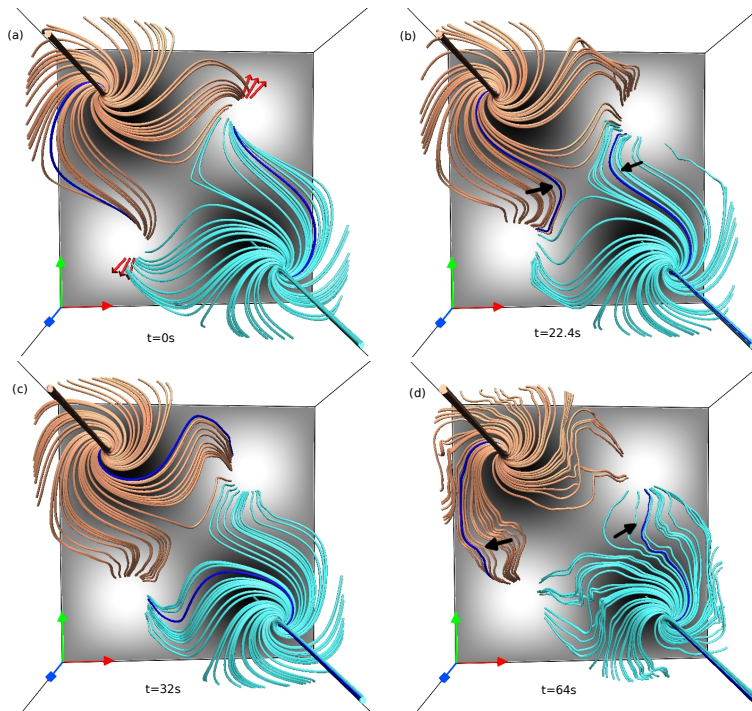


Figure 5.18: Time profile of the magnetic skeleton (3D nulls, separatrix dome surfaces and spines) of  $\mathbf{B}$  for  $c_0 = 0.1$  (see Figs.-5.10(a) and (b)). Red arrows in panel (a) show the direction of Lorentz force at the lower boundary. Evident is rotational motion of the separatrix domes, as illustrated by the blue MFLs and black arrows.

MFLs move toward the 3D null and change their connectivities from the inner to the outer connectivity domain. This reveals the onset of the MRs at the 3D null. Identical dynamics is realized for the other 3D null also (not shown).

Further, to explore the possibility of the reconnections at the QSLs, we show the time evolution of the topological skeleton superimposed with the  $Q$ -map at the bottom boundary in Fig.-5.21. To keep the presentation tidy, we focus only on the QSL located around the line  $(\pi, \pi, z)$  as a representative case. For this case, the domes almost touch each-other and result-in a favorable MFL geometry around the line (Fig.-5.11). To clearly illustrate this, in Fig.-5.21, we further plot two sets of MFLs (in colors purple and green) near the line. Moreover, the plasma flow (white arrows), tangential to the  $z = 0$  plane, is depicted in the vicinity of the QSL location. Notably, at  $t = 0s$ , the geometry of the purple and green MFLs is what is expected for a quasi-separator or hyperbolic flux tube. Under the favorable initial Lorentz force (marked by red arrows in panel (a)),

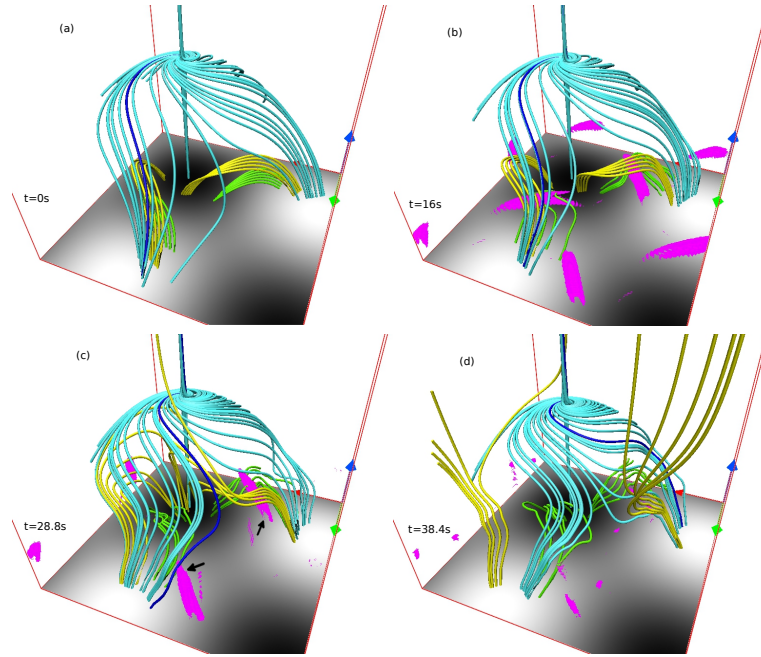


Figure 5.19: Time evolution of a 3D null with the fan surface and spine (denoted by cyan MFLs) for  $c_0 = 0.1$ . The figure is further overlaid with two sets of magnetic loops located at different heights (in colors green and yellow) under the fan surface at  $t = 0s$  and, the  $J - 70$  surfaces (in pink). The motion of dome MFLs can be tracked by a blue MFL. Notable are the appearances of the  $J - 70$  surfaces inside the fan surface which later extend toward the fan (marked by black arrows in panel (c)). With time, the yellow MFLs change their connectivities.

the oppositely directed purple and green MFLs are pushed toward each other. With time, the MFLs appear to change their connectivities, as evident from the panels (b)-(d) of the figure. This is a marker of reconnections, which repeat in time, near the QSL. The post-reconnection MFLs move away from central region around the line  $(\pi, \pi, z)$  because of the plasma flow (panel (d)). Here also, like  $c_0 = 0.5$ , the CSs develop near the QSL location (not shown). For  $c_0 = 0.1$ , the rotating separatrix domes being in close proximity, interact rather strongly about the  $(\pi, \pi, z)$  line and cause the reconnections at the QSL that are more prominent in comparison to the case  $c_0 = 0.5$ . Identical dynamical evolution is observed near the other QSLs located above the X-type nulls of the transverse field (Fig.-5.10(a)) for  $c_0 = 0.1$  which is not presented here.

To have an overall comparison of the dynamics for  $c_0 = 0.5$  and  $c_0 = 0.1$ , in Fig.-5.22, the histories of kinetic and magnetic energies (normalized to the corresponding initial total energies) are plotted for  $c_0 = 0.1$  and  $0.5$ . For both the

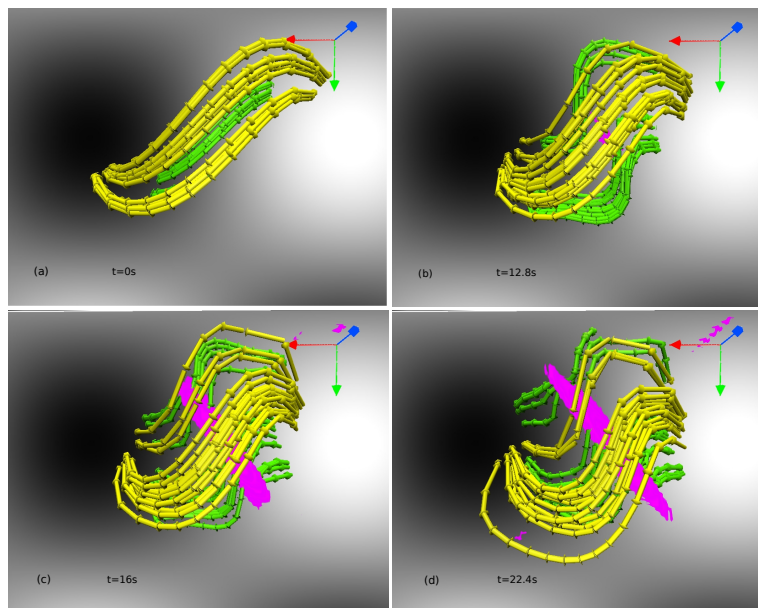


Figure 5.20: Time evolution of MFLs in the vicinity of a  $J - 70$  surface for  $c_0 = 0.1$ . Initially, the MFLs are in form of closed parallel loops situated at two different heights (panel (a)). As time progresses, the loops become increasingly non-parallel, resulting in the formation of CS.

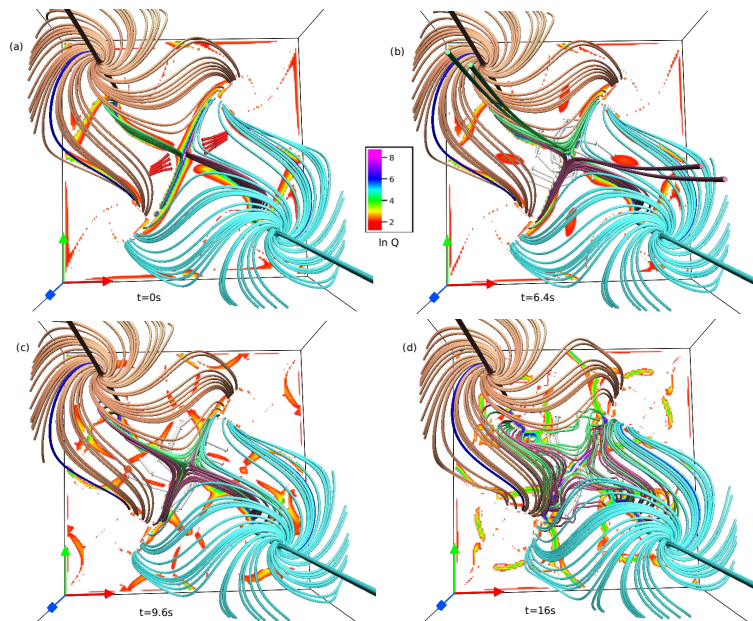


Figure 5.21: Time profile of 3D nulls with  $\ln Q$  being superimposed at the lower boundary for  $c_0 = 0.1$ . Two sets of MFLs (in colors purple and green) are plotted near the QSL located in the central region around  $(\pi, \pi, z)$ . The figure also shows the streamlines of plasma flow (grey arrows) and initial Lorentz force (red arrows) near the QSL. Notable is the change in the topology of the purple and green MFLs.

cases, the plasma flow is generated via the corresponding initial Lorentz force and the MRs. Subsequently, the flow gets arrested by the viscous drag, leading to the formation of peaks in kinetic energy plots. From Eq.-5.20, evident is the larger magnitude of the Lorentz force for  $c_0 = 0.5$  than  $c_0 = 0.1$ . Although, the height of kinetic energy peaks for  $c_0 = 0.1$  is greater in comparison to  $c_0 = 0.5$  (top panel of Fig.-5.22). In addition, the depletion of the magnetic energy is larger for  $c_0 = 0.1$  (around 24% from its initial value) than  $c_0 = 0.5$  (approximately 10% from the corresponding initial value), as shown in the bottom panel of Fig.-5.22. The higher peak height of the kinetic energy and larger decay of the magnetic energy for  $c_0 = 0.1$  case (along with a lower magnitude of initial Lorentz force) indicate that the MRs for  $c_0 = 0.1$  case are more energetically efficient and generate stronger flow than  $c_0 = 0.5$  case. We note that, with an identical MFL geometry in the vicinity of the 3D nulls, reconnections at the 3D nulls are expected to be similar for both the cases. Then, the reconnections at the QSLs for  $c_0 = 0.1$  are expected to be more energetically efficient than the ones for  $c_0 = 0.5$ . This can be attributed to the existence of the more favorable MFL geometry and flow near the QSLs (as illustrated near the central region around  $(\pi, \pi, z)$ ) for  $c_0 = 0.1$  than  $c_0 = 0.5$  (Kumar et al., 2015b).

### 5.3 Inferences

The presented simulations make the concept of spontaneous generation of 3D nulls in nature credible. An extension of the idea to the solar corona is interesting. The quiescent corona, being in approximate equilibrium, is expected to have 3D nulls. The slow photospheric motion deforms the anchored field lines, increasing their magnetic energy and eventually attaining a state favorable for MRs. The motion, being at a rate much slower than the coronal reconnection, can be neglected and with no loss of generality the field lines can be idealized to be in a steady state just prior to an eruptive event. Consequently, during the eruptive event a monotonic decay of magnetic energy is assured which leads to secondary 3D nulls, and the whole process repeats itself culminating into repeated

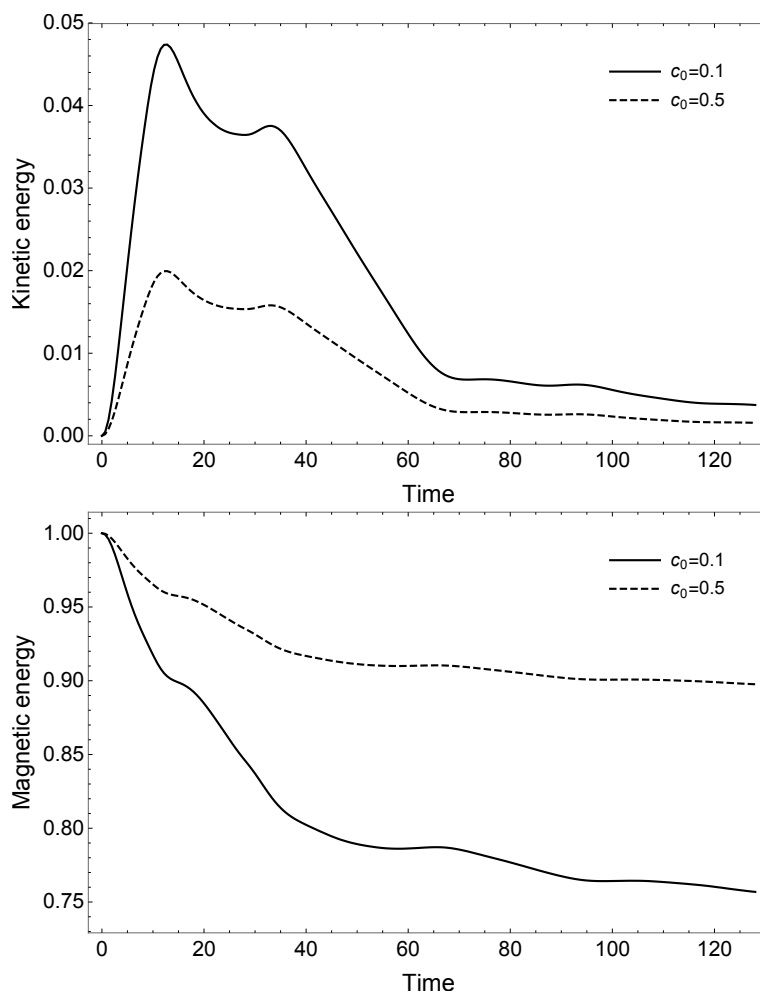


Figure 5.22: Histories of kinetic (top panel) and magnetic (bottom panel) energies for  $c_0 = 0.1$  and  $c_0 = 0.5$ . The solid line is for  $c_0 = 0.1$ , while the dashed line corresponds to  $c_0 = 0.5$ . The energies are normalized to the initial total energies. Notable is the higher height of the peaks in the kinetic energy and the larger decay of the magnetic energy for  $c_0 = 0.1$  than  $c_0 = 0.5$ .

reconnections. Such repeated reconnections can influence the coronal dynamics. Admittedly, these inferences are based on a limited number of case studies that only concur with the idea rather than providing a rigorous proof. However, having the ubiquity of 3D nulls in an equilibrium magnetofluid is thought-provoking and merits further attention.

Then, the mere presence of QSLs in initial field is not sufficient to initiate energetically efficient reconnections. The nature and magnitude of the flow is equally crucial in commencing such reconnections. Noticeably, the presented simulations identify the rotation of the MFLs associated with the dome-shaped

---

fan surfaces of the 3D nulls—also observed in the solar corona. Interestingly, under similar magnetic configuration used in the simulations, a physical scenario can be envisioned in which the charged particles accelerated through MRs at 3D nulls located in the corona can move along the MFLs of dome-shaped fan surfaces and potentially cause the observed circular brightening in the denser lower solar atmosphere during solar flares. In addition, the spontaneous development of the CSs can be crucial to the coronal heating.



# Chapter 6

## Summary and Future Scopes

### 6.1 Summary of The Thesis Work

The thesis explores the role of magnetic field and electric current in relation to magnetic reconnections which, are primarily responsible for the solar transients. Abundant observational evidences document the importance of magnetic topology at the sites of reconnection in piling up and releasing the magnetic energy while driving the transients. Specifically, the active region transients are crucial because of their impact on space weather and are routinely observed in high spatial and temporal resolutions.

Over the years, attempts are made to obtain the coronal magnetic field by an indirect approach—the extrapolation techniques. Several algorithms have been devised to model the coronal magnetic field using the state-of-the-art photospheric vector magnetograms. Standalone numerical simulations have also been performed to understand the dynamics during the activities.

In the above backdrop, the focus of the thesis is to study magnetic topology responsible for reconnection in different solar transients, varying temporally and spatially over large ranges. The topologies are identified by using the non-force-free-field extrapolation model for the corona. The advantage in using this model is its ability to mimic the real corona where Lorentz force is non-zero on the photosphere but drops sharply with height. The photospheric magnetogram data from HMI/SDO are employed for extrapolations reported in the thesis. The ex-

extrapolated magnetic field lines are also compared with the observational features extracted from AIA/SDO to add further credibility. In the extrapolated field, we find the presence of different magnetic topologies viz. magnetic null points, QSLs, magnetic flux ropes near the vicinity of the transients. Primarily the reconnection onsets at the null points and quasi-separatrix layers, subsequently sustaining the transients. Notable is the good quantitative and qualitative correlation between the extrapolated and the observed magnetic structures.

To understand the topological evolution during the events, MHD simulations are carried out. For the purpose, we have utilized the well established magnetohydrodynamic code, EULAG-MHD model. The simulation is started with the extrapolated field and the non-zero Lorentz force drives the plasma to generate mass flow. The evolution relaxes to a terminal quasi-steady state by dissipating magnetic and kinetic energies via reconnection and viscous dissipation. The simulation covers the duration from start time to end time of all the events. The findings from the data-constrained simulations are condensed below.

1. In the study of a blowout jet, the eruption in the simulation is caused by the presence of null points and flux rope (mini-filament) that excellently matches with the existing conjecture for a blowout jet model. Whereas, the flare occurring possibly simultaneously is the result of reconnection near the null point and quasi-separatrix layer.
2. The study of an eruptive X-class flare highlights the effect of a complex and multiple flux system on the reconnection process. Most of the observed aspects are captured profoundly by both the extrapolation and the corresponding simulated dynamics.
3. In the case of a circular flare ribbon, we again find a 3D null point in the proximity of the flaring region in the extrapolation. The corresponding simulation successfully explains the genesis of the the flare and flare ribbon by exhibiting the dynamics of the field lines topology associated to the null point.

The extrapolation and simulation of transients not only explain the observed phenomena but also highlights the importance of reconnection sites. Generally, the extrapolated fields exhibit the presence of null points co-located with the transients. However, their generation in the corona is non-trivial. Their effect on reconnection in the simultaneous presence of other potential sites is again intriguing. To explore these problems,

1. by our two way approaches with analytical fields, we have shown the generation of 3D null points spontaneously as a dissipative self-organized state for a plasma similar to the solar corona. The simulations show many promising results like formation of current in the topological system and preservation of topological degree even when morphed from the original configuration and importantly may explain the ubiquitous nature of the 3D nulls in the solar atmosphere.
2. in the second study, we investigate the reconnection process in a system accompanying 3D nulls and QSLs concurrently. Here too, we have varied the initial magnetic field with different strength of Lorentz force and with topological complexity. In one case, the 3D nulls lead in driving the reconnection with preferable Lorentz force whereas in the second case, the reconnection is guided by the QSLs with generation of suitable plasma flow. This encourages us to examine reconnection carefully while analyzing the transients with such complex topologies.

The inference of the thesis can be summarized as the reconnection in 3D is definitely complex, particularly owing to the presence of different topologies. Study of different transients culminates to the understanding that a single geometry can lead to different transients, which indicates the requirement of further research to identify the building blocks of reconnection exquisitely. The null points indeed play a crucial role in dictating the process of reconnection in spite of presence of other plausible topologies. Due to their ubiquity, the 3D nulls, along with the QSLs can help in explaining the upper atmospheric dynamics like solar wind generation and can be an important area of future research.

The non-force-free-field extrapolation technique is efficient in obtaining the coronal magnetic field. One of the advantages of this model will be its employment into the upcoming high-resolution data sets, where the force-free-field approximation at the bottom boundary is inaccurate. Though it is natural, but an attempt to study different transients at different layers with multi-instrument data sets, accompanied with numerical modeling will help in understanding the multifaceted reconnection process in solar atmosphere as well as in other astrophysical phenomena.

## 6.2 Future scopes

The thesis work can be extended

1. to develop a more realistic model like a data-driven EULAG-MHD model for the study of transients. In their work, (Tiwari et al., 2014, 2019) point out the role of magnetic flux changes on the photospheric layer in influencing the transients in the upper layer of the atmosphere like chromosphere and lower corona. Majorly reported is the flux cancellation that primarily affect the disturbances. Hence, in this direction, the extended work will focus on the incorporation of variable bottom boundary particularly on varying the line-of-sight component of the magnetic field with updating observed plasma flow.
2. to study the small scale transients are important in understanding the long-standing coronal heating problem. According to Parker's nano-flare model (Parker, 1988), the magnetic field upon small and any arbitrary perturbation, will relax to a state with tangential discontinuity assisting reconnection and dissipation of energy (Pontin & Hornig, 2020). The process is known as the topological dissipation or the idea as Parker problem. There are several attempts are continuously being made to address the problem by studying micro/nano flares both observationally or with the numerical simulation to capture the source of heating in the solar corona. The thesis will focus on this aspect with multi-instrument and high-resolution data

---

sets to explore the contribution of these small scale energetic to the heating and mass motions of the corona.



# Appendix A

## Appendix

### A.1 Ideal limit of MHD, $R_M \gg 1$

Under the ideal limit the induction equation is,

$$\partial \mathbf{B} / \partial t - \nabla \times (\mathbf{v} \times \mathbf{B}) = \mathbf{0}, \quad (\text{A.1})$$

which helps the magnetic field lines to be tied with the plasma parcel as the flux-freezing condition holds.

Alfvén's flux-freezing theorem: In a perfectly conducting plasma, the magnetic flux through any closed contour in the plasma, each element of which moves with the local plasma velocity, is a conserved quantity.

Proof: To prove the above statement, we need to show that the rate of change of magnetic flux in a closed contour moving with a local plasma velocity remains constant with time.

Let's consider a surface  $S$  bounded by a closed contour  $C$ , which moves with a plasma velocity. Then an elementary magnetic flux  $\phi$ , for a constant magnetic field, through an infinitesimal area  $dA$  is

$$d\phi = \mathbf{B} \cdot \hat{n} dA, \quad (\text{A.2})$$

where  $\mathbf{B}$  is a constant magnetic field and  $\hat{n}$  is the unit vector normal to  $A$ . The change in the flux will be achieved by

1. change in magnetic field strength crossing at a fixed location with time  $(\frac{\partial \mathbf{B}}{\partial t} \cdot \hat{n} dA)$ , and
2. the change in the magnetic field at two points separated by an infinitesimal length  $dl$  moving with velocity  $\mathbf{v}$  with respect to time  $(\mathbf{B} \cdot (\mathbf{v} \times dl))$ .

Combining these, we can write the total flux change through the contour C,

$$\frac{d}{dt} \int_S \mathbf{B} \cdot \hat{n} dA = \int_S \frac{\partial \mathbf{B}}{\partial t} \cdot \hat{n} dA + \int_C \mathbf{B} \cdot (\mathbf{v} \times dl). \quad (\text{A.3})$$

Using vector identity,  $\mathbf{a} \cdot (\mathbf{b} \times \mathbf{c}) = (\mathbf{a} \times \mathbf{b}) \cdot \mathbf{c}$ , the second term on the R.H.S. of Eq.-A.3 can be transformed to

$$\mathbf{B} \cdot (\mathbf{v} \times dl) = -(\mathbf{v} \times \mathbf{B}) \cdot dl. \quad (\text{A.4})$$

Now, Eq.-A.3 can be cast as,

$$\frac{d}{dt} \int_S \mathbf{B} \cdot \hat{n} dA = \int_S \frac{\partial \mathbf{B}}{\partial t} \cdot \hat{n} dA - \int_C (\mathbf{v} \times \mathbf{B}) \cdot dl. \quad (\text{A.5})$$

According to Stoke's theorem,

$$\int_C (\mathbf{v} \times \mathbf{B}) \cdot dl = \int_S (\nabla \times (\mathbf{v} \times \mathbf{B})) \cdot \hat{n} dA, \quad (\text{A.6})$$

Therefore, Eq.-A.5 becomes

$$\frac{d}{dt} \int_S \mathbf{B} \cdot \hat{n} dA = \int_S \left( \frac{\partial \mathbf{B}}{\partial t} - \nabla \times (\mathbf{v} \times \mathbf{B}) \right) \cdot \hat{n} dA, \quad (\text{A.7})$$

Applying induction equation, the Eq.-A.7 turns out to be

$$\frac{d}{dt} \int_S \mathbf{B} \cdot \hat{n} dA = 0, \quad (\text{A.8})$$

hence, the magnetic flux remains conserved.

## A.2 Diffusive limit of MHD, $R_M \ll 1$

In the diffusive limit of MHD, the induction equation is

$$\partial \mathbf{B} / \partial t = \lambda \nabla^2 \mathbf{B}. \quad (\text{A.9})$$

above equation has a solution

$$\mathbf{B} = B_0 \exp(-t/\tau_d) \quad (\text{A.10})$$

where  $\tau_d = L^2/\lambda$ . In the above expression,  $L \equiv$  length scale over which magnetic field varies and  $\lambda \equiv$  magnetic diffusivity. Evidently, the magnetic field diffuses faster for a smaller length scale.



# Bibliography

Abramenko, V. I., & Yurchishin, V. B. 1996, *Solar Phys.*, 168, 47

Albright, B. J. 1999, *Physics of Plasmas*, 6, 4222

Alfvén, H. 1942, *Nature*, 150, 405

Alissandrakis, C. E. 1981, *Astron. Astrophys.*, 100, 197

Aly, J. J. 1990, *Computer Physics Communications*, 59, 13

Amari, T., Aly, J. J., Luciani, J. F., Boulmezaoud, T. Z., & Mikic, Z. 1997, *Solar Phys.*, 174, 129

Amari, T., Boulmezaoud, T. Z., & Aly, J. J. 2006, *Astron. Astrophys.*, 446, 691

Amari, T., Boulmezaoud, T. Z., & Maday, Y. 1998, *Astron. Astrophys.*, 339, 252

Amari, T., Boulmezaoud, T. Z., & Mikic, Z. 1999, *Astron. Astrophys.*, 350, 1051

Amari, T., & Luciani, J. F. 1999, *Astrophys. J. Lett.*, 515, L81

Amari, T., Luciani, J. F., Aly, J. J., Mikic, Z., & Linker, J. 2003, *Astrophys. J.*, 595, 1231

Antiochos, S. K., Dahlburg, R. B., & Klimchuk, J. A. 1994, *Astrophys. J. Lett.*, 420, L41

Antiochos, S. K., DeVore, C. R., & Klimchuk, J. A. 1999, *Astrophys. J.*, 510, 485

- Archontis, V., & Török, T. 2008, *Astron. Astrophys.*, 492, L35
- Aschwanden, M. J., Xu, Y., & Jing, J. 2014, *Astrophys. J.*, 797, 50
- Aulanier, G., DeLuca, E. E., Antiochos, S. K., McMullen, R. A., & Golub, L. 2000, *Astrophys. J.*, 540, 1126
- Aulanier, G., & Demoulin, P. 1998, *Astron. Astrophys.*, 329, 1125
- Aulanier, G., Pariat, E., & Démoulin, P. 2005, *Astron. Astrophys.*, 444, 961
- Aulanier, G., Pariat, E., Démoulin, P., & DeVore, C. R. 2006, *Solar Phys.*, 238, 347
- Aulanier, G., Golub, L., DeLuca, E. E., et al. 2007, *Science*, 318, 1588
- Barnes, G., Longcope, D. W., & Leka, K. D. 2005, *Astrophys. J.*, 629, 561
- Bateman, G. 1978, MHD instabilities
- Beaudoin, P., Charbonneau, P., Racine, E., & Smolarkiewicz, P. K. 2013, *Solar Phys.*, 282, 335
- Benz, A. O. 2017, *Living Reviews in Solar Physics*, 14, 2
- Bhattacharyya, R., & Janaki, M. S. 2004, *Physics of Plasmas*, 11, 5615
- Bhattacharyya, R., Janaki, M. S., Dasgupta, B., & Zank, G. P. 2007, *Solar Phys.*, 240, 63
- Bhattacharyya, R., Low, B. C., & Smolarkiewicz, P. K. 2010, *Physics of Plasmas*, 17, 112901
- Book, D. L., Boris, J. P., & Hain, K. 1975, *Journal of Computational Physics*, 18, 248
- Boris, J. P., & Book, D. L. 1973, *Journal of Computational Physics*, 11, 38
- . 1976, *Journal of Computational Physics*, 20, 397
- Borrero, J. M., Tomczyk, S., Kubo, M., et al. 2011, *Solar Phys.*, 273, 267

- Canfield, R. C., Hudson, H. S., & McKenzie, D. E. 1999, *Geophys. Res. Lett.*, 26, 627
- Canfield, R. C., Reardon, K. P., Leka, K. D., et al. 1996, *Astrophys. J.*, 464, 1016
- Carmichael, H. 1964, A Process for Flares, Vol. 50, 451
- Carrington, R. C. 1859, *Mon. Not. Roy. Astron. Soc.*, 20, 13
- Chandrasekhar, S. 1956, Proceedings of the National Academy of Science, 42, 1
- Chandrasekhar, S., & Kendall, P. C. 1957, *Astrophys. J.*, 126, 457
- Chen, H., Zhang, J., Ma, S., et al. 2015, *Astrophys. J. Lett.*, 808, L24
- Chen, J. 1989, *Astrophys. J.*, 338, 453
- Chen, P. F. 2008, *Journal of Astrophysics and Astronomy*, 29, 179
- . 2011, *Living Reviews in Solar Physics*, 8, 1
- Chen, P. F., & Shibata, K. 2000, *Astrophys. J.*, 545, 524
- Chiu, Y. T., & Hilton, H. H. 1977, *Astrophys. J.*, 212, 873
- Clegg, J. R., Bromage, B. J. I., & Browning, P. K. 1999, *Space Sci. Rev.*, 87, 145
- Clegg, J. R., Browning, P. K., Laurence, P., Bromage, B. J. I., & Stredulinsky, E. 2000, *Astron. Astrophys.*, 361, 743
- Clyne, J., & Rast, M. 2005, in Society of Photo-Optical Instrumentation Engineers (SPIE) Conference Series, Vol. 5669, Visualization and Data Analysis 2005, ed. R. F. Erbacher, J. C. Roberts, M. T. Gröhn, & K. Börner, 284–294
- Contopoulos, I. 2013, *Solar Phys.*, 282, 419
- Courant, R., Friedrichs, K., & Lewy, H. 1967, *IBM Journal of Research and Development*, 11, 215

- Culhane, J. L., Harra, L. K., James, A. M., et al. 2007, *Solar Phys.*, 243, 19
- Cuperman, S., Ofman, L., & Semel, M. 1989, *Astron. Astrophys.*, 216, 265
- . 1990a, *Astron. Astrophys.*, 230, 193
- . 1990b, *Astron. Astrophys.*, 227, 583
- Dahlburg, R. B., Antiochos, S. K., & Zang, T. A. 1991, *Astrophys. J.*, 383, 420
- De Pontieu, B., Title, A. M., Lemen, J. R., et al. 2014, *Solar Phys.*, 289, 2733
- De Rosa, M. L., Schrijver, C. J., Barnes, G., et al. 2009, *Astrophys. J.*, 696, 1780
- Démoulin, P. 2006, *Advances in Space Research*, 37, 1269
- Demoulin, P., Bagala, L. G., Mandrini, C. H., Henoux, J. C., & Rovira, M. G. 1997, *Astron. Astrophys.*, 325, 305
- Demoulin, P., Cuperman, S., & Semel, M. 1992, *Astron. Astrophys.*, 263, 351
- Demoulin, P., Henoux, J. C., Priest, E. R., & Mandrini, C. H. 1996, *Astron. Astrophys.*, 308, 643
- Deng, Y., Wang, J., Yan, Y., & Zhang, J. 2001, *Solar Phys.*, 204, 11
- Domaradzki, J. A., & Radhakrishnan, S. 2005, *Fluid Dynamics Research*, 36, 385
- Domaradzki, J. A., Xiao, Z., & Smolarkiewicz, P. K. 2003, *Physics of Fluids*, 15, 3890
- Dombre, T., Frisch, U., Henon, M., Greene, J. M., & Soward, A. M. 1986, *Journal of Fluid Mechanics*, 167, 353
- Domingo, V., Fleck, B., & Poland, A. I. 1995, *Solar Phys.*, 162, 1
- Drenkhahn, G., & Spruit, H. C. 2002, *Astron. Astrophys.*, 391, 1141

- Dungey, J. W. 1953, *The London, Edinburgh, and Dublin Philosophical Magazine and Journal of Science*, 44, 725
- Durrant, C. J. 1989, *Australian Journal of Physics*, 42, 317
- Eisenstat, S. C. 1983, *SIAM Journal on Numerical Analysis*, 20, 358
- Eisenstat, S. C., Elman, H. C., & Schultz, M. H. 1983, *SIAM Journal on Numerical Analysis*, 20, 345
- Fan, Y., & Gibson, S. E. 2007, *Astrophys. J.*, 668, 1232
- Feynman, J., & Martin, S. F. 1995, *J. Geophys. Res.*, 100, 3355
- Galsgaard, K., Priest, E. R., & Titov, V. S. 2003, *Journal of Geophysical Research (Space Physics)*, 108, 1042
- Gary, G. A. 1989, *Astrophys. J. Suppl.*, 69, 323
- . 2001, *Solar Phys.*, 203, 71
- Gary, G. A., & Alexander, D. 1999, *Solar Phys.*, 186, 123
- Gary, G. A., & Hagyard, M. J. 1990, *Solar Phys.*, 126, 21
- Ghizaru, M., Charbonneau, P., & Smolarkiewicz, P. K. 2010, *Astrophys. J. Lett.*, 715, L133
- Giannios, D. 2010, *Mon. Not. Roy. Astron. Soc.*, 408, L46
- Giovanelli, R. G. 1947, *Mon. Not. Roy. Astron. Soc.*, 107, 338
- . 1948, *Mon. Not. Roy. Astron. Soc.*, 108, 163
- Gopalswamy, N., & Kundu, M. R. 1992, *Astrophys. J. Lett.*, 390, L37
- Greene, J. M. 1992, *Journal of Computational Physics*, 98, 194
- Griebel, M., Dornseifer, T., & Neunhoeffler, T. 1998, *Numerical simulation in fluid dynamics: a practical introduction (the Society for Industrial and Applied Mathematics)*

- Grinstein, F. F., Margolin, L. G., & Rider, W. J. 2007, *Implicit large eddy simulation: computing turbulent fluid dynamics* (Cambridge university press), doi:10.1017/CBO9780511618604
- Handy, B. N., Acton, L. W., Kankelborg, C. C., et al. 1999, *Solar Phys.*, 187, 229
- Haynes, A. L., & Parnell, C. E. 2007, *Physics of Plasmas*, 14, 082107
- He, H., & Wang, H. 2008, *Journal of Geophysical Research (Space Physics)*, 113, A05S90
- Hirayama, T. 1974, *Solar Phys.*, 34, 323
- Hodgson, R. 1859, *Mon. Not. Roy. Astron. Soc.*, 20, 15
- Hood, A. W., & Priest, E. R. 1979, *Solar Phys.*, 64, 303
- Hornig, G., & Schindler, K. 1996, *Physics of Plasmas*, 3, 781
- Hoyle, F. 1950, *Quarterly Journal of the Royal Meteorological Society*, 76, 112
- Hu, Q., & Dasgupta, B. 2006, *Geophys. Res. Lett.*, 33, L15106
- . 2008, *Solar Phys.*, 247, 87
- Hu, Q., Dasgupta, B., Choudhary, D. P., & Büchner, J. 2008, *Astrophys. J.*, 679, 848
- Hu, Q., Dasgupta, B., Derosa, M. L., Büchner, J., & Gary, G. A. 2010, *Journal of Atmospheric and Solar-Terrestrial Physics*, 72, 219
- Hudson, H. S., Acton, L. W., & Freeland, S. L. 1996, *Astrophys. J.*, 470, 629
- Inhester, B., & Wiegmann, T. 2006, *Solar Phys.*, 235, 201
- Inoue, S., Hayashi, K., & Kusano, K. 2016, *Astrophys. J.*, 818, 168
- Inoue, S., & Kusano, K. 2006, *Astrophys. J.*, 645, 742
- Jackson, B. V. 1985, *Solar Phys.*, 100, 563

- Janvier, M. 2017, *Journal of Plasma Physics*, 83, 535830101
- Jiang, C., Feng, X., Wu, S. T., & Hu, Q. 2013, *Astrophys. J. Lett.*, 771, L30
- Jiang, C., Wu, S. T., Yurchyshyn, V., et al. 2016, *Astrophys. J.*, 828, 62
- Joshi, B., Kushwaha, U., Veronig, A. M., et al. 2017a, *Astrophys. J.*, 834, 42
- Joshi, B., Thalmann, J. K., Mitra, P. K., Chandra, R., & Veronig, A. M. 2017b, *Astrophys. J.*, 851, 29
- Judge, P. G., Kleint, L., & Sainz Dalda, A. 2015, *Astrophys. J.*, 814, 100
- Kahler, S. W., Reames, D. V., & Sheeley, N. R., J. 2001, *Astrophys. J.*, 562, 558
- Kaiser, M. L., Kucera, T. A., Davila, J. M., et al. 2008, *Space Sci. Rev.*, 136, 5
- Kleint, L., Battaglia, M., Reardon, K., et al. 2015, *Astrophys. J.*, 806, 9
- Kleint, L., Wheatland, M. S., Mastrano, A., & McCauley, P. I. 2018, *Astrophys. J.*, 865, 146
- Kliem, B., & Török, T. 2006, *Phys. Rev. Lett.*, 96, 255002
- Kopp, R. A., & Pneuman, G. W. 1976, *Solar Phys.*, 50, 85
- Kosugi, T., Matsuzaki, K., Sakao, T., et al. 2007, *Solar Phys.*, 243, 3
- Kumar, D., Bhattacharyya, R., & Smolarkiewicz, P. K. 2013, *Physics of Plasmas*, 20, 112903
- . 2015a, *Physics of Plasmas*, 22, 012902
- Kumar, S., & Bhattacharyya, R. 2016, *Physics of Plasmas*, 23, 044501
- . 2017, *Physics of Plasmas*, 24, 064503
- Kumar, S., Bhattacharyya, R., Dasgupta, B., & Janaki, M. S. 2017, *Physics of Plasmas*, 24, 082902

- Kumar, S., Bhattacharyya, R., Joshi, B., & Smolarkiewicz, P. K. 2016, *Astrophys. J.*, 830, 80
- Kumar, S., Bhattacharyya, R., & Smolarkiewicz, P. K. 2014, *Physics of Plasmas*, 21, 052904
- . 2015b, *Physics of Plasmas*, 22, 082903
- Kusano, K., Maeshiro, T., Yokoyama, T., & Sakurai, T. 2004, *Astrophys. J.*, 610, 537
- Kusano, K., & Nishikawa, K. 1996, *Astrophys. J.*, 461, 415
- Lau, Y.-T., & Finn, J. M. 1990, *Astrophys. J.*, 350, 672
- Leka, K. D. 1999, *Solar Phys.*, 188, 21
- Leka, K. D., Barnes, G., Crouch, A. D., et al. 2009, *Solar Phys.*, 260, 83
- Leka, K. D., & Skumanich, A. 1999, *Solar Phys.*, 188, 3
- Lemen, J. R., Title, A. M., Akin, D. J., et al. 2012, *Solar Phys.*, 275, 17
- Levine, R. H., & Altschuler, M. D. 1974, *Solar Phys.*, 36, 345
- Li, Y., & Luhmann, J. 2006, *Astrophys. J.*, 648, 732
- Lin, R. P., Dennis, B. R., Hurford, G. J., et al. 2002, *Solar Phys.*, 210, 3
- Lites, B. W. 2000, *Reviews of Geophysics*, 38, 1
- Liu, R., Kliem, B., Titov, V. S., et al. 2016, *Astrophys. J.*, 818, 148
- Longcope, D. W. 1996, *Solar Phys.*, 169, 91
- . 2005, *Living Reviews in Solar Physics*, 2, 7
- Longcope, D. W., & Cowley, S. C. 1996, *Physics of Plasmas*, 3, 2885
- Longcope, D. W., & Parnell, C. E. 2009, *Solar Phys.*, 254, 51
- Low, B. C. 1996, *Solar Phys.*, 167, 217

- Lüst, R., & Schlüter, A. 1954, *Zeitschrift für Astrophysik*, 34, 263
- Lynch, B. J., Antiochos, S. K., DeVore, C. R., Luhmann, J. G., & Zurbuchen, T. H. 2008, *Astrophys. J.*, 683, 1192
- Lynch, B. J., Antiochos, S. K., MacNeice, P. J., Zurbuchen, T. H., & Fisk, L. A. 2004, *Astrophys. J.*, 617, 589
- MacTaggart, D., & Hood, A. W. 2009, *Astron. Astrophys.*, 508, 445
- Malanushenko, A., Longcope, D. W., & McKenzie, D. E. 2009, *Astrophys. J.*, 707, 1044
- Margolin, L. G., Rider, W. J., & Grinstein, F. F. 2006, *Journal of Turbulence*, 7, 15
- Masson, S., Pariat, E., Aulanier, G., & Schrijver, C. J. 2009, *Astrophys. J.*, 700, 559
- Metcalf, T. R. 1994, *Solar Phys.*, 155, 235
- Metcalf, T. R., De Rosa, M. L., Schrijver, C. J., et al. 2008, *Solar Phys.*, 247, 269
- Mikic, Z., & Linker, J. A. 1994, *Astrophys. J.*, 430, 898
- Mikic, Z., Schnack, D. D., & van Hoven, G. 1990, *Astrophys. J.*, 361, 690
- Moore, R. L., Cirtain, J. W., Sterling, A. C., & Falconer, D. A. 2010, *Astrophys. J.*, 720, 757
- Moore, R. L., Sterling, A. C., Falconer, D. A., & Robe, D. 2013, *Astrophys. J.*, 769, 134
- Moore, R. L., Sterling, A. C., Hudson, H. S., & Lemen, J. R. 2001, *Astrophys. J.*, 552, 833
- Mulay, S. M., Tripathi, D., Del Zanna, G., & Mason, H. 2016, *Astron. Astrophys.*, 589, A79

- Mullan, D. J. 1986, M dwarfs: Theoretical work, Vol. 492, 455–479
- Murphy, N. A., Parnell, C. E., & Haynes, A. L. 2015, *Physics of Plasmas*, 22, 102117
- Nakagawa, Y., & Raadu, M. A. 1972, *Solar Phys.*, 25, 127
- Nakagawa, Y., Wu, S. T., & Tandberg-Hanssen, E. 1978, *Astron. Astrophys.*, 69, 43
- Nayak, S. S., Bhattacharyya, R., Prasad, A., et al. 2019, *Astrophys. J.*, 875, 10
- Nayak, S. S., Bhattacharyya, R., Smolarkiewicz, P. K., Kumar, S., & Prasad, A. 2020, *Astrophys. J.*, 892, 44
- Olshevsky, V., Pontin, D. I., Williams, B., et al. 2020, *Astron. Astrophys.*, 644, A150
- Panesar, N. K., Sterling, A. C., & Moore, R. L. 2017, *Astrophys. J.*, 844, 131
- . 2018, *Astrophys. J.*, 853, 189
- Panesar, N. K., Sterling, A. C., Moore, R. L., & Chakrapani, P. 2016, *Astrophys. J. Lett.*, 832, L7
- Parker, E. N. 1957, *J. Geophys. Res.*, 62, 509
- . 1972, *Astrophys. J.*, 174, 499
- . 1988, *Astrophys. J.*, 330, 474
- . 1994, Spontaneous current sheets in magnetic fields : with applications to stellar x-rays. International Series in Astronomy and Astrophysics, Vol. 1. New York : Oxford University Press, 1994., 1
- . 2012, *Plasma Physics and Controlled Fusion*, 54, 124028
- Parnell, C. E., Haynes, A. L., & Galsgaard, K. 2010a, *Journal of Geophysical Research (Space Physics)*, 115, A02102

- Parnell, C. E., Maclean, R. C., & Haynes, A. L. 2010b, *Astrophys. J. Lett.*, 725, L214
- Parnell, C. E., Maclean, R. C., Haynes, A. L., & Galsgaard, K. 2011, in *Astrophysical Dynamics: From Stars to Galaxies*, ed. N. H. Brummell, A. S. Brun, M. S. Miesch, & Y. Ponty, Vol. 271, 227–238
- Parnell, C. E., Neukirch, T., Smith, J. M., & Priest, E. R. 1997, *Geophysical and Astrophysical Fluid Dynamics*, 84, 245
- Parnell, C. E., Smith, J. M., Neukirch, T., & Priest, E. R. 1996, *Physics of Plasmas*, 3, 759
- Pesnell, W. D., Thompson, B. J., & Chamberlin, P. C. 2012, *Solar Phys.*, 275, 3
- Petschek, H. E. 1964, *Magnetic Field Annihilation*, Vol. 50, 425
- Platten, S. J., Parnell, C. E., Haynes, A. L., Priest, E. R., & Mackay, D. H. 2014, *Astron. Astrophys.*, 565, A44
- Pontin, D., Hornig, G., & Priest, E. 2005, *Geophysical & Astrophysical Fluid Dynamics*, 99, 77
- Pontin, D. I. 2012, *Philosophical Transactions of the Royal Society of London Series A*, 370, 3169
- Pontin, D. I., & Galsgaard, K. 2007, *Journal of Geophysical Research (Space Physics)*, 112, A03103
- Pontin, D. I., & Hornig, G. 2020, *Living Reviews in Solar Physics*, 17, 5
- Pontin, D. I., Hornig, G., & Priest, E. R. 2004, *Geophysical and Astrophysical Fluid Dynamics*, 98, 407
- Pontin, D. I., Priest, E. R., & Galsgaard, K. 2013, *Astrophys. J.*, 774, 154
- Prasad, A., Bhattacharyya, R., Hu, Q., Kumar, S., & Nayak, S. S. 2018, *Astrophys. J.*, 860, 96

- Prasad, A., Bhattacharyya, R., & Kumar, S. 2017, *Astrophys. J.*, 840, 37
- Prasad, A., Dissauer, K., Hu, Q., et al. 2020, *Astrophys. J.*, 903, 129
- Priest, E. 2014, Magnetohydrodynamics of the Sun, doi:10.1017/CBO9781139020732
- Priest, E., & Forbes, T. 2000, Magnetic Reconnection
- Priest, E. R., & Forbes, T. G. 1989, *Solar Phys.*, 119, 211
- . 1992, *J. Geophys. Res.*, 97, 1521
- Priest, E. R., & Pontin, D. I. 2009, *Physics of Plasmas*, 16, 122101
- Priest, E. R., & Titov, V. S. 1996, *Philosophical Transactions of the Royal Society of London Series A*, 354, 2951
- Prusa, J. M., & Smolarkiewicz, P. K. 2003, *Journal of Computational Physics*, 190, 601
- Prusa, J. M., Smolarkiewicz, P. K., & Wyszogrodzki, A. A. 2008, *Computers & Fluids*, 37, 1193
- Pucci, S., Poletto, G., Sterling, A. C., & Romoli, M. 2013, *Astrophys. J.*, 776, 16
- Ram, A. K., Dasgupta, B., Krishnamurthy, V., & Mitra, D. 2014, *Physics of Plasmas*, 21, 072309
- Raouafi, N. E., Patsourakos, S., Parlat, E., et al. 2016, *Space Sci. Rev.*, 201, 1
- Régnier, S. 2013, *Solar Phys.*, 288, 481
- Régnier, S., & Amari, T. 2004, *Astron. Astrophys.*, 425, 345
- Régnier, S., Parnell, C. E., & Haynes, A. L. 2008, *Astron. Astrophys.*, 484, L47
- Rickard, G. J., & Titov, V. S. 1996, *Astrophys. J.*, 472, 840

- Rider, W. J. 2006, *International Journal for Numerical Methods in Fluids*, 50, 1145
- Riley, P., Lionello, R., Mikić, Z., & Linker, J. 2008, *Astrophys. J.*, 672, 1221
- Romanova, M. M., & Lovelace, R. V. E. 1992, *Astron. Astrophys.*, 262, 26
- Roussev, I. I., Forbes, T. G., Gombosi, T. I., et al. 2003, *Astrophys. J. Lett.*, 588, L45
- Ruderman, M. S., & Roberts, B. 2002, *Astrophys. J.*, 577, 475
- Sakurai, T. 1976, *Pub. Astron. Soc. Japan*, 28, 177
- . 1981, *Solar Phys.*, 69, 343
- Sarkar, R., & Srivastava, N. 2018, *Solar Phys.*, 293, 16
- Savcheva, A., & van Ballegoijen, A. 2009, *Astrophys. J.*, 703, 1766
- Schindler, K., Hesse, M., & Birn, J. 1988, *J. Geophys. Res.*, 93, 5547
- Schou, J., Scherrer, P. H., Bush, R. I., et al. 2012, *Solar Phys.*, 275, 229
- Schrijver, C. J., De Rosa, M. L., Metcalf, T. R., et al. 2006, *Solar Phys.*, 235, 161
- Schrijver, C. J., DeRosa, M. L., Metcalf, T., et al. 2008, *Astrophys. J.*, 675, 1637
- Seehafer, N. 1978, *Solar Phys.*, 58, 215
- Semel, M. 1988, *Astron. Astrophys.*, 198, 293
- Shafranov, V. D. 1966, *Reviews of Plasma Physics*, 2, 103
- Shen, Y. 2021, *Proceedings of the Royal Society of London Series A*, 477, 217
- Shibata, K. 1999, *Astrophys. Space Sci.*, 264, 129
- Shibata, K., & Magara, T. 2011, *Living Reviews in Solar Physics*, 8, 6
- Shibata, K., Masuda, S., Shimojo, M., et al. 1995, *Astrophys. J. Lett.*, 451, L83

- Shibata, K., Nitta, N., Matsumoto, R., et al. 1994, in X-ray solar physics from Yohkoh, ed. Y. Uchida, T. Watanabe, K. Shibata, & H. S. Hudson, 29
- Shibata, K., Ishido, Y., Acton, L. W., et al. 1992, *Pub. Astron. Soc. Japan*, 44, L173
- Shimojo, M., Hashimoto, S., Shibata, K., et al. 1996, *Pub. Astron. Soc. Japan*, 48, 123
- Shimojo, M., & Shibata, K. 2000, *Astrophys. J.*, 542, 1100
- Shimojo, M., Shibata, K., & Harvey, K. L. 1998, *Solar Phys.*, 178, 379
- Smolarkiewicz, P., & Szmelter, J. 2011, *Acta Geophysica*, 59, 1109
- Smolarkiewicz, P. K. 1983, *Monthly Weather Review*, 111, 479
- . 1984, *Journal of Computational Physics*, 54, 325
- . 1991, *Monthly Weather Review*, 119, 2505
- . 2006, *International Journal for Numerical Methods in Fluids*, 50, 1123
- Smolarkiewicz, P. K., & Charbonneau, P. 2013, *Journal of Computational Physics*, 236, 608
- Smolarkiewicz, P. K., & Clark, T. L. 1986, *Journal of Computational Physics*, 67, 396
- Smolarkiewicz, P. K., & Grabowski, W. W. 1990, *Journal of Computational Physics*, 86, 355
- Smolarkiewicz, P. K., Grubišić, V., & Margolin, L. G. 1997, *Monthly Weather Review*, 125, 647
- Smolarkiewicz, P. K., & Margolin, L. G. 1993, *Monthly Weather Review*, 121, 1847
- . 1997, *Atmosphere Ocean*, 35, 127

- . 1998, *Journal of Computational Physics*, 140, 459
- Smolarkiewicz, P. K., & Prusa, J. M. 2002, *International Journal for Numerical Methods in Fluids*, 39, 799
- Smolarkiewicz, P. K., & Pudykiewicz, J. A. 1992, *Journal of Atmospheric Sciences*, 49, 2082
- Smolarkiewicz, P. K., & Szmelter, J. 2009, *Journal of Computational Physics*, 228, 33
- Song, M. T., Fang, C., Tang, Y. H., Wu, S. T., & Zhang, Y. A. 2006, *Astrophys. J.*, 649, 1084
- Song, M. T., Fang, C., Zhang, H. Q., et al. 2007, *Astrophys. J.*, 666, 491
- Sterling, A. C., Moore, R. L., Falconer, D. A., & Adams, M. 2015, *Nature*, 523, 437
- Sturrock, P. A. 1966, *Nature*, 211, 695
- Su, Y. 2007, PhD thesis, Purple Mountain Observatory
- Sun, X., Bobra, M. G., Hoeksema, J. T., et al. 2015, *Astrophys. J. Lett.*, 804, L28
- Svestka, Z., & Cliver, E. W. 1992, History and Basic Characteristics of Eruptive Flares, ed. Z. Svestka, B. V. Jackson, & M. E. Machado, Vol. 399, 1
- Sweet, P. A. 1958, in *Electromagnetic Phenomena in Cosmical Physics*, ed. B. Lehnert, Vol. 6, 123
- Tang, F. 1987, *Solar Phys.*, 107, 233
- Thurgood, J. O., Pontin, D. I., & McLaughlin, J. A. 2017, *Astrophys. J.*, 844, 2
- Titov, V. S. 2007, *Astrophys. J.*, 660, 863
- Titov, V. S., Hornig, G., & Démoulin, P. 2002, *Journal of Geophysical Research (Space Physics)*, 107, 1164

- Tiwari, S. K., Alexander, C. E., Winebarger, A. R., & Moore, R. L. 2014, *Astrophys. J. Lett.*, 795, L24
- Tiwari, S. K., Panesar, N. K., Moore, R. L., et al. 2019, *Astrophys. J.*, 887, 56
- Török, T., & Kliem, B. 2005, *Astrophys. J. Lett.*, 630, L97
- Tsuneta, S., Acton, L., Bruner, M., et al. 1991, *Solar Phys.*, 136, 37
- Ugarte-Urra, I., Warren, H. P., & Winebarger, A. R. 2007, *Astrophys. J.*, 662, 1293
- van Ballegooijen, A. A. 2004, *Astrophys. J.*, 612, 519
- van Ballegooijen, A. A., & Martens, P. C. H. 1989, *Astrophys. J.*, 343, 971
- Vasyliunas, V. M. 1975, *Reviews of Geophysics and Space Physics*, 13, 303
- Venkatakrishnan, P., & Gosain, S. 2008, Chapter 4: Solar Magnetism, ed. B. N. Dwivedi & U. Narain, 39–60
- Verbunt, F. 1982, *Space Sci. Rev.*, 32, 379
- Wheatland, M. S. 2006, *Solar Phys.*, 238, 29
- Wheatland, M. S., & Régnier, S. 2009, *Astrophys. J. Lett.*, 700, L88
- Wheatland, M. S., Sturrock, P. A., & Roumeliotis, G. 2000, *Astrophys. J.*, 540, 1150
- Wiegmann, T. 2004, *Solar Phys.*, 219, 87
- Wiegmann, T., & Neukirch, T. 2006, *Astron. Astrophys.*, 457, 1053
- Wiegmann, T., Neukirch, T., Ruan, P., & Inhester, B. 2007, *Astron. Astrophys.*, 475, 701
- Wiegmann, T., & Sakurai, T. 2012, *Living Reviews in Solar Physics*, 9, 5
- Woods, M. M., Harra, L. K., Matthews, S. A., et al. 2017, *Solar Phys.*, 292, 38

- Woods, M. M., Inoue, S., Harra, L. K., et al. 2018, *Astrophys. J.*, 860, 163
- Wu, F., & Wang, Z. Z. 1984, *Acta Astrophysica Sinica*, 4, 272
- Wu, F., & Wang, Z.-z. 1985, *Chin.Astron.Astrophys.*, 9, 44
- Wu, S. T., Sun, M. T., Chang, H. M., Hagyard, M. J., & Gary, G. A. 1990, *Astrophys. J.*, 362, 698
- Wyper, P., & Jain, R. 2010, *Physics of Plasmas*, 17, 092902
- Wyper, P. F., Antiochos, S. K., & DeVore, C. R. 2017, *Nature*, 544, 452
- Wyper, P. F., Jain, R., & Pontin, D. I. 2012, *Astron. Astrophys.*, 545, A78
- Wyper, P. F., & Pontin, D. I. 2014a, *Physics of Plasmas*, 21, 102102
- . 2014b, *Physics of Plasmas*, 21, 082114
- Yan, Y. 1995, *Solar Phys.*, 159, 97
- Yan, Y., Deng, Y., Karlický, M., et al. 2001, *Astrophys. J. Lett.*, 551, L115
- Yan, Y., & Sakurai, T. 1997, *Solar Phys.*, 174, 65
- . 2000, *Solar Phys.*, 195, 89
- Yang, K., Guo, Y., & Ding, M. D. 2016, *Astrophys. J.*, 824, 148
- Yang, W. H., Sturrock, P. A., & Antiochos, S. K. 1986, *Astrophys. J.*, 309, 383
- Yokoyama, T., & Shibata, K. 1995, *Nature*, 375, 42
- Young, P. R., Tian, H., & Jaeggli, S. 2015, *Astrophys. J.*, 799, 218
- Zhang, J., Li, T., & Chen, H. 2017, *Astrophys. J.*, 845, 54
- Zweibel, E. G., & Yamada, M. 2009, *Annu. Rev. Astron. Astrophys.*, 47, 291



# List of Publications

## Publications in Journals

1. A. Prasad, R. Bhattacharyya, Qiang Hu, Sanjay Kumar, and **Sushree S. Nayak**, “A Magnetohydrodynamic Simulation of Magnetic Null-Point Reconnections in NOAA 12192, Initiated with an Extrapolated Non-Force-Free- Field”, *The Astrophysical Journal*, 2018, 860, 96, doi: <https://doi.org/10.3847/1538-4357/aac265>
2. **Sushree S. Nayak**, R. Bhattacharyya, A. Prasad, Qiang Hu, Sanjay Kumar, and B. Joshi, “A Data-constrained Magnetohydrodynamic Simulation of Successive Events of Blowout Jet and C-class Flare in NOAA AR 12615”, *The Astrophysical Journal*, 2019, 875, 10, doi: <https://doi.org/10.3847/1538-4357/ab0a0b>
3. **Sushree S. Nayak**, R. Bhattacharyya, P. K. Smolarkiewicz, Sanjay Kumar, and A. Prasad, “On the Spontaneous Generation of Three-dimensional Magnetic Nulls”, *The Astrophysical Journal*, 2020, 892, 44, doi: <https://doi.org/10.3847/1538-4357/ab75bb>
4. Sanjay Kumar, **Sushree S. Nayak**, Avijeet Prasad, and Ramit Bhattacharyya, “Magnetic Reconnections in the presence of Three-Dimensional Magnetic Nulls and Quasi-Separatrix Layers”, *Solar Physics*, 2021, 296, 26, doi: <https://doi.org/10.1007/s11207-021-01768-7>
5. **Sushree S. Nayak**, R. Bhattacharyya, and Sanjay Kumar, “Magnetohydrodynamics model of an X-class flare in NOAA active region 12017

initiated with non-force-free extrapolation”, *Physics of Plasmas*, 2021, 28, 024502, doi: <https://doi.org/10.1063/5.0035086>

## Conference Proceedings

1. **Sushree S. Nayak**, R. Bhattacharyya, A. Prasad, Q. Hu, (2018), “Magnetic Field Topology from Non-Force-Free-Field Extrapolation and Magnetohydrodynamic Simulation of Its Eventual Dynamics”, *Proceedings of the International Astronomical Union*, 13(S340), 183-184. doi:10.1017/S1743921318001163